Intelligent Model Predictive/Feedback Linearization Control of Half-Car Vehicle Suspension Systems

John Ekoru

A dissertation submitted to the Faculty of Engineering and the Built Environment, University of the Witwatersrand, Johannesburg, in fulfilment of the requirements for the degree of Master of Science in Engineering.

Johannesburg, August 2012

Declaration

I declare that this dissertation is my own, unaided work, except where otherwise acknowledged. It is being submitted for the degree of Master of Science in Engineering at the University of the Witwatersrand, Johannesburg. It has not been submitted before for any degree or examination at any other University.

Signed this ___ day of _____ 20___

_____

John Ekoru.

Acknowledgements

First and foremost, I would like to express deep gratitude to God Almighty for the life, health and grace to carry out this project. I would also like to thank the following people:

- My Mother, Father and the rest of my family for the financial support and encouragement throughout this project.
- Dr. J. O. Pedro, whose deep insight, direction and encouragement were invaluable throughout this project.
- Mr. O. A. Dahunsi, thank you for the foundation you gave me.

Abstract

There exists a level of parametric uncertainty in dynamic systems which if left unaccounted, could impact negatively on performance during implementation. This thesis aims to investigate the effect of acceptably bounded uncertainty, on the performance of Vehicle Suspension Systems (VSS) in the presence of model constraints. The uncertain parameters selected in this work are vehicle sprung mass loading, vehicle forward velocity, suspension spring stiffness coefficients and suspension damper coefficients. A model of a nonlinear, 4 Degree-of-Freedom (DOF) half-car Active Vehicle Suspension Systems (AVSS) with hydraulic actuator dynamics and a similar nonlinear, 4 DOF half-car Passive Vehicle Suspension System (PVSS) model are developed in MATLAB/Simulink®. A two-loop control configuration is designed for the AVSS. This consists of an inner Proportional plus Integral plus Derivative (PID) force feedback control loop; to stabilize the hydraulic actuator and enables tracking of a desired force and an outer control loop for suspension travel control, with the aim of preventing damage by "topping" or "bottoming" (banging of the suspension components on the top or bottom of the suspension workspace). Three control methods are applied to this outer control loop: PID for performance benchmarking, Model Predictive Control (MPC) and Neural Network-based Feedback Linearization (NNFBL). MPC allows for control of systems in the presence of model constraints. NNFBL utilizes an indirect adaptive Neural Network (NN) based identification to linearize highly nonlinear systems into linear ones, allowing application of other control methods thereafter. The performance of the various AVSS controllers are compared with that of the PVSS in the frequency and time domains. In the frequency domain, a road input disturbance with frequency sweeping from $0 - 100\,Hz$ is employed to obtain output data for spectral analysis. In the time domain, a sinusoidal bump road input disturbance and a random road input disturbance are utilized to test vehicle performance. The results indicate that the AVSS is less sensitive to uncertainty in model parameters as compared to the PVSS, by performing better under varying conditions.

Published Work

Aspects of this thesis have been published in the following references:

- Ekoru, J. E. D., Dahunsi, O. A. and Pedro, J. O. (2011). PID Control of a Nonlinear Half-Car Active Suspension System via Force Feedback, *Proceedings of the International IEEE Africon 2011, Livingstone, Zambia, 13-15 September 2011, pp. 1-6*
- Ekoru, J. E. D. and Pedro, J. O. (2012). PID Controller Design for a Nonlinear Half-Car Electro-hydraulic Active Suspension System, *Submitted to the Journal of Zhejiang University-SCIENCE A (Applied Physics & Engineering)*
- Ekoru, J. E. D. and Pedro, J. O. (2012). Intelligent Feedback Linearization-based Control of Half-Car Active Suspension Systems, *Proceedings of the Fourth IASTED African Conference on Modelling and Simulation, AfricaMS 2012, Gaborone, Botswana, 3-5 September 2012*
- Pedro, J and Ekoru, J (2012). NARMA-L2 Control of a Nonlinear Half-Car Servo-Hydraulic Vehicle Suspension System, *Submitted to Acta Polytechnica Hungarica*

Contents

Declaration **i**

Acknowledgements **ii**

Abstract **iii**

Published Work **iv**

Contents **v**

List of Figures **xii**

List of Tables **xxvii**

List of Symbols **xxxi**

List of Acronyms **xxxix**

1 INTRODUCTION **1**

1.1 Research Background and Motivation 1

1.2 Problem Statement 2

1.3 Research Aims and Objectives 3

1.4 Research Scope and Limitations 4

1.5 Research Strategy and Methodology 5

1.6 Research Contributions 5

1.7 Dissertation Outline 7

2 LITERATURE REVIEW **9**

2.1 Introduction 9

2.2 Suspension Systems 9

2.3 Classification of Vehicle Suspension Systems 10

2.4 Vehicle Suspension System Mathematical Models 11

2.5 High and Low Bandwidth Active Vehicle Suspension Systems 13

2.6 Nonlinearity in Suspension Systems 15

2.6.1 Suspension System Constraints 17

2.7 Actuators in Active Vehicle Suspension Systems 17

2.8 The Need for Actuator Force Feedback 18

2.9 Control of Active Vehicle Suspension Systems 19

2.9.1 Robust Control Methods 19

2.9.2 Nonlinear Control Methods 21

2.10 Control Methods Directly Related to this Work 21

2.10.1 Application of PID control for AVSS 21

2.10.2 Application of Feedback Linearization Control for AVSS . . . 22

2.10.3 Application of Model Predictive Control for AVSS 22

2.10.4 Application of Neural Network-based Control for AVSS . . . 23

2.10.4.1 Artificial Neural Networks 23

2.10.4.2 Application of Neural Network-based Feedback Linearization Control for AVSS 26

2.11 Conclusion 27

3 PHYSICAL AND MATHEMATICAL MODELLING 28

3.1 Introduction 28

3.2 Modelling Assumptions 28

3.3 Nonlinear Suspension Modelling 29

3.4 Tyre Force Modelling 31

3.5 Input Disturbance Modelling 32

3.5.1 Discrete Input Disturbance 33

3.5.2 Random Input Disturbance 34

3.6 Hydraulic Actuator Modelling 36

3.7 Nonlinear AVSS with Hydraulic Actuator Dynamics 37

3.8 Nonlinear Passive Vehicle Suspension System 38

3.9 State-Space Form of AVSS Equations of Motion 40

3.10 Conclusion 42

4 PERFORMANCE SPECIFICATIONS 44

4.1 Introduction 44

4.2 Performance Specifications 44

4.3 Conclusion 48

5 PID CONTROL OF A NONLINEAR ACTIVE SUSPENSION VIA PID FORCE FEEDBACK 50

5.1 Introduction 50

5.2 Controller Design 51

5.2.1 Controller Architecture 51

5.2.2 PID Force Control Loop Design 51

5.2.3 PID Suspension Travel Control Loop Design 52

5.3 Simulation Results and Discussion 53

5.3.1 Sinusoidal Bump Input Disturbance 54

5.3.1.1 System Response at $V = 45\,km/h$ 54

5.3.1.2 System Response at $V = 60\,km/h$ 60

5.3.1.3 System Response at $V = 75\,km/h$ 66

5.3.2 Random Input Disturbance 74

5.3.2.1 System Response at $V = 45\,km/h$ 74

5.3.2.2 System Response at $V = 60\,km/h$ 81

5.3.2.3 System Response at $V = 75\,km/h$ 90

5.3.3 Uncertainty Analysis 97

5.3.3.1 Variation of Sprung Mass Loading 97

5.3.3.2 Variation of Suspension Spring Coefficient 101

5.3.3.3 Variation of Suspension Damping Coefficient 105

5.4 Conclusion 109

6 MODEL PREDICTIVE CONTROL OF A NONLINEAR ACTIVE SUSPENSION VIA PID FORCE FEEDBACK 111

6.1 Introduction 111

6.2 Controller Design 112

6.2.1 Controller Architecture 112

6.2.2 PID Force Control Loop Design 113

6.2.3 MPC Suspension Travel Control Loop 113

6.3 Simulation Results and Discussion 116

6.3.1 Variation of suspension spring coefficient in the frequency domain 117

6.3.2 Variation of suspension spring coefficients: Sinusoidal Bump Input Disturbance 119

6.3.3 Variation of suspension spring coefficients: Random Input Disturbance 129

6.4 Conclusion 136

7 NEURAL NETWORK-BASED FEEDBACK LINEARIZATION CONTROL OF A NONLINEAR ACTIVE SUSPENSION VIA PID FORCE FEEDBACK 140

7.1 Introduction 140

7.2 Controller Design 141

7.2.1 PID Force Control Loop Design 141

7.2.2 NNFBL Suspension Travel Control Loop Design 142

7.2.2.1 Experimentation 143

7.2.2.2 Model Structure Selection 146

7.2.2.3 Model Estimation 148

7.2.2.4 Model Validation 149

7.3 Simulation Results and Discussion 151

7.3.1 Sinusoidal Bump Input Disturbance 158

7.3.1.1 System Response at $V = 45\,km/h$ 158

7.3.1.2 System Response at $V = 60\,km/h$ 164

7.3.1.3 System Response at $V = 75\,km/h$ 171

7.3.2 Random Input Disturbance 180

7.3.2.1 System Response at $V = 45\,km/h$ 180

7.3.2.2 System Response at $V = 60\,km/h$ 187

7.3.2.3 System Response at $V = 75\,km/h$ 194

7.3.3 Uncertainty Analysis 202

7.3.3.1 Variation of Sprung Mass Loading 202

7.3.3.2 Variation of Suspension Spring Coefficient 207

7.3.3.3 Variation of Suspension Damping Coefficient 211

7.4 Conclusion 214

8 CONCLUSIONS AND FUTURE RECOMMENDATIONS 216

8.1 Conclusions 216

8.2 Future Recommendations 217

REFERENCES 219

A Mathematical Model Implementation in Matlab/Simulink® 229

A.1 Nonlinear Suspension Implementation 229

A.2 Tyre Model Implementation 232

A.3 Input Disturbance Implementation 233

A.4 Hydraulic Actuator Implementation 234

A.5 Nonlinear Suspension with Hydraulic Actuator Dynamics 236

List of Figures

1.1 Research methodology. 6

2.1 Differences between quarter-car PVSS, SAVSS and AVSS. 12

2.2 Schematic of a half-car AVSS model for observing vehicle pitching motion. 12

2.3 Difference between Low Bandwidth type 1 and type 2 AVSS. 16

3.1 Free-body diagram of a half-car AVSS. 30

3.2 Parameters used in computing the discrete road input disturbance (Sinusoidal bump on a smooth road). 33

3.3 Discrete road input disturbance height w_i vs. disturbance wavelength λ. 34

3.4 Random road input disturbance. 35

3.5 A double-acting hydraulic actuator. 37

4.1 Positions of axes on human body for measurement of vibration-induced discomfort. 47

5.1 Control architecture for PID control of a nonlinear AVSS via PID force feedback. 51

5.2 Inner PID force feedback control loop. 52

5.3 Front suspension travel for 80%, 100% and 120% Ms at $V = 45\,km/h$. 56

5.4 Rear suspension travel for 80%, 100% and 120% Ms at $V = 45\,km/h$. 57

5.5 Front dynamic tyre force for 80%, 100% and 120% Ms at $V = 45\,km/h$. 57

5.6 Rear dynamic tyre force for 80%, 100% and 120% Ms at $V = 45\,km/h$. 58

5.7 Sprung mass acceleration for 80%, 100% and 120% Ms at $V = 45\,km/h$. 58

5.8 Pitch angular acceleration for 80%, 100% and 120% Ms at $V = 45\,km/h$. 59

5.9 Front and rear actuator control voltage for 80%, 100% and 120% Ms at $V = 45\,km/h$. 60

5.10 Front and rear actuator spool-valve displacement for 80%, 100% and 120% Ms at $V = 45\,km/h$. 61

5.11 Front and rear actuator force for 80%, 100% and 120% Ms at $V = 45\,km/h$. 61

5.12 Front suspension travel for 80%, 100% and 120% Ms at $V = 60\,km/h$. 63

5.13 Rear suspension travel for 80%, 100% and 120% Ms at $V = 60\,km/h$. 63

5.14 Front dynamic tyre force for 80%, 100% and 120% Ms at $V = 60\,km/h$. 64

5.15 Rear dynamic tyre force for 80%, 100% and 120% Ms at $V = 60\,km/h$. 65

5.16 Sprung mass acceleration for 80%, 100% and 120% Ms at $V = 60\,km/h$. 65

5.17 Pitch angular acceleration for 80%, 100% and 120% Ms at $V = 60\,km/h$. 67

5.18 Front and rear actuator control voltage for 80%, 100% and 120% Ms at $V = 60\,km/h$. 67

5.19 Front and rear actuator spool-valve displacement for 80%, 100% and 120% Ms at $V = 60\,km/h$. 68

5.20 Front and rear actuator force for 80%, 100% and 120% Ms at $V = 60\,km/h$. 68

5.21 Front suspension travel for 80%, 100% and 120% Ms at $V = 75\,km/h$. 70

5.22 Rear suspension travel for 80%, 100% and 120% Ms at $V = 75\,km/h$. 71

5.23 Front dynamic tyre force for 80%, 100% and 120% Ms at $V = 75\,km/h$. 71

5.24 Rear dynamic tyre force for 80%, 100% and 120% Ms at $V = 75\,km/h$. 72

5.25 Sprung mass acceleration for 80%, 100% and 120% Ms at $V = 75\,km/h$. 72

5.26 Pitch angular acceleration for 80%, 100% and 120% Ms at $V = 75\,km/h$. 73

5.27 Front and rear actuator control voltage for 80%, 100% and 120% Ms at $V = 75\,km/h$. 74

5.28 Front and rear actuator spool-valve displacement for 80%, 100% and 120% Ms at $V = 75\,km/h$. 75

5.29 Front and rear actuator force for 80%, 100% and 120% Ms at $V = 75\,km/h$. 75

5.30 Front suspension travel for 80%, 100% and 120% Ms at $V = 45\,km/h$. 77

5.31 Rear suspension travel for 80%, 100% and 120% Ms at $V = 45\,km/h$. 78

5.32 Front dynamic tyre force for 80%, 100% and 120% Ms at $V = 45\,km/h$. 78

5.33 Rear dynamic tyre force for 80%, 100% and 120% Ms at $V = 45\,km/h$. 79

5.34 Sprung mass acceleration for 80%, 100% and 120% Ms at $V = 45\,km/h$. 79

5.35 Pitch angular acceleration for 80%, 100% and 120% Ms at $V = 45\,km/h$. 80

5.36 Front and rear actuator control voltage for 80%, 100% and 120% Ms at $V = 45\,km/h$. 81

5.37 Front and rear actuator spool-valve displacement for 80%, 100% and 120% Ms at $V = 45\,km/h$. 82

5.38 Front and rear actuator force for 80%, 100% and 120% Ms at $V = 45\,km/h$. 82

5.39 Front suspension travel for 80%, 100% and 120% Ms at $V = 60\,km/h$. 84

5.40 Rear suspension travel for 80%, 100% and 120% Ms at $V = 60\,km/h$. 85

5.41 Front dynamic tyre force for 80%, 100% and 120% Ms at $V = 60\,km/h$. 85

5.42 Rear dynamic tyre force for 80%, 100% and 120% Ms at $V = 60\,km/h$. 86

5.43 Sprung mass acceleration for 80%, 100% and 120% Ms at $V = 60\,km/h$. 87

5.44 Pitch angular acceleration for 80%, 100% and 120% Ms at $V = 60\,km/h$. 88

5.45 Front and rear actuator control voltage for 80%, 100% and 120% Ms at $V = 60\,km/h$. 88

5.46 Front and rear actuator spool-valve displacement for 80%, 100% and 120% Ms at $V = 60\,km/h$. 89

5.47 Front and rear actuator force for 80%, 100% and 120% Ms at $V = 60\,km/h$. 89

5.48 Front suspension travel for 80%, 100% and 120% Ms at $V = 75\,km/h$. 90

5.49 Rear suspension travel for 80%, 100% and 120% Ms at $V = 75\,km/h$. 92

5.50 Front dynamic tyre force for 80%, 100% and 120% Ms at $V = 75\,km/h$. 92

5.51 Rear dynamic tyre force for 80%, 100% and 120% Ms at $V = 75\,km/h$. 93

5.52 Sprung mass acceleration for 80%, 100% and 120% Ms at $V = 75\,km/h$. 94

5.53 Pitch angular acceleration for 80%, 100% and 120% Ms at $V = 75\,km/h$. 95

5.54 Front and rear actuator control voltage for 80%, 100% and 120% Ms at $V = 75\,km/h$. 95

5.55 Front and rear actuator spool-valve displacement for 80%, 100% and 120% Ms at $V = 75\,km/h$. 96

5.56 Front and rear actuator force for 80%, 100% and 120% Ms at $V = 75\,km/h$. 96

5.57 Front suspension travel PSD for $\Delta = \pm 20\%$ variation in Ms and I_θ about their nominal values. 98

5.58 Rear suspension travel PSD for $\Delta = \pm 20\%$ variation in Ms and I_θ about their nominal values. 99

5.59 Front dynamic tyre force PSD for $\Delta = \pm 20\%$ variation in Ms and I_θ about their nominal values. 99

5.60 Rear dynamic tyre force PSD for $\Delta = \pm 20\%$ variation in Ms and I_θ about their nominal values. 100

5.61 Sprung mass acceleration PSD for $\Delta = \pm 20\%$ variation in Ms and I_θ about their nominal values. 101

5.62 Pitch angular acceleration PSD for $\Delta = \pm 20\%$ variation in Ms and I_θ about their nominal values. 102

5.63 Front suspension travel PSD for $\Delta = \pm 30\%$ variation in ks_i^l and ks_i^{nl} about their nominal values. 102

5.64 Rear suspension travel PSD for $\Delta = \pm 30\%$ variation in ks_i^l and ks_i^{nl} about their nominal values. 103

5.65 Front dynamic tyre force PSD for $\Delta = \pm 30\%$ variation in ks_i^l and ks_i^{nl} about their nominal values. 104

5.66 Rear dynamic tyre force PSD for $\Delta = \pm 30\%$ variation in ks_i^l and ks_i^{nl} about their nominal values. 104

5.67 Sprung mass acceleration PSD for $\Delta = \pm 30\%$ variation in ks_i^l and ks_i^{nl} about their nominal values. 105

5.68 Pitch angular acceleration PSD for $\Delta = \pm 30\%$ variation in ks_i^l and ks_i^{nl} about their nominal values. 106

5.69 Front suspension travel PSD for $\Delta = \pm 30\%$ variation in bs_i^l, bs_i^{nl} and bs_i^{sym} about their nominal values. 106

5.70 Rear suspension travel PSD for $\Delta = \pm 30\%$ variation in bs_i^l, bs_i^{nl} and bs_i^{sym} about their nominal values. 107

5.71 Front dynamic tyre force PSD for $\Delta = \pm 30\%$ variation in bs_i^l, bs_i^{nl} and bs_i^{sym} about their nominal values. 108

5.72 Rear dynamic tyre force PSD for $\Delta = \pm 30\%$ variation in bs_i^l, bs_i^{nl} and bs_i^{sym} about their nominal values. 108

5.73 Sprung mass acceleration PSD for $\Delta = \pm 30\%$ variation in bs_i^l, bs_i^{nl} and bs_i^{sym} about their nominal values. 109

5.74 Pitch angular acceleration PSD for $\Delta = \pm 30\%$ variation in bs_i^l, bs_i^{nl} and bs_i^{sym} about the nominal values. 110

6.1 Control architecture for MPC Control of a nonlinear active vehicle suspension via PID force feedback. 112

6.2 Inner PID force feedback control loop. 113

6.3 Illustration of MPC control at sampling instant k. 115

6.4 Front suspension travel PSD for $\Delta = \pm 30\%$ variation in ks_i^l and ks_i^{nl} about their nominal values. 117

6.5 Rear suspension travel PSD for $\Delta = \pm 30\%$ variation in ks_i^l and ks_i^{nl} about their nominal values. 118

6.6 Front dynamic tyre force PSD for $\Delta = \pm 30\%$ variation in ks_i^l and ks_i^{nl} about their nominal values. 118

6.7 Rear dynamic tyre force PSD for $\Delta = \pm 30\%$ variation in ks_i^l and ks_i^{nl} about their nominal values. 119

6.8 Sprung mass acceleration PSD for $\Delta = \pm 30\%$ variation in ks_i^l and ks_i^{nl} about their nominal values. 120

6.9 Pitch angular acceleration PSD for $\Delta = \pm 30\%$ variation in ks_i^l and ks_i^{nl} about their nominal values. 120

6.10 Front suspension travel time history for $\Delta = \pm 30\%$ variation in ks_i^l and ks_i^{nl} about their nominal values. 121

6.11 Rear suspension travel time history for $\Delta = \pm 30\%$ variation in ks_i^l and ks_i^{nl} about their nominal values. 123

6.12 Front dynamic tyre force time history for $\Delta = \pm 30\%$ variation in ks_i^l and ks_i^{nl} about their nominal values. 124

6.13 Rear dynamic tyre force time history for $\Delta = \pm 30\%$ variation in ks_i^l and ks_i^{nl} about their nominal values. 125

6.14 Sprung mass acceleration time history for $\Delta = \pm 30\%$ variation in ks_i^l and ks_i^{nl} about their nominal values. 125

6.15 Pitch angular acceleration time history for $\Delta = \pm 30\%$ variation in ks_i^l and ks_i^{nl} about their nominal values. 126

6.16 Front and rear actuator control voltage time history for $\Delta = \pm 30\%$ variation in ks_i^l and ks_i^{nl} about their nominal values. 127

6.17 Front and rear actuator spool-valve displacement time history for $\Delta = \pm 30\%$ variation in ks_i^l and ks_i^{nl} about their nominal values. 128

6.18 Front and rear actuator force time history for $\Delta = \pm 30\%$ variation in ks_i^l and ks_i^{nl} about their nominal values. 129

6.19 Front suspension travel time history for $\Delta = \pm 30\%$ variation in ks_i^l and ks_i^{nl} about their nominal values. 131

6.20 Rear suspension travel time history for $\Delta = \pm 30\%$ variation in ks_i^l and ks_i^{nl} about their nominal values. 132

6.21 Front dynamic tyre force time history for $\Delta = \pm 30\%$ variation in ks_i^l and ks_i^{nl} about their nominal values. 133

6.22 Rear dynamic tyre force time history for $\Delta = \pm 30\%$ variation in ks_i^l and ks_i^{nl} about their nominal values. 133

6.23 Sprung mass acceleration time history for $\Delta = \pm 30\%$ variation in ks_i^l and ks_i^{nl} about their nominal values. 134

6.24 Pitch angular acceleration time history for $\Delta = \pm 30\%$ variation in ks_i^l and ks_i^{nl} about their nominal values. 135

6.25 Front and rear actuator control voltage time history for $\Delta = \pm 30\%$ variation in ks_i^l and ks_i^{nl} about their nominal values. 136

6.26 Front and rear actuator spool-valve displacement time history for $\Delta = \pm 30\%$ variation in ks_i^l and ks_i^{nl} about their nominal values. 137

6.27 Front and rear actuator force time history for $\Delta = \pm 30\%$ variation in ks_i^l and ks_i^{nl} about their nominal values. 138

7.1 Control architecture for NNFBL control of a nonlinear active vehicle suspension via PID force feedback. 141

7.2 Inner PID force feedback control loop. 142

7.3 System identification of a nonlinear half-car AVSS for NNFBL control. 143

7.4 Front suspension I/O data for Neural Network system identification for NNFBL control. 144

7.5 Rear suspension I/O data for Neural Network system identification for NNFBL control. 145

7.6 NARMA-L2 NN model for approximation of nonlinear functions $f[\cdot]$ and $g[\cdot]$. 147

7.7 Use of the identified NARMA model to obtain NARMA-L2 control input $u_i(t+1)$. 147

7.8 NARMA-L2 Controller implementation. 148

7.9 Front suspension NN training data for NNFBL control. 151

7.10 Rear suspension NN training data for NNFBL control. 152

7.11 Front suspension NN validation data for NNFBL control. 152

7.12 Rear suspension NN validation data for NNFBL control. 153

7.13 Front suspension NN testing data for NNFBL control. 153

7.14 Rear suspension NN testing data for NNFBL control. 154

7.15 Front suspension data regression plot for NNFBL Input-Output (I/O) data. 154

7.16 Rear suspension data regression plot for NNFBL Input-Output (I/O) data. 155

7.17 Front suspension data MSE plot for NNFBL Input-Output (I/O) data. 155

7.18 Rear suspension data MSE plot for NNFBL Input-Output (I/O) data. 156

7.19 Front suspension data training state plot for NNFBL Input-Output (I/O) data. 156

7.20 Rear suspension data training state plot for NNFBL Input-Output (I/O) data. 157

7.21 Front suspension travel for 80%, 100% and 120% Ms at $V = 45\,km/h$. 160

7.22 Rear suspension travel for 80%, 100% and 120% Ms at $V = 45\,km/h$. 160

7.23 Front dynamic tyre force for 80%, 100% and 120% Ms at $V = 45\,km/h$. 161

7.24 Rear dynamic tyre force for 80%, 100% and 120% Ms at $V = 45\,km/h$. 161

7.25 Sprung mass acceleration for 80%, 100% and 120% Ms at $V = 45\,km/h$. 162

7.26 Pitch angular acceleration for 80%, 100% and 120% Ms at $V = 45\,km/h$. 163

7.27 Front and rear actuator control voltage for 80%, 100% and 120% Ms at $V = 45\,km/h$. 164

7.28 Front and rear actuator spool-valve displacement for 80%, 100% and 120% Ms at $V = 45\,km/h$. 165

7.29 Front and rear actuator force for 80%, 100% and 120% Ms at $V = 45\,km/h$. 165

7.30 Front suspension travel for 80%, 100% and 120% Ms at $V = 60\,km/h$. 167

7.31 Rear suspension travel for 80%, 100% and 120% Ms at $V = 60\,km/h$. 167

7.32 Front dynamic tyre force for 80%, 100% and 120% Ms at $V = 60\,km/h$. 168

7.33 Rear dynamic tyre force for 80%, 100% and 120% Ms at $V = 60\,km/h$. 169

7.34 Sprung mass acceleration for 80%, 100% and 120% Ms at $V = 60\,km/h$. 169

7.35 Pitch angular acceleration for 80%, 100% and 120% Ms at $V = 60\,km/h$. 170

7.36 Front and rear actuator control voltage for 80%, 100% and 120% Ms at $V = 60\,km/h$. 171

7.37 Front and rear actuator spool-valve displacement for 80%, 100% and 120% Ms at $V = 60\,km/h$. 172

7.38 Front and rear actuator force for 80%, 100% and 120% Ms ator $V = 60\,km/h$. 172

7.39 Front suspension travel for 80%, 100% and 120% Ms at $V = 75\,km/h$. 174

7.40 Rear suspension travel for 80%, 100% and 120% Ms at $V = 75\,km/h$. 175

7.41 Front dynamic tyre force for 80%, 100% and 120% Ms at $V = 75\,km/h$. 175

7.42 Rear dynamic tyre force for 80%, 100% and 120% Ms at $V = 75\,km/h$. 176

7.43 Sprung mass acceleration for 80%, 100% and 120% Ms at $V = 75\,km/h$. 177

7.44 Pitch angular acceleration for 80%, 100% and 120% Ms at $V = 75\,km/h$. 178

7.45 Front and rear actuator control voltage for 80%, 100% and 120% Ms at $V = 75\,km/h$. 178

7.46 Front and rear actuator spool-valve displacement for 80%, 100% and 120% Ms at $V = 75\,km/h$. 179

7.47 Front and rear actuator force for 80%, 100% and 120% Ms at $V = 75\,km/h$. 179

7.48 Front suspension travel for 80%, 100% and 120% Ms at $V = 45\,km/h$. 180

7.49 Rear suspension travel for 80%, 100% and 120% Ms at $V = 45\,km/h$. 182

7.50 Front dynamic tyre force for 80%, 100% and 120% Ms at $V = 45\,km/h$. 182

7.51 Rear dynamic tyre force for 80%, 100% and 120% Ms at $V = 45\,km/h$. 183

7.52 Sprung mass acceleration for 80%, 100% and 120% Ms at $V = 45\,km/h$. 184

7.53 Pitch angular acceleration for 80%, 100% and 120% Ms at $V = 45\,km/h$. 185

7.54 Front and rear actuator control voltage for 80%, 100% and 120% Ms at $V = 45\,km/h$. 185

7.55 Front and rear actuator spool-valve displacement for 80%, 100% and 120% Ms at $V = 45\,km/h$. 186

7.56 Front and rear actuator force for 80%, 100% and 120% Ms at $V = 45\,km/h$. 186

7.57 Front suspension travel for 80%, 100% and 120% Ms at $V = 60\,km/h$. 187

7.58 Rear suspension travel for 80%, 100% and 120% Ms at $V = 60\,km/h$. 189

7.59 Front dynamic tyre force for 80%, 100% and 120% Ms at $V = 60\,km/h$. 189

7.60 Rear dynamic tyre force for 80%, 100% and 120% Ms at $V = 60\,km/h$. 190

7.61 Sprung mass acceleration for 80%, 100% and 120% Ms at $V = 60\,km/h$. 191

7.62 Pitch angular acceleration for 80%, 100% and 120% Ms at $V = 60\,km/h$. 192

7.63 Front and rear actuator control voltage for 80%, 100% and 120% Ms at $V = 60\,km/h$. 192

7.64 Front and rear actuator spool-valve displacement for 80%, 100% and 120% Ms at $V = 60\,km/h$. 193

7.65 Front and rear actuator force for 80%, 100% and 120% Ms at $V = 60\,km/h$. 193

7.66 Front suspension travel for 80%, 100% and 120% Ms at $V = 75\,km/h$. 194

7.67 Rear suspension travel for 80%, 100% and 120% Ms at $V = 75\,km/h$. 196

7.68 Front dynamic tyre force for 80%, 100% and 120% Ms at $V = 75\,km/h$. 197

7.69 Rear dynamic tyre force for 80%, 100% and 120% Ms at $V = 75\,km/h$. 197

7.70 Sprung mass acceleration for 80%, 100% and 120% Ms at $V = 75\,km/h$. 198

7.71 Pitch angular acceleration for 80%, 100% and 120% Ms at $V = 75\,km/h$. 199

7.72 Front and rear actuator control voltage for 80%, 100% and 120% Ms at $V = 75\,km/h$. 200

7.73 Front and rear actuator spool-valve displacement for 80%, 100% and 120% Ms at $V = 75\,km/h$. 201

7.74 Front and rear actuator force for 80%, 100% and 120% Ms at $V = 75\,km/h$. 201

7.75 Front suspension travel PSD for $\Delta = \pm 20\%$ variation in Ms and I_θ about their nominal values. 203

7.76 Rear suspension travel PSD for $\Delta = \pm 20\%$ variation in Ms and I_θ about their nominal values. 204

7.77 Front dynamic tyre force PSD for $\Delta = \pm 20\%$ variation in Ms and I_θ about their nominal values. 204

7.78 Rear dynamic tyre force PSD for $\Delta = \pm 20\%$ variation in Ms and I_θ about their nominal values. 205

7.79 Sprung mass acceleration PSD for $\Delta = \pm 20\%$ variation in Ms and I_θ about their nominal values. 206

7.80 Pitch angular acceleration PSD for $\Delta = \pm 20\%$ variation in Ms and I_θ about their nominal values. 206

7.81 Front suspension travel PSD for $\Delta = \pm 30\%$ variation in ks_i^l and ks_i^{nl} about their nominal values. 207

7.82 Rear suspension travel PSD for $\Delta = \pm 30\%$ variation in ks_i^l and ks_i^{nl} about their nominal values. 208

7.83 Front dynamic tyre force PSD for $\Delta = \pm 30\%$ variation in ks_i^l and ks_i^{nl} about their nominal values. 208

7.84 Rear dynamic tyre force PSD for $\Delta = \pm 30\%$ variation in ks_{si}^{l} and ks_{i}^{nl} about their nominal values. 209

7.85 Sprung mass acceleration PSD for $\Delta = \pm 30\%$ variation in ks_{i}^{l} and ks_{i}^{nl} about their nominal values. 210

7.86 Pitch angular acceleration PSD for $\Delta = \pm 30\%$ variation in ks_{i}^{l} and ks_{i}^{nl} about their nominal values. 210

7.87 Front suspension travel PSD for $\Delta = \pm 30\%$ variation in bs_{i}^{l}, bs_{i}^{nl} and bs_{i}^{sym} about their nominal values. 211

7.88 Rear suspension travel PSD for $\Delta = \pm 30\%$ variation in bs_{i}^{l}, bs_{i}^{nl} and bs_{i}^{sym} about their nominal values. 212

7.89 Front dynamic tyre force PSD for $\Delta = \pm 30\%$ variation in bs_{i}^{l}, bs_{i}^{nl} and bs_{i}^{sym} about their nominal values. 213

7.90 Rear dynamic tyre force PSD for $\Delta = \pm 30\%$ variation in bs_{i}^{l}, bs_{i}^{nl} and bs_{i}^{sym} about their nominal values. 213

7.91 Sprung mass acceleration PSD for $\Delta = \pm 30\%$ variation in bs_{i}^{l}, bs_{i}^{nl} and bs_{i}^{sym} about their nominal values. 214

7.92 Pitch angular acceleration PSD for $\Delta = \pm 30\%$ variation in bs_{i}^{l}, bs_{i}^{nl} and bs_{i}^{sym} about the nominal values. 215

A.1 Matlab/Simulink® implementation of front displacement z_f and front velocity $\dot{z}_f$ of the vehicle body (sprung mass) for large angular displacements about the vehicle center of gravity from Equations 3.1 and 3.2, in Section 3.3. 229

A.2 Matlab/Simulink® implementation of rear displacement z_r and rear velocity $\dot{z}_r$ of the vehicle body (sprung mass) for large angular displacements about the vehicle center of gravity from Equations 3.3 and 3.4, in Section 3.3. 230

A.3 Matlab/Simulink® implementation of the nonlinear front suspension spring force F_{ksf} of Equation 3.5, Section 3.3. 230

A.4 Matlab/Simulink® implementation of the nonlinear rear suspension spring force F_{ksr} of Equation 3.6, Section 3.3. 230

A.5 Matlab/Simulink® implementation of nonlinear front suspension damper force F_{bsf} of Equation 3.7, Section 3.3. 231

A.6 Matlab/Simulink® implementation of nonlinear rear suspension damper force F_{bsr} of Equation 3.8, Section 3.3. 231

A.7 Matlab/Simulink® implementation of front tyre force F_{tf}, the sum of F_{ktf} (front tyre spring force) given in Equation 3.11 and F_{btf} (front tyre damping force) of Equation 3.12, Section 3.4. 232

A.8 Matlab/Simulink® implementation of rear tyre force F_{tr}, the sum of F_{ktr} and F_{btr}, rear tyre spring force and rear tyre damping force given in Equations 3.14 and 3.15 respectively, Section 3.4. 232

A.9 Matlab/Simulink® implementation of the Discrete Input Disturbance at the front wheel, w_f, (see Equation 3.17, Section 3.5.1). 233

A.10 Matlab/Simulink® implementation of the Random Input Disturbance at the front wheel, w_f, (see Equation 3.21, Section 3.5.2). 233

A.11 Matlab/Simulink® implementation of front actuator hydraulic load flow, Q_f, (see Equation 3.29 from Section 3.6). 234

A.12 Matlab/Simulink® implementation of rear actuator hydraulic load flow, Q_r, (see Equation 3.29 from Section 3.6). 234

A.13 Matlab/Simulink® implementation of front actuator pressure drop across the hydraulic piston, Pl_f, (see Equation 3.30 from Section 3.6). 234

A.14 Matlab/Simulink® implementation of rear actuator pressure drop across the hydraulic piston, Pl_r, (see Equation 3.30 from Section 3.6). 235

A.15 Matlab/Simulink® implementation of front hydraulic actuator Servo-Valve displacement, x_{vf}, from Equation 3.23, in Section 3.6. 235

A.16 Matlab/Simulink® implementation of rear hydraulic actuator Servo-Valve displacement, x_{vr}, from Equation 3.23, in Section 3.6. 235

A.17 Matlab/Simulink® implementation of $\ddot{z}_c$, acceleration of the sprung mass center of gravity given in Equation 3.34, in Section 3.7. 236

A.18 Matlab/Simulink® implementation of sprung mass inertia, I_θ, see Equation 3.35, in Section 3.7. 236

A.19 Matlab/Simulink® implementation of $\ddot{z}_{tf}$, front unsprung mass acceleration, in Equation 3.36, Section 3.7. 236

A.20 Matlab/Simulink® implementation of $\ddot{z}_{tr}$, rear unsprung mass acceleration, in Equation 3.37, Section 3.7. 237

List of Tables

2.1 Half-car suspension model DOF 11

2.2 Summary of modelling complexity and limitations of the types of analysis possible for different vehicle suspension system models . . . 14

3.1 Discrete road input disturbance 34

3.2 ISO road surface roughness classification $G(n_0)$ at n_0=0.1$cycle/m$. 35

3.3 Hydraulic actuator parameters 37

3.4 Half-car model parameters 39

4.1 F_{ti}^{stat} for ±20% Nominal sprung mass loading $Ms = 580\,kg$ 45

4.2 Frequency weightings for calculation of vibration-induced discomfort 47

4.3 ISO 2631-1 weighted RMS acceleration ranges and associated vibration-induced discomfort levels 48

5.1 PID tuning parameters for front and rear suspension inner and outer control loops 53

5.2 RMS values for discrete input disturbance with ±20% variation in sprung mass loading about the nominal value, $Ms = 580\,kg$ with ±20% variation, at $V = 45\,km/h$ 55

5.3 Weighted RMS acceleration and discomfort levels as PVSS and AVSS traverse a sinusoidal bump input disturbance at $V = 45\,km/h$ 59

5.4 RMS values for discrete input disturbance with ±20% variation in sprung mass loading about the nominal value, $Ms = 580\,kg$, at $V = 60\,km/h$ 62

5.5 Weighted RMS acceleration and discomfort levels as PVSS and AVSS traverse a sinusoidal bump input disturbance at $V = 60\,km/h$ 66

5.6 RMS values for discrete input disturbance with ±20% variation in sprung mass loading about the nominal value, $Ms = 580\,kg$ at $V = 75\,km/h$ 69

5.7 Weighted RMS acceleration and discomfort levels as PVSS and AVSS traverse a sinusoidal bump input disturbance at $V = 75\,km/h$ 73

5.8 RMS values for random input disturbance with ±20% variation in sprung mass loading about the nominal value, $Ms = 580\,kg$ with ±20% variation, at $V = 45\,km/h$ 76

5.9 Weighted RMS acceleration and discomfort levels as PVSS and AVSS traversed a random road input disturbance at $V = 45\,km/h$ 80

5.10 RMS values for random input disturbance with ±20% variation in sprung mass loading about the nominal value, $Ms = 580\,kg$, at $V = 60\,km/h$ 83

5.11 Weighted RMS acceleration and discomfort levels as PVSS and AVSS traversed a random road input disturbance at $V = 60\,km/h$ 86

5.12 RMS values for random input disturbance with ±20% variation in sprung mass loading about the nominal value, $Ms = 580\,kg$ at $V = 75\,km/h$ 91

5.13 Weighted RMS acceleration and discomfort levels as PVSS and AVSS traversed a random road input disturbance at $V = 75\,km/h$ 93

6.1 PID force control loop tuning parameters 113

6.2 MPC Parameters for Front and Rear Suspension 114

6.3 RMS values for discrete input disturbance with at $V = 75\,km/h$ for $\Delta = \pm 30\%$ variation in ks_i^l and ks_i^{nl} about their nominal values. . . 122

6.4 Weighted RMS acceleration, a_{wi}^{RMS}, and discomfort levels as PVSS and AVSS traverse a sinusoidal bump input disturbance at $V = 75\,km/h$ for $\Delta = \pm 30\%\,\{ks_i^l, ks_i^{nl}\}$ 127

6.5 RMS values for a random input disturbance with at $V = 75\,km/h$ for $\Delta = \pm 30\%$ variation in ks_i^l and ks_i^{nl} about their nominal values. . . 130

6.6 Weighted RMS acceleration, a_{wi}^{RMS}, and discomfort levels as PVSS and AVSS traverse a random road input disturbance at $V = 75\,km/h$ for $\Delta = \pm 30\%\,\{ks_i^l, ks_i^{nl}\}$ 134

7.1 PID force control loop tuning parameters 142

7.2 NNFBL parameters for front and rear suspension 149

7.3 Performance of NNFBL training algorithms for front and rear suspension 150

7.4 RMS values for discrete input disturbance with ±20% variation in sprung mass loading about the nominal value, $Ms = 580\,kg$, at $V = 45\,km/h$ 159

7.5 Weighted RMS acceleration and discomfort levels as PVSS and AVSS traverse a sinusoidal bump input disturbance at $V = 45\,km/h$ 163

7.6 RMS values for discrete input disturbance with ±20% variation in sprung mass loading about the nominal value, $Ms = 580\,kg$, at $V = 60\,km/h$ 166

7.7 Weighted RMS acceleration and discomfort levels as PVSS and AVSS traverse a sinusoidal bump input disturbance at $V = 60\,km/h$ 170

7.8 RMS values for discrete input disturbance with ±20% variation in sprung mass loading about the nominal value, $Ms = 580\,kg$, at $V = 75\,km/h$ 173

7.9 Weighted RMS acceleration and discomfort levels as PVSS and AVSS traverse a sinusoidal bump input disturbance at $V = 75\,km/h$ 176

7.10 RMS values for random input disturbance with ±20% variation in sprung mass loading about the nominal value, $Ms = 580\,kg$, at $V = 45\,km/h$ 181

7.11 Weighted RMS acceleration and discomfort levels as PVSS and AVSS traversed a random road input disturbance at $V = 45\,km/h$ 183

7.12 RMS values for random input disturbance with ±20% variation in sprung mass loading about the nominal value, $Ms = 580\,kg$, at $V = 60\,km/h$ 188

7.13 Weighted RMS acceleration and discomfort levels as PVSS and AVSS traversed a random road input disturbance at $V = 60\,km/h$ 190

7.14 RMS values for random input disturbance with ±20% variation in sprung mass loading about the nominal value, $Ms = 580\,kg$, at $V = 75\,km/h$ 195

7.15 Weighted RMS acceleration and discomfort levels as PVSS and AVSS traversed a random road input disturbance at $V = 75\,km/h$ 198

List of Symbols

Latin Alphabets

a	Bump amplitude
A	Hydraulic piston area
bs	Suspension damping coefficient
bt	Tyre damping coefficient
C_{tp}	Total leakage coefficient
e_i	$i^{th}-$ tracking error
$f\left[\cdot\right]$	Nonlinear function
F	Nonlinear function
F	Force
f_f	Sum of suspension component forces
$\mathbf{f}\left(x\right)$	System vector
g	Acceleration due to gravity
$g\left[\cdot\right]$	Nonlinear function
$G(n_0)$	Road surface roughness coefficient

$\mathbf{g}(x)$	Control input matrix
$\mathbf{h}(x)$	Control output matrix
$\mathbf{h}_m(x)$	Measured plant output matrix
I	Sprung mass pitch moment of inertia
k	Sampling instant coefficient
ks	Suspension stiffness coefficient
kt	Tyre stiffness coefficient
K	Gain
Kv	Servo-valve gain
l_f	Length between vehicle centre of mass and vehicle front axle
l_r	Length between vehicle centre of mass and vehicle rear axle
Ms	Sprung mass
mu	Unsprung mass
n	Spatial frequency
N	Total number of samples
n_0	Reference spacial frequency
na	Number of past inputs
nb	Number of past outputs
$\mathbf{p}$	Disturbance input matrix
Pl	Hydraulic piston pressure drop

$\dot{P}l$	Hydraulic piston pressure drop rate
Ps	Supply pressure
Q	Hydraulic flow rate
R	Suspension reference signal
t	Time
u_i	$i^{th}-$ control input or control voltage
$\mathbf{u}$	Control input vector
$u_i\,(k)$	$i^{th}-$ system input
u_{max}	Maximum control voltage
V	Vehicle forward velocity
V_t	Total actuator volume
w	Road profile displacement
$\mathbf{w}$	Disturbance input vector
$\dot{w}$	Road profile time-derivative at front wheel
$W_0(t)$	Zero variance white noise signal
x	Servo-valve displacement
$\mathbf{x}$	State vector
$\mathbf{y}$	Controlled output vector
$y_i\,(k)$	$i^{th}-$ system output

$\mathbf{y}_m$	Measured plant output
z	Sprung mass displacement
Z	I/O data collection form
z_{ti}	$i^{th}-$ Unsprung mass displacement
$\dot{z}$	Sprung mass velocity
$\dot{z}_{ti}$	$i^{th}-$ Unsprung mass velocity
$\ddot{z}$	Sprung mass acceleration
$\ddot{z}_{ti}$	$i^{th}-$ Unsprung mass acceleration

Latin Subscripts

af	Front actuator
ai	$i^{th}-$ actuator
ar	Rear actuator
$axis$	Axis
bsf	Front suspension damper
bsi	$i^{th}-$ suspension damper
bsr	Rear suspension damper
btf	Front tyre damper

bti	$i^{th}-$ tyre damper
btr	Rear tyre damper
c	Center of gravity
d	Delay
dis	Discharge
e	Effective
D	Derivative
f	Front
hyd	Hydraulic
i	Subscript denoting either front or rear suspension
I	Integral
ksf	Front suspension spring
ksi	$i^{th}-$ suspension spring
ksr	Rear suspension spring
ktf	Front tyre spring
kti	$i^{th}-$ tyre spring
ktr	Rear tyre spring
l	Linear
max	Maximum
min	Minimum

n	Total number of samples
nl	Nonlinear
P	Proportional
r	Rear
ref	Reference
RMS	Root Mean Square
t	Total
tf	Front tyre
ti	$i^{th}-$ tyre
tp	Total leakage coefficient
tr	Rear tyre
vf	Front spool-valve
vi	$i^{th}-$ spool-valve
vr	Rear spool-valve

Latin Superscripts

l	Linear
n	Total number of samples

nl	Nonlinear
RMS	Root Mean Square
$stat$	Static
sym	Symmetric

Greek Symbols

α	Actuator parameter
β	Actuator parameter
β_e	Effective bulk modulus
γ	Actuator parameter
Δ	Variation
ϵ	Waviness of the road
λ	Input disturbance wavelength
Ω	Spool-valve gradient
ρ	Density
τ	Hydraulic actuator time constant
θ	Pitch angular displacement
$\dot{\theta}$	Pitch angular velocity
$\ddot{\theta}$	Pitch angular acceleration

Greek Subscripts

θ	Pitch Angular Displacement

List of Acronyms

AFSMC Adaptive Fuzzy Sliding Mode Control

ANSMC Adaptive Sliding Mode Controller

ANN Artificial Neural Networks

AVSS Active Vehicle Suspension Systems

DOF Degree-of-Freedom

EHA Electro-Hydro Static Actuator

FBL Feedback Linearization

FLC Fuzzy Logic Control

GA Genetic Algorithm

I/O Input-Output

ISO International Organization for Standardization

HB High Bandwidth

LB Low Bandwidth

LB1 Low Bandwidth type-1

LB2 Low Bandwidth type-2

LM Levenberg-Marquardt

LMI Linear Matrix Inequalities

LPV Linear Parameter Varying

LQ Linear Quadratic

LQG Linear Quadratic Gaussian

LQR Linear Quadratic Regulator

LTI Linear Time Invariant

LTR Loop Transfer Recovery

MIMO Multiple Input Multiple Output

MLP Multi-Layer Perceptron

MPC Model Predictive Control

MP/FBLC Model Predictive/Feedback Linearization Control

MRAC Model Reference Adaptive Control

MSE Mean Square Error

NARMA Nonlinear AutoRegressive-Moving Average

NF Neuro-Fuzzy

NN Neural Network

NNAPC Neural Network-based Approximate Predictive Control

NNARX Neural Network AutoRegressive eXternal input

NNFBL Neural Network-based Feedback Linearization

NNMPC Neural Network-based Model Predictive Control

NNMP/FBLC Neural Network-based Model Predictive/Feedback Linearization Control

ODE Ordinary Differential Equation

PD Proportional plus Derivative

PI Proportional plus Integral

PID Proportional plus Integral plus Derivative

PIDNN Proportional plus Integral plus Derivative Neural Network

PSD Power Spectral Density

PVSS Passive Vehicle Suspension System

QFT Quantitative Feedback Theory

RBF Radial Basis Function

RMS Root Mean Square

RNN Robust Neural Network

SANAFC Skyhook and Adaptive Neuro Active Force Control

SAVSS Semi-Active Vehicle Suspension Systems

SISO Single Input Single Output

SMC Sliding Mode Control

SOFC Self-Organizing Fuzzy Control

TPMA Tubular Permanent Magnet Actuators

VSS Vehicle Suspension Systems

1 INTRODUCTION

1.1 Research Background and Motivation

Vehicle suspension consists of shock absorbers (dampers), springs and mechanical linkages (wishbones) that connect the wheels to the body (Fischer and Isermann, 2004). Suspension design is a multi-objective design problem. The aim is to improve vehicle ride comfort and road holding, while maintaining suspension deflection within the physical limits of suspension travel. An additional function is to reduce the road surface damage caused by moving vehicles driving over the road surface (Williams, 1997a). Vehicle ride comfort is related to the vertical acceleration of the vehicle body. Improving ride comfort requires the use of soft suspension springs. Vehicle road holding is a function of the tyre dynamic load variation. Improvement in road holding requires minimizing the variation of tyre dynamic load, keeping its value below that of the vehicle's static load. This prevents tyre lift-off phenomenon that would render the vehicle uncontrollable (poor vehicle handling) and compromise passenger safety. Road holding requires stiff suspension springs (Canale et al., 2006). Increasing damping can improve ride comfort but will result in deterioration of road holding capability (Bouazara et al., 2006).

Helical and leaf springs were developed during the 17th century. However, their use in combination with dampers, in conventional (passive) suspension systems, is only recorded to have begun during the early part of the 20th century (Guglielmino et al., 2008). Spring and damper characteristics cannot be modified in passive vehicle suspensions. As a result, these suspensions have to be designed to accommodate a wide variety of road conditions simultaneously. Meeting the ride comfort and road holding demands simultaneously is physically impossible in passive vehicle suspensions (Williams, 1997a). It would require a spring which can be stiff and soft at the same time. Thus, passive vehicle suspension design is a compromise between comfort and safety (Fischer and Isermann, 2004; Canale et al., 2006).

Semi-active and active suspension systems have been proposed to address this compromise. This is achieved in semi-active suspensions by the application of real-time variation of damping (Hrovat, 1997). The drawback of semi-active suspension systems is that they are only able to absorb forces induced by the road input disturbance. Active Vehicle Suspension Systems (AVSS) have been shown to address the compromise, by the incorporation of a force introducing actuator into the passive suspension. AVSS have the ability to both store and dissipate energy, putting them at an advantage over passive and semi-active suspension systems. However, this comes at an added cost of components, increased energy requirement and added complexity (Fischer and Isermann, 2004).

Advances in computer processing capabilities and development of more affordable sensors and actuators hardware, have made implementation of AVSS feasible in mass market vehicles. The earliest documented research into active suspension design is dated as early as the 1950's. Since that time AVSS research has increased exponentially, the most rapid growth being during the last 20 years (Guglielmino and Edge, 2004). AVSS design focuses on selection of appropriate actuators, sensors and development of feedback control algorithms that will result in the desired vehicle response (Williams, 1997a).

1.2 Problem Statement

Real active suspension systems have highly nonlinear and time-varying behaviour. This behaviour is brought about by inherent nonlinear characteristics of passive suspension elements (springs, dampers and suspension bushes), active suspension elements (actuator) and suspension geometry. The difficulty involved in modelling such behaviour results in simplifications which lead to model uncertainty. Conventional and nonlinear modelling techniques require exact system models for accuracy. Some system behaviours are challenging to model, for example, hydraulic friction is a complex nonlinear time-varying behaviour. It is dependent on external loading, stick-slip and Coulomb friction. Control system complexity also increases with model complexity for modern control systems, adding to computational burden (Huang and Lin, 2007).

Suspension systems are free to move within the confines of the suspension travel workspace (rattlespace). Any movement beyond the confines of this area would cause a nonlinear behaviour known as "topping" or "bottoming", in which the suspension components bang on the top or bottom of the rattlespace, damaging the vehicle. The

AVSS's actuators are also limited in the amount of output force they can supply, as well as the amount of control input voltage that can be supplied to them (Du and Zhang, 2009; Dahunsi et al., 2009; Dahunsi and Pedro, 2010).

It is in the light of the previously introduced issues that this project proposes the development of Model Predictive Control (MPC) and Neural Network-based Feedback Linearization (NNFBL) based controllers for half-car servo-hydraulic vehicle suspension systems. MPC is capable of dealing with systems with input and output constraints (Deng et al., 2009). It is therefore applicable to AVSS which have suspension travel and hydraulic actuator constraints. Feedback Linearization (FBL) allows for linearization of highly nonlinear systems into linear ones, thereby enabling the application of linear control methods thereafter (Deng et al., 2009). Intelligent control systems are capable of dealing with nonlinear uncertain systems without the need of an exact system model. Neural Network (NN) control systems are the basis for the intelligent design. NN are utilized in this project because of their learning capability. NN are also known for their ability to approximately map complex nonlinear systems. Adequately trained NN are capable of fault tolerant operation (Hunt et al., 1992).

Dynamic systems like AVSS contain model parameters, for example sprung mass loading, suspension damping and suspension spring stiffness, tyre damping and tyre spring stiffness etc., whose exact values are uncertain. Hence the need for controller design which takes into account parametric uncertainty within acceptable bounds. This could help reduce the possibility of poor performance on implementation due to parametric uncertainty (Chen et al., 2005; Gao et al., 2006; Ryu et al., 2008).

1.3 Research Aims and Objectives

This research project aims to investigate performance of VSS in the presence of parametric uncertainty. The research objectives are listed below:

1. Develop the mathematical model of the nonlinear half-car the PVSS and AVSS with hydraulic actuator dynamics and various controllers.

2. Build, numerically simulate and compare performance of the various AVSS and PVSS under conditions of parametric uncertainty in the form of variation in vehicle forward velocity, sprung mass payload, suspension spring stiffness coefficients and suspension damping coefficients.

1.4 Research Scope and Limitations

This research is focused on mathematical model development, control system design, implementation and computer based simulation of a nonlinear half-car active suspension. The half-car suspension system model is a 4-Degree-of-Freedom (DOF) model comprising a rigid sprung mass (vehicle body) supported at the front and rear by the front and rear suspension elements (springs, dampers and actuators). These suspension elements are mounted between the vehicle body and the front and rear wheels (unsprung masses). The nonlinearity in the half-car suspension system is caused by the use of nonlinear springs and nonlinear damper models. Nonlinear hydraulic actuator dynamics have been incorporated into the active suspension system model. The half-car suspension system is developed to rotate about the vehicle lateral axis which is the vehicle pitching axis. It is assumed that the vehicle body is able to make large pitch angular displacements about the vehicle pitching axis. Vehicle rolling about its longitudinal axis is not considered in this work. Nonlinear effects caused by variation of wheel camber due to the suspension geometry are ignored since the half-car model is a two dimensional model. Tyre damping is included in the model.

Performance of the developed control systems are compared with each other and with that of a passive half-car suspension system, with the same model parameters. Performance is evaluated based on ride comfort, road holding and suspension travel. The case of suspension travel regulation will be considered, in which the suspension travel reference signal was set to zero, as the vehicle traversed the road input disturbance.

Only two different types of road input disturbances are considered in this work. These are:

- A sinusoidal bump on an otherwise smooth road
- A random road profile

The robustness of the designed controllers is tested by variations in vehicle forward velocity, sprung mass payload, suspension spring stiffness and suspension damping coefficients.

1.5 Research Strategy and Methodology

The research methodology applied during this project is listed below in step sequence:

1. The nonlinear half-car AVSS is modelled mathematically, based on application of Newton's 2nd law. The model includes nonlinear springs, dampers and hydraulic actuator dynamics. Input disturbance models are also developed.
2. Model parameters and controller specifications are selected.
3. The following control systems, with two control loops, are developed: PID, MPC and NNFBL in the outer control loop. All have PID controller based hydraulic actuator force feedback in the inner control loops.
4. Simulation is carried out in the MATLAB/Simulink® environment, the results are collated and evaluated. Controllers are redesigned if their performance is found to be poor.
5. Each controller's performance is analyzed individually and then compared with each other.
6. Conclusions are then drawn and recommendations made.

The research methodology applied in the design of the control systems for the half-car servo-hydraulic AVSS is illustrated in Figure 1.1.

1.6 Research Contributions

This research work makes two contributions:

- The main contribution of this study is the comparison between conventional (non-intelligent) PID and MPC with Intelligent (Neural Network based) FBL applied to a nonlinear half-car AVSS. All these control methods are applied in conjunction with PID control force-feedback of the hydraulic actuator force. Nonlinear springs, dampers and servo-hydraulic actuator dynamics as well as suspension travel and actuator input voltage constraints are considered in the system's mathematical model development.

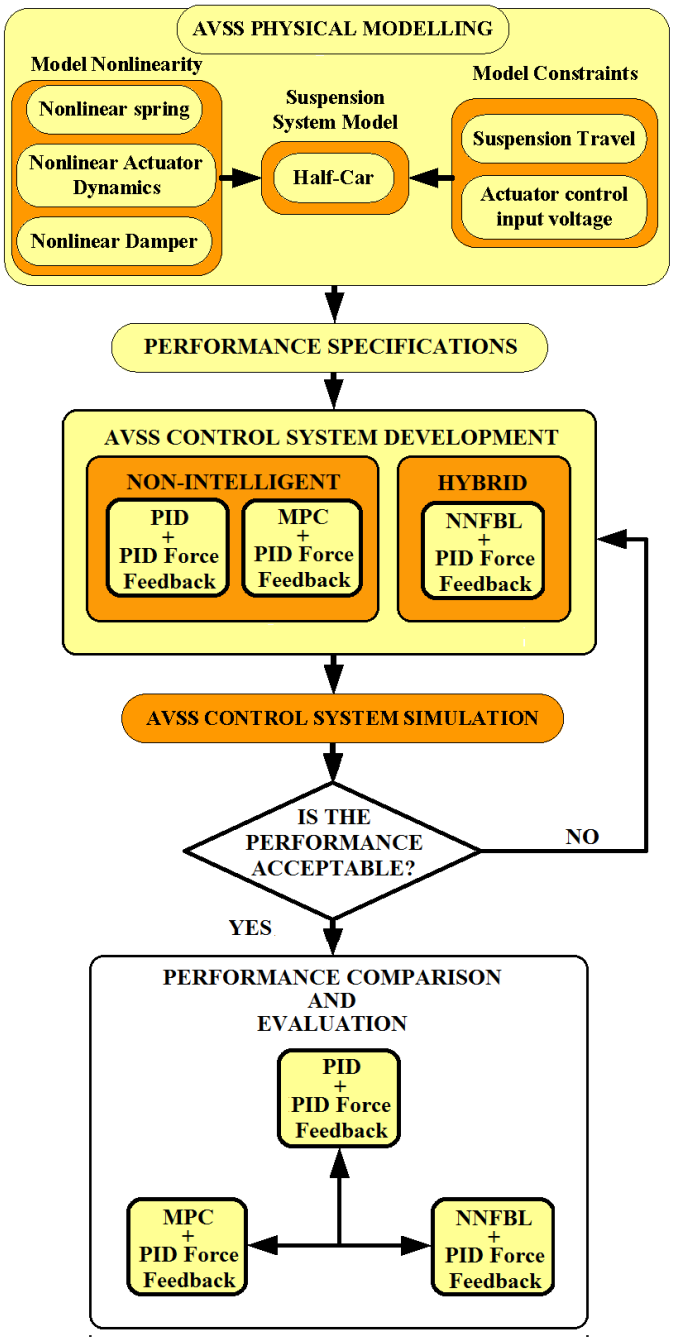

Figure 1.1: Research methodology.

- A secondary contribution is the application of Conventional MPC and NNFBL to a nonlinear half-car AVSS. MPC techniques are noted for the ability to handle Multiple Input Multiple Output (MIMO) systems with input and output constraints. FBL enables linearization of nonlinear systems, allowing application of linear control methods thereafter (Deng et al., 2009).

1.7 Dissertation Outline

This dissertation is structured as follows:
A review of the current literature in the subject area is given in Chapter 2, beginning with a general overview of AVSS and the force actuators they use, followed by a look at the road input disturbances that are used to evaluate suspension system performance. Half-car AVSS are then introduced and an investigation of the control techniques applied to their control is presented. A further study into conventional and intelligent control systems is also provided.

The physical and mathematical models of the nonlinear half-car AVSS are derived in Chapter 3 starting with the modelling assumptions and a look at the physical model. The nonlinear spring and damper models are developed, followed by the tyre force model, the road disturbance inputs and hydraulic actuator dynamics. A nonlinear half-car active vehicle suspension with hydraulic actuator dynamics is then formed based on the models developed in the previous sections.

Before beginning controller implementation, the performance specifications used throughout this work are given in Chapter 4. Chapters 5 to 7 contain controller implementations of the PID suspension travel controller with PID force feedback, MPC suspension travel controller with PID hydraulic actuator force feedback and the NNFBL suspension travel controller with PID force feedback, respectively. Each chapter begins with an introduction, description of the controller design method, presentation of the simulation results with a discussion and finally a conclusion. Simulations are performed in the time domain testing the AVSS and PVSS robustness to variations in vehicle speeds and along with variations in sprung mass loading. For uncertainty analysis, a frequency sweep is performed on both the AVSS and PVSS with the aid of a chirp road input disturbance signal; the chirp signal's frequency varies with time. A spectral analysis of all model outputs is performed and the results plotted in the frequency domain for variations in sprung mass loading and pitch moment of inertia, suspension spring coefficients and suspension damping coefficients.

The appendices contain MATLAB/Simulink® implementation of the half-car active suspension system and input disturbance models given in Chapter 3.

2 LITERATURE REVIEW

2.1 Introduction

A review of the literature related to AVSS is presented in this chapter. Beginning with the functions of suspension systems, their classification and the types of mathematical models used to design suspension systems in Sections 2.2, 2.3 and 2.4. The different suspension system actuator/spring and damper setups are presented in Section 2.5, followed by a look at the causes of nonlinearity in vehicle suspension systems 2.6. Types of actuators commonly used in AVSS are given in section 2.7 and the need for force feedback is highlighted in Section 2.8. Sections 2.9 to 2.10.4.2 present in detail the control methods that have been applied to AVSS, before concluding the chapter in Section 2.11.

2.2 Suspension Systems

As introduced in Section 1.1 of Chapter 1, Vehicle Suspension Systemss (VSSs) consist of shock absorbers (dampers), springs and mechanical linkages (wishbones) that connect the vehicle wheels to the vehicle body (Fischer and Isermann, 2004). A vehicle suspension system serves the following functions:

1. Supporting the vehicles static weight.
2. Improving vehicle ride quality (comfort) by isolating the vehicle body from road disturbances.
3. Minimizing loss of traction between the tyre and the road (maintaining road holding) which contributes toward improving vehicle handling. Vehicle handling is the ability of the vehicle to respond to the drivers commands. It is a function of road holding and the vehicles physical properties.

4. Ensuring that suspension travel does not exceed suspension workspace limits.

A vehicle suspension's effectiveness at carrying out these functions is used as a measure of performance. Vehicle suspensions also have the additional function of reducing road surface damage caused by vehicles driving over it (Williams, 1997a).

2.3 Classification of Vehicle Suspension Systems

According to Williams (1997a) and Williams (1997b) Vehicle Suspension Systems (VSS) can be classified into two broad categories:

1. Conventional VSS
   Also known as Passive Vehicle Suspension System (PVSS), is characterized by fixed damping and spring ratios.

2. Controlled VSS
   These systems are marked by their use of the mechatronic approach to input a control force into the otherwise passive suspension system, or to alter either spring or damping properties. They are divided into the following groups (Williams, 1997b; Fischer and Isermann, 2004):

   (a) Load levelling Adaptive Suspension Systems:
   These systems compensate for sprung mass variation with the aim of providing constant suspension workspace. It is the spring that does the compensation. Examples of these systems are air springs and oleo-pneumatic springs. Oleo-pneumatic springs are controlled in open-loop, using simple logic circuits.

   (b) Adaptive Damping:
   Controlled in open-loop, these systems use simple logic circuit control to vary damping ratio discretely.

   (c) Semi-Active Vehicle Suspension Systems (SAVSS):
   In these systems the spring rate remains constant, however the damping ratio can be varied in real-time by use of a closed-loop feedback control system. The result is controlled energy dissipation and hence improved performance over passive systems. Examples of dampers used in SAVSS are servo-valve hydraulic dampers, magneto-rheological and electro-rheological dampers.

(d) Active Vehicle Suspension Systems (AVSS):
These systems have actuators controlled using closed-loop feedback, incorporated into the suspension system. The actuator introduces a control force which gives AVSS superior performance at vibration attenuation in comparison with both PVSS and SAVSS. It should be noted that this superior performance is achieved at a high energy and financial cost with increased complexity. Figure 2.1 illustrates the differences between PVSS, SAVSS and AVSS.

2.4 Vehicle Suspension System Mathematical Models

Three models are commonly used in mathematical modelling of vehicle suspension systems, (Hrovat, 1997). These are:

1. Quarter-car model:
   This is a simple 2 DOF vehicle suspension system model. This model is suitable for analysis of vehicle ride comfort. It is used to monitor sprung mass acceleration, suspension travel and tyre deflection (Williams, 1997b; Hrovat, 1997). Figure 2.1 highlights the differences between quarter-car models of Passive, Semi-active and Active Vehicle Suspension Systems.

2. Half-car model:
   The simplest form of a half-car vehicle suspension system model has four DOFs, see Figure 2.2. These DOFs are determined by the vehicle cross-section represented by the model. Half-car models are developed to observe either vehicle pitching (Szaszi et al., 2002) or rolling motion (Gysen et al., 2009), the corresponding DOFs are given in Table 2.1. Figure 2.2 shows a half-car models developed to observe vehicle pitching motion.

Table 2.1: Half-car suspension model DOF

	Half-Car Suspension Pitch Model (Szaszi et al., 2002)	Half-Car Suspension Roll Model (Gysen et al., 2009)
Degree of Freedom	(1) Vehicle heave	(1) Vehicle heave
	(2) Pitch	(2) Roll
	(3) Front axle vertical translation	(3) Left wheel vertical translation
	(4) Rear axle vertical translation	(4) Right wheel vertical translation

3. Full-car model:

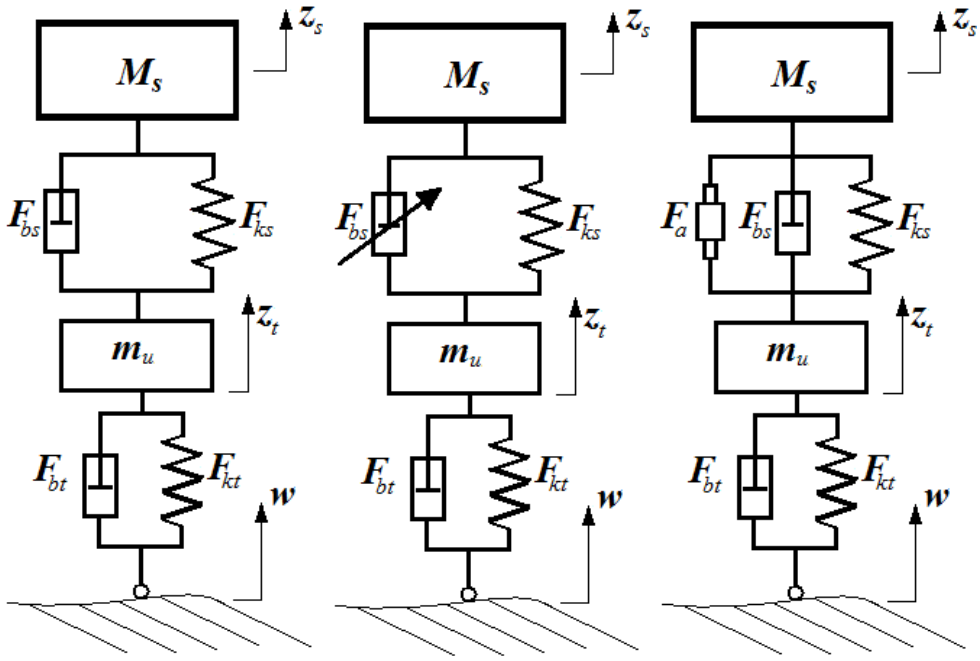

(a) PVSS. (b) SAVSS, with variable damper. (c) AVSS, with force actuator.

Figure 2.1: Differences between quarter-car PVSS, SAVSS and AVSS.

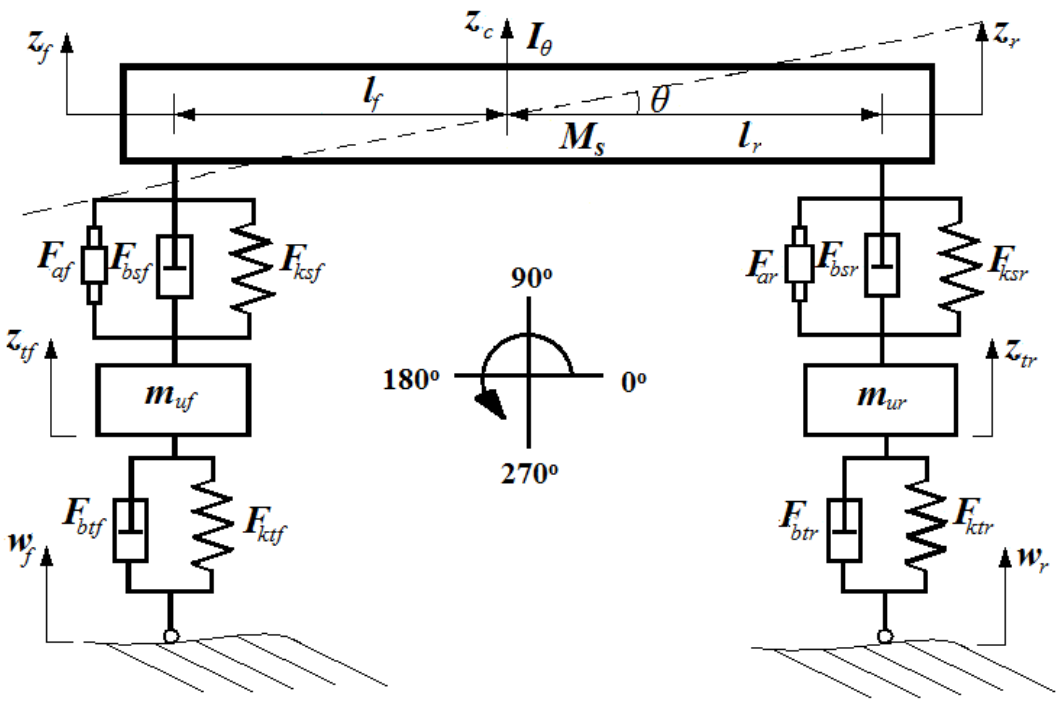

Figure 2.2: Schematic of a half-car AVSS model for observing vehicle pitching motion.

The simplest form is a 7-DOF vehicle suspension system model. The seven DOF are: Vehicle heave, pitch, roll and 4-DOF for the 4 wheels of the vehicle. Different suspension system physical setups have been modelled; a full-car AVSS modelled with fully independent front and rear suspension, mixed (front independent and rear dependent) and fully dependent suspension as modelled by Pedro (2007), Youn et al. (2006) and Vatankhah et al. (2009) respectively.

Simultaneous analysis of vehicle handling and ride comfort at passenger level is possible by addition of passenger seats in half and full-car models (Li et al., 2008; Guclu and Gulez, 2008). In addition, suspension system modelling has been applied to purposes other than passenger comfort, such as numerical simulation of damage to fruits in transit using a passive half-car vehicle suspension model (Van Zeebroeck et al., 2008).

The quarter-car, half-car and full-car suspension models are capable of providing information for ride comfort and vehicle handling analysis. The quarter-car is the least computationally demanding of the three models and is limited to analysis at one wheel. It therefore does not enable observation of vehicle pitching or rolling. Lower computational complexity is the advantage of the half-car over the full-car model. However, separate models are required to monitor either vehicle pitch or roll, together with axle or wheel translation and suspension travel. The full-car model enables simultaneous monitoring of all these states (Hrovat, 1997). The levels of modelling complexity and limitations of the types of analysis possible on quarter-car, half-car and full-car AVSS are summarized in Table 2.2.

2.5 High and Low Bandwidth Active Vehicle Suspension Systems

The positional relationship between the spring, damper and actuator affects the bandwidth (frequency range of operation) of the actuator (Koch et al., 2010). A survey indicated the two commonly cited types of setups in the literature:

1. High Bandwidth (HB):
   HB are also known as broad-bandwidth (Hrovat, 1997; Williams, 1997b). In these systems a double-acting actuator is connected directly to the body and wheel, see Figure 2.1(c). If the actuator supports the total sprung mass weight

[1] Used in Vehicle Ride Comfort Analysis

Table 2.2: Summary of modelling complexity and limitations of the types of analysis possible for different vehicle suspension system models

Item	Quarter-Car Suspension Model	Half-Car Suspension Model	Full-Car Suspension Model
Mathematical Modelling Complexity	Low	Medium	High
Heave Acceleration [1]	Single wheel only	Half vehicle	Full vehicle
Pitch Angular Acceleration [1]	-	Model Dependent	Full vehicle
Roll Angular Acceleration [1]	-	Model Dependent	Full vehicle
Road Holding Analysis	Single wheel only	Either front and rear or left and right wheels depending on the model	All wheels
Suspension Travel Analysis	Single wheel only	Either front and rear or left and right suspension workspace depending on the model	All suspension workspaces

it is called fully-loaded. The system is partially loaded if there is a spring and or damper in parallel with the actuator (Fischer and Isermann, 2004). Partially loaded systems have the following advantages over fully loaded systems:

(a) The spring supports the static vehicle load.

(b) In case of actuator failure the spring and damper behave like a passive suspension system.

2. Low Bandwidth (LB):
   LB are also known as narrow-bandwidth (Hrovat, 1997; Williams, 1997b). Two variants of this system have been noted in the literature. The first, Low Bandwidth type-1 (LB1), consists of an actuator in series with a spring; the combination is setup parallel to a damper (if a damper is present). In the second variation, Low Bandwidth type-2 (LB2), the actuator is in series with a spring and damper pair. The resulting system realizes the same advantages described for partially loaded HB AVSS. Single acting actuators are used in LB AVSS. The difference between LB1 and LB2 AVSS is illustrated in Figure 2.3.

HB AVSS have a wider frequency operating range thus requiring high bandwidth controllers, actuators and sensors, increasing costs. Williams (1997b) found that the addition of variable damping in both HB and LB AVSS could result in energy saving. This was confirmed by Koch et al. (2010). Simulation results indicated that replacement of the passive damper with a variable damper can increase the LB1 AVSS range of operation, making it more comparable with that of HB AVSS.

Advantages and disadvantages and performance comparison of HB and LB AVSS can be found in Williams (1997b). In this report, a HB suspension setup will be applied due to its wide operating range.

2.6 Nonlinearity in Suspension Systems

Suspension systems often in the past have been modelled as linear systems (Pedro, 2003; Pedro, 2007; Koch et al., 2010). However, the nonlinear nature of real suspension system components, coupled with uncertainties makes linear modelling inadequate. In contrast, modelling nonlinearities comes at a higher computational cost (Cao et al., 2008).

Springs display elastic hysteresis behaviour. Hydraulic dampers produce different

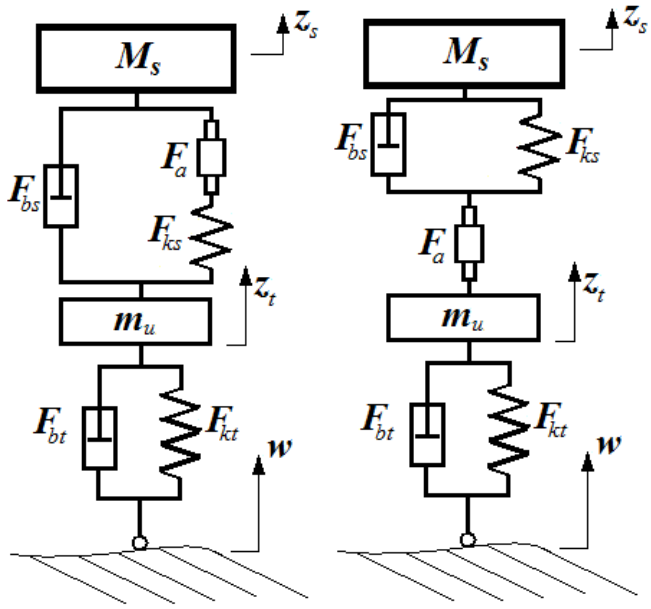

(a) A Low Bandwidth type-1 AVSS.

(b) A Low Bandwidth type-2 AVSS.

Figure 2.3: Difference between Low Bandwidth type 1 and type 2 AVSS.

force-velocity response characteristics on compression and expansion strokes. This type of hysteresis is evident when viewing force-velocity plots of hydraulic dampers (Foale, 2006; Guglielmino et al., 2008).

Nonlinearities in servo hydraulic actuators are caused by: hydraulic fluid compressibility, valve flow pressure nonlinearities, backpressure due to sprung mass-actuator interaction, dead-zone due to spool-valve overlap and leakage of hydraulic fluid (Ji et al., 2007; Cao et al., 2008; Bessa et al., 2010). Difficulty in modelling and estimation of hydraulic friction adds to model uncertainty. Hydraulic friction is nonlinear and varies with time. It is a function of stick-slip friction, Coulomb friction and external loading (Foale, 2006; Huang and Lin, 2007; Cao et al., 2008).

The 2-DOF model of a quarter-car, common place in the literature, is a simplified linear model of the suspension geometry. Kinematic modelling is required to capture the true dynamics at the wheel. Al-Holou et al. (2002) proposed the use of a kinematic model of a quarter-car suspension that showed how wheel camber, upper arm and lower arm angle and upper and lower control arm masses affect wheel dynamics. This model is highly nonlinear.

2.6.1 Suspension System Constraints

Suspension travel bottoming and topping are another cause of nonlinear behaviour. It occurs when discrete-event road input disturbances, like potholes and bumps, cause wheel displacements large enough for the wheel to hit suspension travel limits (Hrovat, 1997). In spite of suspension strut bushing's ability to reduce road disturbance harshness, they are another source of nonlinear behaviour. There are hard-limit/constraints to the voltage that can be applied to an actuator. This is dependent on the capacity of the vehicle's power supply, and also the actuator's ability to survive high voltages. The amount of force an actuator can supply is also finite. This is nonlinear behaviour (Du and Zhang, 2009; Dahunsi et al., 2009; Dahunsi et al., 2010; Pedro and Dahunsi, 2011). All the previously discussed effects need to be accounted for in order to produce a more realistic suspension model (Cao et al., 2008).

2.7 Actuators in Active Vehicle Suspension Systems

AVSS utilize force introducing actuators to achieve improved performance over PVSS and SAVSS. Some of the actuators in the literature have been listed below:

1. Hydraulic
   These actuators are divided into two categories:
   (a) Servo-Hydraulic Actuators with a central hydraulic fluid reservoir (Williams, 1997b; Huang and Lin, 2007).
   (b) Electro-Hydro Static Actuator (EHA) which eliminates the need for a central hydraulic fluid reservoir, replacing it with a motor driven hydraulic pump at each actuator (Farong and Zongde, 2007; Bessa et al., 2010).
2. Pneumatic (Anakwa et al., 2002; Yoshimura and Teramura, 2005; Ballo, 2007; Priyandoko et al., 2009).
3. Electromagnetic Motors which are divided into two categories:
   (a) Rotary Electromagnetic Motor actuator. These actuators consist of rotary electrical motors with gearboxes or ball screws that convert the rotary motion of the motors to linear motion. The linear movement is applied to control the suspension (Martins et al., 2006).

(b) Linear Brushless Tubular Permanent Magnet Actuators (TPMA) and Linear Electromagnetic Motors (Jones, 2005; Martins et al., 2006; Lee and Kim, 2010; Gysen et al., 2010). These actuators use linear electromagnetic motors, eliminating the need for a gearbox (unlike their rotary counterpart). However, these systems are often larger than hydraulic actuators and produce excessive heat in sustained load bearing (Martins et al., 2006; Bessa et al., 2010).

4. Hybrid Actuators
   An example of these actuators combines an electromagnetic rotary motor with a ball-screw (for rotary to linear motion conversion) with hydraulic dampers (Sahin et al., 2010).

Servo-hydraulic actuators are often selected for use in AVSS because they exhibit the following characteristics (Farong and Zongde, 2007; Du and Zhang, 2008; Dahunsi et al., 2009; Bessa et al., 2010):

1. High power to weight ratio, quick response;
2. Lower cost and high stiffness;
3. Sustained force generation without overheating;
4. Compact in size.

Servo-hydraulic actuators have therefore been chosen for this project. It should be noted though, that these systems suffer from leakage in valve and pressure hoses. They also need a large central hydraulic fluid reservoir coupled with a large power supply and require constant pressurization to avoid pressure fluctuations (Farong and Zongde, 2007; Gysen et al., 2010). A comparison of EHA and servo-hydraulic actuator characteristics is given in (Farong and Zongde, 2007).

2.8 The Need for Actuator Force Feedback

Most AVSS research work in the past has focused on design of an outer control loop which calculates the desired actuator control force. This force is calculated based on measurements or estimates of vehicle states and the road input disturbance. This approach has limited the amount of experimental validation possible

because it does not account for the dynamics of the actuator (Chantranuwathana and Peng, 2004; Sam and Hudha, 2006). Hydraulic actuators have highly nonlinear behaviour as stated in Section 2.6 and are prone to chattering in AVSS applications (Chantranuwathana and Peng, 2004). In addition, it is difficult to achieve the desired force because the hydraulic force generation is tightly coupled to the vehicle body motion, creating backpressure (Sam and Hudha, 2006). Therefore actuator force feedback is required to ensure that the hydraulic actuator is stabilized, attaining the desired forces to improve the vehicle ride comfort and road holding.

As a result, most of the current literature is either focused on design of both the inner force control loop and the outer desired force generating loop, or the inner loop alone. Examples of works in which both control loops are designed include Chantranuwathana and Peng (2004) using Model Reference Adaptive Control (MRAC), Sam and Hudha (2006) with a PI inner force control loop and a state feedback outer loop, Priyandoko et al. (2009) with a combination of several NN-based outer loops with skyhook control and an inner control loop. Fateh and Alavi (2009) developed a FBL inner control loop with FLC to generate the desired force signal. Marusak and Kuntanapreeda (2011) presented an MPC force controller for a hydraulic actuator.

2.9 Control of Active Vehicle Suspension Systems

Results of a literature survey of the different control methodologies that have been applied to AVSS are listed below. Due to the integration of different control system methods, classification into strict categories was difficult. Nevertheless, several different control methods are discussed in Sections 2.9.1 to 2.10.4.2.

2.9.1 Robust Control Methods

Marzbanrad et al. (2002) conducted a comparative performance analysis of optimally controlled full-car AVSS models with time delay and preview control. Linear Quadratic Gaussian (LQG) with state estimation was presented as the main suspension control in the work of Chantranuwathana and Peng (2004) on a quarter-car AVSS model. Modular adaptive robust control was applied to achieve force control of the nonlinear actuator that was used. Hrovat (1997) reviewed LQR optimal control techniques. Koch et al. (2010) determined the frequency response range of an LQR controlled LB1 AVSS with variable damping ratio and compared it to a

HB AVSS. Normalized Root Mean Square (RMS) plots, similar to those plotted in Hrovat (1997), were derived from the results. Pedro (2003) designed an LQR controller for a half-car AVSS, including seat dynamics. Pedro and Mgwenya (2004) presented LQR control method for a full-car AVSS with actuator dynamics.

Akcay and Turkay (2008) developed an H_2 AVSS controller to investigate the effect of tyre damping on quarter-car control system performance. Yousefi et al. (2007) highlighted the need for low-order control design, focusing on H_∞ AVSS control. A comparative analysis of 6 different H_∞ order reducing methods was provided in this work. Akcay and Turkay (2009) studied the influence of tyre damping on mixed H_2/H_∞ control of a quarter-car AVSS. The MATLAB Linear Time Invariant (LTI) toolbox was used to determine the suitable compromise between comfort and road holding. Pedro (2006) compared H_2/H_∞ control of a full-car AVSS, subject to a deterministic road input. Sun and Chen (2003) proposed an H_2/GH_2 control scheme for a half-car AVSS. Actuator dynamics were considered in this work, where H_2 control was applied to the sprung mass vertical acceleration, and GH_2 was applied to deal with power supply, suspension deflection and tyre dynamic load (to prevent loss of contact between the tyre and road) constraints. Linear Matrix Inequalities (LMI) was then used for closed-loop feedback optimization. Du and Zhang (2008) did similar work but went further to use a combination of GA and LMI to obtain the optimum feedback solution. Lauwerys et al. (2005) and Gaspar and Kuti (2005) applied H_∞ and μ synthesis for linear control of a quarter-car AVSS with nonlinear actuator and a full-body (2148-DOF) truck with flexible chassis respectively. Pedro (2007) employed an $H_2 - LQG/$ Loop Transfer Recovery (LTR) method for active control of a 7-DOF full-car suspension system. The controller was optimized using H_2 methods.

Fiahlo and Balas (2002) and Gaspar and Szederkenyi (2007) developed Linear Parameter Varying (LPV) controllers with nonlinear backstepping for control of a quarter-car AVSS with actuator dynamics. Du and Zhang (2008) developed a robust LMI/GA based controller for a quarter-car AVSS. The controller maintained good suspension system performance in spite of actuator response lag and changes in sprung mass load.

Liberzon et al. (2001) investigated the use of Quantitative Feedback Theory (QFT) to control a nonlinear 3-DOF quarter-car, off-road vehicle model. The model was linearized and represented in LTI form. Liu and Luo (2006) modelled a quarter-car AVSS with actuator dynamics using a combination of different techniques. LQG was used to design the optimal controller gain. A backstepping technique was applied

to model nonlinear hydraulic actuator dynamics. The authors then employed gain-scheduling to vary the LQG controller gain according to road conditions. In a comparative study on ride comfort, Mantaras and Luque (2006) reduced sprung mass acceleration of a simple 2-DOF, quarter-car AVSS model using classical pole-assignment controller design. The performance was judged against other AVSS controller designed using intelligent, robust and optimal methods.

2.9.2 Nonlinear Control Methods

Yoshimura et al. (2001) and Xiao and Kulakowski (2003) developed Sliding Mode Control (SMC) for a nonlinear pneumatic quarter-car test-rig and half-car AVSS respectively. In both models the sliding surfaces were obtained by Linear Quadratic (LQ) methods. Yagiz and Hacioglu (2008) studied backstepping control design for a 7-DOF full-car AVSS. The springs in this model were nonlinear and the dampers were assumed piece-wise linear. Actuator dynamics were not considered.

2.10 Control Methods Directly Related to this Work

2.10.1 Application of PID control for AVSS

Guclu (2003) developed a PID controller for an 8-DOF full-car model with active seat and suspension control, testing the system response for a road bump. Dry friction of the dampers was included in the model. PID controller gain tuning for the two systems described above was achieved using Ziegler-Nichols rules. Performance comparison of the two systems was carried out against passive suspension systems. Sam and Hudha (2006) used PI control techniques to perform force control of an AVSS hydraulic actuator with nonlinear actuator dynamics. A bump on an otherwise smooth road was the input disturbance. All the PID-controlled AVSS described in the text above were able to minimize sprung mass acceleration and deflection, suspension deflection and tyre deflection. Kumar (2008) designed a PID controller for a linear, quarter-car AVSS. Random and step road input disturbances were applied. In (Fateh, 2010), robust impedance control of a nonlinear AVSS with actuator dynamics was developed. A robust PID controller was used for force tracking via actuator control current. A separate robust PID controller was used for sprung mass position control.

2.10.2 Application of Feedback Linearization Control for AVSS

Chien et al. (2008) and Huang et al. (2009) presented detailed approaches on the application of Feedback Linearization (FBL) to a Multiple Input Multiple Output (MIMO) system, by applying it to nonlinear half-car and full-car AVSSs respectively. The nonlinearity in the models was due to the assumption that the vehicles could roll or pitch through large angles about their centres of gravity. Actuator dynamics were ignored and all suspension system components were considered linear. Huang et al. (2009) further developed the ideas presented in (Chien et al., 2008) by augmenting the FBL with Fuzzy Logic Control (FLC).

Fateh and Alavi (2009) focused on a multi-objective approach, by designing an impedance controller to deal with the compromise between ride comfort and road holding. This was applied to a linear, quarter-car AVSS with nonlinear hydraulic actuator dynamics. Two control loops were used: FBL for the inner hydraulic actuator force control loop and FLC for the outer sprung mass position control loop. The author proved stability of the impedance controller via Routh-Hurwitz method. For an input disturbance consisting of two sinusoidal bumps on an otherwise smooth road, the AVSS significantly improved the vehicle performance compared to a similar passive suspension system.

In (Shi et al., 2010), a hydropneumatic spring actuator was applied to an AVSS. The actuator mathematical model was first developed. The close correlation between the mathematical model simulation results and experimental results from the actual model, validated the mathematical model. Selection of the vehicle body position as the controlled variable enabled exact FBL of the suspension system (since the system dimension was equal to the system relative degree). SMC was then utilized to control the linearized model. The AVSS performed better than the passive vehicle suspension for both random road and shock-inducing force input.

2.10.3 Application of Model Predictive Control for AVSS

With regards to Semi-Active Vehicle Suspension Systems (SAVSS) control, (Giorgetti et al., 2006) considered the hybrid control of a quarter-car SAVSS using Model Predictive Control (MPC). Canale et al. (2006) proposed a fast MPC controller for a decoupled half-car SAVSS with nonlinear damping.

Mehra et al. (1997) demonstrated real-time nonlinear control of a quarter-car AVSS using MPC. Nonlinearities considered in the model were variation of spring force near suspension limits, and tyre lift-off phenomenon. Chen and Scherer (2004) developed a robust MPC for a quarter-car AVSS using LMI optimization. Kashtiban et al. (2009) designed a predictive optimal controller for a half-car active suspension system. A Taylor series expansion was employed to estimate future values of the system state variables. The half-car model included actuator dynamics and nonlinear springs and dampers.

Shoukry et al. (2010) developed a generalized predictive controller for a quarter-car AVSS model for online application. Li et al. (2010) proposed the application of traditional MPC to real-time control of a half-car AVSS. Nonlinear servo-hydraulic actuator dynamics were considered in the model. The controller proved effective during experimental testing on a half-car test-rig. Apart from Kashtiban et al. (2009), no consideration was given to the presence of nonlinearity due to the use of nonlinear springs, dampers and hydraulic actuator dynamics simultaneously in the MPC AVSS described in the preceding text.

2.10.4 Application of Neural Network-based Control for AVSS

2.10.4.1 Artificial Neural Networks

Artificial Neural Networks (ANN), referred to in this report as Neural Network (NN), are computational structures that imitate natural neurons found in the brain. ANN have the following attributes (Hunt et al., 1992; Burns, 2001):

1. Ability to approximately map nonlinear systems.
2. Parallel distribution of ANN and hence parallel information processing (good for MIMO systems) results in fault tolerance and rapid processing speeds.
3. Capable of experiential learning and generalizing, based on previous knowledge, when presented with unknown data.
4. Can be trained on or off-line.
5. ANN performance degrades gradually if some neurons fail or are removed (fail-safe property).

A survey of the literature revealed some of the current control techniques used to design intelligent AVSS. Vatankhah et al. (2009) combined the benefits of NNs and

FLC in a Neuro-Fuzzy (NF) control scheme. Spentzas and Kanarachos (2002) proposed a hybrid NN-based controller to reduce high energy consumption inherent in AVSS. (Huang and Lin, 2007) developed and tested an adaptive NN-based sliding mode controller. A Radial Basis Function (RBF) NN was used in this work. Both Priyandoko et al. (2009) and Dahunsi et al. (2010) developed intelligent controllers based on combining PID and NN techniques.

Spentzas and Kanarachos (2002) described a nonlinear hybrid control method for active suspension systems. A Taylor series structured NN was used to control the AVSS. The global optimum weights for the NN were obtained by the use of semi-stochastic parameter optimization procedure. Modelling of the quarter-car, AVSS emphasized the suspension travel constraints; in this case the maximum suspension travel allowable was 8 cm. Two case-scenarios are described namely continuous and discontinuous operation. In the continuous mode, the AVSS controller remains active throughout the simulation. In discontinuous mode, an assumption was made that the passive suspension system was designed well enough to cope with bumps of amplitude below a certain threshold, named A_{mean}. Above A_{mean}, the NN controller would be activated to provide disturbance rejection. Simulation results indicated that the control action only occurred when bumps of amplitude above A_{mean} were encountered. The discontinuous mode therefore lead to energy savings. However, the nonlinearity in the model was not so obvious.

Renn and Wu (2007) introduced two control schemes for the nonlinear servo-hydraulic, quarter-car, AVSS. The nonlinearity was attributed to nonlinear actuator dynamics. The first control system was a discrete-time PID control. Ziegler-Nichols rules were used to determine the PID gain parameters. The second control was a NN. Individual neurons were sigmoid function activated and the gradient steepest descent backpropagation method was used to train the network. Simulation was carried out in MATLAB and experimental validation on a quarter-car test-rig. The quarter-car model was excited by a sinusoidal bump followed by a sinusoidal pothole on an otherwise smooth road. Agreement in both simulation and experimental results indicated that the NN-based controller was better at suppressing sprung mass oscillation (for body acceleration and deflection) than the PID controller.

Huang and Lin (2007) developed a Neural Network-based Adaptive Sliding Mode Controller (ANSMC). This application used 11 hidden neurons for the RBF NN, utilizing adaptive rule for weights adjustment of RBF NN in real-time. Modifications were made to minimize sliding mode chattering. The nonlinear, time-varying actuator dynamics were taken into account in the quarter-car model, justifying the need

for model-free intelligent control. The SMC output was used as the RBF NN input. The RBF NN neurons were Gaussian function activated. The system was designed to require measurement of only two states, sprung mass and tyre axis displacement. The quarter-car was excited by a concave-convex bump road profile and a random road profile. The ANSMC was able to minimize a large margin sprung mass displacement and acceleration compared to a passive suspension system for both road profiles. Controller performance comparison was done against a Self-Organizing Fuzzy Control (SOFC) and an Adaptive Fuzzy Sliding Mode Control (AFSMC). The ANSMC produced the shortest settling time for both road profiles. The ANSMC also had the smallest magnitude for Power Spectral Density (PSD) analysis of the sprung mass acceleration response to both road profiles.

In the work done by Vatankhah et al. (2009), a 7-DOF, full-car vehicle model with dependent front and rear suspension was developed. A 6-layer NF control structure was implemented. Takagi-Sugeno-Kang rules were used for the fuzzy inference system on the 5th layer of the NF network. Controller performance was evaluated by a critic agent, which in turn produced a reinforcement signal to update the neuro-fuzzy weights. Reinforcement learning was the learning method used to train the NF controller, adapting the weights. Open and closed-loop simulation of the system response to wheel unbalance and road surface roughness was performed, plotting the time responses of system state variables. Comparison of the results indicated the effectiveness of the NF controller at reducing sprung mass vibration, pitching and rolling.

Priyandoko et al. (2009) employed Skyhook and Adaptive Neuro Active Force Control (SANAFC) for vibration attenuation on a quarter-car model. It was assumed that the wheel always maintained contact with the road surface during operation. The control system consisted of four control loops. Loop 1 used a PID to track sprung mass trajectory and input disturbances. Loop 2 used a PI controller to track the actuating force of a nonlinear pneumatic actuator. Loop 3 used skyhook damping control and loop 4 was used for active force control. A neural network trained using Levenberg-Marquardt (LM) algorithm was implemented to approximate nonlinear behaviour of the pneumatic actuator using inverse mapping. In comparison to passive and PID controlled suspension systems, the SANAFC significantly improved the ride comfort. However, not much improvement was obvious for SANAFC over the PID for suspension and tyre deflections. The experimental results validated the SANAFC method.

A hybrid PID feedback controller with Multi-Layer Perceptron (MLP) feedforward

NN, PIDNN, was presented by Dahunsi et al. (2010) to control a quarter-car AVSS, with nonlinear hydraulic actuator dynamics. The suspension system was set to track a square-wave suspension travel reference trajectory, in the presence of a sinusoidal bump on a smooth road. The PIDNN-based AVSS was then compared to a PID controlled AVSS. Both controllers produced good disturbance rejection, however, the PIDNN did not produce better tracking results than the PID; it had greater overshoot. In addition, PIDNN control input voltage exceeded the limits at certain instances and chattered throughout the length of the simulation. However, the authors concluded that the PIDNN was the controller of choice because of PIDs reputation of lack of robustness to parameter variation, modelling uncertainties and the nonlinear nature of AVSS.

2.10.4.2 Application of Neural Network-based Feedback Linearization Control for AVSS

Buckner et al. (2000) employed RBF NNFBL to control a quarter-car AVSS, with a specially designed linear electro-mechanical force actuator, for application on off-road military vehicles. The RBF NN were used to estimate the nonlinear suspension damping and spring forces, to cancel out nonlinear suspension dynamics by application of feedback linearization. RBF NN training was performed using input-output data, obtained from a quarter-car suspension test-rig's response to a sinusoidal road input disturbance. The input disturbance amplitude remained constant, while, the frequency varied between the vehicle body-hop and wheel-hop frequencies. This ensured that the data captured contained important vehicle body dynamic behaviour. Online testing of the controller on the quarter-car suspension test-rig showed a marked improvement in sprung mass acceleration reduction of the RBF NN controller over a Proportional plus Derivative (PD) controller (used as a performance benchmark). RBF NN had the ability to update weights online, hence it was adaptive.

A nonlinear, quarter-car AVSS (with electro-hydraulic actuation) was used by Pedro and Dahunsi (2011) to demonstrate the application of NNFBL control, for nonlinear systems. LM trained MLP NNs were used for nonlinear function approximation. The NN-based controller out-performed a PID controlled suspension system at tracking a square-wave suspension travel reference signal, by producing better tracking at a lower cost (in terms of energy).

2.11 Conclusion

AVSS offer a better compromise between ride comfort and road holding when compared to PVSS, SAVSS and other forms of controlled vehicle suspension systems. This is because of the addition of a force generating actuator into a passive suspension system. Half-car AVSS mathematical modelling offers more observable vehicle states compared to quarter-car AVSS but at a higher computational cost. Although the half-car AVSS model is less complex than the full-car, two separate models are required to observe all the vehicle states that are observable on the full-car AVSS. Increasing the AVSS operating bandwidth by placing the actuator in parallel with the spring and /or damper, results in better performance but at a higher energy cost.

Nonlinearities present in actual AVSS motivates the need for inclusion of nonlinearity in AVSS mathematical modelling. This would ensure that simulation results obtained are more realistic. In AVSS design, hydraulic actuator are the most widely used of all actuators; this is because they possess characteristics suitable for this application such as high power to weight ratio and lower cost. However, the high degree of nonlinearity associated with these systems requires the application of actuator force feedback. The actuator force feedback control methods need to perform well in the presence of uncertainty and parameter variation. Furthermore, suspension travel constraints, power supply and actuator force generating limitations highlight the need for control methods that account for system constraints. Application of FBL would enable linearization of nonlinear AVSS models, enabling usage of linear control methods like MPC. MPC is capable of handling model constraints present in AVSS. Inclusion of Neural Networks (NNs) would be advantageous in the presence of model uncertainties and parameter variations, due to their learning and generalizing ability when presented with unknown data (Hunt et al., 1992). Controllers such as NNFBL, MPC have been applied mostly to quarter-car AVSS making application of such controllers to half-car AVSS an important contribution.

3 PHYSICAL AND MATHEMATICAL MODELLING

3.1 Introduction

This chapter presents the mathematical modelling of the nonlinear half-car AVSS with nonlinear hydraulic actuator dynamics, that is utilized throughout the numerical simulations in the rest of this work. A similar nonlinear PVSS model, for comparison is also modelled. The chapter is introduced in Section 3.1, this is followed immediately in Section 3.2 by a statement of the assumptions taken in the modelling. Suspension system modelling then commences with the suspension springs and dampers (Section 3.3), deriving the tyre force model in Section 3.4, input disturbance modelling (Section 3.5), development of the hydraulic actuator model in Section 3.6 and finally, presentation of the complete nonlinear suspension model with actuator dynamics in Section 3.7, the difference between the AVSS and PVSS is highlighted in Section 3.8 just before concluding the chapter in Section 3.10. All MATLAB/Simulink® implementations of the models are given in Appendices A.1 to A.5.

3.2 Modelling Assumptions

The following simplifying assumptions are made during the mathematical modelling of the nonlinear, half-car active suspension system (Pedro, 2007):

1. All joints connecting suspension system components are considered to be ideal.
2. The vehicle is moving in a straight line in the horizontal direction at a constant velocity. Different vehicle velocities are applied to test controller robustness to variation in speed. Forces and moments due to cornering, accelerating and braking of the vehicle are neglected.

3. Both the sprung and unsprung masses (the vehicle body and the wheels) are assumed to be uniform in mass.

4. Sprung mass loading does not vary with time (Chen and Huang, 2005b; Gao et al., 2006; Du et al., 2008). Different sprung mass loading are applied to test controller robustness to parameter variations.

5. The vehicle body is taken as rigid.

6. Road surface roughness and irregularities are the sole source of vehicular vibration (road surface elastic deformation and engine induced vibrations are ignored).

7. Both non-uniformity of the tyre as well as wheel unbalance effects are disregarded.

8. The sprung mass centre of mass rests along the vehicle body's longitudinal centreline.

9. Sensors used respond instantly to changes in measured parameters (Du and Zhang, 2007; Lei and Tang, 2008).

10. Heaving and pitching are taken as the main vehicle body movements. Other possible motions such as yawing, rocking and lateral motions of the sprung mass centre of gravity about the nominal travel path are neglected.

11. The simulation is carried out at the point of dynamic equilibrium. Therefore, weight of the vehicle is ignored.

12. The vehicle body pitch angular displacement, θ, varied through large angles about the point of equilibrium (Huang et al., 2010).

13. Tyre damping couples the wheel and the vehicle body motion at the wheel-hop frequency and thus is not ignored (Turkay and Akcay, 2007).

3.3 Nonlinear Suspension Modelling

A half-car AVSS is illustrated in Figure 2.2, showing the suspension system components and their relative positions. Using the free body diagram given in Figure 3.1, the suspension forces can be determined.

Since the vehicle pitch angular displacement, θ, is assumed to vary through large

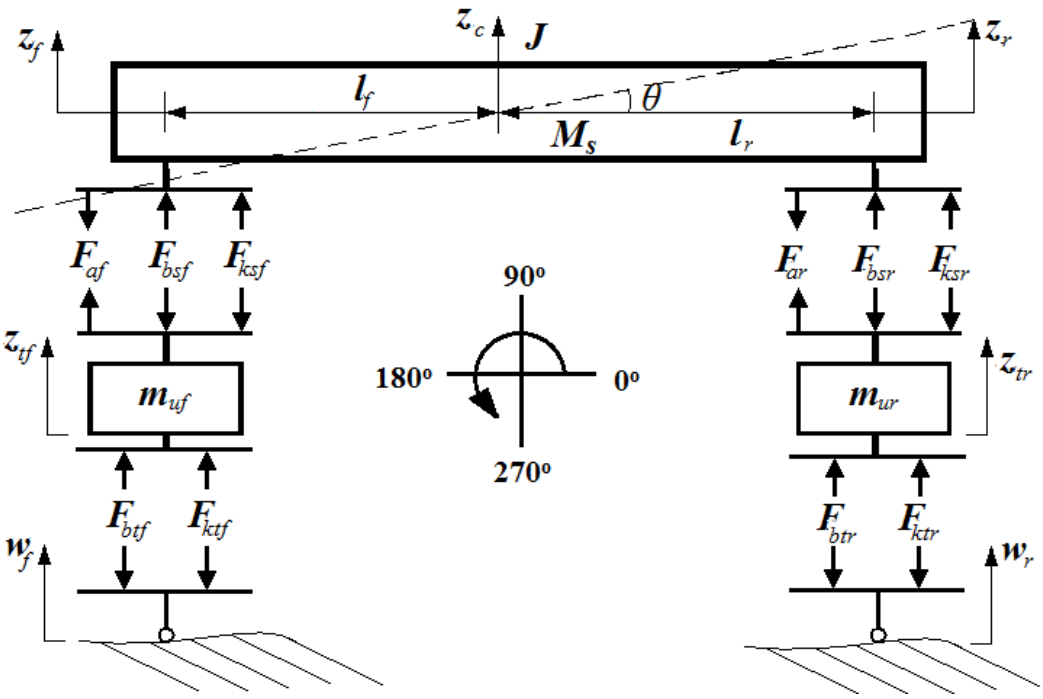

Figure 3.1: Free-body diagram of a half-car AVSS.

angles about the point of equilibrium (Modelling Assumption No.: 12), small angle approximations such as those found in (Szaszi et al., 2002) and (Hassanzadeh et al., 2010) do not apply. Thus, the front and rear sprung mass displacements z_f and z_r are given below; the front and rear sprung mass velocities, $\dot{z}_f$ and $\dot{z}_r$ respectively, are the time-derivatives of z_f and z_r (Huang et al., 2010):

$$z_f = z_c - l_f \sin\theta \tag{3.1}$$

$$\dot{z}_f = \dot{z}_c - l_f\dot{\theta}\cos\theta \tag{3.2}$$

$$z_r = z_c + l_r \sin\theta \tag{3.3}$$

$$\dot{z}_r = \dot{z}_c + l_r\dot{\theta}\cos\theta \tag{3.4}$$

with l_f and l_r denoting the front and rear axle distances from the sprung mass centre of gravity, while $\dot{\theta}$ is the pitch angular velocity.

The suspension springs have linear components: ks_f^l and ks_r^l are the front and rear linear spring constants, and nonlinear components: ks_f^{nl} and ks_r^{nl} are the front and rear suspension nonlinear spring constants respectively. Taking the relative displacements between the front and rear unsprung masses and the sprung mass, front and rear suspension system spring forces F_{ksf} and F_{ksr} are calculated as:

$$F_{ksf} = ks_f^l(z_{tf} - z_f) + ks_f^{nl}(z_{tf} - z_f)^3 \tag{3.5}$$

$$F_{ksr} = ks_r^l(z_{tr} - z_r) + ks_r^{nl}(z_{tr} - z_r)^3 \tag{3.6}$$

where z_{tf} and z_{tr} are the front and rear unsprung mass displacements respectively. The suspension dampers have linear, bs_f^l and bs_r^l, asymmetric bs_f^{sym} and bs_r^{sym} and nonlinear bs_f^{nl} and bs_r^{nl} components. Considering the relative velocity between the unsprung masses and the sprung mass, F_{bsf} (the front damping force) and F_{bsr} (the rear damping force) are expressed in Equations (3.7) and (3.8) as:

$$\begin{aligned} F_{bsf} &= bs_f^l(\dot{z}_{tf} - \dot{z}_f) - bs_f^{sym}\,|\dot{z}_{tf} - \dot{z}_f| \\ &\quad + bs_f^{nl}\left(\sqrt{|\dot{z}_{tf} - \dot{z}_f|}\right) sgn(\dot{z}_{tf} - \dot{z}_f) \qquad (3.7) \\ F_{bsr} &= bs_r^l(\dot{z}_{tr} - \dot{z}_r) - bs_r^{sym}\,|\dot{z}_{tr} - \dot{z}_r| \\ &\quad + bs_r^{nl}\left(\sqrt{|\dot{z}_{tr} - \dot{z}_r|}\right) sgn(\dot{z}_{tr} - \dot{z}_r) \qquad (3.8) \end{aligned}$$

where $\dot{z}_{tf}$ and $\dot{z}_{tr}$ are the front and rear unsprung mass velocities respectively and "*sgn*" is the *signum* function. Appendix A.1 contains MATLAB/Simulink® Implementation of nonlinear suspension system components in Section 3.3.

3.4 Tyre Force Modelling

The value of tyre damping is determined by tyre type, tyre wear, applied pressure and whether the tyre is free or rotating. Simulation results in the research carried out by (Turkay and Akcay, 2007) indicated that tyre damping couples the wheel and sprung mass motion, eliminating a constraint at the wheel-hop frequency. Due to difficulty in estimating its value, tyre damping is a factor often neglected in the literature (Szaszi et al., 2002; Hassanzadeh et al., 2010). Turkay and Akcay (2007) found a tyre damping equal to 10% of the suspension damping (bs_i^l) as a realistic estimate. Therefore, in this work, the front and rear tyre damping coefficients, bt_f and bt_r respecively, are calculated as:

$$bt_f = 0.1(bs_f^l) \qquad (3.9)$$

$$bt_r = 0.1(bs_r^l) \qquad (3.10)$$

The tyre force at each wheel (F_{tf} at the front and F_{tr} at the rear) is therefore equal to sum of the corresponding tyre spring and damping forces. The front tyre force components F_{ktf} and F_{btf} in Equations (3.11) and (3.12) are the front spring and damping forces, while the rear tyre spring and damping forces are F_{ktr} and F_{btr} respectively. F_{ktr} and F_{btr} are expressed in Equations (3.14) and (3.15). kt_f, kt_r, represent the front and rear tyre spring coefficients respectively.

$$F_{ktf} = kt_f(z_{tf} - w_f) \qquad (3.11)$$

$$F_{btf} = bt_f(\dot{z}_{tf} - \dot{w}_f) \tag{3.12}$$

$$F_{tf} = F_{ktf} + F_{btf} \tag{3.13}$$

$$F_{ktr} = kt_r(z_{tr} - w_r) \tag{3.14}$$

$$Fbt_r = bt_r(\dot{z}_{t_r} - \dot{w}_r) \tag{3.15}$$

$$F_{tr} = F_{ktr} + F_{btr} \tag{3.16}$$

The input disturbance models at the front and rear wheels (w_f and w_r) which appear in Equations 3.11 and 3.14 will be developed in Section 3.5. $\dot{w}_f$ and $\dot{w}_r$ are the time-derivatives of w_f and w_r respectively. Appendix A.2 contains MATLAB/Simulink® Implementation of nonlinear suspension system components in Section 3.4.

3.5 Input Disturbance Modelling

Vehicular vibration can be attributed to the following causes (Hrovat, 1997):

1. Wind gusts and vehicle aerodynamics;
2. Poorly damped engine vibrations;
3. Road surface conditions;
4. Vehicle attitude during manoeuvring (cornering, braking and accelerating) (Canale et al., 2006).

In vehicle suspension system design, road surface conditions are considered as the sole cause of input disturbance to the system. Road input disturbances are classified as either shock inducing or vibration inducing (Hrovat, 1997; Cao et al., 2008; Guglielmino et al., 2008).

In this research, vehicle suspension system performance was evaluated as the vehicle traversed two different road conditions commonly encountered by road vehicles:

1. A discrete road input disturbance, given in Section 3.5.1.
2. A random road input disturbance, given in Section 3.5.2.

3.5.1 Discrete Input Disturbance

This type of input disturbance is classified as a shock-inducing road disturbances because they result in impact forces being transmitted to the vehicle over a very short period of time (a few seconds). Examples of such road input disturbances are speed bumps, potholes and steps (Hrovat, 1997; Williams, 1997a). Speed bumps are "traffic calming devices". They are used to force drivers to reduce vehicle speed to levels within the speed limits for a given area, for example in areas with high pedestrian traffic such as residential, school etc. (Elizer Jr., 1993; Weber and Braaksma, 2000).

The input disturbance, illustrated in Figures 3.2 and 3.3 (a sinusoidal bump on a smooth road) was the first input disturbance used to excite the vehicle. It is discrete in nature and applies a high intensity shock to the vehicle over a short period of time (Hrovat, 1997; Cao et al., 2008). The front and rear wheel input disturbances, w_f and w_r respectively, are expressed in Equations (3.17) and (3.18) in which a is the bump amplitude, t is the simulation time in seconds, t_d is the time delay between the front and rear wheels, λ is the disturbance wavelength and V is the vehicle forward velocity. The parameters used for this disturbance, listed in Table 3.1, were obtained from the recommendations presented in (Weber and Braaksma, 2000) for a small passenger vehicle travelling on a non-bus route.

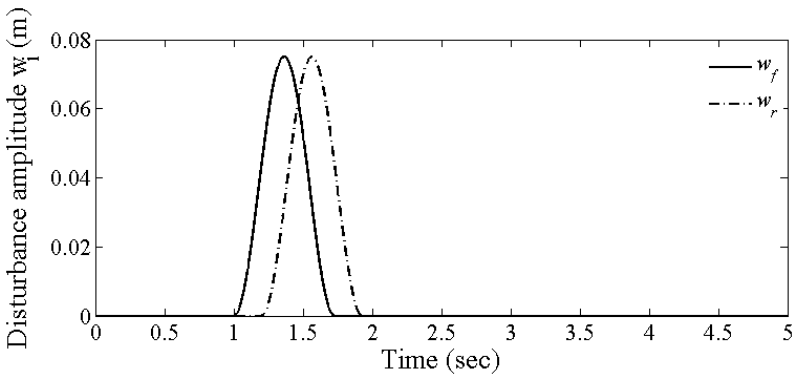

Figure 3.2: Parameters used in computing the discrete road input disturbance (Sinusoidal bump on a smooth road).

$$w_f = \begin{cases} \frac{a}{2}\left(1 - cos\left(\frac{2\pi V t_f}{\lambda}\right)\right) & 1 \leq t_f \leq 1 + \frac{\lambda}{V} \\ 0 & \text{otherwise} \end{cases} \tag{3.17}$$

$$w_r = \begin{cases} \frac{a}{2}\left(1 - cos\left(\frac{2\pi V t_r}{\lambda}\right)\right) & 1 + t_d \leq t_r \leq 1 + t_d + \frac{\lambda}{V} \\ 0 & \text{otherwise} \end{cases} \tag{3.18}$$

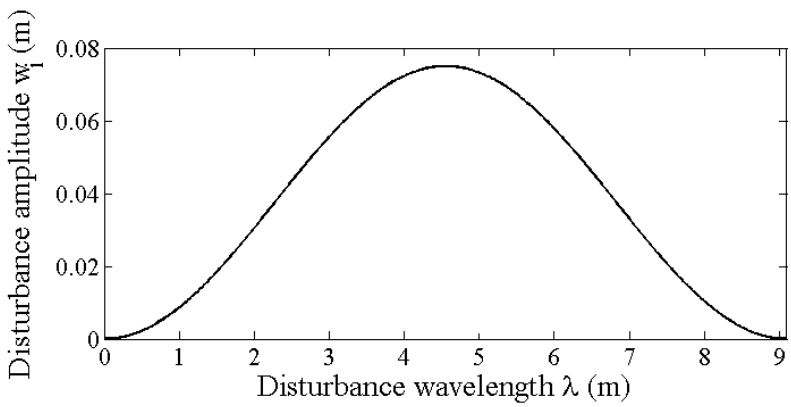

Figure 3.3: Discrete road input disturbance height w_i vs. disturbance wavelength λ.

where t_d is the time delay between the front and rear wheel written as:

$$t_d = \frac{l_f + l_r}{V} \tag{3.19}$$

Table 3.1: Discrete road input disturbance

Parameter	Value
Vehicle forward velocity (V)	$45\,km/h$
Bump amplitude (a)	$0.075\,m$
Input disturbance wavelength (λ)	$9.1\,m$

3.5.2 Random Input Disturbance

A random road input disturbance represents high frequency road surface roughness. This input can be described as a power spectral density (PSD) function that induces sustained vehicular vibration (Hrovat, 1997; Williams, 1997a).

Figure 3.4 shows a random road profile, the third input disturbance used to excite the vehicle. In space domain, road surface roughness power spectral density (PSD), $G(n)$, is expressed below in Equation (3.20) as:

$$G(n) = G(n_0)\left(\frac{n}{n_0}\right)^{-\epsilon} \tag{3.20}$$

with reference spatial frequency $n_0 = 0.1\,cycles/m$, spatial frequency n and road surface roughness coefficient $G(n_0)$. ϵ is a number that varies between $1.75 \leq \epsilon \leq 2.25$ and is often set to $\epsilon = 2$. It is an indicator of the presence of a greater number of short wavelengths for small values of ϵ or long wavelengths for large ϵ therefore

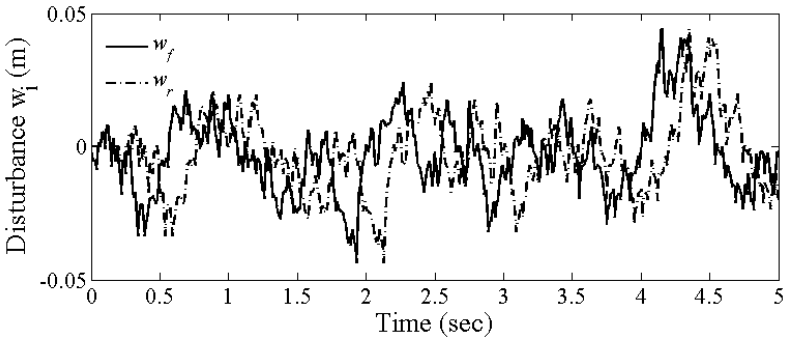

Figure 3.4: Random road input disturbance.

specifying road surface undulation. ISO values of $G(n_0)$ for different road surfaces are listed in Table 3.2 (Cao et al., 2008). The integral white noise method was here applied to generate a random road profile. This method has been used in other works such as (Cao et al., 2008) and (Lu et al., 2010) because of its simplicity and low computational burden when compared to other methods such as harmonic superposition and noise-shaping filter (Lu et al., 2010).

$$\dot{w}_f = -2\pi n_0 w_f + 2\pi\sqrt{G(n_0)V}W_0(t) \tag{3.21}$$

$$\dot{w}_r = -2\pi n_0 w_r + 2\pi\sqrt{G(n_0)V}W_0(t + t_d) \tag{3.22}$$

where $\dot{w}_i$ and w_i are the wheel vertical velocity and displacement respectively, $W_0(t)$ is a zero variance white noise signal with a PSD of 1, and V is the velocity of the vehicle in the horizontal direction. For numerical simulation, the vehicle forward velocity was set to $V = 45\,km/h$ on a class D (poor road), that is $G(n_0)$=256 $\times$ $(10^{-6}\,m^2/(cycle/m))$. Appendix A.3 contains MATLAB/Simulink® implementation

Table 3.2: ISO road surface roughness classification $G(n_0)$ at n_0=0.1$cycle/m$

Road Class	Range $\times(10^{-6}\,m^2/(cycle/m))$	Geometric Mean $\times(10^{-6}\,m^2/(cycle/m))$
A (Very Good)	< 8	4
B (Good)	$8 - 32$	16
C (Average)	$32 - 128$	64
D (Poor)	$128 - 512$	256
E (Very Poor)	$512 - 2048$	1024

of the input disturbance described in Section 3.5.

3.6 Hydraulic Actuator Modelling

The AVSS designed thus far makes use of hydraulic actuators to introduce forces into the suspension system. The magnitude of the hydraulic actuation forces F_{ai}, where subscript "i" represents either the front or rear suspension, is controlled by three-land four-way spool servo-valves. These servo-valves are specified to operate within the range $|u_i| \leq u_{max}$, where u_{max} is the maximum control voltage input allowable. For a given input voltage u_i, the rate of change of servo-valve displacement $\dot{x}_{vi}$ is expressed in Equation 3.23 as:

$$\dot{x}_{vi} = \frac{1}{\tau}(-x_{vi} + Kv_i u_i) \tag{3.23}$$

It is a linear filter with hydraulic actuator time constant τ, servo-valve displacement x_{vi} and servo-valve gain Kv_i. Kv_i is the conversion ratio of control input voltage u_i to servo-valve displacement in meters in the servo-valve (the distance the servo-valve is displaced for every unit of control voltage supplied) (Chen and Huang, 2005a).

The resulting hydraulic load flow Q_i and pressure drop across the piston Pl_i are written as:

$$Q_i = sgn\left[Ps - sgn(x_{vi})Pl_i\right]C_{dis}\Omega x_{vi}\sqrt{\frac{1}{\rho}\left|Ps - sgn(x_{vi})Pl_i\right|} \tag{3.24}$$

$$\dot{P}l_i = \frac{4\beta_e}{V_t}\left[Q_i - C_{tp}Pl_i - A_{hyd}(\dot{z}_i - \dot{z}_{ti})\right] \tag{3.25}$$

where hydraulic pressure supply is represented by Ps, discharge coefficient by C_{dis}, spool-valve area gradient by Ω, effective bulk modulus by β_e, total actuator volume by V_t, total leakage coefficient by C_{tp}, hydraulic piston area A_{hyd} and hydraulic fluid density by ρ. Equations 3.24 and 3.25 can be simplified by introducing three new parameters α, β and γ, such that:

$$\alpha = \frac{4\beta_e}{V_t} \tag{3.26}$$

$$\beta = \alpha C_{tp} \tag{3.27}$$

$$\gamma = \alpha C_{dis}\Omega x_{vi}\sqrt{\frac{1}{\rho}} \tag{3.28}$$

Equations 3.24 and 3.25 can now be rewritten as:

$$Q_i = sgn\left[Ps - sgn(x_{vi})Pl_i\right]\sqrt{|Ps - sgn(x_{vi})Pl_i|} \tag{3.29}$$

$$\dot{P}l_i = \gamma Q_i x_{vi} - \beta Pl_i - \alpha A_{hyd}(\dot{z}_i - \dot{z}_{ti}) \tag{3.30}$$

Therefore, the resulting hydraulic actuation force, F_{ai}, for a hydraulic piston area A_{hyd} is given by Equation 3.31:

$$F_{ai} = A_{hyd} Pl_i \tag{3.31}$$

The hydraulic actuator parameters have been provided in Table 3.3 (Szaszi et al., 2002; Fiahlo and Balas, 2002; Du and Zhang, 2009). Figure 3.5 is a diagram of a double-acting hydraulic actuator. The MATLAB/Simulink® implementation of the front suspension hydraulic actuator has been provided in Appendix A.4.

Table 3.3: Hydraulic actuator parameters

Parameters	Value
α	$4.515 \times 10^{13}\, N/m^{-5}$
β	$1\, s^{-1}$
γ	$1.545 \times 10^{9}\, N/m^{5/2}/kg^{1/2}$
Piston area (A_{hyd})	$3.35 \times 10^{-4}\, m^2$
Supply pressure (Ps)	$10342500\, Pa$
Time constant (τ)	$1/30\, s$
Servo-valve gains (Kv_f, Kv_r)	$0.001\, m/V$

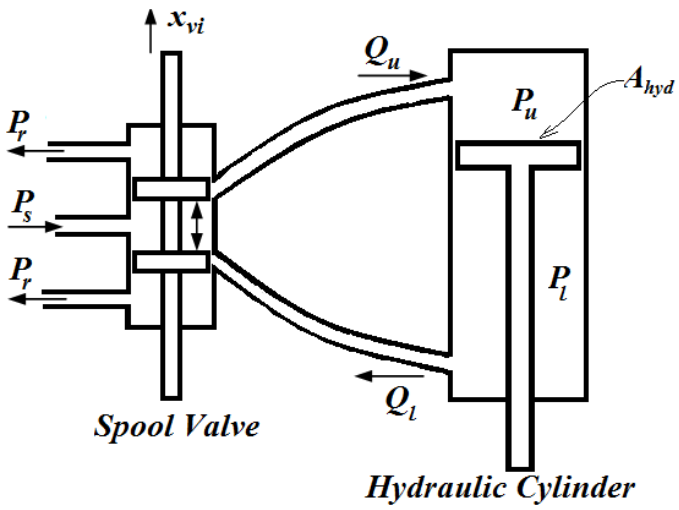

Figure 3.5: A double-acting hydraulic actuator.

3.7 Nonlinear AVSS with Hydraulic Actuator Dynamics

By combining the forces due to the suspension springs and dampers (obtained in Section 3.3) and the hydraulic actuator forces (obtained in section 3.6), it is now

possible to calculate the forces due to the front and rear suspension components, f_f and f_r. These are written as follows:

$$f_f = F_{ksf} + F_{bsf} - F_{af} \tag{3.32}$$

$$f_r = F_{ksr} + F_{bsr} - F_{ar} \tag{3.33}$$

Thus, the equations of motion of the nonlinear half-car AVSS, with hydraulic actuator dynamics, can now be derived by applying Newton's second law of motion. With reference to Figure 2.2, the equations of motion of a half-car AVSS of mass Ms are:

$$\ddot{z}_c = \frac{1}{Ms}[f_f + f_r] \tag{3.34}$$

$$\ddot{\theta} = \frac{1}{I_\theta}\left[-l_f f_f \cos\theta + l_r f_r \cos\theta\right] \tag{3.35}$$

$$\ddot{z}_{tf} = \frac{1}{mu_f}\left[-F_{tf} - f_f\right] \tag{3.36}$$

$$\ddot{z}_{tr} = \frac{1}{mu_r}\left[-F_{tr} - f_r\right] \tag{3.37}$$

where $\ddot{z}_c$, $\ddot{z}_{tf}$ and $\ddot{z}_{tr}$ are the accelerations of the sprung mass centre of gravity, front unsprung mass and rear unsprung mass respectively, $\ddot{\theta}$ and I_θ correspond to the vehicle body pitch angular acceleration and pitch moment of inertia, mu_f and mu_r are the front and rear unsprung masses (Szaszi et al., 2002; Akcay and Turkay, 2009; Hassanzadeh et al., 2010; Huang et al., 2010). The half-car AVSS model parameter values are listed in Table 3.4 (Szaszi et al., 2002; Fiahlo and Balas, 2002). Appendix A.5 contains the MATLAB/Simulink® implementation of Equations 3.34, 3.35, 3.36 and 3.37.

3.8 Nonlinear Passive Vehicle Suspension System

The half-car PVSS suspension model used for performance comparison is similar to the AVSS model derived thus far, excluding the hydraulic actuator dynamics given in Section 3.6. Actuator forces, F_{af} and F_{ar} are therefore omitted from Equations 3.32 and 3.33. The forces due to the front and rear suspension components now become:

$$f_f = F_{ksf} + F_{bsf} \tag{3.38}$$

$$f_r = F_{ksr} + F_{bsr} \tag{3.39}$$

Table 3.4: Half-car model parameters

Parameters	Value
Sprung mass (Ms)	$580\,kg$
Sprung mass pitch moment of inertia (I_θ)	$1100\,kgm^2$
Front unsprung mass (mu_f)	$40\,kg$
Rear unsprung mass (mu_r)	$40\,kg$
Front suspension linear stiffness (ks_f^l)	$2.35 \times 10^4\,N/m$
Rear suspension linear stiffness (ks_r^l)	$2.35 \times 10^4\,N/m$
Front suspension nonlinear stiffness (ks_f^{nl})	$2.35 \times 10^6\,N/m$
Rear suspension nonlinear stiffness (ks_r^{nl})	$2.35 \times 10^6\,N/m$
Front tyre stiffness (kt_f)	$1.90 \times 10^5\,N/m$
Rear tyre stiffness (kt_r)	$1.90 \times 10^5\,N/m$
Front suspension linear damping coefficient (bs_f^l)	$700\,Ns/m$
Rear suspension linear damping coefficient (bs_r^l)	$800\,Ns/m$
Front suspension nonlinear damping coefficient (bs_f^{nl})	$400\,Ns/m$
Rear suspension nonlinear damping coefficient (bs_r^{nl})	$400\,Ns/m$
Front suspension symmetric damping coefficient (bs_f^{sym})	$400\,Ns/m$
Rear suspension symmetric damping coefficient (bs_r^{sym})	$400\,Ns/m$
Front tyre damping coefficient (bt_f) (See Equation 3.9)	$70\,Ns/m$
Rear tyre damping coefficient (bt_r) (See Equation 3.10)	$80\,Ns/m$
Length between sprung mass centre of gravity and front axle (l_f)	$1.0\,m$
Length between sprung mass centre of gravity and rear axle (l_r)	$1.5\,m$

3.9 State-Space Form of AVSS Equations of Motion

The AVSS equations of motion can be expressed in state-space form:

$$\dot{\mathbf{x}} = \mathbf{f}(\mathbf{x}) + \mathbf{g}(\mathbf{x})\,\mathbf{u} + \mathbf{p}\mathbf{w} \tag{3.40}$$

where $\mathbf{x}$ is the state vector, $\mathbf{u}$ is the control input vector, $\mathbf{w}$ is the disturbance input vector, $\mathbf{f}(x)$ is the system vector, $\mathbf{g}(x)$ is the control input matrix and $\mathbf{p}$ is the disturbance input matrix.

$$\begin{aligned}\mathbf{x} &= \left[z_c, \theta, z_{tf}, z_{tr}, \dot{z}_c, \dot{\theta}, \dot{z}_{tf}, \dot{z}_{tr}, Pl_f, Pl_r, x_{vf}, x_{vr}\right]^T \\ &= [x_1, x_2, x_3, x_4, x_5, x_6, x_7, x_8, x_9, x_{10}, x_{11}, x_{12}]^T\end{aligned} \tag{3.41}$$

$$\mathbf{u} = [v_f, v_r]^T = [u_1, u_2]^T \tag{3.42}$$

$$\mathbf{w} = [w_f, w_r, \dot{w}_f, \dot{w}_r]^T \tag{3.43}$$

The output equation is given as:

$$\mathbf{y} = \mathbf{h}(\mathbf{x}) = \begin{bmatrix} x_3 - x_1 + l_f \sin x_2 \\ x_4 - x_1 - l_r \sin x_2 \end{bmatrix} \tag{3.44}$$

$$\mathbf{f}(x) = [f_1, f_2, f_3, f_4, f_5, f_6, f_7, f_8, f_9, f_{10}, f_{11}, f_{12}]^T \tag{3.45}$$

The state equations are given in Equations 3.46 to 3.54 below:

$$f_1 = x_5, f_2 = x_6, f_3 = x_7, f_4 = x_8 \tag{3.46}$$

$$\begin{aligned} f_5 = \frac{1}{Ms}\Big[& ks_f^l(x_3 - x_1 + l_f \sin x_2) + ks_f^{nl}(x_3 - x_1 + l_f \sin x_2)^3 \\ & + bs_f^l(x_7 - x_5 + l_f x_6 \cos x_2) - bs_f^{sym}|x_7 - x_5 + l_f x_6 \cos x_2| \\ & + bs_f^{nl}\sqrt{(|x_7 - x_5 + l_f x_6 \cos x_2)}sgn(x_7 - x_5 + l_f x_6 \cos x_2) \\ & - A_{hyd}x_9 + ks_r^l(x_4 - x_1 - l_r \sin x_2) + ks_r^{nl}(x_4 - x_1 - l_r \sin x_2)^3 \\ & + bs_r^l(x_8 - x_5 - l_r x_6 \cos x_2) - bs_r^{sym}|x_8 - x_5 - l_r x_6 \cos x_2| \\ & + bs_r^{nl}\sqrt{(|x_8 - x_5 - l_r x_6 \cos x_2|)}sgn(x_8 - x_5 - l_r x_6 \cos x_2) - A_{hyd}x_{10}\Big] \end{aligned} \tag{3.47}$$

$$\begin{aligned} f_6 = \frac{1}{I_\theta}\Big[& -l_f\Big(ks_f^l(x_3 - x_1 + l_f \sin x_2) + ks_f^{nl}(x_3 - x_1 + l_f \sin x_2)^3 \\ & + bs_f^l(x_7 - x_5 + l_f x_6 \cos x_2) - bs_f^{sym}\,|x_7 - x_5 + l_f x_6 \cos x_2| \\ & + bs_f^{nl}(|x_7 - x_5 + l_f x_6 \cos x_2|)^{\frac{1}{2}} sgn(x_7 - x_5 + l_f x_6 \cos x_2) - A_{hyd}x_9\Big) \\ & + l_r\Big(ks_r^l(x_4 - x_1 - l_r \sin x_2) + ks_r^{nl}(x_4 - x_1 - l_r \sin x_2)^3 \\ & + bs_r^l(x_8 - x_5 - l_r x_6 \cos x_2) - bs_r^{sym}|x_8 - x_5 - l_r x_6 \cos x_2| \\ & + bs_r^{nl}\sqrt{(|x_8 - x_5 - l_r x_6 \cos x_2|)}sgn(x_8 - x_5 - l_r x_6 \cos x_2) - A_{hyd}x_{10}\Big)\Big] \cos x_2 \end{aligned} \tag{3.48}$$

$$
\begin{aligned}
f_7 &= \frac{1}{mu_f}\Big[-kt_f x_3 - bt_f x_7 - ks_f^l(x_3 - x_1 + l_f \sin x_2) - ks_f^{nl}(x_3 - x_1 + l_f \sin x_2)^3 \\
&\quad -bs_f^l(x_7 - x_5 + l_f x_6 \cos x_2) + bs_f^{sym}|x_7 - x_5 + l_f x_6 \cos x_2| \\
&\quad -bs_f^{nl}\sqrt{(|x_7 - x_5 + l_f x_6 \cos x_2|)}sgn(x_7 - x_5 + l_f x_6 \cos x_2) + A_{hyd}x_9\Big]
\end{aligned} \tag{3.49}
$$

$$
\begin{aligned}
f_8 &= \frac{1}{mu_r}\Big[-kt_r x_4 - bt_r x_8 - ks_r^l(x_4 - x_1 - l_r \sin x_2) - ks_r^{nl}(x_4 - x_1 - l_r \sin x_2)^3 \\
&\quad -bs_r^l(x_8 - x_5 - l_r x_6 \cos x_2) + bs_r^{sym}|x_8 - x_5 - l_r x_6 \cos x_2| \\
&\quad -bs_r^{nl}\sqrt{(|x_8 - x_5 - l_r x_6 \cos x_2|)}sgn(x_8 - x_5 - l_r x_6 \cos x_2) + A_{hyd}x_{10}\Big]
\end{aligned} \tag{3.50}
$$

$$
\begin{aligned}
f_9 &= \gamma sgn\left[Ps - sgn(x_{11})x_9\right]\sqrt{(|Ps - sgn(x_{11})x_9|)}x_{11} - \beta x_9 \\
&\quad -\alpha A_{hyd}(x_5 - l_f x_6 \cos x_2 - x_7)
\end{aligned} \tag{3.51}
$$

$$
\begin{aligned}
f_{10} &= \gamma sgn\left[Ps - sgn(x_{12})x_{10}\right]\sqrt{(|Ps - sgn(x_{12})x_{10}|)}x_{12} - \beta x_{10} \\
&\quad -\alpha A_{hyd}(x_5 + l_r x_6 \cos x_2 - x_8)
\end{aligned} \tag{3.52}
$$

$$
f_{11} = \ddot{x}_{vf} = -\frac{1}{\tau}x_{11} \tag{3.53}
$$

$$
f_{12} = \dot{x}_{vr} = -\frac{1}{\tau}x_{12} \tag{3.54}
$$

$\mathbf{g}(x)$ is the control input matrix given in Equation 3.55 below for control input $\mathbf{u}$ (see Equation 3.42):

$$
\mathbf{g}(x) = \begin{bmatrix} 0 & 0 & 0 & 0 & 0 & 0 & 0 & 0 & 0 & 0 & \frac{K_{vf}}{\tau} & 0 \\ 0 & 0 & 0 & 0 & 0 & 0 & 0 & 0 & 0 & 0 & 0 & \frac{K_{vr}}{\tau} \end{bmatrix}^T \tag{3.55}
$$

$\mathbf{p}$ is the disturbance input matrix given in Equation 3.56:

$$
\mathbf{p} = \begin{bmatrix} 0 & 0 & 0 & 0 & 0 & 0 & -\frac{kt_f}{mu_f} & 0 & 0 & 0 & 0 & 0 \\ 0 & 0 & 0 & 0 & 0 & 0 & 0 & -\frac{kt_r}{mu_r} & 0 & 0 & 0 & 0 \\ 0 & 0 & 0 & 0 & 0 & 0 & -\frac{bt_f}{mu_f} & 0 & 0 & 0 & 0 & 0 \\ 0 & 0 & 0 & 0 & 0 & 0 & 0 & -\frac{bt_r}{mu_r} & 0 & 0 & 0 & 0 \end{bmatrix}^T \tag{3.56}
$$

Since the PVSS does not have hydraulic actuators, its mathematical model does not include Equations 3.51 to 3.54 and the front and rear actuator force inputs ($A_{hyd}x_9$ and $A_{hyd}x_{10}$ respectively) in Equations 3.47, 3.48, 3.49 and 3.50. Thus, the PVSS system matrix is expressed in Equation 3.57 and the control input term, $\mathbf{g}(x)\,u$, is omitted from state-space Equation 3.40.

$$
\mathbf{f}(x) = [f_1, f_2, f_3, f_4, f_5, f_6, f_7, f_8]^T \tag{3.57}
$$

3.10 Conclusion

In this chapter, the mathematical model of a nonlinear, half-car AVSS, with hydraulic actuator dynamics was developed. This was accomplished firstly by determining the forces due to the nonlinear suspension components (the front and rear suspension springs, dampers and hydraulic actuators). The spring forces were related to relative displacements between the vehicle body and wheels, while damper forces were related to the relative velocities between the vehicle body and wheels. Two models for road input disturbances were given, based on the literature. The road input disturbances exert forces on the vehicle via the wheels. Unlike most models in the literature, this AVSS model does not ignore tyre damping and also assumes angular displacements of the vehicle body about its centre of gravity are large. The complete model was then developed by applying Newton's second law. A nonlinear, half-car PVSS was also developed for results comparison. All MATLAB/Simulink® implementations of the models are given in Appendices A.1 to A.5.

CONTROLLER IMPLEMENTATION

4 PERFORMANCE SPECIFICATIONS

4.1 Introduction

The nature of the AVSS control problem requires improvement of vehicle ride comfort and road holding, while maintaining suspension travel within the limits of the suspension workspace. The "real-life" AVSS is required to perform well in the presence of actuator power supply and force output constraints (Pedro and Dahunsi, 2011).

Chapter 4 gives the performance specifications for controller design, suspension travel, vehicle road holding and ride comfort used throughout this work. In order to enable in-depth comparison of performance of the AVSS with that of the PVSS, formulae for calculating VSS RMS parameters are also given.

4.2 Performance Specifications

The following is a list of the performance specifications:

1. Nominal stability: The closed-loops should be nominally stable.
2. Disturbance rejection: The controller should demonstrate good low frequency disturbance attenuation.
3. Good command following: The controller should be able to avoid any deviation from the reference input.
4. Maximum allowable suspension travel can be written as:

$$|(z_{ti} - z_i)| \leq z_{max} \tag{4.1}$$

   where $i \in (f, r)$. z_{max} is the maximum suspension travel. In this work, z_{max} is set to $0.08\,m$.

5. Maximum allowable control voltage, u_{max} is expressed as:

$$|u_i(t)| \leq u_{max} \tag{4.2}$$

where u_{max} is the maximum allowable control voltage equal to $\pm 10\,V$.

6. Maximum allowable controlled force, F_{ai}, is given by Equation 4.3 below:

$$|F_{ai}| \leq \pm Ms \times g \tag{4.3}$$

where g is the acceleration due to gravity.

7. The dynamic tyre load, F_{ti}, should not exceed the static load, F_{ti}^{stat} in order to prevent tyre lift off phenomenon, maintaining good road holding (that is, $F_{ti} \leq F_{ti}^{stat}$) (Gao et al., 2006). Given that:

$$F_{ti} = kt_i(z_{ti} - w_i) + bt_i\,(\dot{z}_{ti} - \dot{w}_i) \tag{4.4}$$

and

$$F_{ti}^{stat} = g\left[Ms\left(\frac{l_i}{l_f + l_r}\right) + mu_i\right] \tag{4.5}$$

therefore

$$F_{ti} = kt_i(z_{ti} - w_i) + bt_i\,(\dot{z}_{ti} - \dot{w}_i) \leq g\left[Ms\left(\frac{l_i}{l_f + l_r}\right) + mu_i\right] \tag{4.6}$$

Table 4.1: F_{ti}^{stat} for $\pm 20\%$ Nominal sprung mass loading $Ms = 580\,kg$

Sprung Mass Loading	Front Suspension F_{tf}^{stat}	Rear Suspension F_{tr}^{stat}
$80\% Ms = 464\,kg$	$2213.136\,N$	$3123.504\,N$
$100\% Ms = 580\,kg$	$2668.32\,N$	$3806.28\,N$
$120\% Ms = 696\,kg$	$3123.504\,N$	$4489.056\,N$

8. Vehicle suspension parameters in terms of Root Mean Square (RMS) values:

   (a) These values will enable performance comparison of the different AVSS controllers to the PVSS:

      i. Suspension Travel:

$$(z_i - z_{ti})_{RMS} = \sqrt{\frac{1}{n}\sum_{0}^{n}(z_i - z_{ti})^2} \tag{4.7}$$

ii. Dynamic Tyre Force:

$$(F_{ti})_{RMS} = \sqrt{\frac{1}{n}\sum_{0}^{n}\left[kt_i(z_{ti}-w_i)+bt_i\left(\dot{z}_{ti}-\dot{w}_i\right)\right]^2} \quad (4.8)$$

iii. Sprung Mass Acceleration:

$$(\ddot{z}_c)_{RMS} = \sqrt{\frac{1}{n}\sum_{0}^{n}(\ddot{z}_c)^2} \quad (4.9)$$

iv. Pitch Angular Acceleration:

$$(\ddot{\theta})_{RMS} = \sqrt{\frac{1}{n}\sum_{0}^{n}(\ddot{\theta})^2} \quad (4.10)$$

(b) Additional parameters to compare performance of the different AVSS controllers to each other:

i. Actuator Control Voltage:

$$(u_i)_{RMS} = \sqrt{\frac{1}{n}\sum_{0}^{n}(u_i)^2} \quad (4.11)$$

ii. Spool-valve Displacement:

$$(x_{vi})_{RMS} = \sqrt{\frac{1}{n}\sum_{0}^{n}(x_{vi})^2} \quad (4.12)$$

iii. Actuator Force:

$$(F_{ai})_{RMS} = \sqrt{\frac{1}{n}\sum_{0}^{n}(F_{ai})^2} \quad (4.13)$$

where n is the total number of simulation samples.

9. Ride Comfort:

Vehicle ride comfort assessment is based on the calculation of frequency weighted RMS acceleration, according to the ISO 2631-1 standard. The frequency weighting depends on the posture of the human body at the time of measurement, location on the human body at which the comfort is being assessed and the rotational axis that is being considered at that location. Figure 4.1 shows three locations used for a person in a seated position in a vehicle based on the ISO 2631-1 standard (Griffin, 2007; International Organization for Standardization, 1997). These points are listed below:

(a) Seat back

(b) Seat

(c) Feet

Table 4.2 contains the frequency weightings for different locations on the human body as well as rotational axes at each location (Griffin, 2007; International Organization for Standardization, 1997).

Since the AVSS and PVSS models developed in Chapter 3 do not include

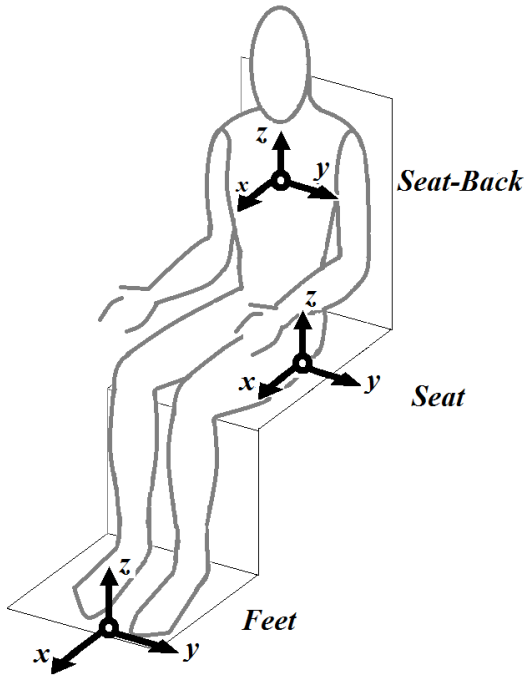

Figure 4.1: Positions of axes on human body for measurement of vibration-induced discomfort.

Table 4.2: Frequency weightings for calculation of vibration-induced discomfort

Acceleration Input Position	Axis of Rotation	Frequency Weighting	Axis Multiplication Factor (k_{axis})
Seat	r_x (Roll)	W_e	$0.63\,m/rad$
	r_y (Pitch)	W_e	$0.40\,m/rad$
	r_z (Yaw)	W_e	$0.20\,m/rad$
Seat-Back	x	W_c	0.80
	y	W_d	0.50
	z	W_d	0.40
Feet	x	W_k	0.25
	y	W_k	0.25
	z	W_k	0.40

vehicle seats, the frequency weighting W_k for acceleration input at the feet is selected. Zuo and Nayfeh (2003) developed low order approximations of the ISO 2631-1 weighting filters, for continuous time applications such as AVSS research. A fifth order approximation of frequency weighting W_k used in this work is given as (Zuo and Nayfeh, 2003):

$$W_k(s) = \frac{87.72s^4 + 1138s^3 + 11336s^2 + 5453s + 5509}{s^5 + 92.6854s^4 + 2549.83s^3 + 25969s^2 + 81057s + 79783} \tag{4.14}$$

The vertical acceleration at the sprung mass center of gravity, $\ddot{z}_c$, is the acceleration input to the system. The axis multiplication factor is therefore set to $k_{axis} = 0.40$ (see Table 4.2). Thus, the weighted acceleration, a_{wi}, is calculated as follows:

$$a_{wi} = k_{axis} W_k(\ddot{z}_c) \tag{4.15}$$

The weighted RMS acceleration, a_{wi}^{RMS}, is therefore given by Equation 4.16 below:

$$a_{wi}^{RMS} = \sqrt{\frac{1}{n}\sum_{0}^{n}(a_{wi})^2} \tag{4.16}$$

Table 4.3 contains vibration-induced discomfort levels associated with various ranges of ISO 2631-1 weighted RMS acceleration values (Griffin, 2007; International Organization for Standardization, 1997).

Table 4.3: ISO 2631-1 weighted RMS acceleration ranges and associated vibration-induced discomfort levels

Vibration-Induced Discomfort Level	ISO 2631-1 Weighted RMS Acceleration Range, a_{wi}^{RMS}
Not Uncomfortable	$a_{wi}^{RMS} \leq 0.315 m/s^2$
A Little Uncomfortable	$0.315 m/s^2 \leq a_{wi}^{RMS} \leq 0.63 m/s^2$
Fairly Uncomfortable	$0.5 m/s^2 \leq a_{wi}^{RMS} \leq 1 m/s^2$
Uncomfortable	$0.8 m/s^2 \leq a_{wi}^{RMS} \leq 1.6 m/s^2$
Very Uncomfortable	$1.25 m/s^2 \leq a_{wi}^{RMS} \leq 2.5 m/s^2$
Extremely Uncomfortable	$2 m/s^2 \leq a_{wi}^{RMS}$

4.3 Conclusion

In this chapter, specifications for controller performance as well as controller input voltage, actuator output and suspension travel constraints have been given. RMS

values of measured parameters introduced to enable in-depth comparison of AVSS performance with that of the PVSS. The ISO 2631-1 weighted RMS acceleration was selected to measure vehicle ride comfort performance. Since both the AVSS and PVSS models do not include seats, the ISO 2631-1 acceleration input was assumed to be from the feet, with axis multiplication factor $k_{axis} = 0.4$, for vertical acceleration.

5 PID CONTROL OF A NONLINEAR ACTIVE SUSPENSION VIA PID FORCE FEEDBACK

5.1 Introduction

PID is a classical control method. The overall simplicity of PID, coupled with the wide variety of tuning techniques available (intuitive methods and tuning rules) has promoted PID's extensive application in industry (Dahunsi et al., 2009). Several authors such as Guclu (2003), Sam and Hudha (2006), Kumar (2008), Dahunsi et al. (2010) and Fateh (2010), have obtained good results by applying PID to design AVSS control systems, in different control configurations. PID control is often used as a performance benchmark for other control methods (Dahunsi et al., 2009; Dahunsi et al., 2010). The disadvantage of PID control systems is that they are sensitive to parameter changes and often require high loop gains (Dahunsi et al., 2009).

In this chapter, the design of a PID controller for a nonlinear AVSS with PID hydraulic actuator force feedback is presented. The controller is designed in Section 5.2, beginning with an introduction of the overall controller architecture in Section 5.2.1, development of the inner PID force and the outer PID suspension travel control loops in Sections 5.2.2 and 5.2.3 respectively. The simulation results are then presented and discussed in Section 5.3, considering variations in vehicle velocity and sprung mass loading as the vehicles traversed different road disturbance inputs. This is followed by a presentation of an analysis of uncertainty due to variations in sprung mass loading, suspension spring coefficients and suspension damping coefficients in section 5.3.3. The chapter is then concluded in Section 5.4.

5.2 Controller Design

5.2.1 Controller Architecture

The control architecture for PID control of a nonlinear AVSS via PID force feedback consists of two control loops:

1. An inner PID force control loop.
2. An outer PID suspension travel loop.

This control architecture is illustrated in Figure 5.1. The function of the outer control loop is to set the desired force tracking signal for the hydraulic actuator, whereas the function of the inner control loop is to ensure that the desired control force, set by the outer control loop, is achieved by the hydraulic actuator.

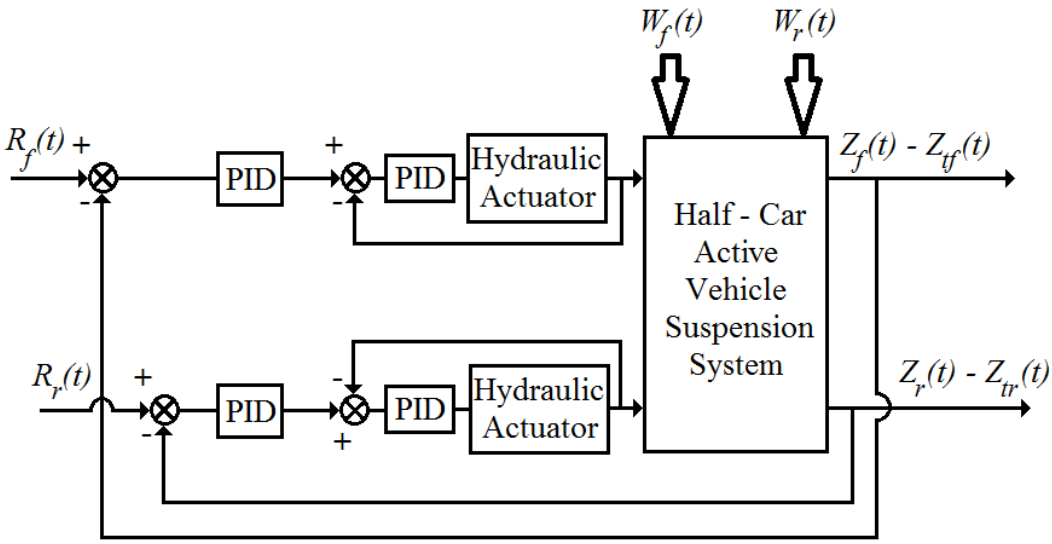

Figure 5.1: Control architecture for PID control of a nonlinear AVSS via PID force feedback.

5.2.2 PID Force Control Loop Design

The hydraulic actuator control voltage u_i, generated by the PID force control loop, is given in Equation 5.1 and the force control loop illustrated in Figure 5.2. The PID controller structure applied, is similar to that applied in (Hanafi, 2010; Gao,

2002; Astrom and Hagglund, 2004).

$$u_i = K_{P\,i} e_i\,(t) + K_{I\,i} \int e_i\,(t)\,dt + K_{D\,i} \frac{de_i\,(t)}{dt} \tag{5.1}$$

$$e_i\,(t) = F_{ai\,ref} - F_{ai} \tag{5.2}$$

where K_{Pi} is the proportional gain, K_{Ii} is the integral gain, K_{Di} is the derivative gain, e_i given in Equation 5.2 is the error between the desired actuator force reference signal $F_{ai\,ref}$, and the actual actuator force F_{ai}. Subscript i represents either the front or rear suspension $i \in (f, r)$. A saturation block was placed in front of the controller output to ensure that the control voltage limits ($|u_i| \leq u_{max}$) were not exceeded in the MATLAB/Simulink® implementation. The PID controller gains for the inner force control loop are listed in Table 5.1. These controller gains were obtained by Ziegler-Nichols tuning rules.

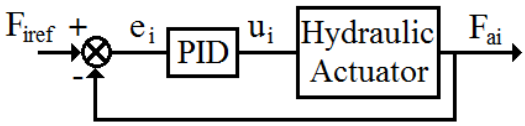

Figure 5.2: Inner PID force feedback control loop.

5.2.3 PID Suspension Travel Control Loop Design

The desired actuator force reference signal, $F_{ai\,ref}$ (see Equation 5.3), is generated by the PID suspension travel loop. The PID controller structure applied, is also similar to that applied in (Hanafi, 2010; Gao, 2002; Astrom and Hagglund, 2004).

$$F_{ai\,ref} = K_{P\,i} e_i\,(t) + K_{I\,i} \int e_i\,(t)\,dt + K_{D\,i} \frac{de_i\,(t)}{dt} \tag{5.3}$$

$$e_i\,(t) = R_i - (z_{ti} - z_i) \tag{5.4}$$

where R_i is the reference signal, $i \in (f, r)$ and e_i is the control error. In suspension travel regulation, the suspension travel reference signal is set to zero ($R_i = 0$) so that $e_i(t) \to 0$, as $t \to \infty$ (Gao, 2002).

The PID controller gains in Table 5.1 were obtained by Ziegler-Nichols method, with three aims:

1. Produce better performance by the AVSS in terms of reduction of RMS parameters specified in Chapter 4, compared with the PVSS.

2. Design a controller robust enough to handle variations in sprung mass loading and vehicle forward velocity.

3. Design a controller robust enough to handle variation in terrain (it should not require a separate tuning for each terrain). Although separate tunings could results in better performance for each different road environment, an adaptive switching method is required (Fateh and Alavi, 2009; Huang et al., 2010).

Coupling effects present in the AVSS require the use of different PID controller gains for the outer control loops. The developed PID controller parameters are listed in Tables 5.1.

Table 5.1: PID tuning parameters for front and rear suspension inner and outer control loops

		PID Gains		
Suspension	Control loop	K_P	K_I	K_D
Front	Inner loop	0.001	0.0145	0.0003
	Outer loop	0.00075	0.0375	0.0001875
Rear	Inner loop	0.001	0.0145	0.0003
	Outer loop	0.0006	0.03	0.00015

5.3 Simulation Results and Discussion

The half-car AVSS model was built in the MATLAB/Simulink® environment. The Bogacki-Shampine, Ordinary Differential Equation (ODE)-3, fixed-step solver was selected for use in the simulations. Fixed-step solvers allow users to set a fixed-sampling time throughout the duration of the simulation. A sampling time of $T_s = 0.0001s$ was selected. To enable observation of all model dynamics, T_s is set to be smaller in magnitude than the fastest half-car AVSS model dynamics (Dahunsi and Pedro, 2010). The tasking mode for periodic sampling times was set to "Single Tasking", since the model does not have multiple sampling times.

The half-car suspension system was set to pass over two different road input disturbances for suspension travel regulation ($R_i(t) = 0$). The two input disturbances are listed:

1. A $0.075m$ amplitude sinusoidal bump on a smooth road (Weber and Braaksma, 2000).

2. A random Class E (Poor) road profile disturbance of road roughness $\mathrm{G}(n_0) = 256 \times 10^{-6}\, m^2/(cycle/m)$ as given in Table 3.2.

To test the controller's robustness to parameter variation, two tests were conducted as the vehicle traversed the road input disturbances:

1. Variation of vehicle forward velocity, V:
   The vehicle forward velocity remains constant through the duration of the simulation, however, different forward velocities are used:
   (a) $V = 45\,km/h$.
   (b) $V = 60\,km/h$.
   (c) $V = 75\,km/h$.
2. Variation of vehicle sprung mass payload, Ms:
   The sprung mass payload Ms was varied $\pm 20\%$ of its nominal value, $Ms = 580\,kg$. Therefore, three values for sprung mass were tested (Du et al., 2008):
   (a) $80\% Ms = 464\,kg$
   (b) $100\% Ms = 580\,kg$
   (c) $120\% Ms = 696\,kg$

   Since the pitch moment of inertia I_θ is related to the vehicle body mass, it is assumed that the pitch moment of inertia also varies by the same amount about its nominal value (Chen et al., 2005).

The likelihood of parameter variation at different speeds motivated observation of the controller performance with sprung mass payload variation at each speed. The simulation results are therefore presented and discussed in that format.

5.3.1 Sinusoidal Bump Input Disturbance

5.3.1.1 System Response at $V = 45\,km/h$

The RMS values obtained as the PVSS and AVSS traversed a discrete (sinusoidal bump) input disturbance at $V = 45\,km/h$ are given in Table 5.2. Table 5.2 shows that the percentage improvement in RMS suspension travel remained relatively constant for both the front and rear suspension as the sprung mass increased; the front suspension reduced by 2%, whereas the rear suspension reduced by 1%, when comparing the percentage RMS reduction by the AVSS at the minimum sprung mass loading to that at the maximum sprung mass loading. The effect of sprung mass variation at this speed is minimal. The minimum and maximum peak front and

Table 5.2: RMS values for discrete input disturbance with ±20% variation in sprung mass loading about the nominal value, $Ms = 580\,kg$ with ±20% variation, at $V = 45\,km/h$

Parameters	$80\% Ms = 464\,kg$			$100\% Ms = 580\,kg$			$120\% Ms = 696\,kg$		
	PVSS	AVSS	% Reduction by AVSS	PVSS	AVSS	% Reduction by AVSS	PVSS	AVSS	% Reduction by AVSS
Front Suspension Travel $[m]$	0.0154	0.0092	40.26	0.0186	0.0114	38.71	0.0212	0.0131	38.21
Rear Suspension Travel $[m]$	0.0069	0.0048	30.43	0.0085	0.0059	30.59	0.0099	0.0070	29.29
Front Dynamic Tyre Force $[N]$	481.8700	402.9763	16.37	588.8717	477.0348	18.99	675.2629	531.4855	21.29
Rear Dynamic Tyre Force $[N]$	222.0276	228.1936	-2.78	262.2865	268.3817	-2.32	302.0889	305.2691	-1.05
Sprung Mass Acceleration $[m/s^2]$	1.0753	0.8277	23.03	1.1293	0.8649	23.41	1.1395	0.8663	23.98
Pitch Angular Acceleration $[rad/s^2]$	0.6453	0.6166	4.45	0.5849	0.5560	4.94	0.5231	0.4945	5.47
Front Actuator Control Voltage $[V]$	–	0.2709	–	–	0.3084	–	–	0.3311	–
Rear Actuator Control Voltage $[V]$	–	0.1503	–	–	0.1775	–	–	0.2012	–
Front Spool-Valve Displacement $[m]$	–	2.5327×10^{-4}	–	–	2.9045×10^{-4}	–	–	3.1350×10^{-4}	–
Rear Spool-Valve Displacement $[m]$	–	1.3771×10^{-5}	–	–	1.6426×10^{-4}	–	–	1.8739×10^{-4}	–
Front Actuator Force $[N]$	–	147.8120	–	–	182.2174	–	–	208.5706	–
Rear Actuator Force $[N]$	–	77.4532	–	–	95.3498	–	–	112.0101	–

rear suspension travel values are lower for the AVSS than for the PVSS. Figures 5.3 and 5.4 indicate that the AVSS suspension travel is less sensitive to sprung mass variation than the PVSS suspension travel. The figures also suggest that increase in vehicle mass increases the likelihood of suspension travel hitting on the suspension travel limits.

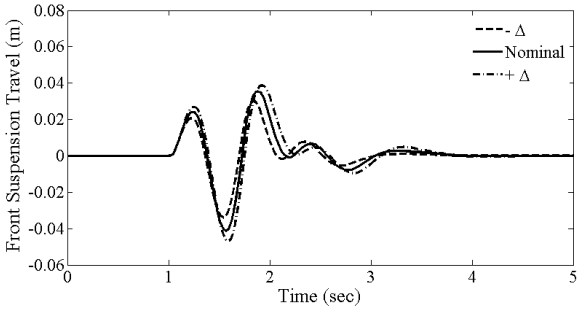

(a) AVSS

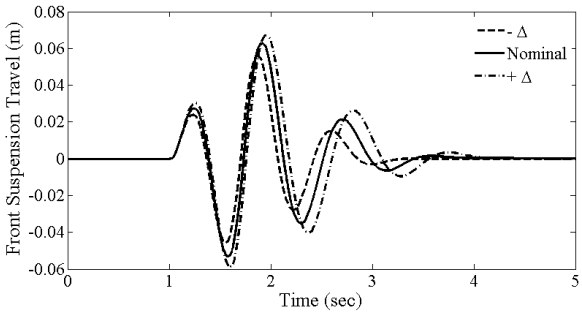

(b) PVSS

Figure 5.3: Front suspension travel for 80%, 100% and 120% Ms at $V = 45\,km/h$.

Figures 5.5 and 5.6 show the front and rear dynamic tyre force. Table 5.2 shows that the RMS front dynamic tyre force for the AVSS reduced with each increase in the sprung mass loading compared with the PVSS, while the rear AVSS rear dynamic tyre force was slightly higher than that of the PVSS (approximately $1-2\%$ higher than the PVSS), see Table 5.2. The AVSS and PVSS peak front and rear dynamic tyre forces were well below the specified limits (see Chapter 4, Table 4.1).

Figure 5.7 shows the sprung mass acceleration at $V = 45\,km/h$. The ISO 2631-1 weighted RMS acceleration given in Table 5.3. Although both the AVSS and PVSS maintained a "Not Uncomfortable" level of discomfort throughout, the AVSS weighted RMS was $21.49-23.27\%$ lower than that of the PVSS for all values of Ms.

The AVSS performance in reducing the vehicle RMS pitch angular acceleration improved with increase in vehicle sprung mass (see Table 5.2). Although the AVSS

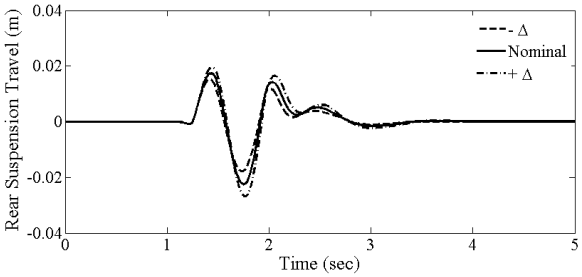

(a) AVSS

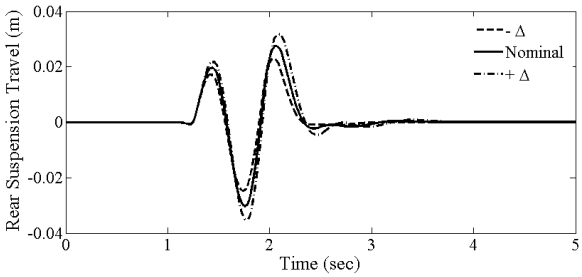

(b) PVSS

Figure 5.4: Rear suspension travel for 80%, 100% and 120% Ms at $V = 45\,km/h$.

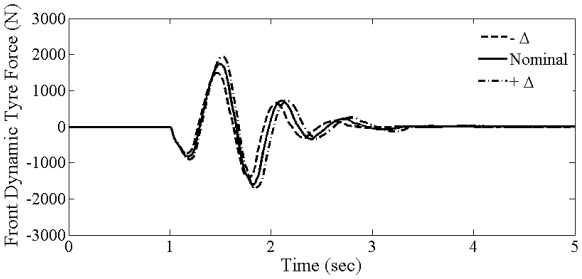

(a) AVSS

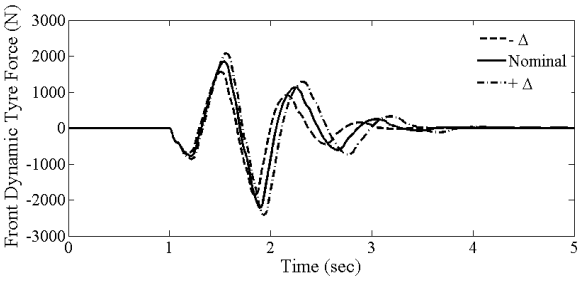

(b) PVSS

Figure 5.5: Front dynamic tyre force for 80%, 100% and 120% Ms at $V = 45\,km/h$.

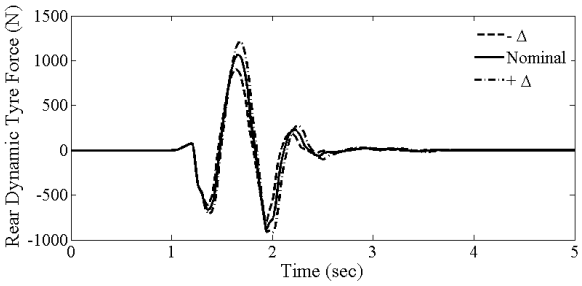

(a) AVSS

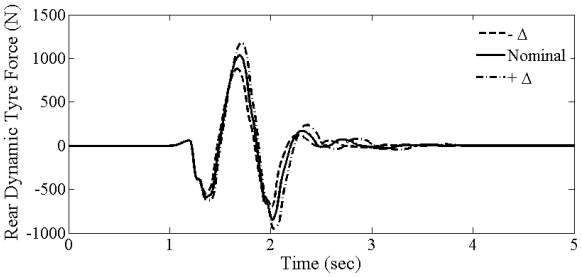

(b) PVSS

Figure 5.6: Rear dynamic tyre force for 80%, 100% and 120% Ms at $V = 45\,km/h$.

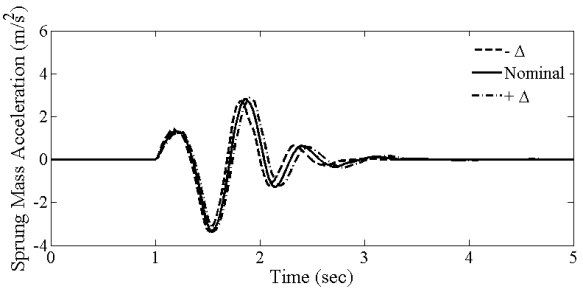

(a) AVSS

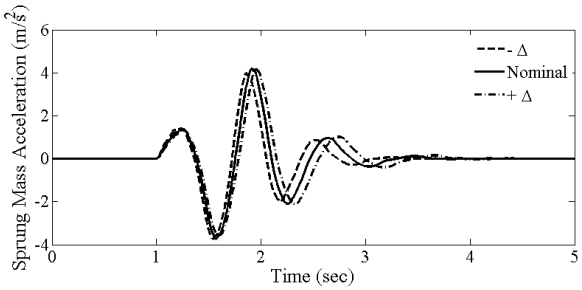

(b) PVSS

Figure 5.7: Sprung mass acceleration for 80%, 100% and 120% Ms at $V = 45\,km/h$.

Table 5.3: Weighted RMS acceleration and discomfort levels as PVSS and AVSS traverse a sinusoidal bump input disturbance at $V = 45\,km/h$

	PVSS		AVSS		%
	Weighted RMS Acceleration a_{wi}^{RMS}	ISO 2631-1 Level of Discomfort	Weighted RMS Acceleration a_{wi}^{RMS}	ISO 2631-1 Level of Discomfort	Reduction of a_{wi}^{RMS} by AVSS
80% Ms	0.2117	Not Uncomfortable	0.1662	Not Uncomfortable	21.4927
100% Ms	0.2205	Not Uncomfortable	0.1712	Not Uncomfortable	22.3583
120% Ms	0.2217	Not Uncomfortable	0.1701	Not Uncomfortable	23.2747

pitch angular acceleration peak values are higher compared with the corresponding PVSS values, Figure 5.8 shows that the AVSS dampens the oscillation approximately $0.5\,s$ faster than the PVSS.

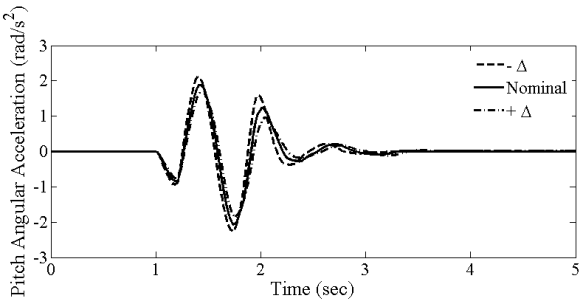

(a) AVSS

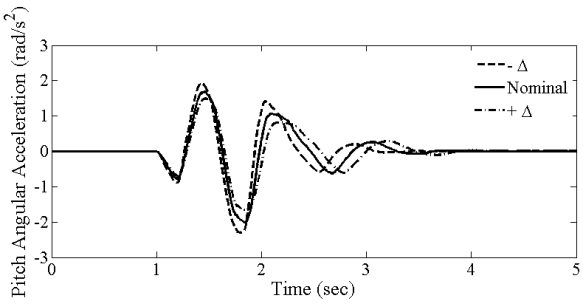

(b) PVSS

Figure 5.8: Pitch angular acceleration for 80%, 100% and 120% Ms at $V = 45\,km/h$.

The control voltage, spool-valve displacement and force for the front and rear actuators for ±20% sprung mass variation at $V = 45\,km/h$ are depicted in Figures 5.9,

5.10 and 5.11, respectively. For all values of Ms, both the front and rear actuator peak control voltages remained below the specified u_{max} limit. The RMS spool-valve displacement increased as the sprung mass increased (see Table 5.2).

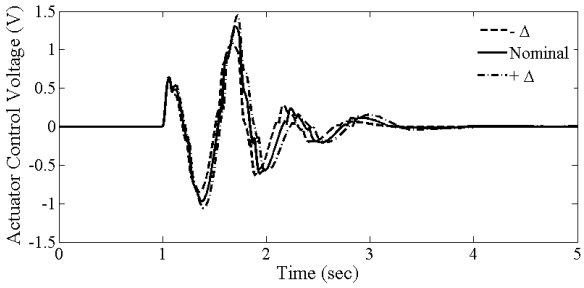

(a) Front suspension

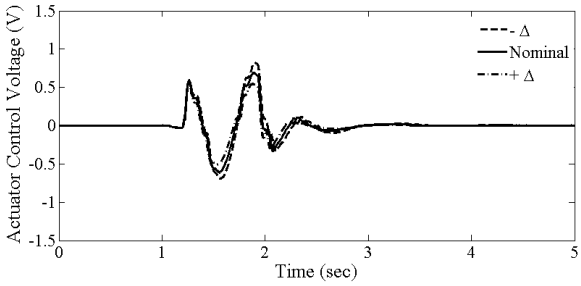

(b) Rear suspension

Figure 5.9: Front and rear actuator control voltage for 80%, 100% and 120% Ms at $V = 45\,km/h$.

The RMS actuator force in Table 5.2 increased with the sprung mass increase since a greater amount of actuator force is required to overcome the additional sprung mass weight. Figure 5.11 shows that the peak actuator force values are considerably lower than the limits specified in Chapter 4.

5.3.1.2 System Response at $V = 60\,km/h$

The RMS values obtained as the PVSS and AVSS traversed a discrete (sinusoidal bump) input disturbance at $V = 60\,km/h$ are given in Table 5.4. The percentage reduction in the front and rear RMS suspension travel of the AVSS over the PVSS are listed in Table 5.2; as the sprung mass increased, both the front and rear suspension performance reduced by approximately 0.7%. Figures 5.12 and 5.13 show the front and rear suspension travel. The minimum and maximum peak values for the front and rear AVSS suspension travel are lower than those of the PVSS, for all values of Ms. Due to increase in vehicle forward velocity from $45\,km/h$ to $60\,km/h$, there is

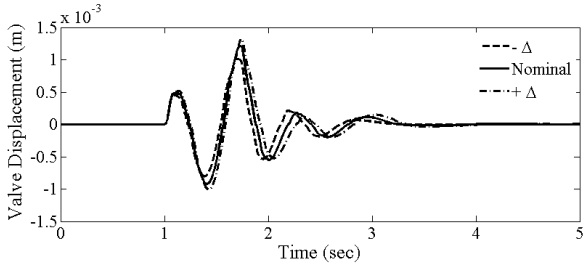

(a) Front suspension

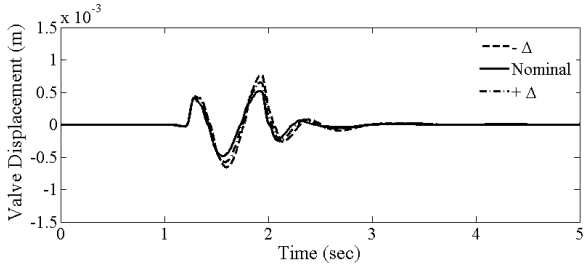

(b) Rear suspension

Figure 5.10: Front and rear actuator spool-valve displacement for 80%, 100% and 120% Ms at $V = 45\,km/h$.

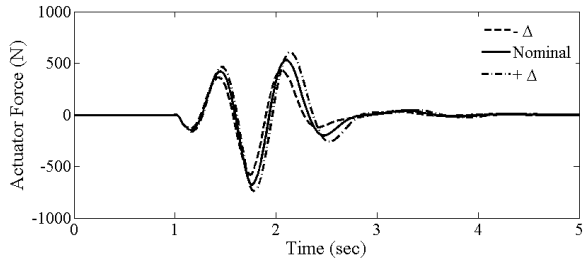

(a) Front suspension

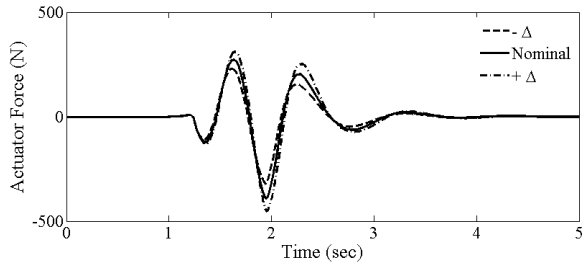

(b) Rear suspension

Figure 5.11: Front and rear actuator force for 80%, 100% and 120% Ms at $V = 45\,km/h$.

Table 5.4: RMS values for discrete input disturbance with ±20% variation in sprung mass loading about the nominal value, $Ms = 580\,kg$, at $V = 60\,km/h$

Parameters	$80\%Ms = 464\,kg$			$100\%Ms = 580\,kg$			$120\%Ms = 696\,kg$		
	PVSS	AVSS	% Reduction by AVSS	PVSS	AVSS	% Reduction by AVSS	PVSS	AVSS	% Reduction by AVSS
Front Suspension Travel $[m]$	0.0177	0.0120	32.20	0.0196	0.0134	31.63	0.0210	0.0144	31.43
Rear Suspension Travel $[m]$	0.0090	0.0065	27.78	0.0107	0.0078	27.10	0.0122	0.0089	27.05
Front Dynamic Tyre Force $[N]$	579.4022	551.0075	4.90	640.9934	601.0352	6.23	678.6571	628.0655	7.45
Rear Dynamic Tyre Force $[N]$	297.4318	321.3689	-8.05	344.9889	368.9622	-6.95	388.1406	409.4527	-5.49
Sprung Mass Acceleration $[m/s^2]$	1.5390	1.3829	10.14	1.4553	1.3123	9.83	1.3521	1.2153	10.12
Pitch Angular Acceleration $[rad/s^2]$	0.6472	0.7182	-10.97	0.5333	0.5985	-10.89	0.4468	0.5089	-13.90
Front Actuator Control Voltage $[V]$	–	0.4245	–	–	0.4349	–	–	0.4341	–
Rear Actuator Control Voltage $[V]$	–	0.2665	–	–	0.2993	–	–	0.3218	–
Front Spool-Valve Displacement $[m]$	–	3.8853×10^{-4}	–	–	4.0148×10^{-4}	–	–	4.0270×10^{-4}	–
Rear Spool-Valve Displacement $[m]$	–	2.3712×10^{-4}	–	–	2.6947×10^{-4}	–	–	2.9218×10^{-4}	–
Front Actuator Force $[N]$	–	183.2520	–	–	209.2311	–	–	226.7520	–
Rear Actuator Force $[N]$	–	97.6491	–	–	117.7360	–	–	135.7671	–

an overall deterioration of approximately 8% in percentage reduction of RMS front suspension travel and 3% in percentage reduction of RMS rear suspension travel (compare Tables 5.2 to 5.4).

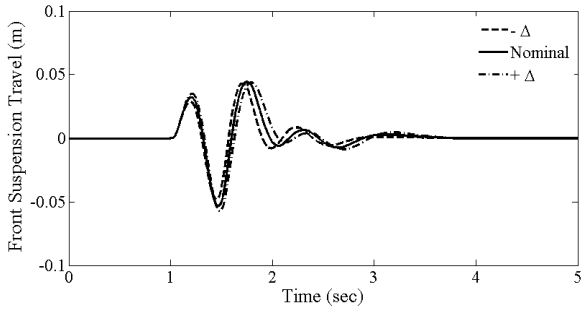

(a) AVSS

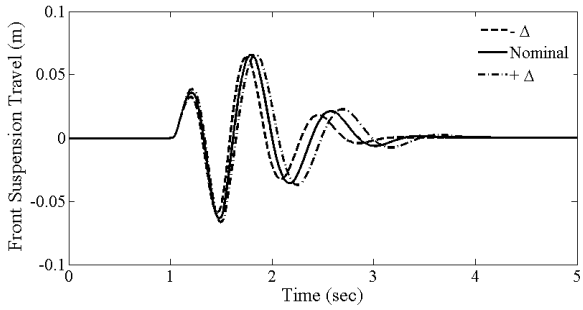

(b) PVSS

Figure 5.12: Front suspension travel for 80%, 100% and 120% Ms at $V = 60\,km/h$.

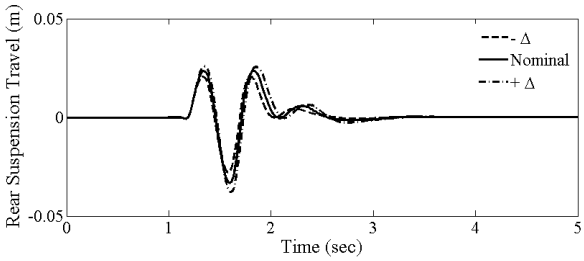

(a) AVSS

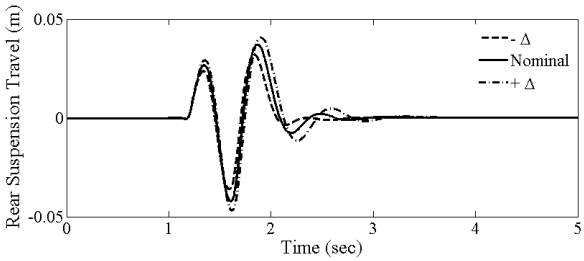

(b) PVSS

Figure 5.13: Rear suspension travel for 80%, 100% and 120% Ms at $V = 60\,km/h$.

Figures 5.14 and 5.15 illustrate the AVSS and PVSS front and rear dynamic tyre forces with $\pm 20\% Ms$ variation at $60\,km/h$. Both the front and rear dynamic tyre forces were damped approximately $0.5\,s$ faster by the AVSS than by the PVSS. The PVSS front and rear dynamic forces were lower than the specified limits (see Table 4.1, Chapter 4). However, the AVSS exceeded the front dynamic tyre force limit for $80\% Ms$ (see Figure 5.14). At $60\,km/h$, the percentage reduction in RMS front dynamic tyre force by the AVSS increased with increase in sprung mass. Although the AVSS RMS rear dynamic tyre force was higher than that of the PVSS, its performance improved with increase in sprung mass (see Table 5.4). The overall performance of the AVSS (in terms of reduction in RMS dynamic tyre force) reduced as the vehicle velocity increased from $45\,km/h$ to $60\,km/h$ (compare Tables 5.2 to 5.4). The increase in vehicle velocity leads to an increase in dynamic tyre forces. However, since Equation 4.6 is independent of vehicle velocity, at higher speed, the likelihood of exceeding the specified limits is higher.

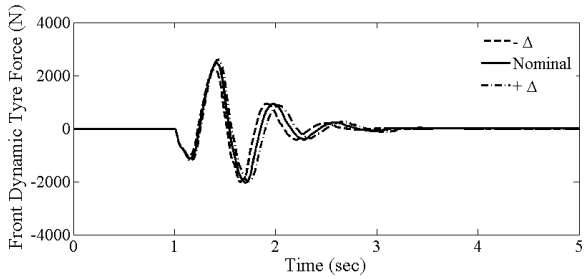

(a) AVSS

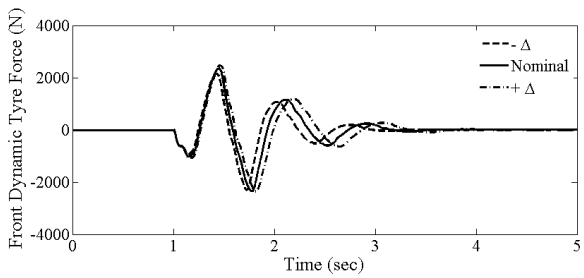

(b) PVSS

Figure 5.14: Front dynamic tyre force for 80%, 100% and 120% Ms at $V = 60\,km/h$.

Figure 5.16 shows the sprung mass acceleration. The ISO 2631-1 weighted RMS acceleration is given in Table 5.5, shows that the AVSS acceleration was $6.52-7.41\%$ lower than that of the PVSS, for all values of Ms. The overall percentage reduction in weighted RMS acceleration dropped by about $14-15\%$ with increase in vehicle velocity from $45\,km/h$ to $60\,km/h$ (compare Table 5.3 with 5.5).

The peak pitch angular accelerations experienced by the AVSS were higher than

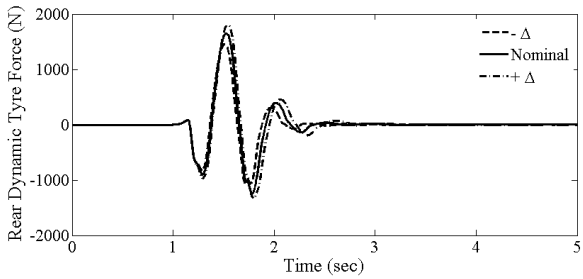

(a) AVSS

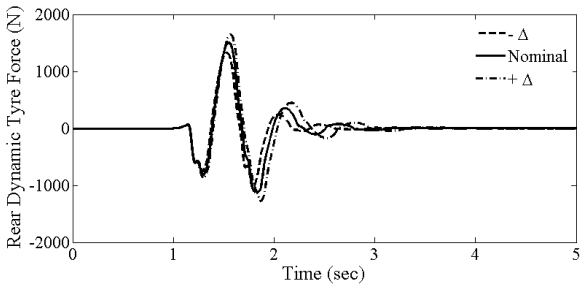

(b) PVSS

Figure 5.15: Rear dynamic tyre force for 80%, 100% and 120% Ms at $V = 60\,km/h$.

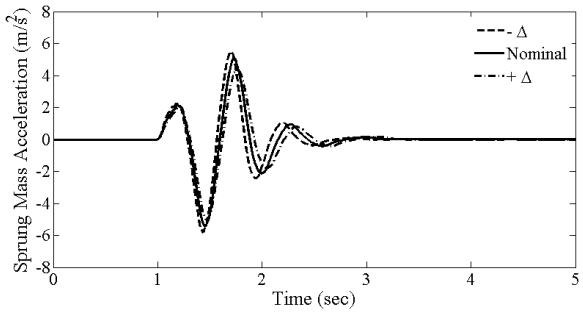

(a) AVSS

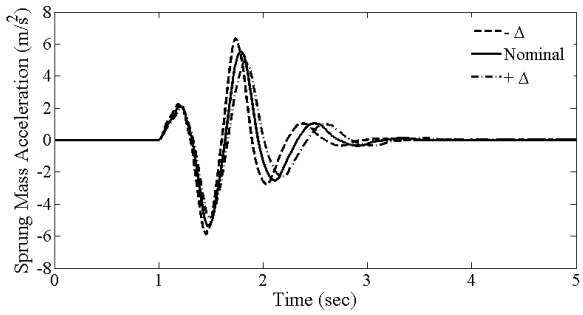

(b) PVSS

Figure 5.16: Sprung mass acceleration for 80%, 100% and 120% Ms at $V = 60\,km/h$.

Table 5.5: Weighted RMS acceleration and discomfort levels as PVSS and AVSS traverse a sinusoidal bump input disturbance at $V = 60\,km/h$

	PVSS		AVSS		%
	Weighted RMS Acceleration a_{wi}^{RMS}	ISO 2631-1 Level of Discomfort	Weighted RMS Acceleration a_{wi}^{RMS}	ISO 2631-1 Level of Discomfort	Reduction of a_{wi}^{RMS} by AVSS
80% Ms	0.3160	A Little Uncomfortable	0.2954	Not Uncomfortable	6.5190
100% Ms	0.2916	Not Uncomfortable	0.2725	Not Uncomfortable	6.5501
120% Ms	0.2671	Not Uncomfortable	0.2473	Not Uncomfortable	7.4130

those experienced by the PVSS as shown in Figure 5.17. The overall percentage reduction in RMS pitch angular acceleration by the AVSS deteriorated with the increase in velocity from $V = 45\,km/h$ to $V = 60\,km/h$ (compare Tables 5.2 to 5.4). In spite of this, the AVSS attenuated the pitch angular acceleration faster than the PVSS.

The front and rear actuator voltages, spool-valve displacements and actuator forces are shown in Figures 5.18, 5.19 and 5.20 respectively. The front and rear actuator peak values were lower than the specified limits ($|u_i| \leq u_{max}$). The RMS front and rear spool-valve displacements increased with sprung mass loading, as shown in Table 5.4. At $V = 60\,km/h$, the actuator forces also increased with sprung mass loading. The minimum and maximum peak forces remained below the specified limits in Chapter 4 (see Figures 5.20(a) and 5.20(b)). Comparison of Tables 5.2 and 5.4 indicates that there was an overall increase in RMS actuator force required to overcome increased dynamic forces at $60\,km/h$ compared with $45\,km/h$. This corresponds with the increase in actuator voltages and spool-valve displacements at the higher speed.

5.3.1.3 System Response at $V = 75\,km/h$

The RMS values obtained as the PVSS and AVSS traversed a discrete (sinusoidal bump) input disturbance at $V = 75\,km/h$ are given in Table 5.6. The AVSS and PVSS front and rear suspension travel plots are shown in Figure 5.21 and 5.22.

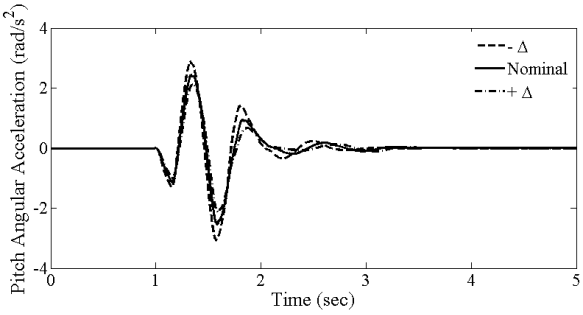

(a) AVSS

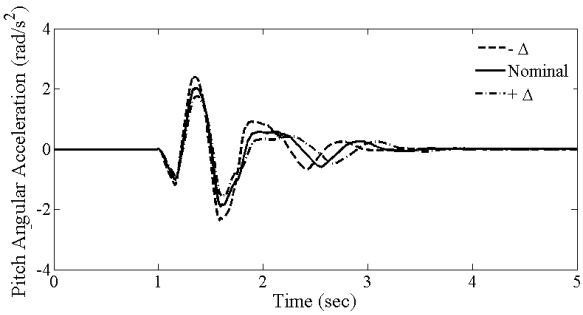

(b) PVSS

Figure 5.17: Pitch angular acceleration for 80%, 100% and 120% Ms at $V = 60\,km/h$.

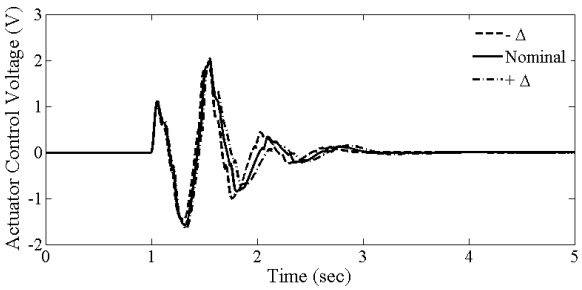

(a) Front suspension

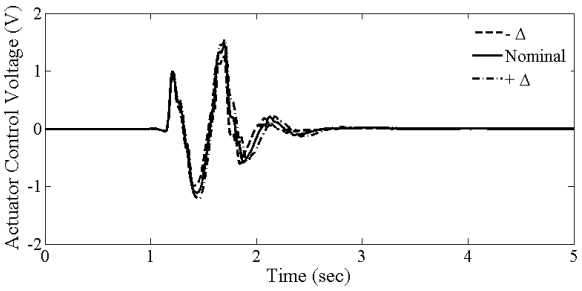

(b) Rear suspension

Figure 5.18: Front and rear actuator control voltage for 80%, 100% and 120% Ms at $V = 60\,km/h$.

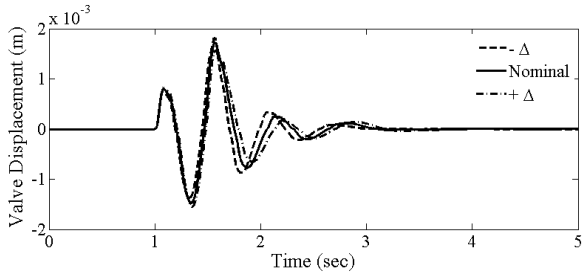

(a) Front suspension

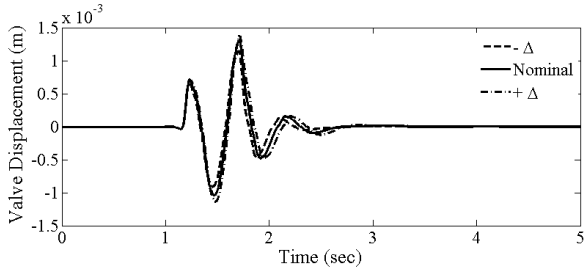

(b) Rear suspension

Figure 5.19: Front and rear actuator spool-valve displacement for 80%, 100% and 120% Ms at $V = 60\,km/h$.

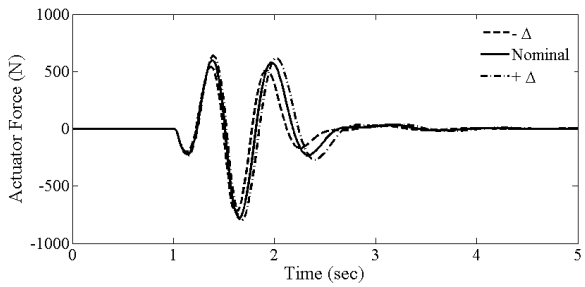

(a) Front suspension

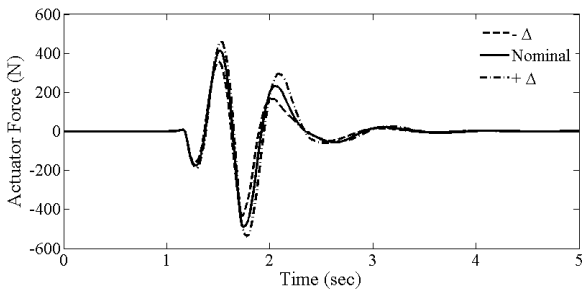

(b) Rear suspension

Figure 5.20: Front and rear actuator force for 80%, 100% and 120% Ms at $V = 60\,km/h$.

Table 5.6: RMS values for discrete input disturbance with ±20% variation in sprung mass loading about the nominal value, $Ms = 580\,kg$ at $V = 75\,km/h$

Parameters	$80\%Ms = 464\,kg$			$100\%Ms = 580\,kg$			$120\%Ms = 696\,kg$		
	PVSS	AVSS	% Reduction by AVSS	PVSS	AVSS	% Reduction by AVSS	PVSS	AVSS	% Reduction by AVSS
Front Suspension Travel $[m]$	0.0173	0.0130	24.86	0.0183	0.0137	25.14	0.0188	0.0141	25
Rear Suspension Travel $[m]$	0.0104	0.0079	24.04	0.0119	0.0091	23.53	0.0132	0.0100	24.24
Front Dynamic Tyre Force $[N]$	573.9147	604.7748	-5.38	593.7066	624.5176	-5.19	598.9838	627.9656	-4.84
Rear Dynamic Tyre Force $[N]$	355.9515	395.9707	-11.24	396.8327	439.6393	-10.79	428.4287	472.1489	-10.20
Sprung Mass Acceleration $[m/s^2]$	1.7252	1.7291	-0.23	1.5206	1.5345	-0.91	1.3408	1.3553	-0.81
Pitch Angular Acceleration $[rad/s^2]$	0.5890	0.7157	-21.51	0.4736	0.5829	-23.08	0.3969	0.4918	-23.91
Front Actuator Control Voltage $[V]$	–	0.5175	–	–	0.5060	–	–	0.4894	–
Rear Actuator Control Voltage $[V]$	–	0.3817	–	–	0.4070	–	–	0.4194	–
Front Spool-Valve Displacement $[m]$	–	4.6211×10^{-4}	–	–	4.5443×10^{-4}	–	–	4.4165×10^{-4}	–
Rear Spool-Valve Displacement $[m]$	–	3.3042×10^{-4}	–	–	3.5620×10^{-4}	–	–	3.6969×10^{-4}	–
Front Actuator Force $[N]$	–	190.0401	–	–	206.7882	–	–	216.8851	–
Rear Actuator Force $[N]$	–	112.2627	–	–	131.3392	–	–	147.1892	–

The peak AVSS and PVSS suspension travel values were lower than the specified limit of $\pm 0.08\,m$. The percentage reduction in RMS suspension travel by the AVSS against the PVSS fluctuated between 24.86% and 25.14% for the front suspension, and fluctuated between 23.53% and 24.24% for the rear suspension (see Table 5.6). Analysis of the RMS for suspension travel in Tables 5.2, 5.4 and 5.6 suggests the AVSS performance in reducing RMS suspension travel was more sensitive to variations in vehicle velocity than to variations in sprung mass.

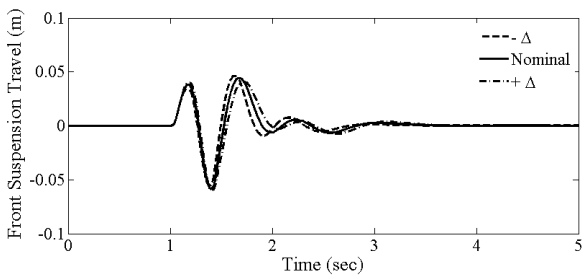

(a) AVSS

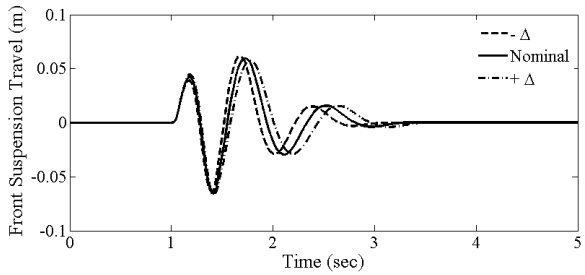

(b) PVSS

Figure 5.21: Front suspension travel for 80%, 100% and 120% Ms at $V = 75\,km/h$.

Both AVSS and PVSS exceeded the maximum allowable front wheel dynamic tyre force for 80%Ms (see Figure 5.23). The AVSS exceeded the maximum allowable front wheel dynamic tyre force at 100%Ms (Figure 5.23). However, Figure 5.23 also shows that the AVSS minimized the front tyre dynamic force $0.5\,s$ faster than the PVSS. The rear dynamic tyre forces are shown in Figure 5.24. Both the rear AVSS and PVSS dynamic tyre force remained below the specified limits for all values of Ms. Figure 5.24 shows that the AVSS rear dynamic tyre force is minimized $0.25\,s$ faster than that of the PVSS, even though the AVSS peak forces are greater in magnitude. Analysis of the RMS performance of the AVSS at $V = 45\,km/h$, $60\,km/h$ and $75\,km/h$ indicates that the AVSS dynamic road holding performance deteriorated with increase in vehicle speed. Increase in sprung mass caused some improvements in both the front and rear dynamic tyre force reduction by the AVSS, even though the rear dynamic tyre force of the AVSS was higher than that of the PVSS (see Tables 5.2, 5.4 and 5.6).

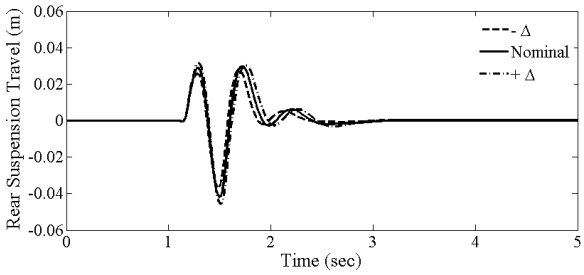

(a) AVSS

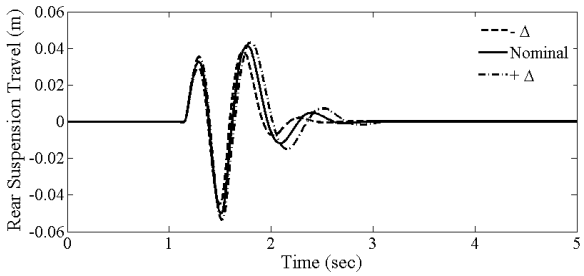

(b) PVSS

Figure 5.22: Rear suspension travel for 80%, 100% and 120% Ms at $V = 75\,km/h$.

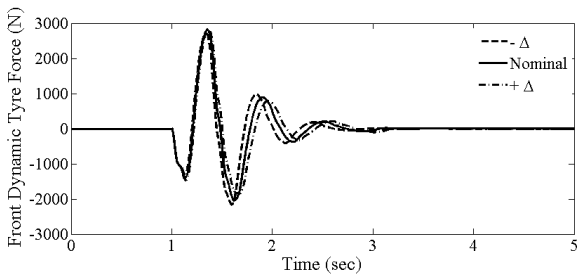

(a) AVSS

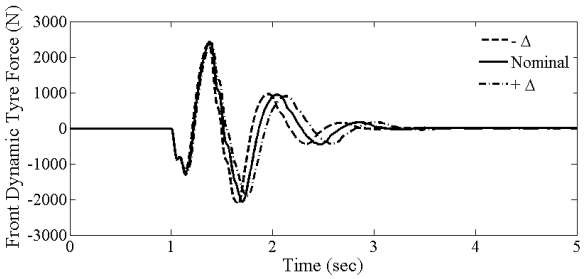

(b) PVSS

Figure 5.23: Front dynamic tyre force for 80%, 100% and 120% Ms at $V = 75\,km/h$.

The sprung mass acceleration is shown in Figure 5.25 with corresponding ISO 2631-1 weighted RMS acceleration in Table 5.7. Though the AVSS weighted RMS acceleration was $5.66 - 6.33\%$ higher than that of the PVSS, the AVSS reduced the

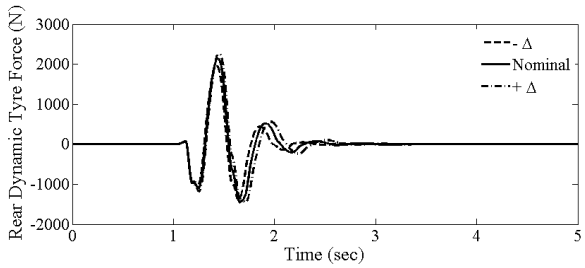

(a) AVSS

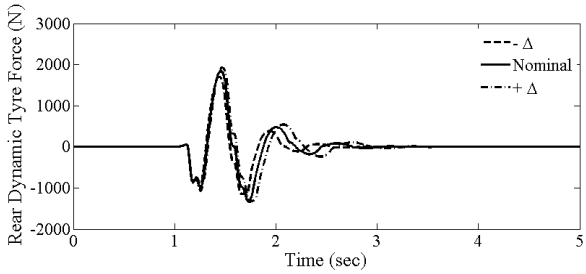

(b) PVSS

Figure 5.24: Rear dynamic tyre force for 80%, 100% and 120% Ms at $V = 75\,km/h$.

acceleration about $0.25\,s$ faster than the PVSS (see Figure 5.25). The overall percentage reduction in weighted RMS acceleration by the AVSS dropped with increase of vehicle velocity from 45 to $75\,km/h$ (see Tables 5.3, 5.5 and 5.7).

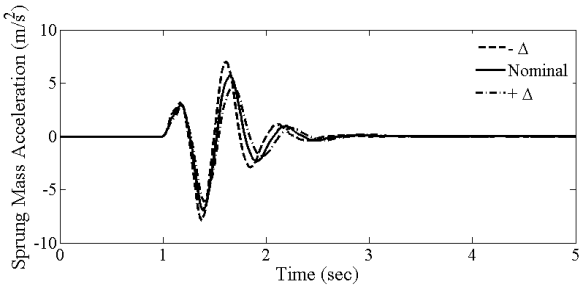

(a) AVSS

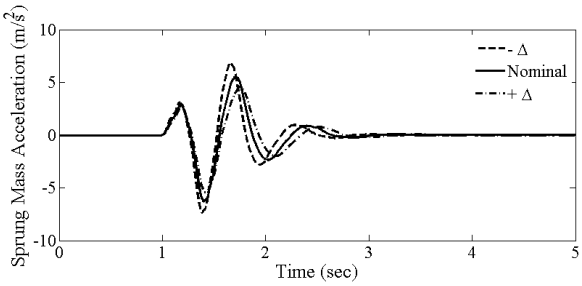

(b) PVSS

Figure 5.25: Sprung mass acceleration for 80%, 100% and 120% Ms at $V = 75\,km/h$.

The vehicle pitch angular acceleration is shown in Figure 5.26, for $V = 75\,km/h$.

Table 5.7: Weighted RMS acceleration and discomfort levels as PVSS and AVSS traverse a sinusoidal bump input disturbance at $V = 75\,km/h$

	PVSS		AVSS		%
	Weighted RMS Acceleration a_{wi}^{RMS}	ISO 2631-1 Level of Discomfort	Weighted RMS Acceleration a_{wi}^{RMS}	ISO 2631-1 Level of Discomfort	Reduction of a_{wi}^{RMS} by AVSS
80% Ms	0.3682	A Little Uncomfortable	0.3915	A Little Uncomfortable	-6.3281
100% Ms	0.3140	Not Uncomfortable	0.3338	A Little Uncomfortable	-6.3057
120% Ms	0.2719	Not Uncomfortable	0.2873	Not Uncomfortable	-5.6638

For all values of Ms, the AVSS maximum and minimum peak values were higher in magnitude than the PVSS peak values. However, Figure 5.26 shows that the AVSS attenuated the pitch angular acceleration $0.5\,s$ faster than the PVSS. The overall AVSS performance to reduce pitch angular acceleration dropped as the vehicle velocity increased (see Tables 5.2, 5.4 and 5.6).

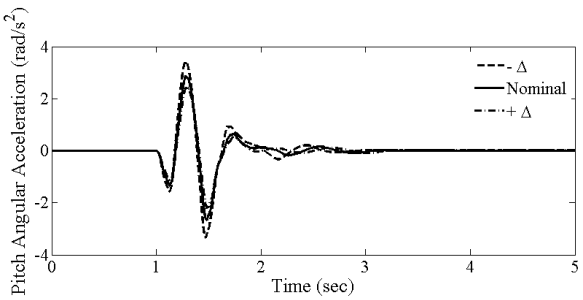

(a) AVSS

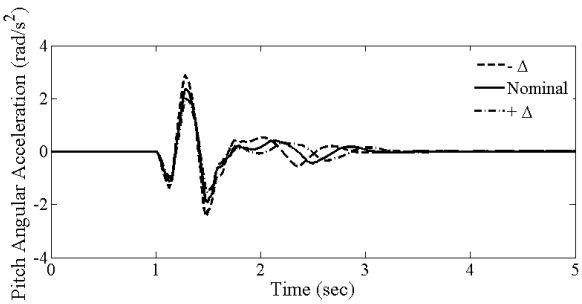

(b) PVSS

Figure 5.26: Pitch angular acceleration for 80%, 100% and 120% Ms at $V = 75\,km/h$.

Figure 5.27 shows the variation of AVSS front and rear actuator voltage at $V = 75\,km/h$. The minimum and maximum peak actuator control voltages were lower than the $\pm 10\,V$ limits. The front and rear actuator spool-valve displacements obtained at $V = 75\,km/h$ are displayed in Figure 5.28, with the corresponding RMS spool-valve displacements given in Table 5.6. Figure 5.29 shows the front and rear actuator forces. The peak front and rear actuator forces were lower than the specified limits given in Chapter 4. Looking at the RMS control voltages, spool-valve displacements and actuator forces obtained in Tables 5.2, 5.4 and 5.6, it is observed that the magnitudes of these parameters increased with increase in vehicle velocity (from $45\,km/h$ to $75\,km/h$) as well as vehicle mass (from $464\,kg$ to $696\,kg$). This was to compensate for the higher dynamic force experienced with increase in vehicle velocity and sprung mass loading.

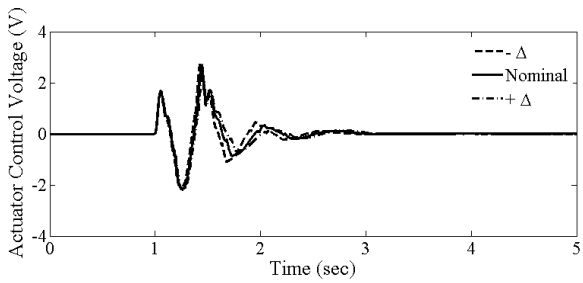

(a) Front suspension

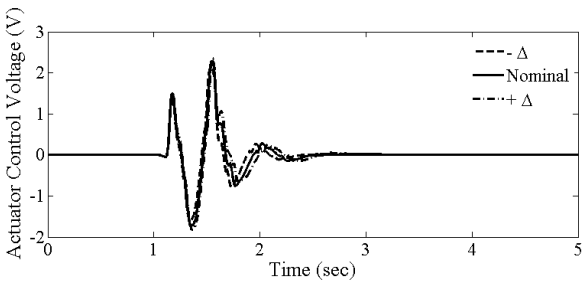

(b) Rear suspension

Figure 5.27: Front and rear actuator control voltage for 80%, 100% and 120% Ms at $V = 75\,km/h$.

5.3.2 Random Input Disturbance

5.3.2.1 System Response at $V = 45\,km/h$

The RMS values obtained as the PVSS and AVSS traversed a random road input disturbance at $V = 45\,km/h$ are given in Table 5.8. RMS percentage reduction of

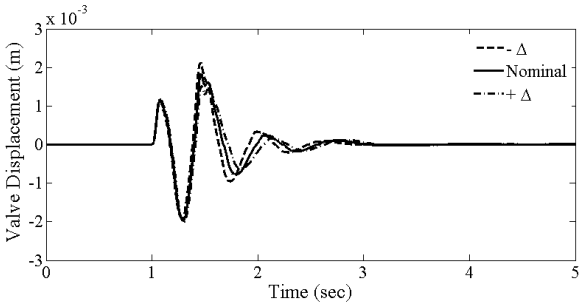

(a) Front suspension

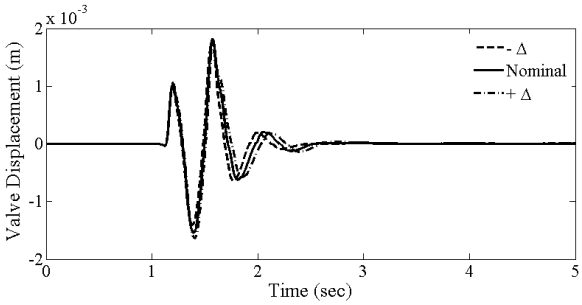

(b) Rear suspension

Figure 5.28: Front and rear actuator spool-valve displacement for 80%, 100% and 120% Ms at $V = 75\,km/h$.

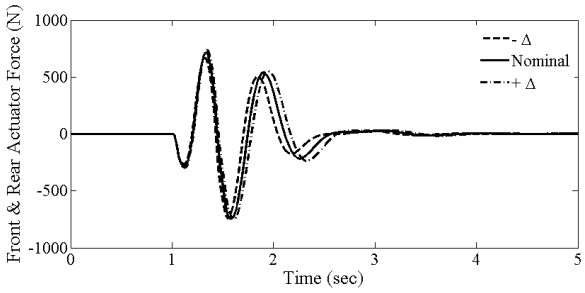

(a) Front suspension

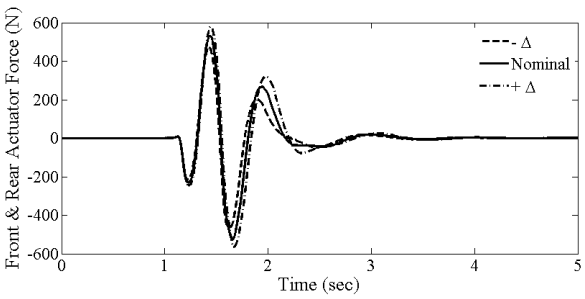

(b) Rear suspension

Figure 5.29: Front and rear actuator force for 80%, 100% and 120% Ms at $V = 75\,km/h$.

Table 5.8: RMS values for random input disturbance with ±20% variation in sprung mass loading about the nominal value, $Ms = 580\,kg$ with ±20% variation, at $V = 45\,km/h$

Parameters	$80\% Ms = 464\,kg$			$100\% Ms = 580\,kg$			$120\% Ms = 696\,kg$		
	PVSS	AVSS	% Reduction by AVSS	PVSS	AVSS	% Reduction by AVSS	PVSS	AVSS	% Reduction by AVSS
Front Suspension Travel $[m]$	0.0053	0.0044	16.98	0.0058	0.0046	20.69	0.0062	0.0047	24.19
Rear Suspension Travel $[m]$	0.0039	0.0035	10.26	0.0041	0.0036	12.20	0.0042	0.0038	9.52
Front Dynamic Tyre Force $[N]$	371.2132	368.1840	0.82	373.9010	365.9652	2.12	377.7547	364.5134	3.51
Rear Dynamic Tyre Force $[N]$	355.5504	353.7741	0.50	352.3982	350.2475	0.61	350.7665	348.0384	0.78
Sprung Mass Acceleration $[m/s^2]$	0.6619	0.7333	-10.79	0.5466	0.5960	-9.04	0.4732	0.5030	-6.30
Pitch Angular Acceleration $[rad/s^2]$	0.4625	0.5410	-16.97	0.3714	0.4349	-17.10	0.3088	0.3628	-17.49
Front Actuator Control Voltage $[V]$	–	0.7717	–	–	0.7701	–	–	0.7685	–
Rear Actuator Control Voltage $[V]$	–	0.7302	–	–	0.7287	–	–	0.7274	–
Front Spool-Valve Displacement $[m]$	–	3.1601×10^{-4}	–	–	3.1356×10^{-4}	–	–	3.1130×10^{-4}	–
Rear Spool-Valve Displacement $[m]$	–	2.9693×10^{-4}	–	–	2.9595×10^{-4}	–	–	2.9488×10^{-4}	–
Front Actuator Force $[N]$	–	66.6798	–	–	69.9125	–	–	72.6417	–
Rear Actuator Force $[N]$	–	52.0552	–	–	54.8667	–	–	56.9959	–

the values for the front suspension travel given in Table 5.8, improved as the sprung mass is increased from $464\,kg$ to $696\,kg$, compared with the PVSS. The AVSS rear suspension travel improvement over the PVSS fluctuated between 15.38% at 80%Ms and 14.29% at 120%Ms. The front and rear suspension travel are shown in Figures 5.30 and 5.31, respectively. These figures show that both the AVSS and PVSS suspension travel remained below the specified limits at the peaks.

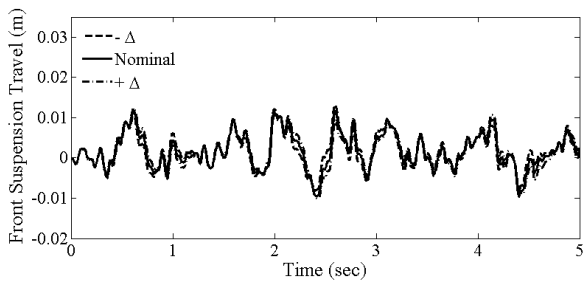

(a) AVSS

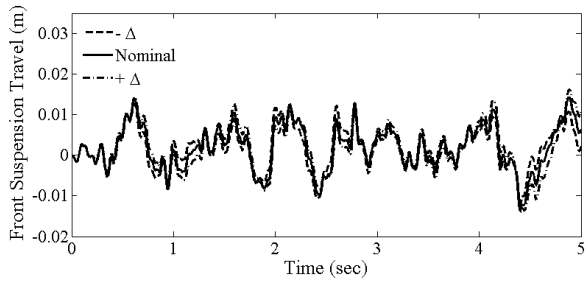

(b) PVSS

Figure 5.30: Front suspension travel for 80%, 100% and 120% Ms at $V = 45\,km/h$.

The dynamic tyre forces for the front and rear suspension are shown in Figures 5.32 and 5.33 respectively. The peak dynamic tyre forces for both the AVSS and PVSS remained below the specified limits in Chapter 4. The front AVSS dynamic tyre force percentage reduction improved with increase in sprung mass, from 0.98% at 80%Ms to 3.37% at 120%Ms, whereas the rear AVSS dynamic tyre force percentage reduction improved but remained just under 1%.

Figure 5.34 shows the sprung mass acceleration at $V = 45\,km/h$, with ISO 2631-1 weighted RMS acceleration is given in Table 5.9. Both the AVSS and PVSS maintained a "Not Uncomfortable" level of discomfort throughout, however, the AVSS weighted RMS was $10.66 - 12.54\%$ higher than that of the PVSS for all values of Ms. Table 5.9 also shows that the AVSS performance improved with increase in sprung mass loading.

The pitch angular acceleration is shown in Figure 5.35. The AVSS RMS pitch

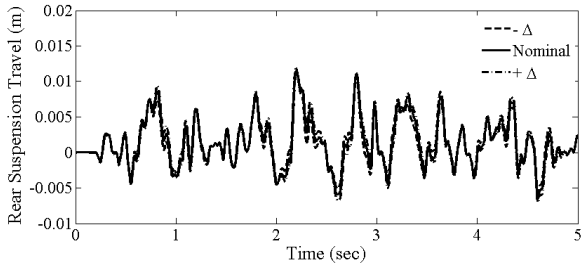

(a) AVSS

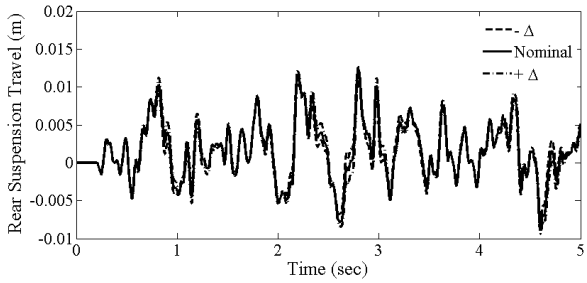

(b) PVSS

Figure 5.31: Rear suspension travel for 80%, 100% and 120% Ms at $V = 45\,km/h$.

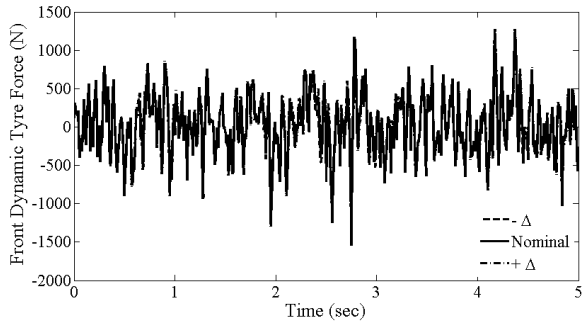

(a) AVSS

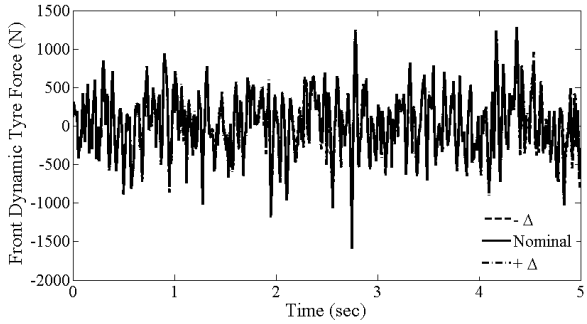

(b) PVSS

Figure 5.32: Front dynamic tyre force for 80%, 100% and 120% Ms at $V = 45\,km/h$.

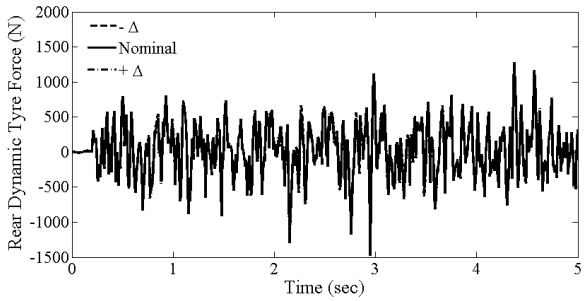

(a) AVSS

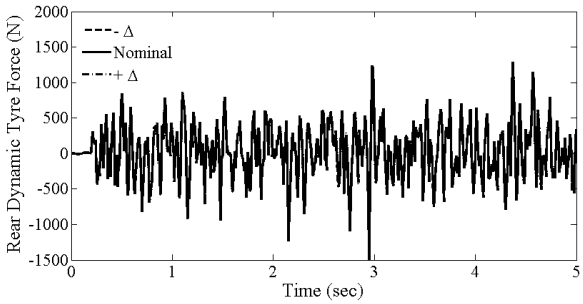

(b) PVSS

Figure 5.33: Rear dynamic tyre force for 80%, 100% and 120% Ms at $V = 45\,km/h$.

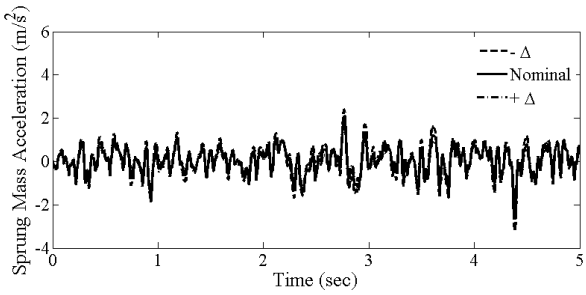

(a) AVSS

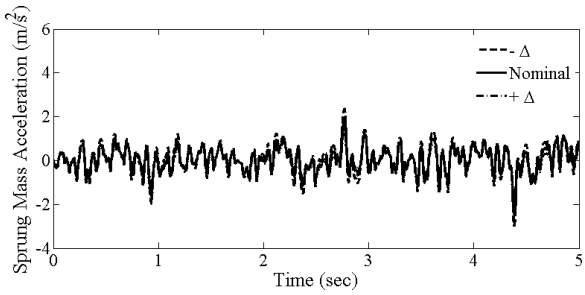

(b) PVSS

Figure 5.34: Sprung mass acceleration for 80%, 100% and 120% Ms at $V = 45\,km/h$.

Table 5.9: Weighted RMS acceleration and discomfort levels as PVSS and AVSS traversed a random road input disturbance at $V = 45\,km/h$

	PVSS		AVSS		%
	Weighted RMS Acceleration a_{wi}^{RMS}	ISO 2631-1 Level of Discomfort	Weighted RMS Acceleration a_{wi}^{RMS}	ISO 2631-1 Level of Discomfort	Reduction of a_{wi}^{RMS} by AVSS
80% Ms	0.2296	Not Uncomfortable	0.2584	Not Uncomfortable	-12.5436
100% Ms	0.1834	Not Uncomfortable	0.2053	Not Uncomfortable	-11.9411
120% Ms	0.1538	Not Uncomfortable	0.1702	Not Uncomfortable	-10.6632

angular acceleration was worse than the PVSS RMS pitch angular acceleration by 16.76% at the minimum sprung mass load and 17.31% at the maximum sprung mass load. The peak pitch angular acceleration values for the AVSS were also higher than those of the PVSS.

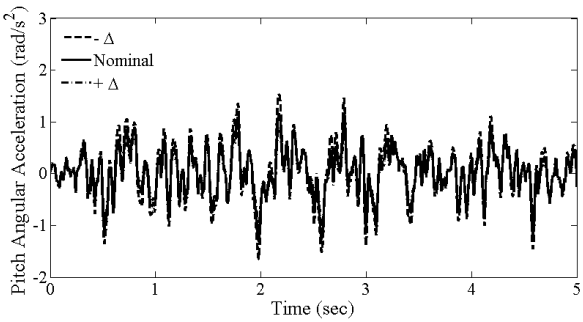

(a) AVSS

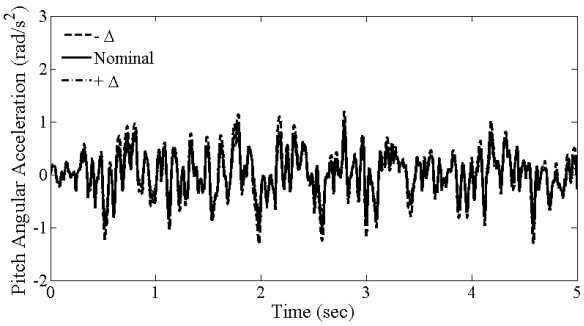

(b) PVSS

Figure 5.35: Pitch angular acceleration for 80%, 100% and 120% Ms at $V = 45\,km/h$.

Figures 5.36 and 5.37 show the front and rear actuator voltages and spool-valve displacements respectively. The front actuator control voltage was lower than the specified limit, however, the rear actuator control voltage peaked at $+10V$ during the first $0.05\,s$ of the simulation.

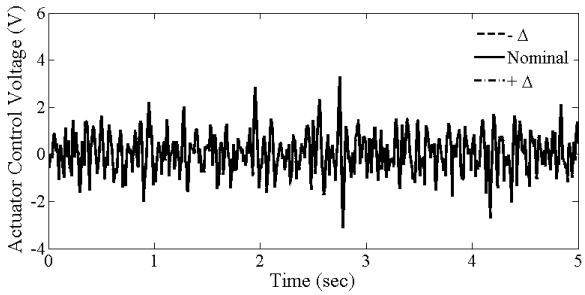

(a) Front suspension

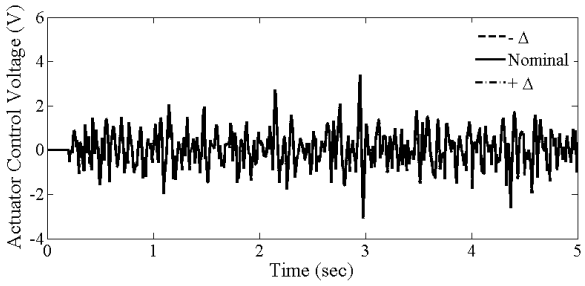

(b) Rear suspension

Figure 5.36: Front and rear actuator control voltage for 80%, 100% and 120% Ms at $V = 45\,km/h$.

The front and rear actuator forces increased to compensate for the increase in sprung mass. This is shown by the increase in RMS front and rear actuator forces in Table 5.8. The peak actuator forces were well within the limits specified in Chapter 4. The front and rear actuator forces are shown in Figure 5.38. Examining the magnitudes of the RMS actuator forces experienced for the sinusoidal bump and random input disturbances shows that the required actuator force reduces with input disturbance amplitude.

5.3.2.2 System Response at $V = 60\,km/h$

The RMS values obtained as the PVSS and AVSS traversed a random road input disturbance at $V = 60\,km/h$ are given in Table 5.10. Figures 5.39 and 5.40 show the front and rear suspension travel. Relative to the PVSS, the AVSS front and rear

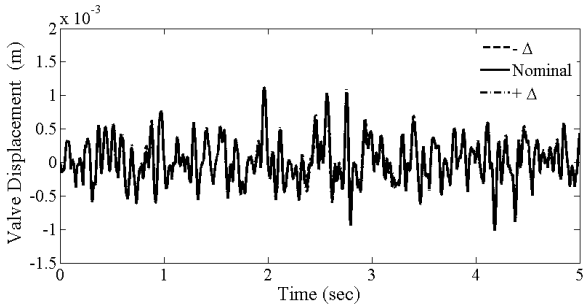

(a) Front suspension

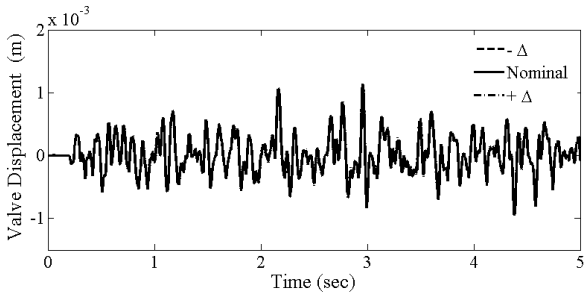

(b) Rear suspension

Figure 5.37: Front and rear actuator spool-valve displacement for 80%, 100% and 120% Ms at $V = 45\,km/h$.

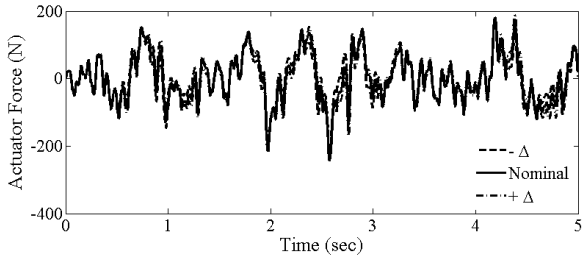

(a) Front suspension

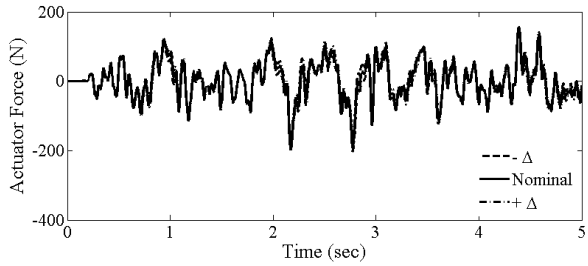

(b) Rear suspension

Figure 5.38: Front and rear actuator force for 80%, 100% and 120% Ms at $V = 45\,km/h$.

Table 5.10: RMS values for random input disturbance with ±20% variation in sprung mass loading about the nominal value, $Ms = 580\,kg$, at $V = 60\,km/h$

Parameters	$80\%Ms = 464\,kg$			$100\%Ms = 580\,kg$			$120\%Ms = 696\,kg$		
	PVSS	AVSS	% Reduction by AVSS	PVSS	AVSS	% Reduction by AVSS	PVSS	AVSS	% Reduction by AVSS
Front Suspension Travel $[m]$	0.0056	0.0047	16.07	0.0059	0.0049	16.95	0.0063	0.0050	20.63
Rear Suspension Travel $[m]$	0.0042	0.0037	11.90	0.0044	0.0039	11.36	0.0046	0.0040	13.04
Front Dynamic Tyre Force $[N]$	422.4601	415.1364	1.73	423.2846	411.9699	2.67	425.4429	409.5151	3.74
Rear Dynamic Tyre Force $[N]$	408.6404	401.6085	1.72	405.6346	398.2043	1.83	404.5175	395.9457	2.12
Sprung Mass Acceleration $[m/s^2]$	0.7692	0.8694	-13.03	0.6311	0.7084	-12.25	0.5410	0.5961	-10.18
Pitch Angular Acceleration $[rad/s^2]$	0.4807	0.5517	-14.77	0.3837	0.4404	-14.78	0.3184	0.3669	-15.23
Front Actuator Control Voltage $[V]$	–	0.8981	–	–	0.8971	–	–	0.8955	–
Rear Actuator Control Voltage $[V]$	–	0.8566	–	–	0.8557	–	–	0.8545	–
Front Spool-Valve Displacement $[m]$	–	3.6152×10^{-4}	–	–	3.5894×10^{-4}	–	–	3.5626×10^{-4}	–
Rear Spool-Valve Displacement $[m]$	–	3.4071×10^{-4}	–	–	3.3988×10^{-4}	–	–	3.3897×10^{-4}	–
Front Actuator Force $[N]$	–	71.6412	–	–	74.2778	–	–	76.2819	–
Rear Actuator Force $[N]$	–	55.7281	–	–	58.8580	–	–	61.2336	–

suspension travel performance improved with increase in sprung mass (see Table 5.8). The minimum and maximum suspension travel obtained for the AVSS and PVSS were below the specified $\pm 0.08\,m$ limit. Comparing the percentage reduction in suspension travel by the AVSS at $45\,km/h$ with that at $60\,km/h$, the overall performance at the front suspension dropped with increase in speed, while the overall performance at the rear suspension improved with increase in speed (compare Table 5.8 to Table 5.10).

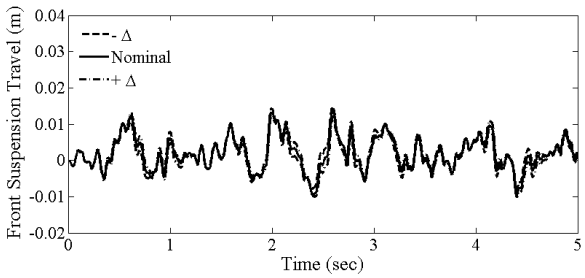

(a) AVSS

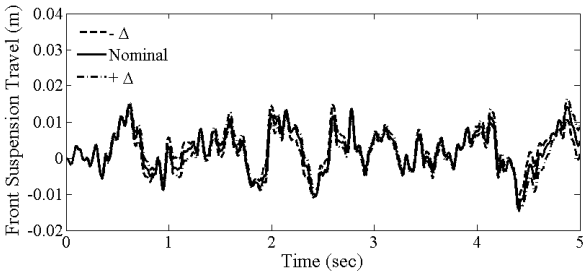

(b) AVSS

Figure 5.39: Front suspension travel for 80%, 100% and 120% Ms at $V = 60\,km/h$.

The front and rear dynamic tyre forces are shown in Figures 5.41 and 5.42 respectively. At $60\,km/h$, both the AVSS and PVSS dynamic tyre forces did not exceed the specified limits (see Table 4.1, Chapter 4), for all values of Ms. Examination of Figures 5.41 and 5.42 shows that the peak dynamic tyre forces for the AVSS tend to be lower than those of the PVSS. Comparing the RMS dynamic tyre forces in Table 5.8 with the RMS dynamic tyre forces Table 5.10, there is a noticeable increase in the overall dynamic tyre forces experienced at greater speed; this is due to higher dynamic forces exerted by the road and the vehicle at higher speed. However, there was an improvement in the percentage reduction in dynamic tyre forces by AVSS at the greater speed; at $45\,km/h$, the percentage improvement varied between $0.82 - 3.51\%$ at the front and $0.50 - 0.78\%$ at the rear, while at $60\,km/h$, the percentage improvement varied between $1.73 - 3.74\%$ at the front and $1.72 - 2.12\%$ at the rear.

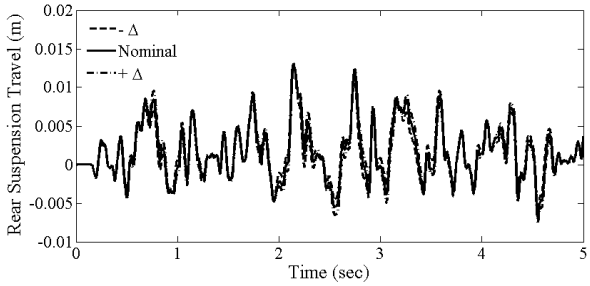

(a) AVSS

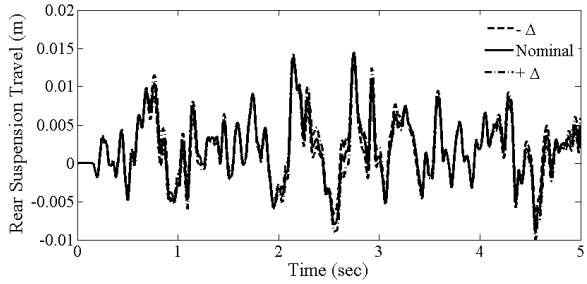

(b) AVSS

Figure 5.40: Rear suspension travel for 80%, 100% and 120% Ms at $V = 60\,km/h$.

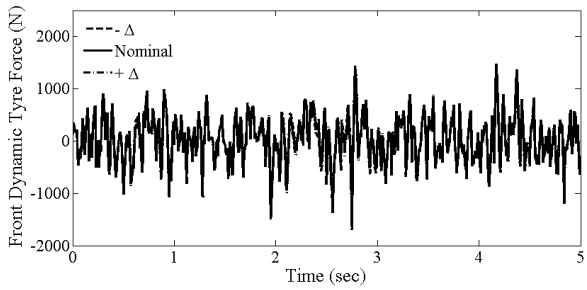

(a) AVSS

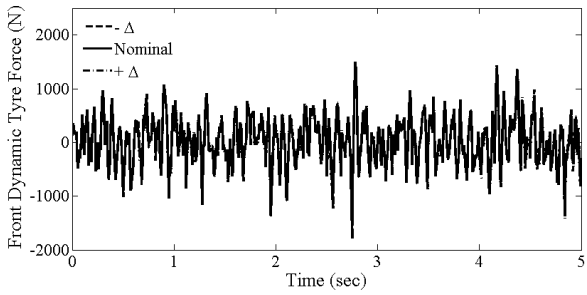

(b) AVSS

Figure 5.41: Front dynamic tyre force for 80%, 100% and 120% Ms at $V = 60\,km/h$.

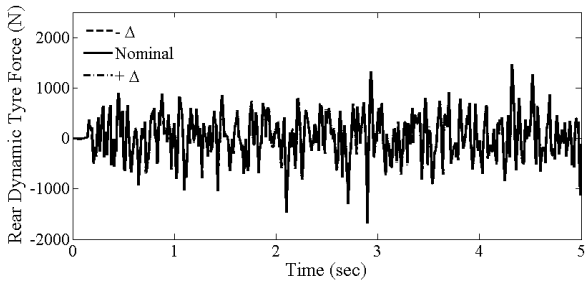

(a) AVSS

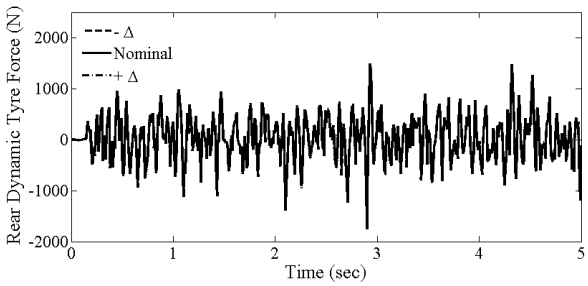

(b) AVSS

Figure 5.42: Rear dynamic tyre force for 80%, 100% and 120% Ms at $V = 60\,km/h$.

The vehicle sprung mass acceleration with accompanying ISO 2631-1 weighted RMS acceleration are given in Figure 5.16 and Table 5.5 respectively. Although the AVSS weighted acceleration was $12.86-14.25\%$ higher than that of the PVSS (for all values of Ms), it remained within the range "Not Uncomfortable". The overall AVSS performance at $60\,km/h$ deteriorated roughly by 2%, compared with the performance at $45\,km/h$ (compare Table 5.9 with 5.11).

Table 5.11: Weighted RMS acceleration and discomfort levels as PVSS and AVSS traversed a random road input disturbance at $V = 60\,km/h$

	PVSS		AVSS		%
	Weighted RMS Acceleration a_{wi}^{RMS}	ISO 2631-1 Level of Discomfort	Weighted RMS Acceleration a_{wi}^{RMS}	ISO 2631-1 Level of Discomfort	Reduction of a_{wi}^{RMS} by AVSS
80% Ms	0.2667	Not Uncomfortable	0.3047	Not Uncomfortable	-14.2482
100% Ms	0.2131	Not Uncomfortable	0.2424	Not Uncomfortable	-13.7494
120% Ms	0.1781	Not Uncomfortable	0.2010	Not Uncomfortable	-12.8579

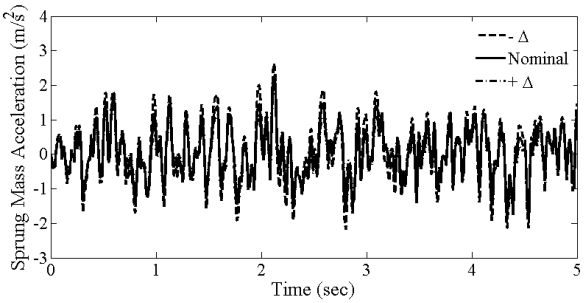

(a) AVSS

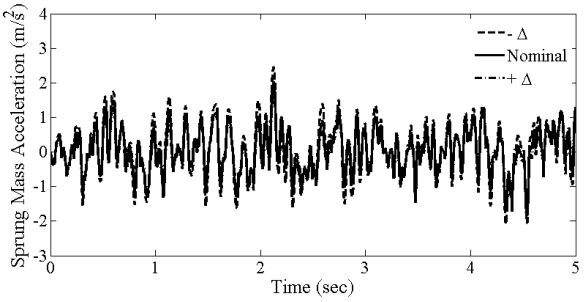

(b) AVSS

Figure 5.43: Sprung mass acceleration for 80%, 100% and 120% Ms at $V = 60\,km/h$.

The AVSS and PVSS pitch angular acceleration are shown in Figure 5.44. The PVSS RMS and peak pitch angular acceleration values were lower than those of the AVSS. Although the PVSS performed better than the AVSS in terms of RMS pitch angular acceleration, the overall percentage reduction in RMS pitch angular acceleration by the AVSS improved from varying between -16.97% and -17.49% at $V = 45\,km/h$ to -14.77% and -15.23% at $V = 60\,km/h$.

The front and rear actuator voltages are shown in Figure 5.45. For all values of Ms tested at $60\,km/h$, the peak actuator control voltages obtained were well below the specified $\pm 10\,V$ limit. Figure 5.47 shows the front and rear spool-valve displacement. Comparing Tables 5.8 and 5.10, the overall RMS actuator voltages and spool-valve displacements increased with increase in vehicle velocity.

The front and rear actuator forces are shown in Figure 5.47. The peak forces remained within the specified limits (see Chapter 4) for all values of Ms. At $60\,km/h$, the RMS actuator forces increased with increase in sprung mass loading (see Table 5.10). Comparing the RMS actuator forces required at $45\,km/h$ to those at $60\,km/h$, there was an overall increase in force required at higher speed.

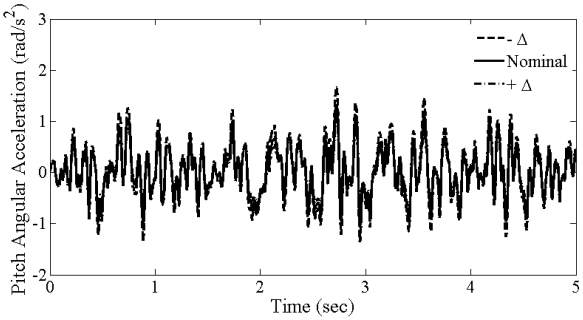

(a) AVSS

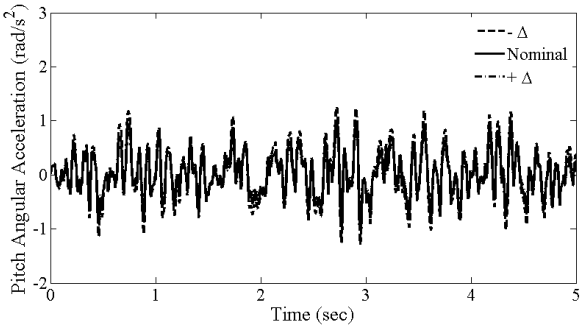

(b) AVSS

Figure 5.44: Pitch angular acceleration for 80%, 100% and 120% Ms at $V = 60\,km/h$.

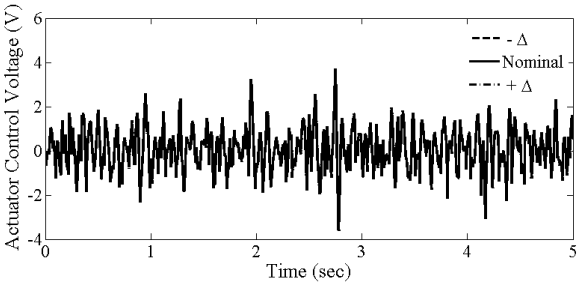

(a) Front suspension

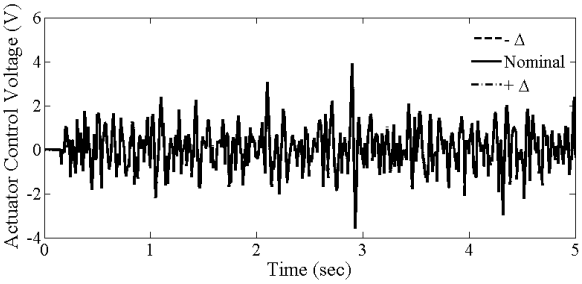

(b) Rear suspension

Figure 5.45: Front and rear actuator control voltage for 80%, 100% and 120% Ms at $V = 60\,km/h$.

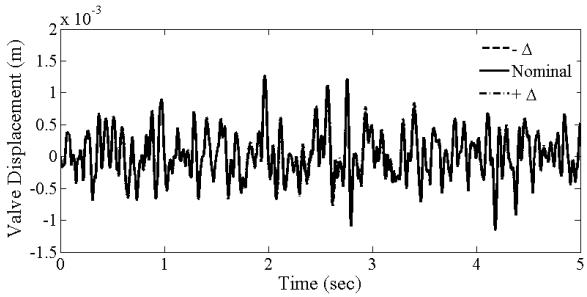

(a) Front suspension

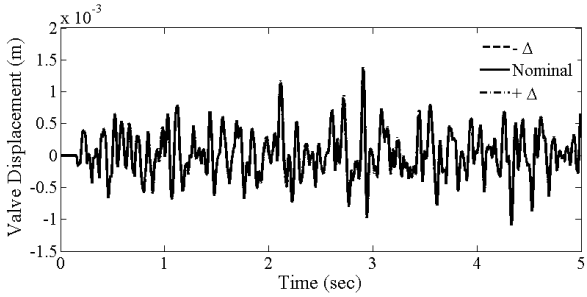

(b) Rear suspension

Figure 5.46: Front and rear actuator spool-valve displacement for 80%, 100% and 120% Ms at $V = 60\,km/h$.

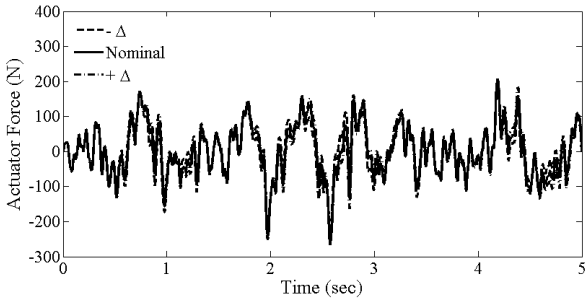

(a) Front suspension

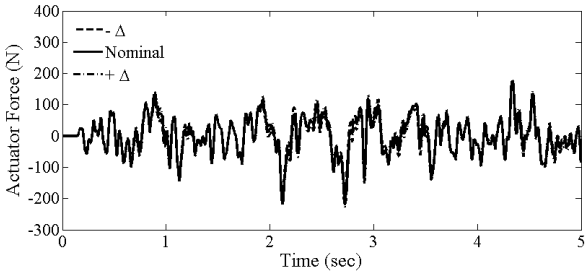

(b) Rear suspension

Figure 5.47: Front and rear actuator force for 80%, 100% and 120% Ms at $V = 60\,km/h$.

5.3.2.3 System Response at $V = 75\,km/h$

The RMS values obtained as the PVSS and AVSS traversed a random road input disturbance at $V = 75\,km/h$ are given in Table 5.12. The front and rear suspension travel are shown in Figures 5.48 and 5.49. Table 5.12 shows that the percentage reduction in RMS front suspension travel by the AVSS improved as the sprung mass increased, while the AVSS RMS rear suspension travel percentage reduction deteriorated by around 1%. The peak suspension travel values for both the AVSS and PVSS were lower than the specified $\pm 0.08\,m$ limit, although the PVSS values were higher than those of the AVSS. Looking at Tables 5.8, 5.10 and 5.12, the overall percentage reduction in front and rear suspension travel by the AVSS reduced with increase in vehicle velocity.

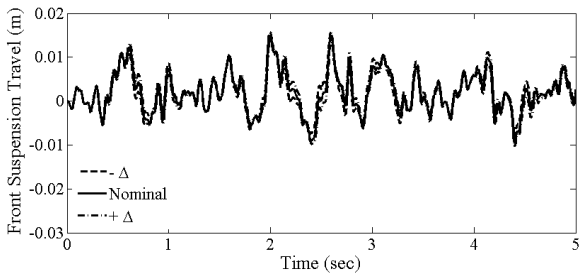

(a) AVSS

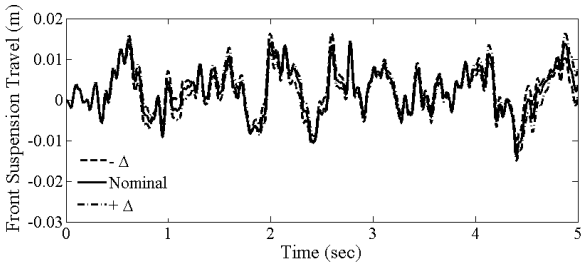

(b) AVSS

Figure 5.48: Front suspension travel for 80%, 100% and 120% Ms at $V = 75\,km/h$.

Figures 5.50 and 5.51 show the front and rear dynamic tyre forces, respectively. For all values of Ms, the peak AVSS and PVSS dynamic tyre forces were lower than the limits specified in Table 4.1, Chapter 4. A comparison of the percentage reduction in RMS dynamic tyre forces by the AVSS in Tables 5.8, 5.10 and 5.12 shows a slight improvement by the AVSS performance with increase in vehicle velocity.

Figure 5.25 shows the sprung mass acceleration at $75\,km/h$. The AVSS ISO 2631-1 weighted RMS acceleration was between $11.87 - 13\%$ higher than that of the PVSS (see Table 5.13). While the PVSS comfort level remained at "Not Uncomfortable"

Table 5.12: RMS values for random input disturbance with ±20% variation in sprung mass loading about the nominal value, $Ms = 580\,kg$ at $V = 75\,km/h$

Parameters	$80\%Ms = 464\,kg$			$100\%Ms = 580\,kg$			$120\%Ms = 696\,kg$		
	PVSS	AVSS	% Reduction by AVSS	PVSS	AVSS	% Reduction by AVSS	PVSS	AVSS	% Reduction by AVSS
Front Suspension Travel $[m]$	0.0057	0.0049	14.04	0.0060	0.0050	16.67	0.0063	0.0051	19.05
Rear Suspension Travel $[m]$	0.0045	0.0039	13.33	0.0047	0.0041	12.77	0.0049	0.0043	12.24
Front Dynamic Tyre Force $[N]$	465.1005	452.6813	2.67	465.1192	448.9272	5.99	466.1840	446.1474	4.30
Rear Dynamic Tyre Force $[N]$	453.4244	441.7648	2.57	449.8584	438.1588	2.60	448.5289	435.4000	2.93
Sprung Mass Acceleration $[m/s^2]$	0.8096	0.9181	-13.40	0.6619	0.7489	-13.14	0.5649	0.6290	-11.35
Pitch Angular Acceleration $[rad/s^2]$	0.5282	0.6003	-13.53	0.4208	0.4779	-13.57	0.3489	0.3977	-13.99
Front Actuator Control Voltage $[V]$	–	1.0052	–	–	1.0042	–	–	1.0034	–
Rear Actuator Control Voltage $[V]$	–	0.9628	–	–	0.9618	–	–	0.9604	–
Front Spool-Valve Displacement $[m]$	–	3.9759×10^{-4}	–	–	3.9494×10^{-4}	–	–	3.9243×10^{-4}	–
Rear Spool-Valve Displacement $[m]$	–	3.7795×10^{-4}	–	–	3.7614×10^{-4}	–	–	3.7155×10^{-4}	–
Front Actuator Force $[N]$	–	74.2859	–	–	76.5319	–	–	78.0909	–
Rear Actuator Force $[N]$	–	59.6343	–	–	62.8511	–	–	65.1399	–

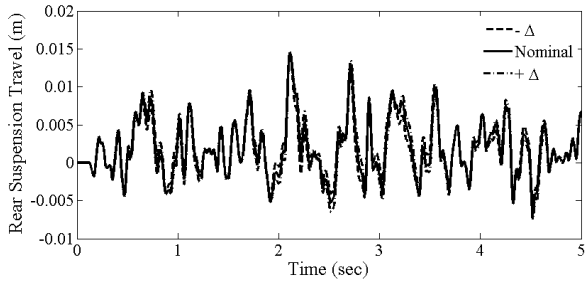

(a) AVSS

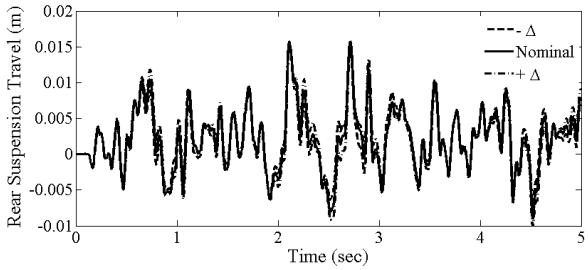

(b) AVSS

Figure 5.49: Rear suspension travel for 80%, 100% and 120% Ms at $V = 75\,km/h$.

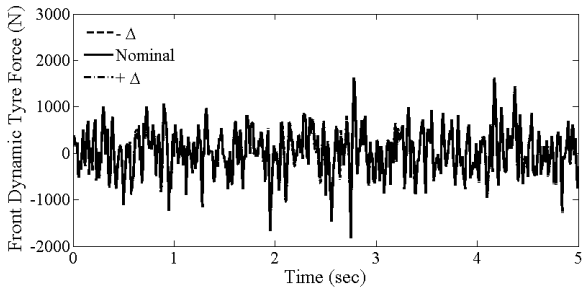

(a) AVSS

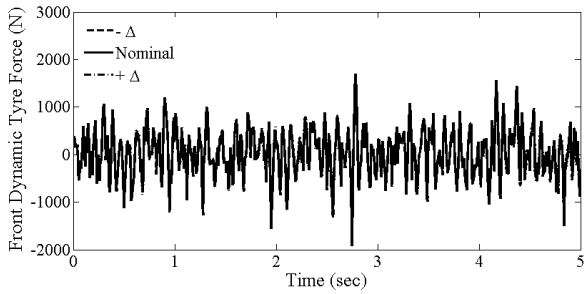

(b) AVSS

Figure 5.50: Front dynamic tyre force for 80%, 100% and 120% Ms at $V = 75\,km/h$.

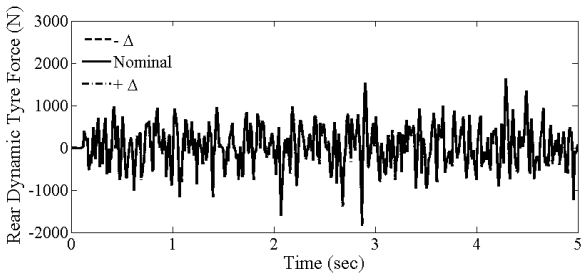

(a) AVSS

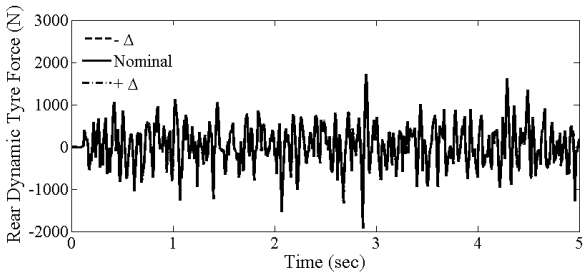

(b) AVSS

Figure 5.51: Rear dynamic tyre force for 80%, 100% and 120% Ms at $V = 75\,km/h$.

throughout, the AVSS comfort level varied between "Not Uncomfortable" and "A Little Uncomfortable" due to the change in sprung mass loading. The overall AVSS performance deteriorated as the vehicle velocity increased from $45\,km/h$ to $60\,km/h$ then improved slightly when the vehicle velocity increased further to $75\,km/h$ (see Tables 5.3, 5.5 and 5.7).

Table 5.13: Weighted RMS acceleration and discomfort levels as PVSS and AVSS traversed a random road input disturbance at $V = 75\,km/h$

	PVSS		AVSS		%
	Weighted RMS Acceleration a_{wi}^{RMS}	ISO 2631-1 Level of Discomfort	Weighted RMS Acceleration a_{wi}^{RMS}	ISO 2631-1 Level of Discomfort	Reduction of a_{wi}^{RMS} by AVSS
80% Ms	0.2800	Not Uncomfortable	0.3164	Not to A Little Uncomfortable	-13
100% Ms	0.2238	Not Uncomfortable	0.2523	Not Uncomfortable	-12.7346
120% Ms	0.1870	Not Uncomfortable	0.2092	Not Uncomfortable	-11.8717

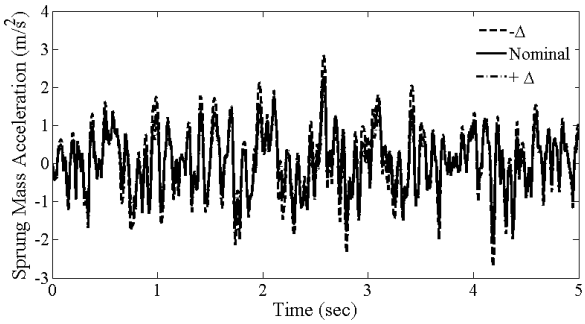

(a) AVSS

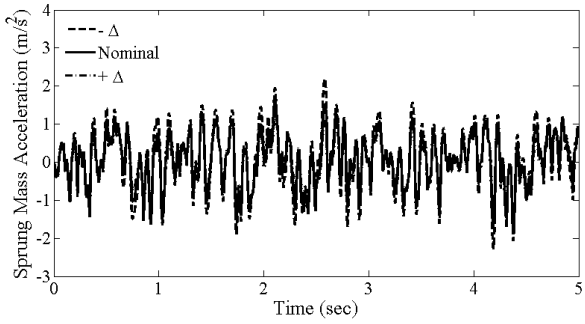

(b) AVSS

Figure 5.52: Sprung mass acceleration for 80%, 100% and 120% Ms at $V = 75\,km/h$.

The AVSS RMS pitch angular acceleration was higher than that of the PVSS for all values of Ms at $75\,km/h$ (see Table 5.12). The overall percentage reduction in RMS pitch angular acceleration by the AVSS showed a trend of improving with vehicle velocity, but deteriorating with increase in vehicle mass.

Figures 5.55 and 5.56 show the actuator voltage and spool-valve displacement at $V = 75\,km/h$, respectively. Both the front and rear actuator control voltage peak values were lower than the specified $\pm 10\,V$ limit. Figure 5.55 shows the spool-valve displacement. The actuator spool-valve RMS are given in Table 5.12. Tables 5.8, 5.10 and 5.12 indicate that the RMS voltage and spool-valve displacement required by the actuator increases with increase in vehicle velocity and increase in sprung mass.

The front and rear actuator force are shown in Figure 5.56. At $75\,km/h$, the RMS actuator forces increased with increase in Table 5.12 sprung mass load. The peak actuator forces at $75\,km/h$ were lower than the actuator force limits specified in Chapter 4. The overall RMS actuator force increased with vehicle velocity as well as increase in sprung mass, compare Tables 5.8, 5.10 and 5.12.

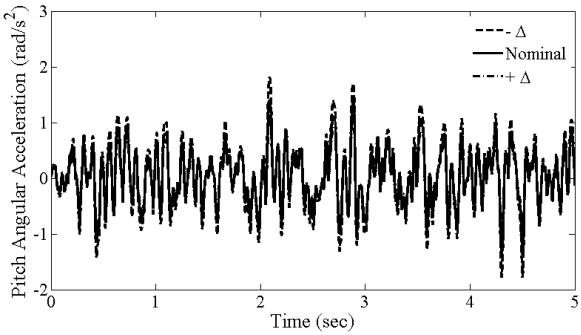

(a) AVSS

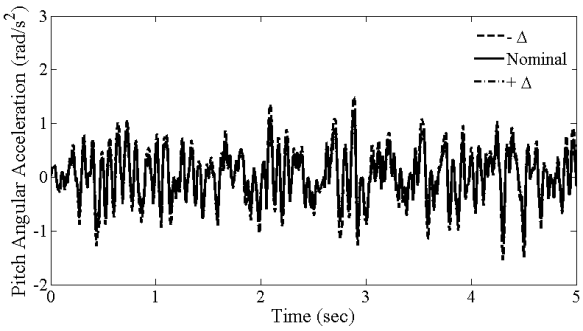

(b) AVSS

Figure 5.53: Pitch angular acceleration for 80%, 100% and 120% Ms at $V = 75\,km/h$.

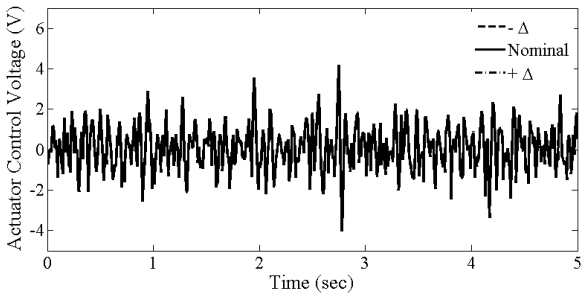

(a) Front suspension

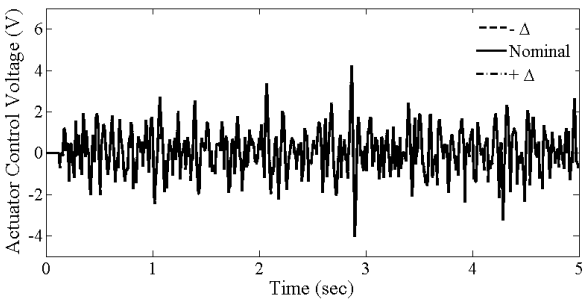

(b) Rear suspension

Figure 5.54: Front and rear actuator control voltage for 80%, 100% and 120% Ms at $V = 75\,km/h$.

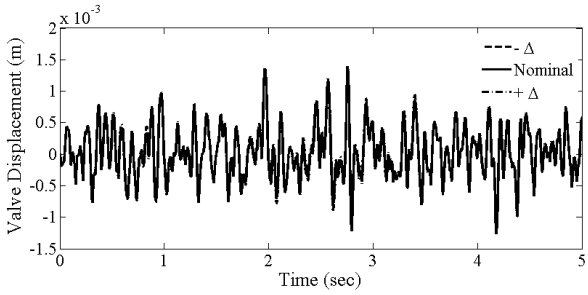

(a) Front suspension

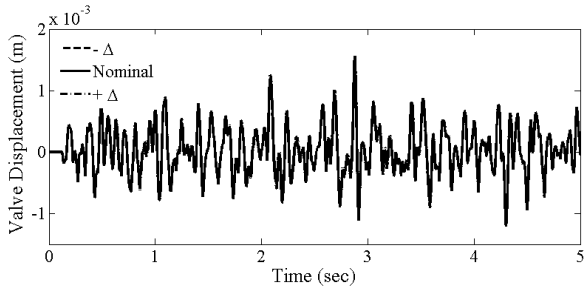

(b) Rear suspension

Figure 5.55: Front and rear actuator spool-valve displacement for 80%, 100% and 120% Ms at $V = 75\,km/h$.

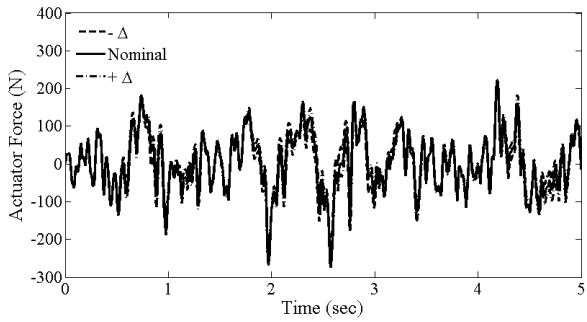

(a) Front suspension

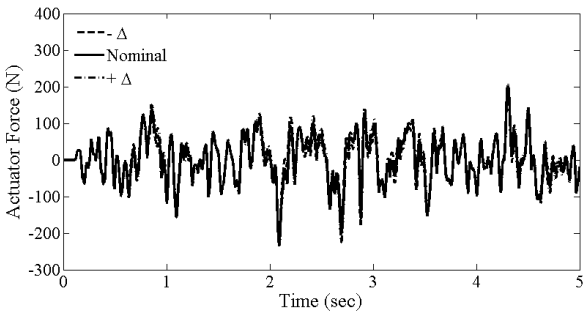

(b) Rear suspension

Figure 5.56: Front and rear actuator force for 80%, 100% and 120% Ms at $V = 75\,km/h$.

5.3.3 Uncertainty Analysis

Uncertainty analysis was performed by taking the frequency responses of both the AVSS and PVSS. The models were built in the MATLAB/Simulink® environment. The MATLAB fixed-step solver, ODE-3, was selected with sampling time set to $T_s = 0.0001s$ and the tasking mode was set to "Single Tasking". The frequency sweep method similar to that used by Savaresi et al. (2010) was applied here, by use of a chirp road input disturbance signal of amplitude $\pm 15\,mm$ (Sammier et al., 2003) with frequency varying between $0 - 100\,Hz$, over a simulation period of $100\,s$. The frequency was set to vary between $0 - 100\,Hz$ in order to expose the vehicle to a wide range of input disturbance frequencies.

The MATLAB Welch algorithm/spectral estimator was utilized to perform a spectral analysis of the AVSS and PVSS model outputs. The "Hamming" window setting with segment length of $N/100$ (where N is the total number of samples) and a percentage overlap of 2^{14} was found to produce clear frequency response plots (The MathWorks Inc., 2001).

The following vehicle parameters were varied and the corresponding frequency responses plotted:

1. Sprung mass loading Ms:
   The sprung mass loading Ms, was varied by $\Delta = \pm 20\%$ (Du and Zhang, 2009). Since the pitch moment of inertia I_θ is related to the vehicle body mass, it is assumed that the pitch moment of inertia also varies by the same amount about its nominal value (Chen et al., 2005).

2. Suspension Spring Coefficients:
   Both the linear and nonlinear spring coefficients ks_i^l and ks_i^{nl} respectively, were varied by $\Delta = \pm 30\%$ about their nominal values (Chen et al., 2005).

3. Suspension Damping Coefficients:
   The linear, nonlinear and symmetric damping coefficients bs_i^l, bs_i^{nl} and bs_i^{sym} respectively, were varied by $\Delta = \pm 30\%$ about their nominal values.

5.3.3.1 Variation of Sprung Mass Loading

The AVSS and PVSS front suspension travel PSD responses are shown in Figures 5.57(a) and 5.57(b), respectively, for $\pm 20\%$ variation in sprung mass loading Ms and pitch moment of inertia I_θ. The magnitude of the "knee" between $1\,Hz$ and the

body-hop frequency ($\approx 2\,Hz$) is smaller for the AVSS than for the PVSS. Both the AVSS and PVSS perform similarly in the region below $4\,Hz$ as well as in the region between $4-8\,Hz$. The high frequency behaviour of the AVSS and PVSS is similar, for frequencies well above the wheel-hop frequency ($> 20\,Hz$). The magnitude of the PVSS response at the wheel-hop frequency ($\approx 12\,Hz$) is greater than that of the AVSS.

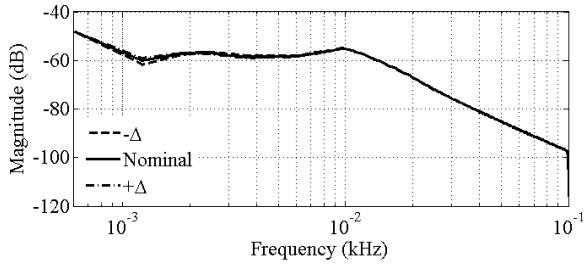

(a) AVSS

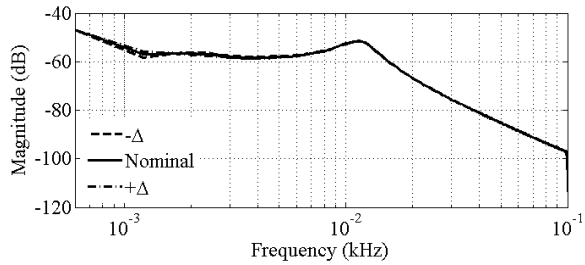

(b) PVSS

Figure 5.57: Front suspension travel PSD for $\Delta = \pm 20\%$ variation in Ms and I_θ about their nominal values.

Figures 5.58(a) and 5.58(b) show the AVSS and PVSS rear suspension travel PSD responses for $\pm 20\%$ variation in sprung mass loading Ms and pitch moment of inertia I_θ, respectively. Both the AVSS and PVSS perform similarly in the region below $4\,Hz$, however, the magnitude of the "knee" between $1\,Hz$ and the body-hop frequency ($\approx 2\,Hz$) is smaller for the AVSS than for the PVSS. The AVSS and PVSS perform similarly in the $4-8\,Hz$ region, as well as above $20\,Hz$. The AVSS response at the wheel-hop frequency ($\approx 12\,Hz$) is lower in magnitude than that of the PVSS.

The AVSS and PVSS front dynamic tyre force PSD for $\pm 20\%$ variation in sprung mass loading Ms and pitch moment of inertia I_θ are shown in figures 5.59(a) and 5.59(b), respectively. The AVSS response at the body-hop frequency ($\approx 2\,Hz$), is greater in magnitude than that of the PVSS. At low frequencies (below $4\,Hz$), the AVSS is less sensitive than the PVSS to variations in Ms and I_θ about their nominal

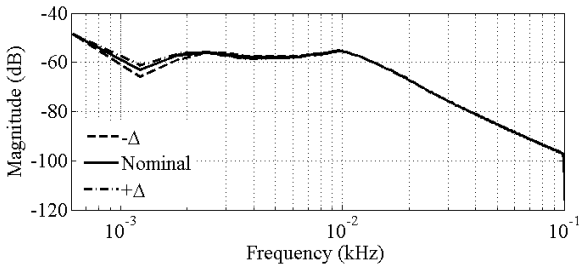

(a) AVSS

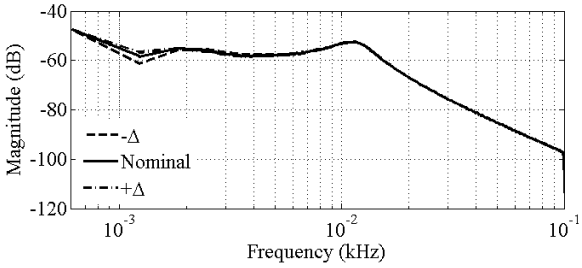

(b) PVSS

Figure 5.58: Rear suspension travel PSD for $\Delta = \pm 20\%$ variation in Ms and I_θ about their nominal values.

values. The PVSS response is greater in magnitude than that of the AVSS at the wheel-hop frequency ($\approx 12\,Hz$), but both perform similarly at higher frequencies ($> 20\,Hz$).

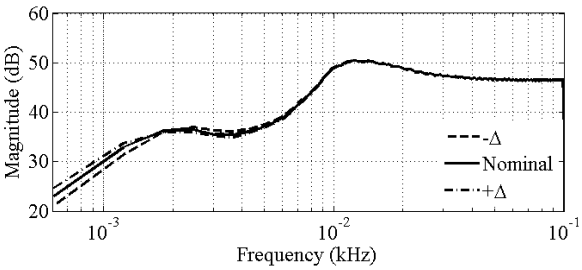

(a) AVSS

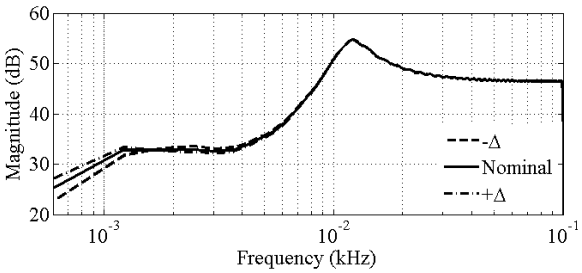

(b) PVSS

Figure 5.59: Front dynamic tyre force PSD for $\Delta = \pm 20\%$ variation in Ms and I_θ about their nominal values.

Figures 5.60(a) and 5.60(b) show the AVSS and PVSS rear dynamic tyre force PSD for $\pm 20\%$ variation in sprung mass loading Ms and pitch moment of inertia I_θ, respectively. At frequencies below $4\,Hz$, the AVSS is less sensitive to variations in Ms and I_θ about their nominal values. The response of the AVSS at the body-hop frequency ($\approx 2\,Hz$) is greater in magnitude than that of the PVSS. The magnitude of the PVSS response at the wheel-hop frequency ($\approx 12\,Hz$) is greater than that of the AVSS. At higher frequencies ($> 20\,Hz$), the AVSS and PVSS performance is similar.

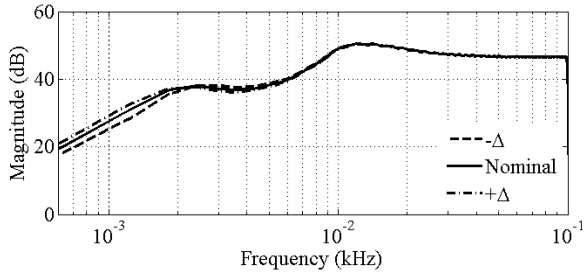

(a) AVSS

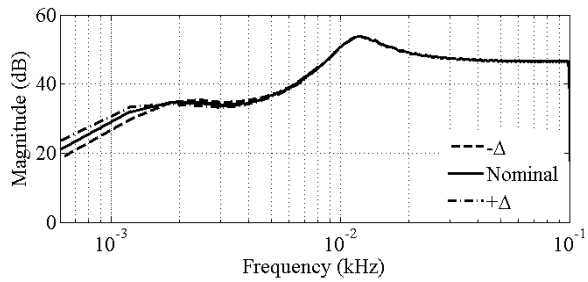

(b) PVSS

Figure 5.60: Rear dynamic tyre force PSD for $\Delta = \pm 20\%$ variation in Ms and I_θ about their nominal values.

Figures 5.61(a) and 5.61(b) show the AVSS and PVSS sprung mass acceleration PSD response for $\pm 20\%$ variation in Ms and I_θ about their nominal values, respectively. Comparison of Figure 5.61(a) with Figure 5.61(b) shows that the AVSS is less sensitive to variation in Ms and I_θ than the PVSS, at frequencies below $4\,Hz$. The AVSS produces a rounded response about wheel-hop frequency ($\approx 12\,Hz$) whereas the PVSS produces a sharp response. At high frequencies (above $20\,Hz$), both the AVSS and PVSS behave similarly.

Figures 5.62(a) and 5.62(b) show the AVSS and PVSS pitch angular acceleration PSD response for $\pm 20\%$ variation in Ms and I_θ about their nominal values, respectively. At low frequency ($< 4\,Hz$), the AVSS is less sensitive to variations in Ms and I_θ, however the magnitude of the AVSS response is greater than that of the

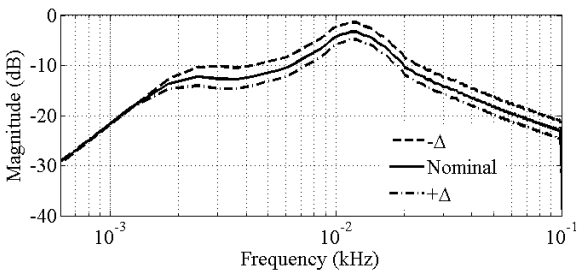

(a) AVSS

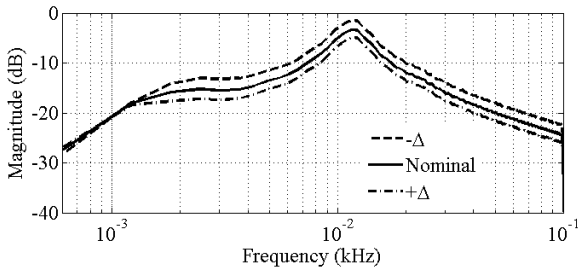

(b) PVSS

Figure 5.61: Sprung mass acceleration PSD for $\Delta = \pm 20\%$ variation in Ms and I_θ about their nominal values.

PVSS within this frequency range. Both the AVSS and PVSS behave similarly in the $4-8\,Hz$ frequency range, around the wheel-hop frequency and at high frequency (above $20\,Hz$).

5.3.3.2 Variation of Suspension Spring Coefficient

The AVSS and PVSS front suspension travel PSD responses are shown in Figures 5.63(a) and 5.63(b), respectively. The figures indicate the AVSS front suspension travel is less sensitive than that of the PVSS to variation of the spring coefficients, for frequencies in the region below $4\,Hz$. In the region between $4-8\,Hz$ as well as above $20\,Hz$, both the AVSS and PVSS perform similarly. The AVSS obtained a lower peak than the PVSS at the wheel-hop frequency ($\approx 12\,Hz$).

The AVSS and PVSS rear suspension travel PSD responses are shown in Figures 5.64(a) and 5.64(b), respectively. The figures show that the AVSS rear suspension travel is less sensitive to variation of the spring coefficients than the PVSS, for frequencies $< 4\,Hz$. Between $4-8\,Hz$ and above $20\,Hz$, the AVSS and PVSS both perform similarly, however, the AVSS obtained a lower peak than the PVSS at the wheel-hop frequency ($\approx 12\,Hz$).

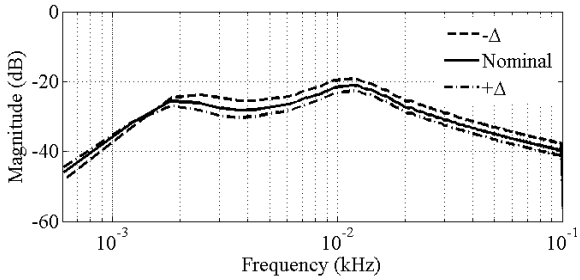

(a) AVSS

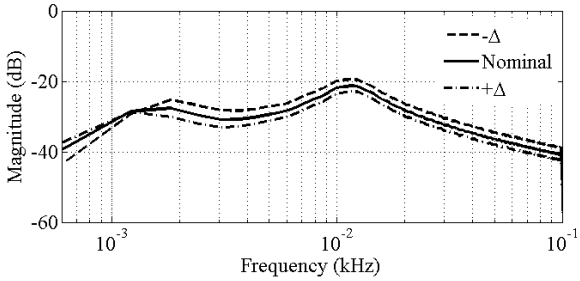

(b) PVSS

Figure 5.62: Pitch angular acceleration PSD for $\Delta = \pm 20\%$ variation in Ms and I_θ about their nominal values.

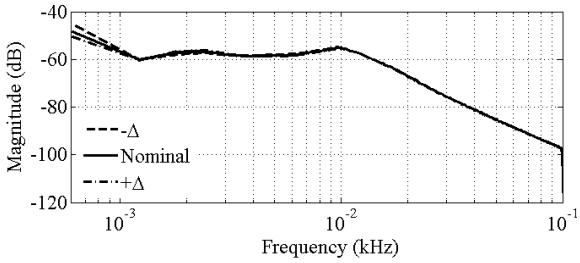

(a) AVSS

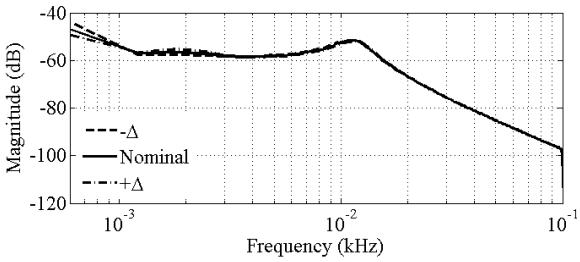

(b) PVSS

Figure 5.63: Front suspension travel PSD for $\Delta = \pm 30\%$ variation in ks_i^l and ks_i^{nl} about their nominal values.

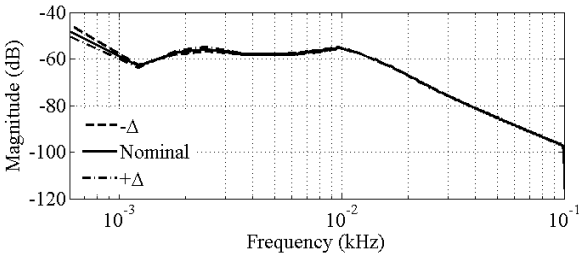

(a) AVSS

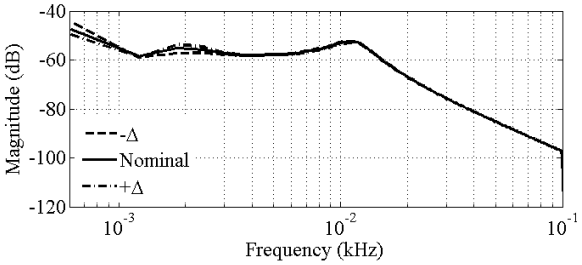

(b) PVSS

Figure 5.64: Rear suspension travel PSD for $\Delta = \pm 30\%$ variation in ks_i^l and ks_i^{nl} about their nominal values.

Figures 5.65(a) and 5.65(b) show that the AVSS front dynamic tyre force is less sensitive to variation of the spring coefficients for frequencies in the region below $4\,Hz$ and between $4-8\,Hz$, than the PVSS. The magnitude of the AVSS response at the wheel-hop frequency ($\approx 12\,Hz$) is lower than that of the PVSS. The performance of both the AVSS and PVSS is similar at frequencies above $20\,Hz$.

Figures 5.66(a) and 5.66(b) show the AVSS and PVSS rear dynamic tyre force PSDs, respectively. At frequencies below $4\,Hz$ as well as frequencies between $4-8\,Hz$, the AVSS is less sensitive than the PVSS to variation of the spring coefficients. The AVSS response at the wheel-hop frequency ($\approx 12\,Hz$) is lower in magnitude than that of the PVSS, both producing similar responses at frequencies above $20\,Hz$.

The AVSS and PVSS sprung mass acceleration PSD responses are given in Figures 5.67(a) and 5.67(b), respectively. The figures show that the AVSS is less sensitive than the PVSS to variation of the spring coefficients at frequencies below $4\,Hz$. At frequencies between $4-8\,Hz$ as well as frequencies above $20\,Hz$ both the AVSS and PVSS perform similarly. However, AVSS produces a less harsh response about wheel-hop frequency than the PVSS.

The AVSS and PVSS pitch angular acceleration PSD responses are given in Figures 5.68(a) and 5.68(b), respectively. The figures show that the AVSS is less sensitive

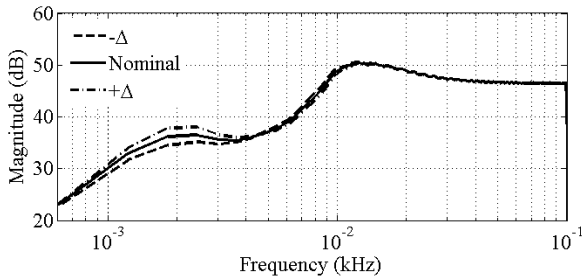

(a) AVSS

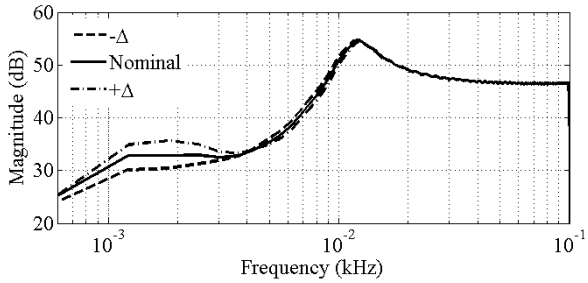

(b) PVSS

Figure 5.65: Front dynamic tyre force PSD for $\Delta = \pm 30\%$ variation in ks_i^l and ks_i^{nl} about their nominal values.

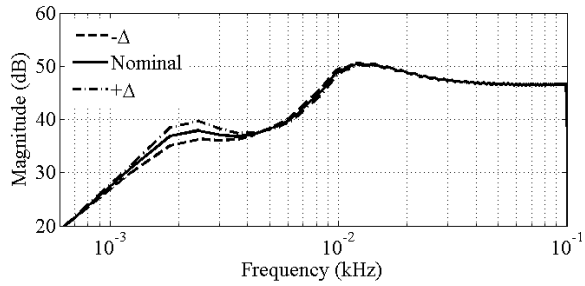

(a) AVSS

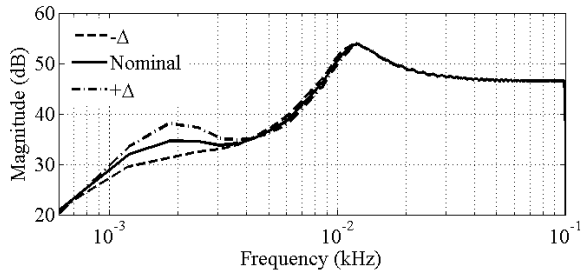

(b) PVSS

Figure 5.66: Rear dynamic tyre force PSD for $\Delta = \pm 30\%$ variation in ks_i^l and ks_i^{nl} about their nominal values.

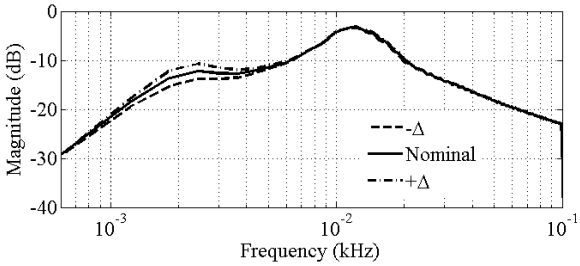

(a) AVSS

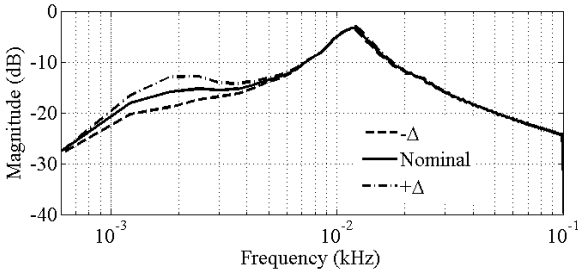

(b) PVSS

Figure 5.67: Sprung mass acceleration PSD for $\Delta = \pm 30\%$ variation in ks_i^l and ks_i^{nl} about their nominal values.

than the PVSS to variation of the spring coefficients at frequencies below $4\,Hz$. At frequencies between $4 - 8\,Hz$, at the wheel-hop frequency, as well as frequencies above $20\,Hz$ both the AVSS and PVSS perform similarly.

5.3.3.3 Variation of Suspension Damping Coefficient

Figures 5.69(a) and 5.69(b) show the AVSS and PVSS front suspension travel PSD responses, respectively. The AVSS response is more robust to variation in suspension damping coefficients in the region below $4\,Hz$ and the region around the wheel-hop frequency ($\approx 12\,Hz$), than that of the PVSS. The PVSS peak at the wheel-hop frequency was higher than that of the AVSS. Between $4 - 8\,Hz$ as well as above $20\,Hz$, both the AVSS and PVSS produce similar performance.

The rear suspension travel PSD response for variation in suspension damping coefficients are given in Figure 5.70(a), for the AVSS and Figure 5.70(b), for the PVSS. The figures show the robustness of the AVSS to variation in suspension damping coefficients in the region below $4\,Hz$ and the region around the wheel-hop frequency ($\approx 12\,Hz$), with lower peak magnitude at the wheel-hop frequency, in comparison to that of the PVSS. In the region between $4 - 8\,Hz$ as well as above $20\,Hz$, both

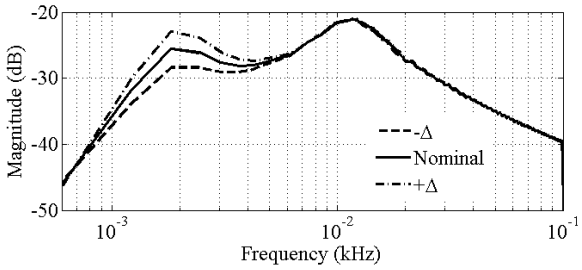

(a) AVSS

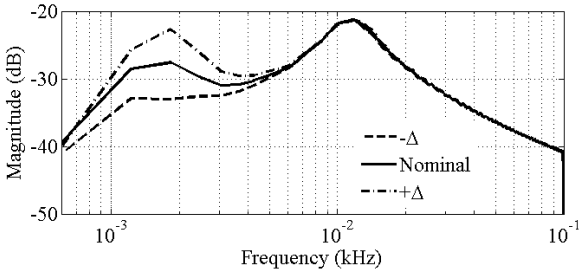

(b) PVSS

Figure 5.68: Pitch angular acceleration PSD for $\Delta = \pm 30\%$ variation in ks_i^l and ks_i^{nl} about their nominal values.

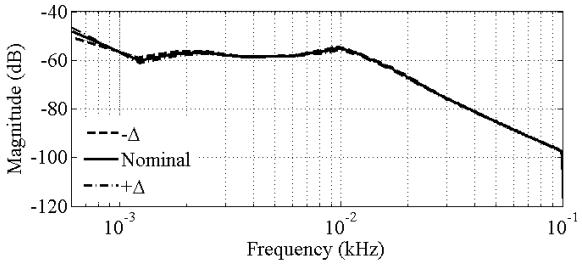

(a) AVSS

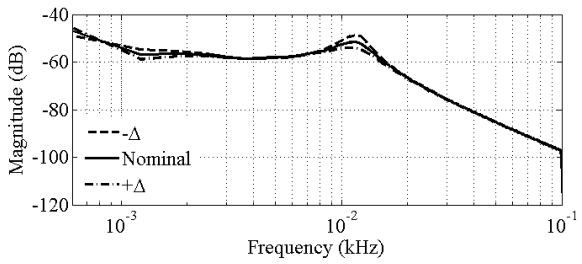

(b) PVSS

Figure 5.69: Front suspension travel PSD for $\Delta = \pm 30\%$ variation in bs_i^l, bs_i^{nl} and bs_i^{sym} about their nominal values.

the AVSS and PVSS performances are similar.

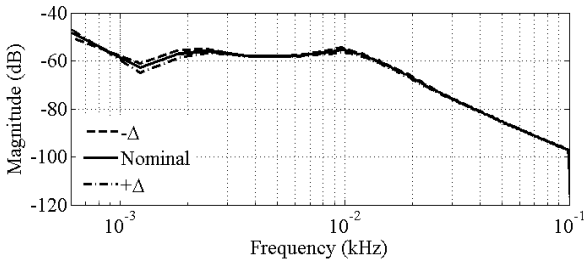

(a) AVSS

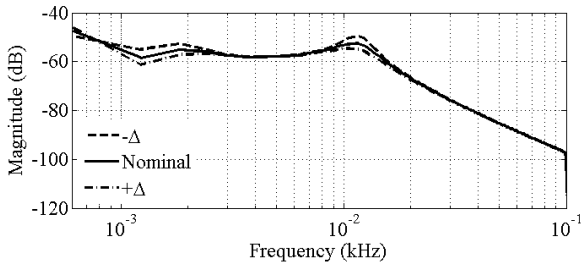

(b) PVSS

Figure 5.70: Rear suspension travel PSD for $\Delta = \pm 30\%$ variation in bs_i^l, bs_i^{nl} and bs_i^{sym} about their nominal values.

The front dynamic tyre force PSD response for variation in suspension damping coefficients are given in Figure 5.71(a), for the AVSS and Figure 5.71(b), for the PVSS. The figures show the robustness of the AVSS to variation in suspension damping coefficients at low frequencies ($< 4\,Hz$) and at the wheel-hop frequency. Between $4 - 8\,Hz$, the AVSS response is slightly better than that of the PVSS. For frequencies $> 20\,Hz$, the AVSS and PVSS perform similarly.

Figures 5.72(a) and Figure 5.72(b) show the PSD rear dynamic tyre force for the AVSS and PVSS respectively. Figure 5.72(a) shows that the AVSS is less sensitive to variations in suspension damping than the PVSS, particularly at low frequencies ($< 4\,Hz$) and at the wheel-hop frequency. In the area between $4 - 8\,Hz$, there is a slight improvement in performance by the AVSS over the PVSS. Beyond $20\,Hz$, both the AVSS and PVSS perform similarly.

Figures 5.73(a) and 5.73(b) show the AVSS and PVSS sprung mass acceleration PSD for $\pm 30\%$ variation in suspension damping, respectively. The figures clearly show that the robustness to variation of suspension damping by the AVSS compared with the PVSS at low frequencies ($< 4\,Hz$), between $4-8\,Hz$, around the wheel-hop frequency and at high frequencies (beyond $20\,Hz$).

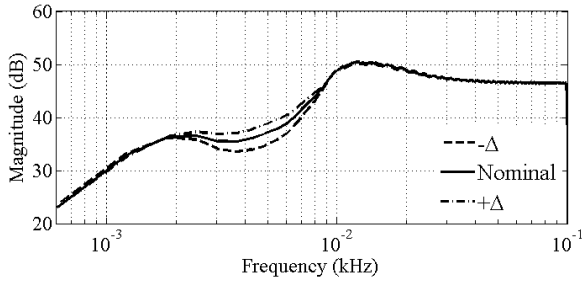

(a) AVSS

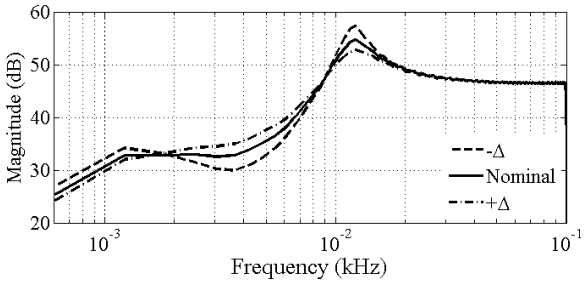

(b) PVSS

Figure 5.71: Front dynamic tyre force PSD for $\Delta = \pm 30\%$ variation in bs_i^l, bs_i^{nl} and bs_i^{sym} about their nominal values.

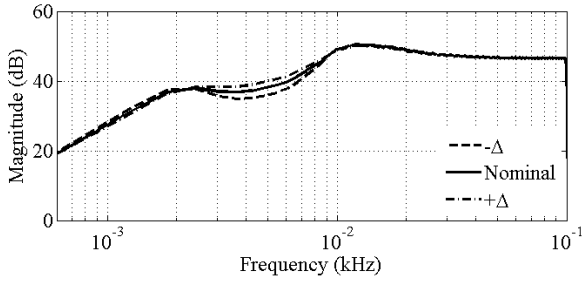

(a) AVSS

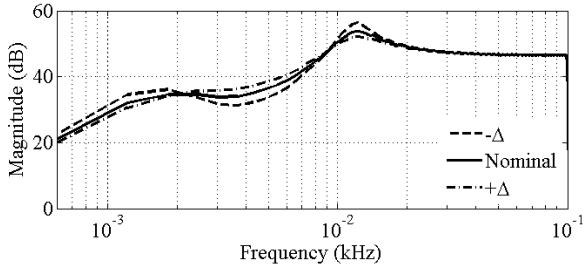

(b) PVSS

Figure 5.72: Rear dynamic tyre force PSD for $\Delta = \pm 30\%$ variation in bs_i^l, bs_i^{nl} and bs_i^{sym} about their nominal values.

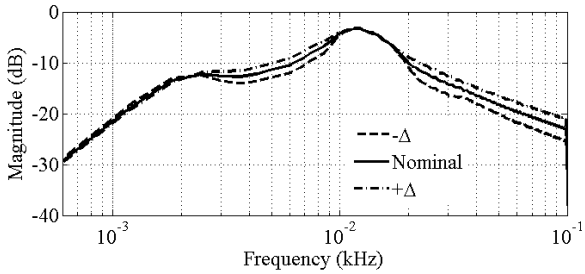

(a) AVSS

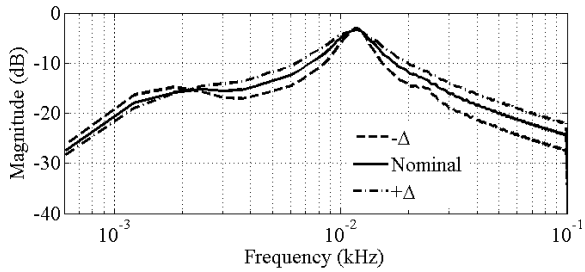

(b) PVSS

Figure 5.73: Sprung mass acceleration PSD for $\Delta = \pm 30\%$ variation in bs_i^l, bs_i^{nl} and bs_i^{sym} about their nominal values.

The AVSS and PVSS pitch angular acceleration PSD are given in Figures 5.74(a) and 5.74(b), respectively. For the entire range of frequencies plotted, both figures show that the AVSS is more robust to variations in suspension damping, compared with the PVSS, that is, at low frequencies ($< 4\,Hz$), between $4 - 8\,Hz$, around the wheel-hop frequency and at high frequencies (beyond $20\,Hz$).

5.4 Conclusion

The design of a PID controller for a nonlinear AVSS with PID force feedback has been achieved. Robustness of controller was tested with variations in sprung mass loading as well as vehicle forward velocity (where applicable) for different road input disturbances. A single set of PID gains was used for all the case scenarios. The overall performance of the AVSS in terms of reduction of RMS parameters was better than that of the PVSS. The AVSS provided better ride comfort and road holding with minimum suspension travel in most cases. The best performance being over the sinusoidal bump followed by the random input disturbance. Although the AVSS suspension travel, control voltage and actuator forces remained within the specified limits, the front dynamic tyre force limits were exceeded on a few instances

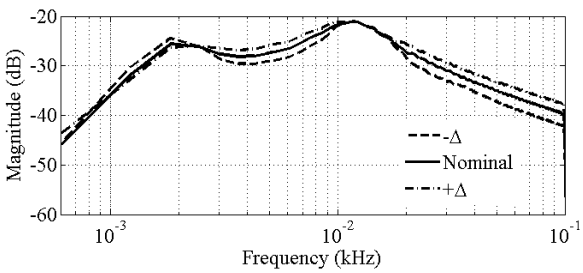

(a) AVSS

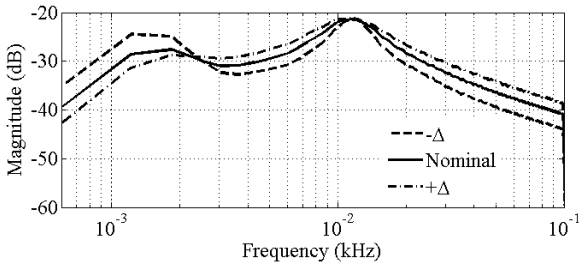

(b) PVSS

Figure 5.74: Pitch angular acceleration PSD for $\Delta = \pm 30\%$ variation in bs_i^l, bs_i^{nl} and bs_i^{sym} about the nominal values.

for the sinusoidal input disturbance. The AVSS rear dynamic tyre force tended to be higher than that of the PVSS for the sinusoidal input disturbance, although it did not exceed the specified limits. The AVSS performance in terms of RMS pitch angular acceleration reduction was poor. Uncertainty analysis indicated that the AVSS is more robust than the PVSS to variations in sprung mass loading and pitch moment of inertia as well as suspension spring and damping coefficients. This is evident in the low frequency region (below $4\,Hz$) and around the wheel-hop frequency. Between $4-8\,Hz$, the AVSS and PVSS performances did not differ too much, however, when there was a difference, the AVSS performance was better than that of the PVSS. At frequencies greater than $20\,Hz$, both the AVSS and PVSS performances are similar.

6 MODEL PREDICTIVE CONTROL OF A NONLINEAR ACTIVE SUSPENSION VIA PID FORCE FEEDBACK

6.1 Introduction

MPC systems are a group of control systems capable of predicting optimal plant responses based on clearly defined plant models. These systems are noise tolerant and have an advantage of being able to handle MIMO plants with constraints, in real-time (Mehra et al., 1997; Qin and Badgwell, 2003; Deng et al., 2009).

MPC has been applied widely in the processing and power generation industries since the 1960's. Model complexity, which leads to computational burden, restricted the application of MPC to systems with slow changing dynamics. However, recent developments in computer hardware storage capacity and software coding, have resulted in faster and more efficient MPC algorithms. This has aided the application of MPC to systems with fast changing system dynamics such as those present in the automotive industry (Qin and Badgwell, 2003; Li et al., 2010). Mehra et al. (1997) developed a MPC controller for a quarter-car AVSS with a nonlinear suspension spring model (to account for suspension travel constraints) and nonlinear model of tyre dynamics.

In this chapter, the development of a MPC suspension travel controller for a nonlinear AVSS with PID hydraulic actuator force feedback is presented. The chapter begins with an introduction, followed by design of the inner PID force control loop in Section 6.2.2 and outer MPC suspension travel control loop in Section 6.2.3. The simulation results are presented and discussed in Section 6.3, for $\pm 30\%$ variation in suspension spring stiffness coefficients in the frequency domain. Time domain results are also given for the AVSS and PVSS traversing a discrete road input disturbance and a random road input disturbance at $75\,km/h$. Finally, concluding remarks are

given in Section 6.4.

6.2 Controller Design

6.2.1 Controller Architecture

The control architecture for MPC control of a nonlinear AVSS via PID force feedback consists of two control loops:

1. An inner PID force control loop.
2. An outer MPC suspension travel loop.

This control architecture is illustrated in Figure 6.1. The function of the outer control loop is to set the desired force tracking signal for the hydraulic actuator, whereas the function of the inner control loop is to ensure that the desired control force, set by the outer control loop, is achieved by the hydraulic actuator.

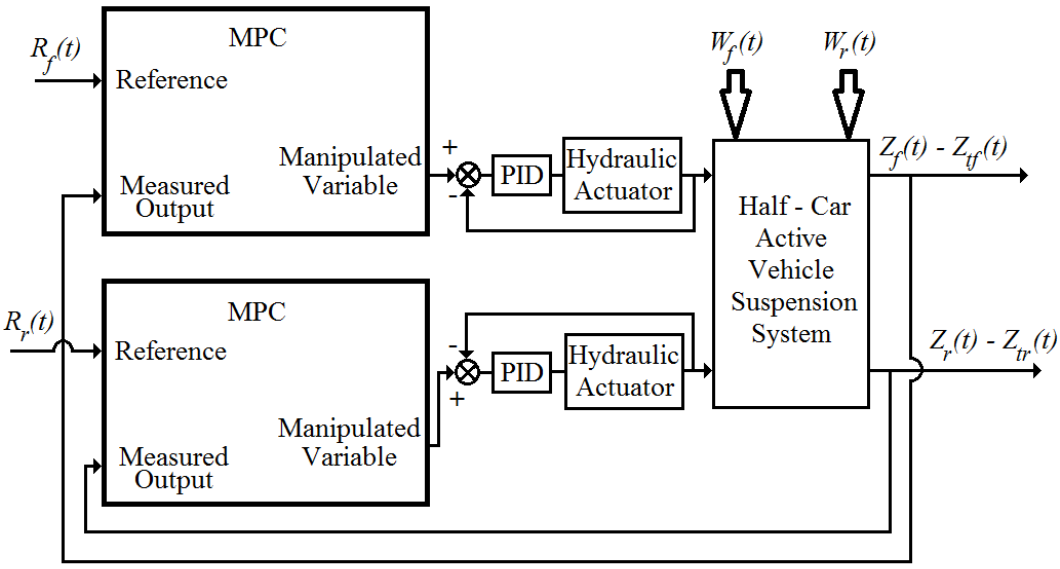

Figure 6.1: Control architecture for MPC Control of a nonlinear active vehicle suspension via PID force feedback.

6.2.2 PID Force Control Loop Design

The PID force control input, u_i to the half-car AVSS actuators is given in Equation 6.1 and illustrated in Figure 6.2:

$$u_i = K_{P\,i} e_i(t) + K_{I\,i} \int e_i(t)\,dt + K_{D\,i} \frac{de_i(t)}{dt} \tag{6.1}$$

$$e_i = F_{ai\,ref} - F_{ai} \tag{6.2}$$

where K_P is the proportional gain, K_I is the integral gain, K_D is the derivative gain, e_i given in Equation 6.2 is the error between the desired actuator force reference signal, $F_{ai\,ref}$, and the actual actuator force, F_{ai}. Subscript i represents either the front or rear suspension $i \in (f, r)$. A saturation block was placed in front of the controller output to ensure that the control voltage limits ($|u_i| \leq u_{max}$) were not exceeded in the MATLAB/Simulink® implementation.

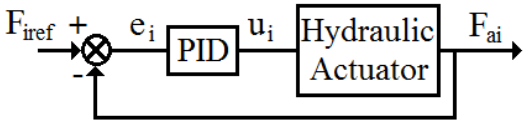

Figure 6.2: Inner PID force feedback control loop.

Table 6.1: PID force control loop tuning parameters

PID Gains	Front Suspension	Rear Suspension
K_P	0.0010	0.0010
K_I	0.0145	0.0145
K_D	0.0003	0.0003

6.2.3 MPC Suspension Travel Control Loop

For the AVSS model given in state-space form (refer to Chapter 3, Section 3.9), the MPC problem is set up as follows (Deng et al., 2009):

$$\dot{\mathbf{x}} = \mathbf{f}(\mathbf{x}) + \mathbf{g}(\mathbf{x})\,\mathbf{u} + \mathbf{p}\mathbf{w} \tag{6.3}$$

$$\mathbf{y} = \mathbf{h}(\mathbf{x}) \tag{6.4}$$

$$\mathbf{y}_m = \mathbf{h}_m(\mathbf{x}) \tag{6.5}$$

where $\mathbf{f}(x)$ is the system vector, $\mathbf{g}(x)$ is the control input matrix, $\mathbf{u}$ is the control input vector, $\mathbf{p}$ is the disturbance input matrix, $\mathbf{w}$ is the disturbance input vector, $\mathbf{y}$ is the controlled system output, $\mathbf{h}(x)$ is the output matrix containing the front and rear suspension travel, $\mathbf{y}_m$ is the measured plant output and $\mathbf{h}_m(x)$ is the measured plant output matrix.

At time t and sampling instant k, the MPC objective function, J, is expressed in Equation 6.6 as (Marusak and Kuntanapreeda, 2011; Bemporad et al., 2011):

$$J = \sum_{k=1}^{N_{1\,i}} (y_{i\,ref} - y[t+k\,|t])^2 + \sum_{k=1}^{N_{u\,i}} \rho_k \Delta u_i[t+k\,|t]^2 \tag{6.6}$$

in which $N_{1\,i}$ is the control horizon, $N_{u\,i}$ is the cost horizon, $y_{i\,ref}$ is the desired reference trajectory, ρ_k is the control input weighting factor, u_i is the control input and subscript i represents either the front or rear suspension. The optimal control input is calculated in the presence of input constraints (see Equation 6.7) and output constraints (see Equation 6.7):

$$u_{i\,min} \leq u_{k+j} \leq u_{i\,max} \tag{6.7}$$

$$\Delta u_{i\,min} \leq u_{k+j} \leq \Delta u_{i\,max} \tag{6.8}$$

$$y_{i\,min} \leq y_{k+j} \leq y_{i\,max} \tag{6.9}$$

where $u_{i\,min}$ and $u_{i\,max}$ are the minimum and maximum control input constraints, $\Delta u_{i\,min}$ and $\Delta u_{i\,max}$ are the minimum and maximum constraint on the rate of change of the control input and $y_{i\,min}$ and $y_{i\,max}$ are the minimum and maximum plant output constraints, respectively.

The Model Predictive Control parameters used for the front and rear half-car AVSS MPC controllers are provided in Table 6.2. An illustration of MPC of a plant model is given in Figure 6.3.

Table 6.2: MPC Parameters for Front and Rear Suspension

Parameters	Value
Control Horizon $(N_{1\,f}, N_{1\,r})$	10 samples
Cost Horizon $(N_{u\,f}, N_{u\,r})$	8 samples
Sampling interval T_s	$0.001\,s$
Maximum plant input	$5000\,N$
Minimum plant input	$-5000\,N$
Maximum plant output	$0.08\,m$
Minimum plant output	$-0.08\,m$

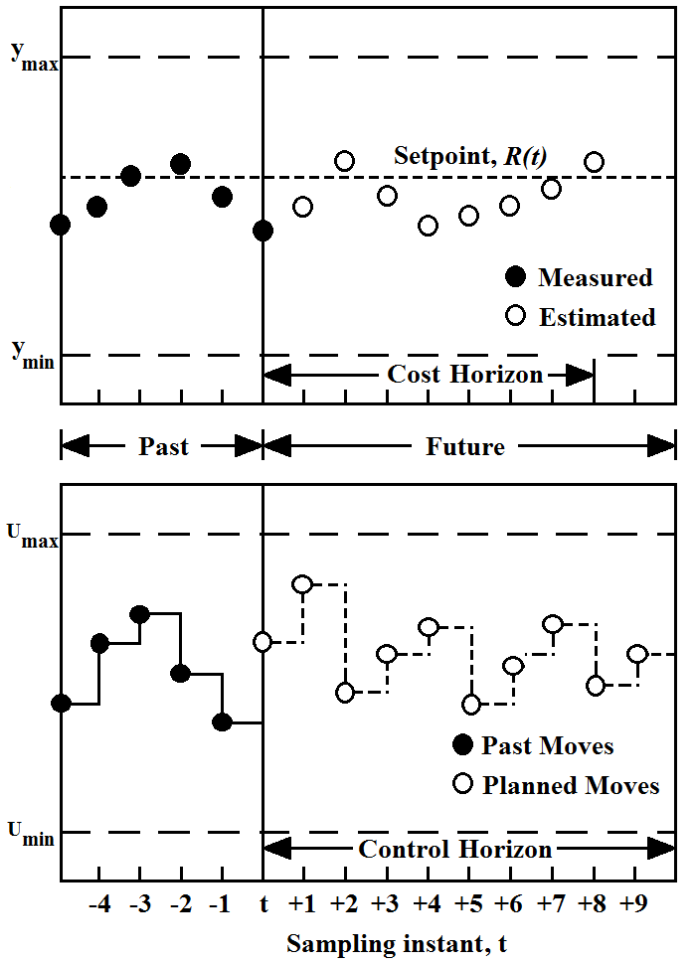

Figure 6.3: Illustration of MPC control at sampling instant k.

6.3 Simulation Results and Discussion

The half-car AVSS model was built in the MATLAB/Simulink® environment. The MATLAB Ordinary Differential Equation (ODE)-3 (Bogacki-Shampine) fixed-step solver, with sampling time set to $T_s = 0.0001s$, was selected for use in the simulations. Fixed-step solvers allow users to set a fixed-sampling time for the duration of the simulation. In order to enable observation of all model dynamics, the magnitude of the step size is set lower than the fastest dynamics of the half-car AVSS model (Dahunsi and Pedro, 2010). The tasking mode for periodic sampling times was set to "Single Tasking", since the model does not have multiple sampling times.

The AVSS and PVSS suspension spring stiffness coefficients were varied by $\pm 30\%$ about their nominal values to test robustness to parameter variation (Chen et al., 2005). Frequency and time domains results are then presented and discussed.

For uncertainty analysis in the frequency domain, a frequency sweep method similar to that used by Savaresi et al. (2010) was applied here. A chirp road input disturbance signal of amplitude $\pm 15\,mm$ (Sammier et al., 2003) with frequency varying between $0 - 100\,Hz$, over a simulation period of $100\,s$. The frequency was set to vary between $0 - 100\,Hz$ in order to expose the vehicle to a wide range of input disturbance frequencies. The MATLAB Welch algorithm/spectral estimator was utilized to perform a spectral analysis of the AVSS and PVSS model outputs. The "Hamming" window setting with segment length of $N/100$ (where N is the total number of samples) and a percentage overlap of 2^{14} was found to produce clear frequency response plots (The MathWorks Inc., 2001).

For uncertainty analysis in the time domain, the Half-Car Suspension system was set to pass over two different Road Input disturbances for suspension travel regulation ($R_i(t) = 0$). The two input disturbances are listed below:

1. A $0.075m$ amplitude sinusoidal bump on a smooth road (Weber and Braaksma, 2000).
2. A random Class E (Poor) road profile disturbance of road roughness $\mathrm{G}(n_0) = 256 \times 10^{-6}\,m^2/(cycle/m)$ as given in Table 3.2.

6.3.1 Variation of suspension spring coefficient in the frequency domain

Figures 6.4(a) and 6.4(b) show the AVSS and PVSS front suspension travel PSD responses, respectively. Comparison of the figures for frequencies in the region below $4\,Hz$ indicates that the AVSS front suspension travel is less sensitive to variation of the spring coefficients, than of the PVSS. Both the AVSS and PVSS perform similarly in the region between $4-8\,Hz$ and above $20\,Hz$. At the wheel-hop frequency ($\approx 12\,Hz$), the AVSS peak response was lower than that of the PVSS.

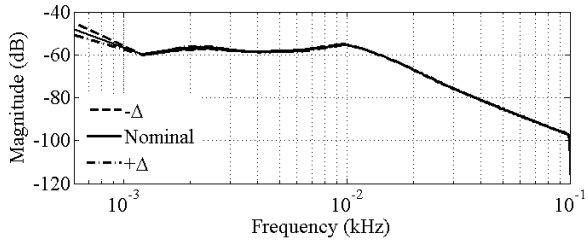

(a) AVSS

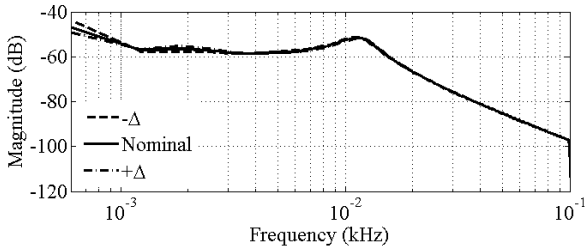

(b) PVSS

Figure 6.4: Front suspension travel PSD for $\Delta = \pm 30\%$ variation in ks_i^l and ks_i^{nl} about their nominal values.

Figures 6.5(a) and 6.5(b) show the AVSS and PVSS rear suspension travel PSD responses, respectively. Examining the figures, the AVSS rear suspension travel is more robust to variation of the spring coefficients than that of the PVSS for frequencies $< 4\,Hz$. The AVSS and PVSS both perform similarly between $4-8\,Hz$ and above $20\,Hz$. The AVSS obtained a lower peak magnitude at the wheel-hop frequency ($\approx 12\,Hz$) than the PVSS.

The front dynamic tyre force PSD for $\pm 30\%$ variation in suspension spring coefficients are shown for the AVSS and PVSS in figures 6.6(a) and 6.6(b), respectively. Below $4\,Hz$ and between $4-8\,Hz$, the AVSS front dynamic tyre force is less sensitive than the PVSS to variation of the spring coefficients. At the wheel-hop frequency ($\approx 12\,Hz$), the magnitude of the AVSS response is lower than that of the PVSS.

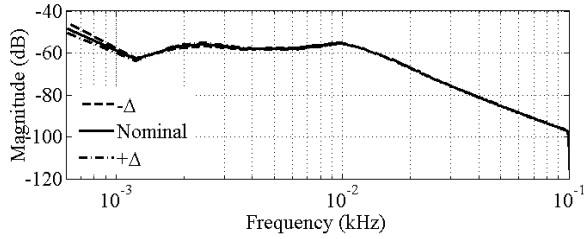

(a) AVSS

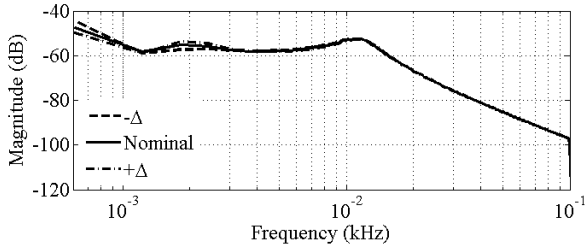

(b) PVSS

Figure 6.5: Rear suspension travel PSD for $\Delta = \pm 30\%$ variation in ks_i^l and ks_i^{nl} about their nominal values.

Above $20\,Hz$, both the AVSS and PVSS perform the is similarly.

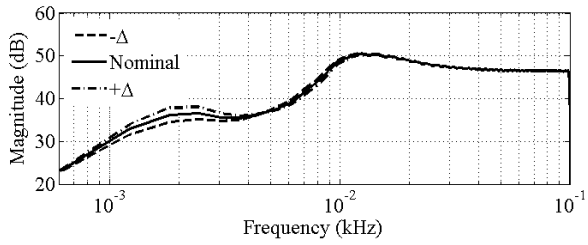

(a) AVSS

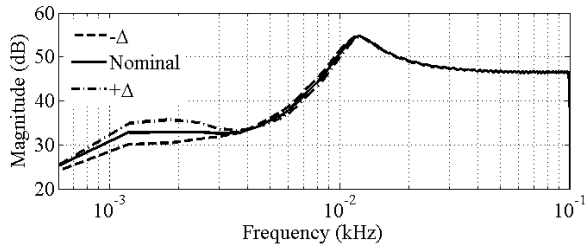

(b) PVSS

Figure 6.6: Front dynamic tyre force PSD for $\Delta = \pm 30\%$ variation in ks_i^l and ks_i^{nl} about their nominal values.

The rear dynamic tyre force PSD for $\pm 30\%$ variation in suspension spring coefficients are shown for the AVSS and PVSS in figures 6.7(a) and 6.7(b) respectively. The AVSS is less sensitive than the PVSS to variation of the spring coefficients at

frequencies below $4\,Hz$ and between $4-8\,Hz$. The PVSS response is higher in magnitude than that of the PVSS at the wheel-hop frequency ($\approx 12\,Hz$). However, both perform similarly at high frequencies (above $20\,Hz$).

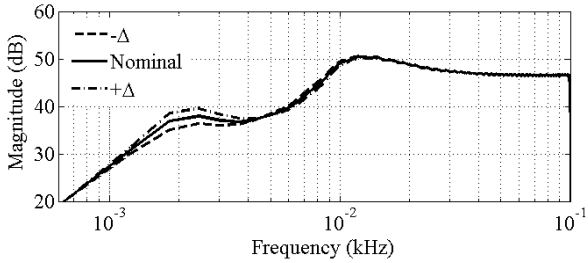

(a) AVSS

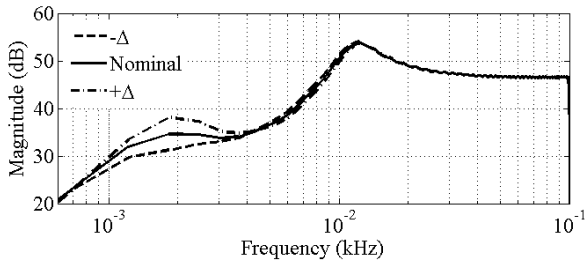

(b) PVSS

Figure 6.7: Rear dynamic tyre force PSD for $\Delta = \pm 30\%$ variation in ks_i^l and ks_i^{nl} about their nominal values.

Figures 6.8(a) and 6.8(b) give the AVSS and PVSS sprung mass acceleration PSD responses, respectively. In the region below $4\,Hz$, the AVSS is less sensitive to variation of the spring coefficients, than the PVSS. The AVSS and PVSS performance between $4-8\,Hz$ and above $20\,Hz$ is similar. Around the wheel-hop frequency, the AVSS produced a more rounded response than that of the PVSS.

Figures 6.9(a) and 6.9(b) show the AVSS and PVSS pitch angular acceleration PSD responses respectively. In the frequency range below $4\,Hz$, the AVSS is less sensitive to variation of the spring coefficients, than the PVSS. Both the AVSS and PVSS perform similarly at frequencies between $4-8\,Hz$, at the wheel-hop frequency, as well as frequencies above $20\,Hz$.

6.3.2 Variation of suspension spring coefficients: Sinusoidal Bump Input Disturbance

Table 6.3 contains the RMS values obtained as the AVSS and PVSS traversed the sinusoidal bump road input disturbance in Section 3.5.1 at $V = 75\,km/h$, for

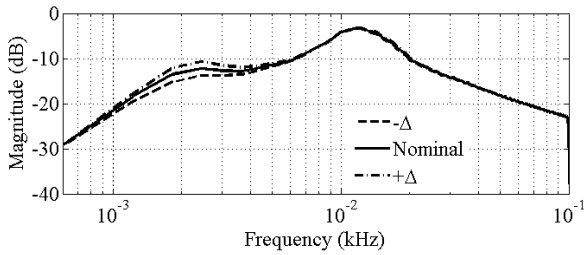

(a) AVSS

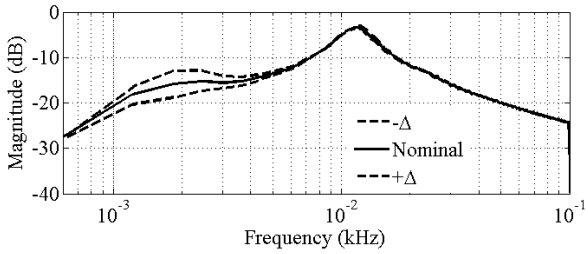

(b) PVSS

Figure 6.8: Sprung mass acceleration PSD for $\Delta = \pm 30\%$ variation in ks_i^l and ks_i^{nl} about their nominal values.

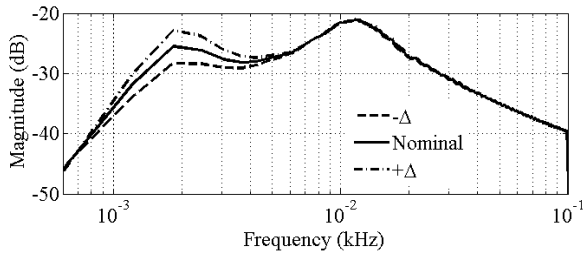

(a) AVSS

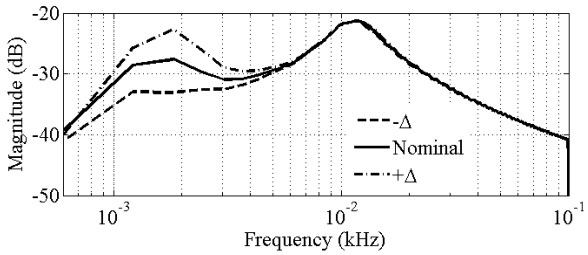

(b) PVSS

Figure 6.9: Pitch angular acceleration PSD for $\Delta = \pm 30\%$ variation in ks_i^l and ks_i^{nl} about their nominal values.

$\Delta = \pm 30\%$ variation in ks_i^l and ks_i^{nl} about their nominal values. The AVSS and PVSS front suspension travel time histories for $\Delta = \pm 30\%$ variation in ks_i^l and ks_i^{nl} about their nominal values, are given in Figures 6.10(a) and 6.10(b) respectively. The figures show that the AVSS front suspension travel is more robust than the PVSS to variation of spring coefficients. The AVSS front suspension travel minimum and maximum peak values are considerably lower than those obtained by the PVSS. Furthermore, the percentage reduction in RMS suspension travel by the AVSS over the PVSS varied between 22.56% and 38.71, the best performance being produced at nominal suspension stiffness (refer to Table 6.3). The AVSS and PVSS did not exceed the suspension travel limit ($\pm 0.08\,m$) set in Chapter 4.

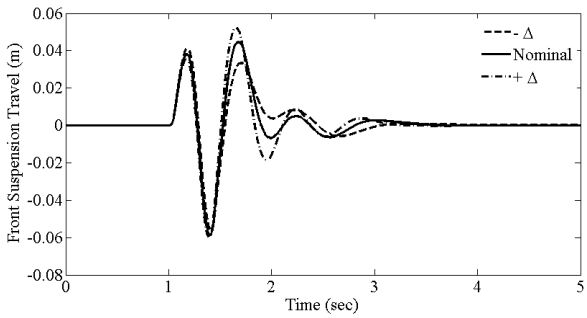

(a) AVSS

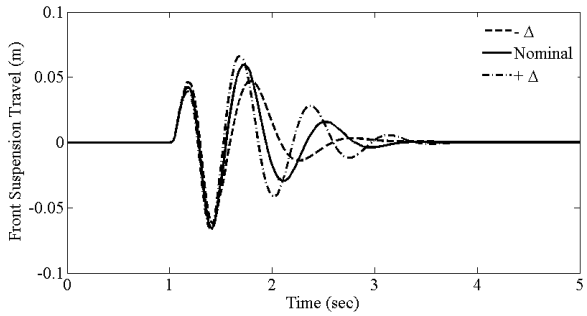

(b) PVSS

Figure 6.10: Front suspension travel time history for $\Delta = \pm 30\%$ variation in ks_i^l and ks_i^{nl} about their nominal values.

Figures 6.11(a) and 6.11(b) give the AVSS and PVSS rear suspension travel time history for $\Delta = \pm 30\%$ variation in suspension stifness coefficients, respectively. Figure 6.11(a) and 6.11(b) show that the AVSS peak rear suspension travel values are lower in magnitude compared with those of the PVSS. There was 22.88% to 30.59% improvement in RMS performance by the AVSS compared with the PVSS, the best performance produced at nominal suspension stifness (see Table 6.3). Both the AVSS and PVSS did not exceed suspension travel limits ($\pm 0.08\,m$) specified in Section 4.

Table 6.3: RMS values for discrete input disturbance with at $V = 75\,km/h$ for $\Delta = \pm 30\%$ variation in ks_i^l and ks_i^{nl} about their nominal values.

Parameters	$-\Delta$			Nominal			$+\Delta$		
	PVSS	AVSS	% Reduction by AVSS	PVSS	AVSS	% Reduction by AVSS	PVSS	AVSS	% Reduction by AVSS
Front Suspension Travel $[m]$	0.0164	0.0127	22.56	0.0183	0.0137	25.14	0.0197	0.0145	26.40
Rear Suspension Travel $[m]$	0.0117	0.0089	23.93	0.0119	0.0091	23.53	0.0118	0.0091	22.88
Front Dynamic Tyre Force $[N]$	392.1042	487.6361	-24.36	593.7066	624.8438	-5.24	820.8481	783.8415	4.51
Rear Dynamic Tyre Force $[N]$	309.6969	379.5833	-22.57	396.8327	439.8761	-10.85	480.7308	500.4420	-4.10
Sprung Mass Acceleration $[m/s^2]$	1.0565	1.2204	-15.51	1.5206	1.5356	-0.99	1.9908	1.8695	6.09
Pitch Angular Acceleration $[rad/s^2]$	0.3643	0.5015	-37.66	0.4736	0.5828	-23.06	0.6225	0.6838	-9.85
Front Actuator Control Voltage $[V]$	–	0.4635	–	–	0.5053	–	–	0.5477	–
Rear Actuator Control Voltage $[V]$	–	0.3937	–	–	0.4101	–	–	0.4224	–
Front Spool-Valve Displacement $[m]$	–	4.1440×10^{-4}	–	–	4.5468×10^{-4}	–	–	4.9512×10^{-4}	–
Rear Spool-Valve Displacement $[m]$	–	3.4040×10^{-4}	–	–	3.5622×10^{-4}	–	–	3.6737×10^{-4}	–
Front Actuator Force $[N]$	–	188.6649	–	–	206.6806	–	–	219.1816	–
Rear Actuator Force $[N]$	–	129.9720	–	–	131.7128	–	–	130.2066	–

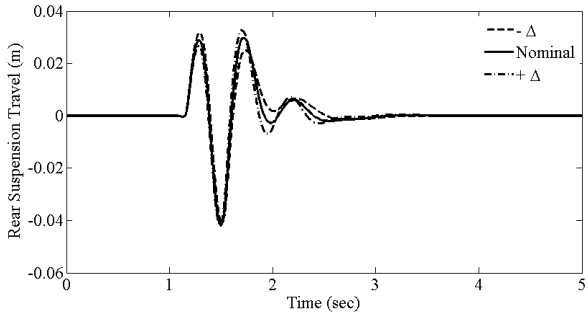

(a) AVSS

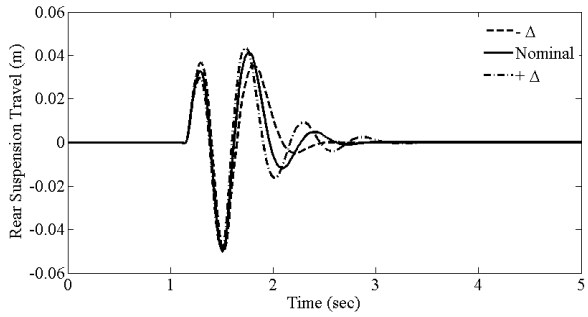

(b) PVSS

Figure 6.11: Rear suspension travel time history for $\Delta = \pm 30\%$ variation in ks_i^l and ks_i^{nl} about their nominal values.

The front dynamic tyre force time histories for $\pm 30\%$ variation in suspension spring coefficients for the AVSS and PVSS are given in Figures 6.12(a) and 6.12(b), respectively. Although these figures show that the AVSS is more robust to variations in suspension stifness, they also indicate that the AVSS front dynamic tyre force peak values tended to be higher than those of the PVSS. The AVSS exeeded the front dynamic tyre force limits specified in Section 4 at the nominal suspension stiffness. Both the AVSS and PVSS exceeded the front dynamic tyre force limits at maximum spring stifness. Although the RMS PVSS performance was better than that of the AVSS, Table 6.3 shows that the AVSS performance improved with increase in suspension stiffness.

Figure 6.13(a) and 6.13(b) are the rear dynamic tyre force time histories for $\Delta = \pm 30\%$ variation in ks_i^l and ks_i^{nl} about their nominal values for the AVSS and PVSS respectively. Comparing the two figures, the AVSS response appears less affected by the variation in suspension stiffness, than the PVSS. However, the AVSS peak rear dynamic tyre forces are higher in magnitude than those of the PVSS. The AVSS and PVSS did not exceed the specified rear dynamic tyre force limits (refer to Section 4). Although the PVSS performance in terms of RMS rear dynamic tyre force

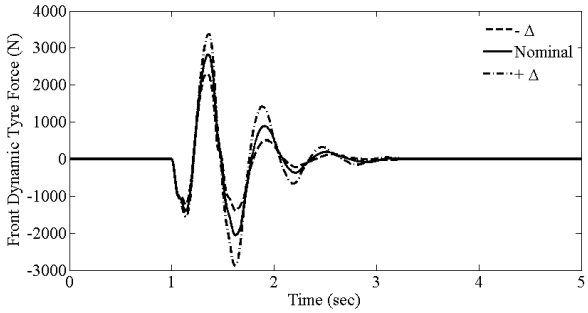

(a) AVSS

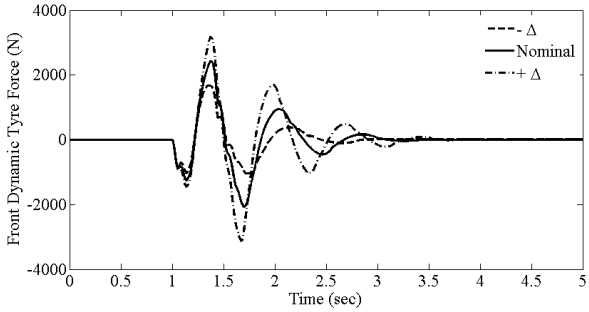

(b) PVSS

Figure 6.12: Front dynamic tyre force time history for $\Delta = \pm 30\%$ variation in ks_i^l and ks_i^{nl} about their nominal values.

was better than that of the AVSS, the AVSS performance improved with increase in suspension stiffness (see Table 6.3).

Figure 6.14(a) and 6.14(b) give the AVSS and PVSS sprung mass acceleration time histories for $\pm 30\%$ variation of suspension stifness, respectively. The figures show that the AVSS is less sensitive to variation of suspension stiffness, compared with the PVSS. The AVSS peak sprung mass acceleration values are higher in magnitude than those of the PVSS. In Table 6.4, the RMS performance of the PVSS was better than that of the AVSS. The performance of the AVSS improved with suspension stiffness. Both the AVSS and PVSS obtained ISO 2631-1 levels of comfort varying between "Not Uncomfortable" at the minimum suspension stifness, to "A Little Uncomfortable" at the maximum suspension stiffness (refer to Table 6.4).

The pitch angular acceleration time histories are given in Figures 6.15(a) and 6.15(b) for $\pm 30\%$ variation in suspension spring coefficients for the AVSS and PVSS , respectively. These figures indicate the AVSS is less sensitive to variations in suspension stiffness, compared with the PVSS. However, the peak pitch angular acceleration values are lower in the PVSS, than in the AVSS. Furthermore, the pitch angular acceleration oscillation is attenuated roughly $0.25\,s$ faster in the AVSS than in the

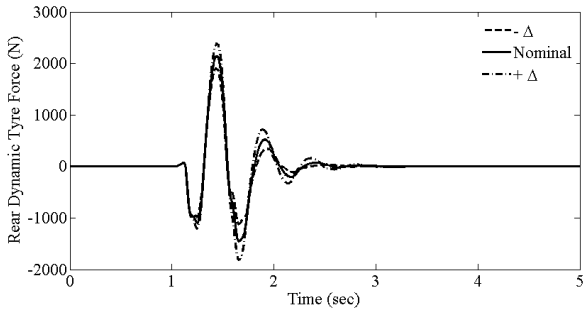

(a) AVSS

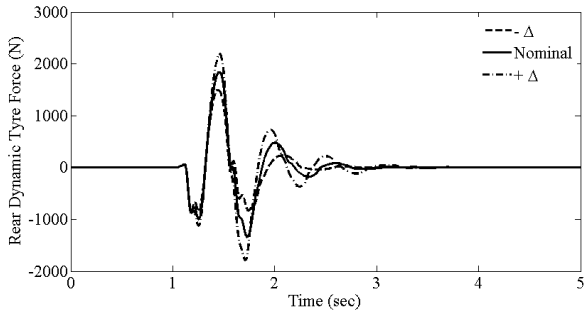

(b) PVSS

Figure 6.13: Rear dynamic tyre force time history for $\Delta = \pm 30\%$ variation in ks_i^l and ks_i^{nl} about their nominal values.

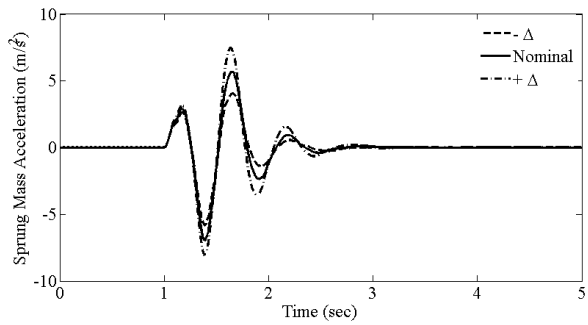

(a) AVSS

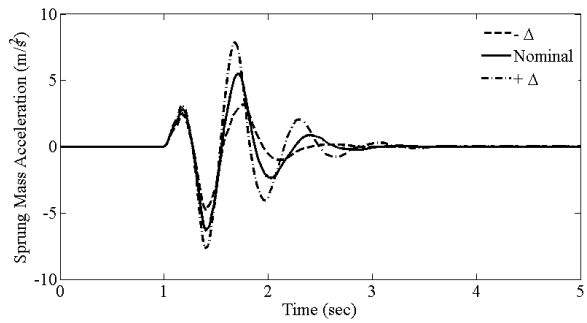

(b) PVSS

Figure 6.14: Sprung mass acceleration time history for $\Delta = \pm 30\%$ variation in ks_i^l and ks_i^{nl} about their nominal values.

PVSS. The RMS pitch angular acceleration was higher in the AVSS than in the PVSS, but the performance of the AVSS improved with increase in suspension stiffness (see Table 6.3).

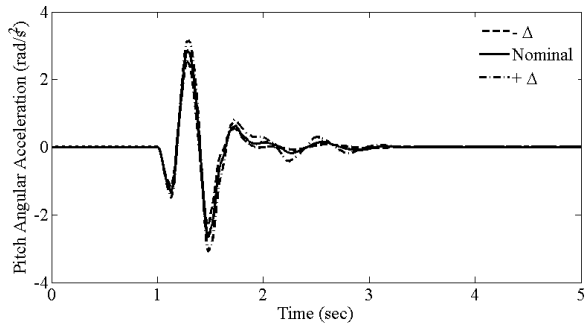

(a) AVSS

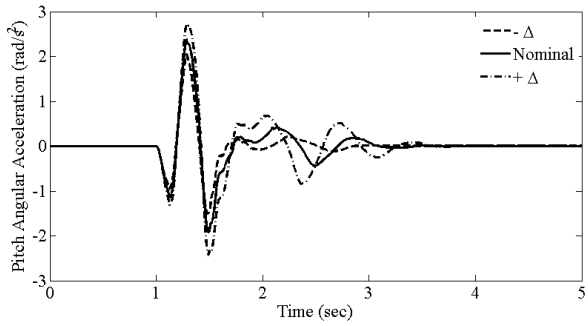

(b) PVSS

Figure 6.15: Pitch angular acceleration time history for $\Delta = \pm 30\%$ variation in ks_i^l and ks_i^{nl} about their nominal values.

Figures 6.16(a) and 6.16(b) are the AVSS front and rear suspension actuator control voltage time histories for $\pm 30\%$ variation in suspension spring coefficients, respectively. The AVSS maintained the front and rear control voltages below the $\pm 10\,V$ limit specified in Section 4 (refer to Figures 6.16(a) and 6.16(b)). The RMS actuator voltages were lower than $0.55V$ at the front actuator and $0.45V$ at the rear actuator (see Table 6.3).

The spool-valve displacement time histories for $\pm 30\%$ variation in suspension spring coefficients are shown in Figures 6.17(a) and 6.17(b) for the front and rear actuators, respectively. The AVSS maintained the peak spool-valve displacement below $\pm 2.1\,mm$ for the front actuator and $\pm 2\,mm$ for the rear actuator. The RMS spool-valve displacements increased with increase in suspension stiffness (see Table 6.3).

Figures 6.18 and 6.18(b) give the front and rear actuator force time histories for $\pm 30\%$ variation in suspension stiffness respectively. AVSS was able to maintain the

Table 6.4: Weighted RMS acceleration, a_{wi}^{RMS}, and discomfort levels as PVSS and AVSS traverse a sinusoidal bump input disturbance at $V = 75\,km/h$ for $\Delta = \pm 30\%\,\{ks_i^l, ks_i^{nl}\}$

	PVSS		AVSS		
	Weighted RMS Acceleration a_{wi}^{RMS} $[m/s^2]$	ISO 2631-1 Level of Discomfort	Weighted RMS Acceleration a_{wi}^{RMS} $[m/s^2]$	ISO 2631-1 Level of Discomfort	% Reduction of a_{wi}^{RMS} by AVSS
$-\Delta$	0.2179	Not Uncomfortable	0.2642	Not Uncomfortable	-24.25
Nominal	0.3140	Not Uncomfortable	0.3341	A Little Uncomfortable	-6.40
$+\Delta$	0.4173	A Little Uncomfortable	0.4114	A Little Uncomfortable	1.41

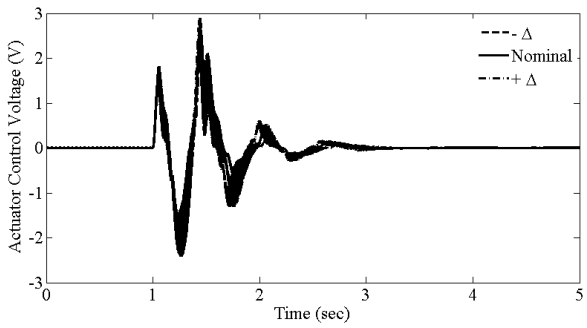

(a) Front suspension

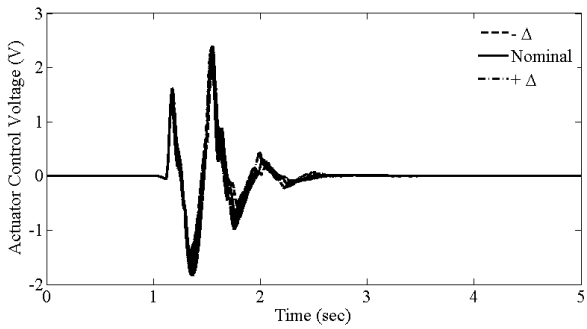

(b) Rear suspension

Figure 6.16: Front and rear actuator control voltage time history for $\Delta = \pm 30\%$ variation in ks_i^l and ks_i^{nl} about their nominal values.

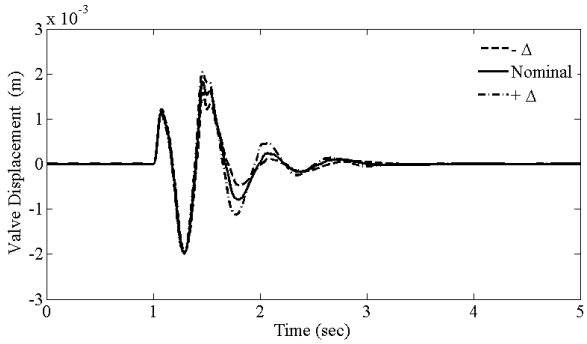

(a) Front suspension

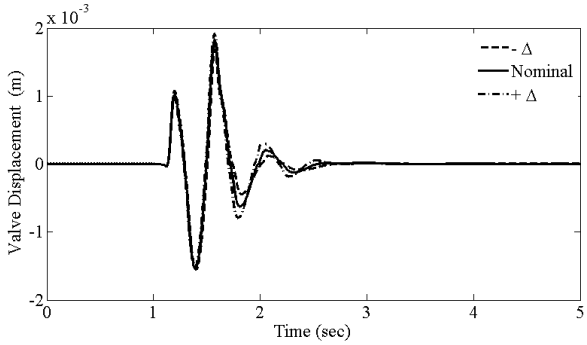

(b) Rear suspension

Figure 6.17: Front and rear actuator spool-valve displacement time history for $\Delta = \pm 30\%$ variation in ks_i^l and ks_i^{nl} about their nominal values.

peak actuator forces below the specified limits given in Section 4, for the simulation period (see Figures 6.18 and 6.18(b)). In Table 6.3, the front and rear RMS actuator forces increased with increase in suspension stiffness.

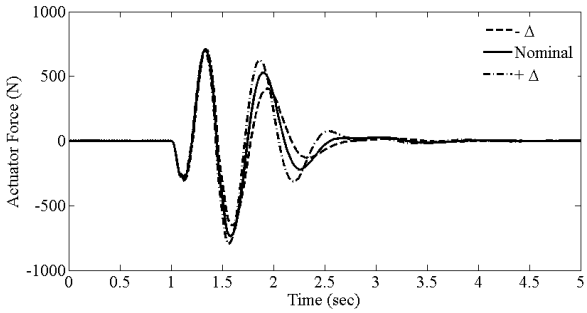

(a) Front suspension

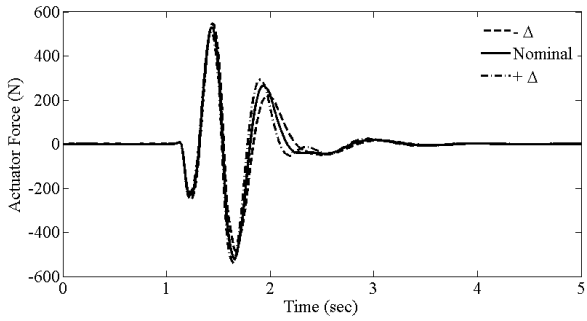

(b) Rear suspension

Figure 6.18: Front and rear actuator force time history for $\Delta = \pm 30\%$ variation in ks_i^l and ks_i^{nl} about their nominal values.

6.3.3 Variation of suspension spring coefficients: Random Input Disturbance

Table 6.5 contains the RMS values obtained as the AVSS and PVSS traversed the sinusoidal bump road input disturbance in Section 3.5.1 for $\Delta = \pm 30\%$ variation in ks_i^l and ks_i^{nl} about their nominal values. The front suspension travel time histories for $\Delta = \pm 30\%$ variation in ks_i^l and ks_i^{nl} about their nominal values are given in Figure 6.19(a) for the AVSS and Figure 6.19(b) for the PVSS. Comparison of both figures indicates that the PVSS is more sensitive than the AVSS to variation in suspension spring stiffness. In addition, the minimum and maximum peak front suspension travel values are lower for the AVSS than for the PVSS (see Figures 6.19(a) and 6.19(b)). The improvement in RMS front suspension travel by the AVSS varied between 17.46% at minimum suspension stiffness to 15.25% at maximum

Table 6.5: RMS values for a random input disturbance with at $V = 75\,km/h$ for $\Delta = \pm 30\%$ variation in ks_i^l and ks_i^{nl} about their nominal values.

Parameters	$-\Delta$			Nominal			$+\Delta$		
	PVSS	AVSS	% Reduction by AVSS	PVSS	AVSS	% Reduction by AVSS	PVSS	AVSS	% Reduction by AVSS
Front Suspension Travel $[m]$	0.0063	0.0052	17.46	0.0060	0.0050	16.67	0.0059	0.0050	15.25
Rear Suspension Travel $[m]$	0.0052	0.0045	13.46	0.0047	0.0041	12.77	0.0046	0.0040	13.04
Front Dynamic Tyre Force $[N]$	467.6565	447.0760	4.40	465.1192	448.9112	3.48	466.0494	456.1994	2.11
Rear Dynamic Tyre Force $[N]$	457.2722	441.0920	3.54	449.8584	438.1208	2.61	446.0701	437.6482	1.89
Sprung Mass Acceleration $[m/s^2]$	0.6239	0.7080	-13.48	0.6619	0.7493	-13.20	0.7138	0.8043	-12.68
Pitch Angular Acceleration $[rad/s^2]$	0.4073	0.4655	-14.29	0.4208	0.4778	-13.55	0.4392	0.4921	-12.04
Front Actuator Control Voltage $[V]$	–	1.0003	–	–	1.0010	–	–	1.0016	–
Rear Actuator Control Voltage $[V]$	–	0.9602	–	–	0.9600	–	–	0.9600	–
Front Spool-Valve Displacement $[m]$	–	3.9576×10^{-4}	–	–	3.9514×10^{-4}	–	–	3.9508×10^{-4}	–
Rear Spool-Valve Displacement $[m]$	–	3.7979×10^{-4}	–	–	3.7728×10^{-4}	–	–	3.7470×10^{-4}	–
Front Actuator Force $[N]$	–	73.4139	–	–	75.9876	–	–	78.3286	–
Rear Actuator Force $[N]$	–	62.4721	–	–	62.6981	–	–	62.5900	–

suspension stiffness, thus the AVSS performance dropped with increase in suspension stiffness (refer to Table 6.5). The AVSS and PVSS did not exceed the suspension travel limit ($\pm 0.08\,m$) set in Chapter 4.

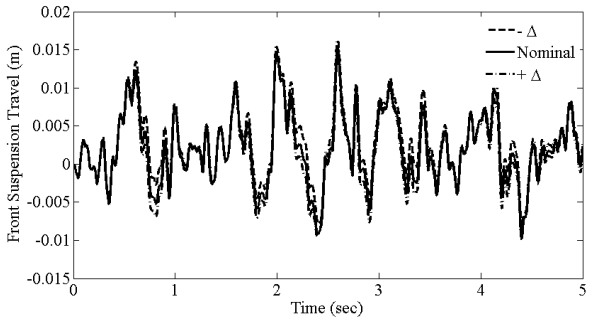

(a) AVSS

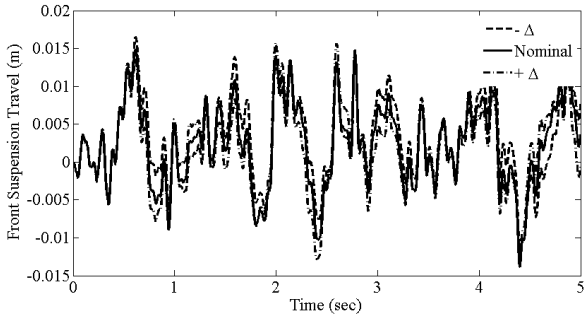

(b) PVSS

Figure 6.19: Front suspension travel time history for $\Delta = \pm 30\%$ variation in ks_i^l and ks_i^{nl} about their nominal values.

The rear suspension travel time history for $\Delta = \pm 30\%$ variation in ks_i^l and ks_i^{nl} about their nominal values, are given in Figures 6.20(a) and 6.20(b) for the AVSS and PVSS, respectively. Close examination of Figures 6.20(a) and 6.20(b) shows that the peak rear suspension travel values are smaller in magnitude in the AVSS, compared with the PVSS. The AVSS improved the rear suspension travel by 12.77 to 13.46%, compared with the PVSS (see Table 6.5). Both the AVSS and PVSS did not exceed the suspension travel limit, $\pm 0.08\,m$, set in Section 4.

The front dynamic tyre force time histories for $\pm 30\%$ variation in suspension spring coefficients are given in Figure 6.21(a) for the AVSS and Figure 6.21(b) for the PVSS, respectively. The AVSS peak front dynamic tyre forces tended to be lower in magnitude compared with the corresponding values of the PVSS. Both the AVSS and PVSS did not exceed the front dynamic tyre force limits specified in Chapter 4. The performance improvement by the AVSS over the PVSS in terms of RMS front dynamic tyre force varied between 4.40% at minimum suspension stiffness to

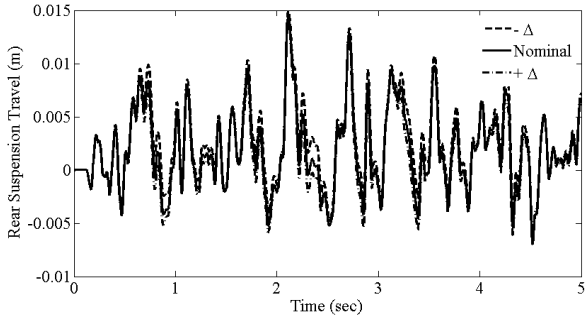

(a) AVSS

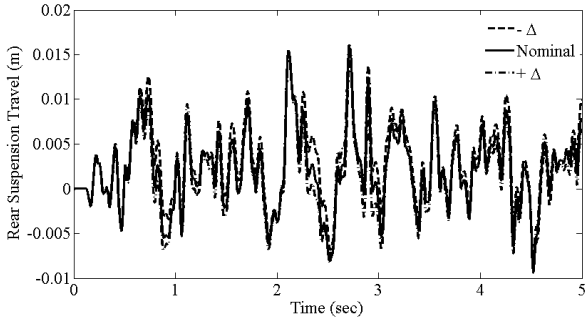

(b) PVSS

Figure 6.20: Rear suspension travel time history for $\Delta = \pm 30\%$ variation in ks_i^l and ks_i^{nl} about their nominal values.

2.11% at maximum suspension stiffness (refer to Table 6.5). The AVSS performance dropped with increase in suspension stiffness.

Figures 6.22(a) and 6.22(b) give the rear dynamic tyre force time histories for $\Delta = \pm 30\%$ variation in ks_i^l and ks_i^{nl} about their nominal values for the AVSS and PVSS, respectively. The AVSS and PVSS did not exceed the rear dynamic tyre force limits specified in Chapter 4. The AVSS obtained lower peak values for rear dynamic tyre force compared with those obtained by the PVSS. Table 6.5 shows that the percentage improvement in RMS rear dynamic tyre force by the AVSS over the PVSS dropped with increase in suspension stiffness; from 3.54% at minimum suspension stiffness, to 1.89% at maximum suspension stiffness (refer to Table 6.5).

The sprung mass acceleration time histories for ±30% variation in suspension spring coefficients are given in Figure 6.23(a) for the AVSS and Figure 6.23(b) for the PVSS. Both the AVSS and PVSS maintained acceleration levels within the ISO 2631-1 "Not Uncomfortable" level of discomfort, thought the AVSS values tended to be approximately 12% higher than those of the PVSS 6.6. The AVSS and PVSS accelerations increased with increase in suspension stiffness.

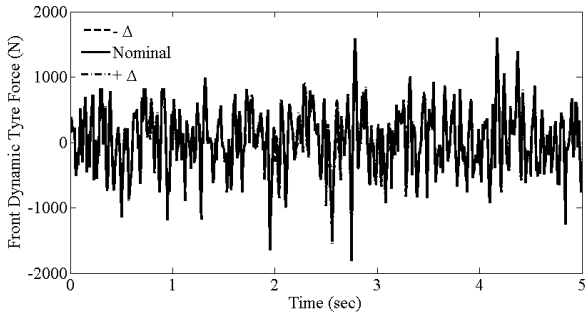

(a) AVSS

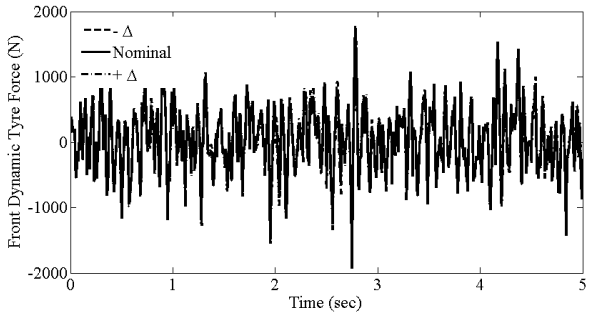

(b) PVSS

Figure 6.21: Front dynamic tyre force time history for $\Delta = \pm 30\%$ variation in ks_i^l and ks_i^{nl} about their nominal values.

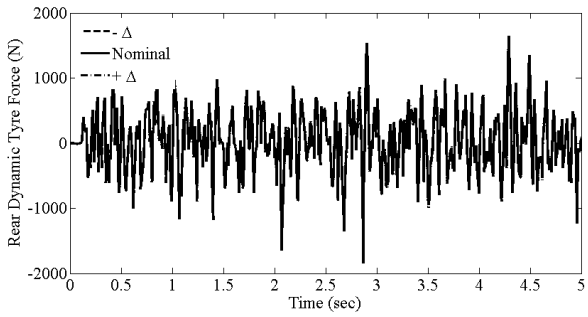

(a) AVSS

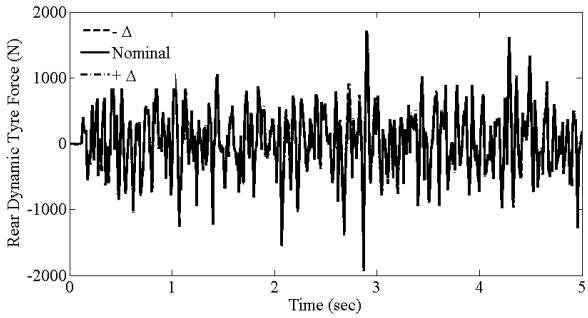

(b) PVSS

Figure 6.22: Rear dynamic tyre force time history for $\Delta = \pm 30\%$ variation in ks_i^l and ks_i^{nl} about their nominal values.

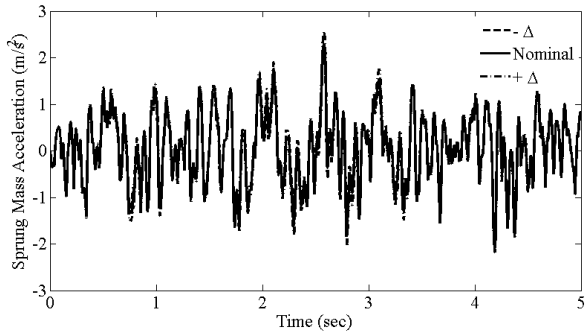

(a) AVSS

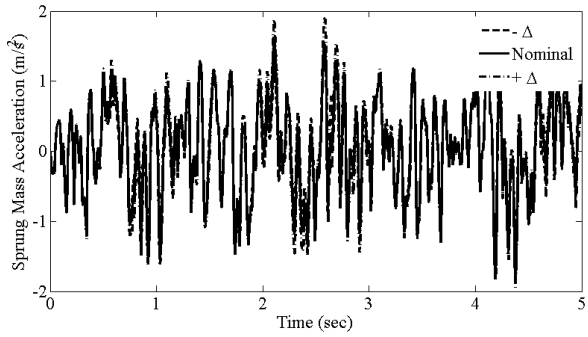

(b) PVSS

Figure 6.23: Sprung mass acceleration time history for $\Delta = \pm 30\%$ variation in ks_i^l and ks_i^{nl} about their nominal values.

Table 6.6: Weighted RMS acceleration, a_{wi}^{RMS}, and discomfort levels as PVSS and AVSS traverse a random road input disturbance at $V = 75\,km/h$ for $\Delta = \pm 30\% \left\{ks_i^l, ks_i^{nl}\right\}$

	PVSS		AVSS		
	Weighted RMS Acceleration a_{wi}^{RMS} $\left[m/s^2\right]$	ISO 2631-1 Level of Discomfort	Weighted RMS Acceleration a_{wi}^{RMS} $\left[m/s^2\right]$	ISO 2631-1 Level of Discomfort	% Reduction of a_{wi}^{RMS} by AVSS
$-\Delta$	0.2203	Not Uncomfortable	0.2472	Not Uncomfortable	-12.21
Nominal	0.2238	Not Uncomfortable	0.2523	Not Uncomfortable	-12.73
$+\Delta$	0.2306	Not Uncomfortable	0.2603	Not Uncomfortable	-12.88

The pitch angular acceleration time histories, for ±30% variation in suspension spring coefficients, are given in Figures 6.24(a) and 6.24(b) for the AVSS and PVSS, respectively. The PVSS peak pitch angular acceleration values obtained are lower in magnitude compared with those of the PVSS. The PVSS RMS pitch angular acceleration values are lower in magnitude than those of the AVSS (see Table 6.5). Both the AVSS and PVSS RMS pitch angular acceleration values increase with increase in suspension stiffness.

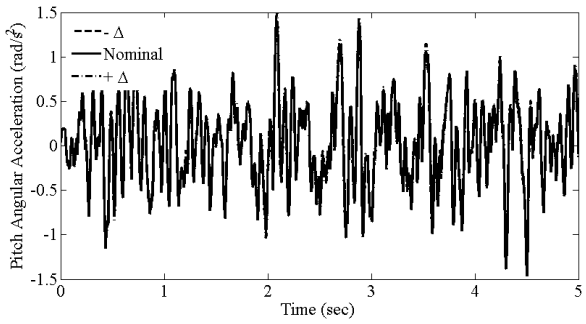

(a) AVSS

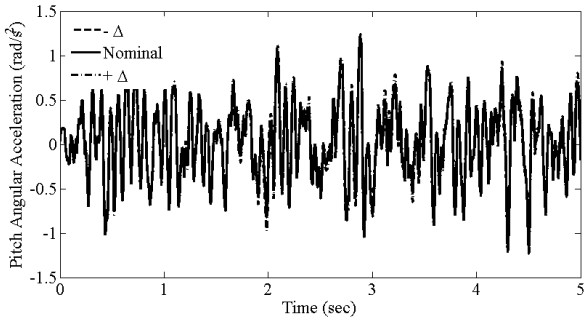

(b) PVSS

Figure 6.24: Pitch angular acceleration time history for $\Delta = \pm 30\%$ variation in ks_i^l and ks_i^{nl} about their nominal values.

Figures 6.25(a) and 6.25(b) give the actuator control voltage time histories for ±30% variation in suspension spring coefficients for the AVSS front and rear actuators, respectively. The front and rear actuator control voltages remained below the limit ($\pm 10\,V$) specified in Chapter 4, for the duration of the simulation. The front and rear RMS actuator voltages remained relatively constant just below $1.05V$ (see Table 6.5).

The spool-valve displacement time histories for ±30% variation in suspension spring coefficients for the front and rear actuators are given in Figures 6.26(a) and 6.26(b), respectively. The peak spool-valve displacements were lower that $\pm 1.3\,mm$ for the front actuator and $0.7\,mm$ for the rear actuator. The RMS spool-valve displacements

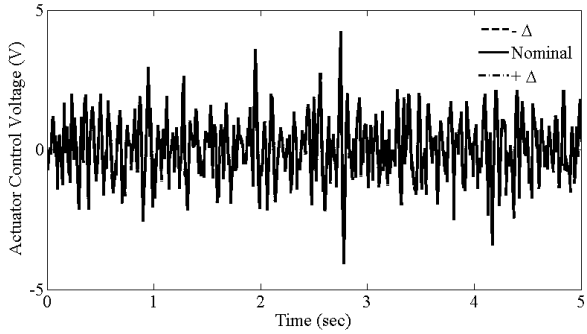

(a) Front suspension

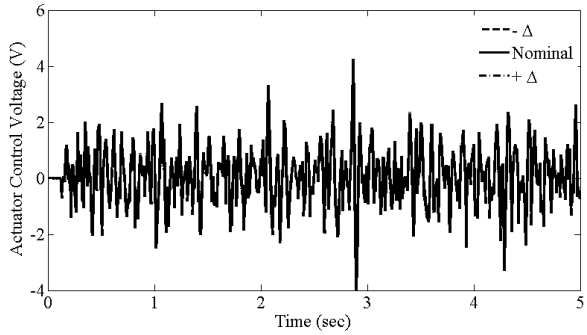

(b) Rear suspension

Figure 6.25: Front and rear actuator control voltage time history for $\Delta = \pm 30\%$ variation in ks_i^l and ks_i^{nl} about their nominal values.

remained relatively constant, with increase in suspension stiffness (see Table 6.5).

Figures 6.27 and 6.27(b) give the actuator force time histories for $\pm 30\%$ variation in suspension stiffness for the front and rear suspension actuators, respectively. Figures 6.27 and 6.27(b) show that the peak actuator forces did not exceed the actuator force limits specified in chapter 4 throughout the simulation. The RMS force at the front actuator increased with increase in suspension stiffness, while the rear actuator RMS force remained relatively constant (refer to Table 6.5).

6.4 Conclusion

In this chapter, controller design for a nonlinear, half-car AVSS with hydraulic actuator dynamics has been presented. The control method involves application of MPC to control suspension travel (outer control loop) and PID control for hydraulic actuator force control (inner control loop). Performance of the AVSS was compared with that of a nonlinear PVSS, with similar model parameters.

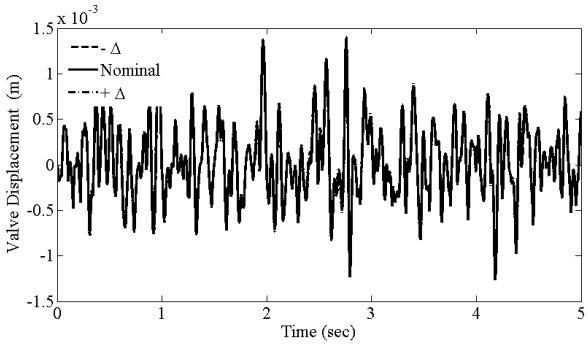

(a) Front suspension

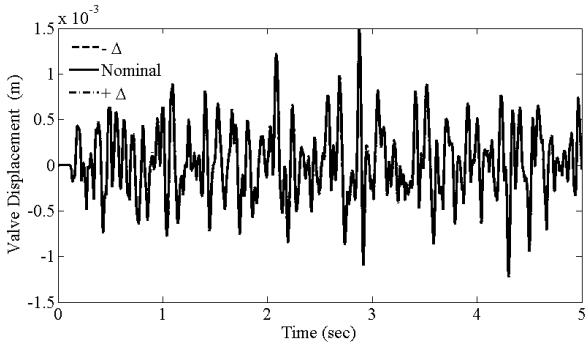

(b) Rear suspension

Figure 6.26: Front and rear actuator spool-valve displacement time history for $\Delta = \pm 30\%$ variation in ks_i^l and ks_i^{nl} about their nominal values.

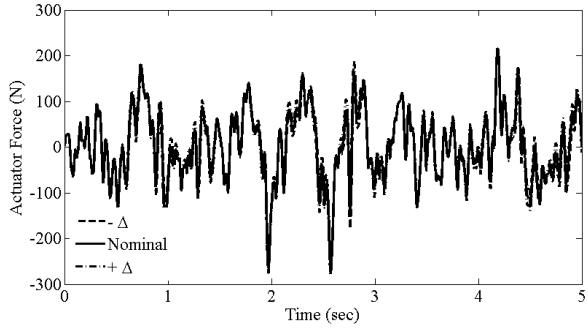

(a) Front suspension

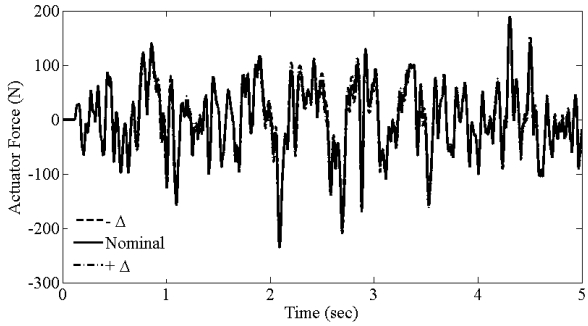

(b) Rear suspension

Figure 6.27: Front and rear actuator force time history for $\Delta = \pm 30\%$ variation in ks_i^l and ks_i^{nl} about their nominal values.

The effect of uncertainty in suspension spring stiffness coefficients on performance of the AVSS and PVSS was tested. This was achieved by varying suspension spring stiffness coefficients by $\pm 30\%$ about their nominal values (Chen et al., 2005), thereafter performing frequency domain and time domain analysis. In the frequency domain, spectral analysis was carried out on AVSS and PVSS model outputs. The output data was obtained from a road input disturbance frequency sweep (Savaresi et al., 2010). In the time domain, the AVSS and PVSS responses were compared as the vehicles traversed a discrete road input disturbance (sinusoidal bump) and a random road input disturbance at forward velocity of $75\,km/h$.

At low frequencies (below $4\,Hz$), the AVSS is more robust than the PVSS to variation of suspension spring stiffness. Furthermore, the AVSS produces lower peak magnitudes for front and rear suspension travels, front and rear dynamic tyre forces, sprung mass vertical acceleration and pitch angular acceleration, at the wheel-hop frequency. The AVSS and PVSS frequency responses to uncertainty in suspension spring stiffness are similar at high frequencies (above $20\,Hz$).

Time domain results confirm the robustness of the AVSS in the presence of uncertainty in suspension spring rate in the low frequency region, compared with the

PVSS. Examination of the time histories of the various AVSS and PVSS outputs indicates that the AVSS is less sensitive to variations in spring stiffness. This is most evident as both vehicles travelled over the sinusoidal bump road input disturbance.

Compared with the PVSS, the AVSS with MPC suspension control and PID force feedback provided a better compromise between vehicle ride comfort and road holding, without exceeding input constraints: control input voltage, and output constraints: suspension travel and hydraulic actuator force. This was aided by the ability of MPC to deal with model constraints present in AVSSs (suspension travel and actuator force output) and the PID based force control of the hydraulic actuator.

7 NEURAL NETWORK-BASED FEEDBACK LINEARIZATION CONTROL OF A NONLINEAR ACTIVE SUSPENSION VIA PID FORCE FEEDBACK

7.1 Introduction

FBL is a method used in nonlinear control to convert highly nonlinear model dynamics to linear model dynamics to enable application of linear control methods (Deng et al., 2009). NNFBL utilizes identified NN functions of the nonlinear plant model to perform the nonlinear dynamics cancellation (Hagan et al., 2002). Buckner et al. (2000) and Pedro and Dahunsi (2011) have applied NNFBL successfully to a quarter-car AVSS design using RBF and MLP NNs respectively, obtaining good performance, in the presence of system nonlinearities.

This chapter presents the development of a NNFBL controller for a nonlinear AVSS with PID hydraulic actuator force feedback. Design of the inner PID force control loop is given in Section 7.2.1. This is followed by development of the NNFBL controller in Section 7.2.2 with experimentation, model structure selection, model estimation and model validation given in Sections 7.2.2.1, 7.2.2.2, 7.2.2.3 and 7.2.2.4 respectively. The simulation results are then presented and discussed in Section 7.3, with consideration given to vehicle velocity and sprung mass loading variation, for various road input disturbances, in the time-domain. Section 7.3.3, contains uncertainty analysis for the variations in sprung mass loading, suspension spring coefficients and suspension damping coefficients. This is followed by conclusions to the chapter in Section 7.4.

7.2 Controller Design

Control of the half-car AVSS is possible by the two-loop feedback control arrangement shown in Figure 7.1. Suspension travel is the main control variable due to ease of measurement and the need to maintain suspension travel within the limits of the suspension workspace (Du and Zhang, 2008). NNFBL is applied on the outer control loop which sets the desired actuator control force signal, based on the relative displacement between the vehicle body and the wheels. The inner PID force control loop enhances the actuator stability, minimizing chattering and enables the controller to achieve the desired force set by the outer loop (Fateh and Alavi, 2009; Marusak and Kuntanapreeda, 2011; Priyandoko et al., 2009). The overall control system architecture applied is shown in Figure 7.1.

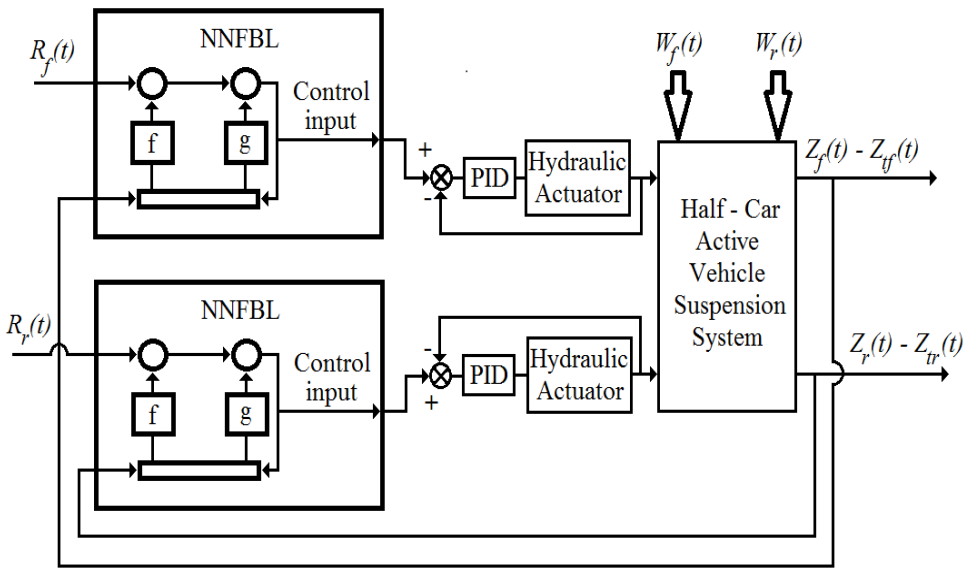

Figure 7.1: Control architecture for NNFBL control of a nonlinear active vehicle suspension via PID force feedback.

7.2.1 PID Force Control Loop Design

The PID force control input, u_i to the half-car AVSS actuators is given in Equation 7.1 and illustrated in Figure 7.2:

$$u_i = K_{P\,i} e_i(t) + K_{I\,i} \int e_i(t)\,dt + K_{D\,i} \frac{d\left(e_i(t)\right)}{dt} \tag{7.1}$$

$$e_i(t) = F_{ai\,ref}(t) - F_{ai}(t) \tag{7.2}$$

where $K_{P\,i}$ is the proportional gain, $K_{I\,i}$ is the integral gain, $K_{D\,i}$ is the derivative gain, e_i is the error between the desired actuator force reference signal, $F_{ai\,ref}$, and the actual actuator force, F_{ai}. Subscript i represents either the front or rear suspension $i \in (f, r)$. A saturation block was placed in front of the controller output to ensure that the control voltage limits ($|u_i| \leq u_{max}$) were not exceeded in the MATLAB/Simulink® implementation. Table 7.1, contains the PID controller gains for the force control loop. These gains were obtained by Ziegler-Nichols tuning method.

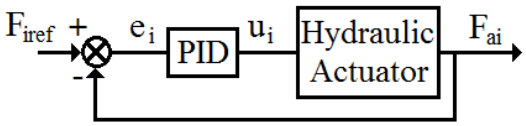

Figure 7.2: Inner PID force feedback control loop.

Table 7.1: PID force control loop tuning parameters

PID Gains	Front Suspension	Rear Suspension
K_P	0.0010	0.0010
K_I	0.0145	0.0145
K_D	0.0003	0.0003

7.2.2 NNFBL Suspension Travel Control Loop Design

The MATLAB/Simulink® NARMA-L2 control toolbox was used to perform Neural Network-based Feedback Linearization (NNFBL) on the outer control loop. Since this tool is a Single Input Single Output (SISO) tool, two separate NARMA-L2 controllers were used for control of the half-car AVSS which is a MIMO system. Furthermore, the SISO nature of the NARMA-L2 controller meant that the half-car AVSS model was modified to allow for collection of the I/O data required for system identification. For front suspension system identification, the rear suspension input and output were grounded and terminated respectively as shown in Figure 7.3. This made the AVSS appear to be a SISO system to the controller, enabling identification. The same process was repeated for the rear suspension system by grounding and terminating the front suspension system input and output respectively. The system identification was then carried out in four steps:

1. Experimentation

2. Model Structure Selection

3. Model Estimation

4. Model Validation

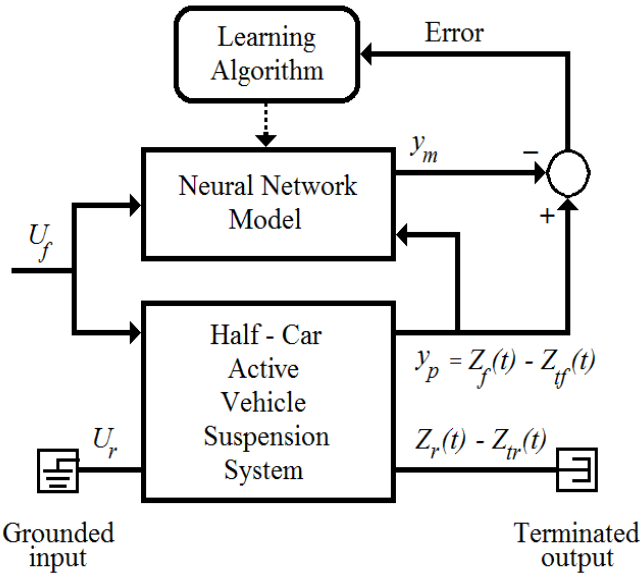

Figure 7.3: System identification of a nonlinear half-car AVSS for NNFBL control.

7.2.2.1 Experimentation

Two random non-saturating input signals covering the entire operational range of the half-car AVSS, were used to generate the I/O data. The sampling time was chosen to be smaller than the fastest system dynamic to ensure that all model dynamics are captured in the data. The data, Z_i^n, was collected in the form presented in Equation 7.3 in which $u_i(k)$ and $y_i(k)$ are the input and output to the system respectively, k is the number of the sampling instant, n is the total number of samples taken and subscript i represents either the front or rear suspension $i = \{f, r\}$ (Pedro et al., 2009; Beale et al., 2010).

$$Z_i^n = f\left\{\left[u_i(k), y_i(k)\right]; k = 1, \ldots, N\right\} \quad (7.3)$$

The I/O data collected from the front and rear suspensions are given in Figures 7.4 and 7.5. The data consists of 10000 samples collected at a sampling rate $T_s = 0.001\,s$. The maximum input force, $F_{ai} = u_i(k)$, was limited to $\pm 5000\,N$ and the suspension travels, $y_f = z_{tf} - zc + l_f \sin\theta$ and $y_r = z_{tr} - zc - l_r \sin\theta$ were limited to $\pm 0.08\,m$.

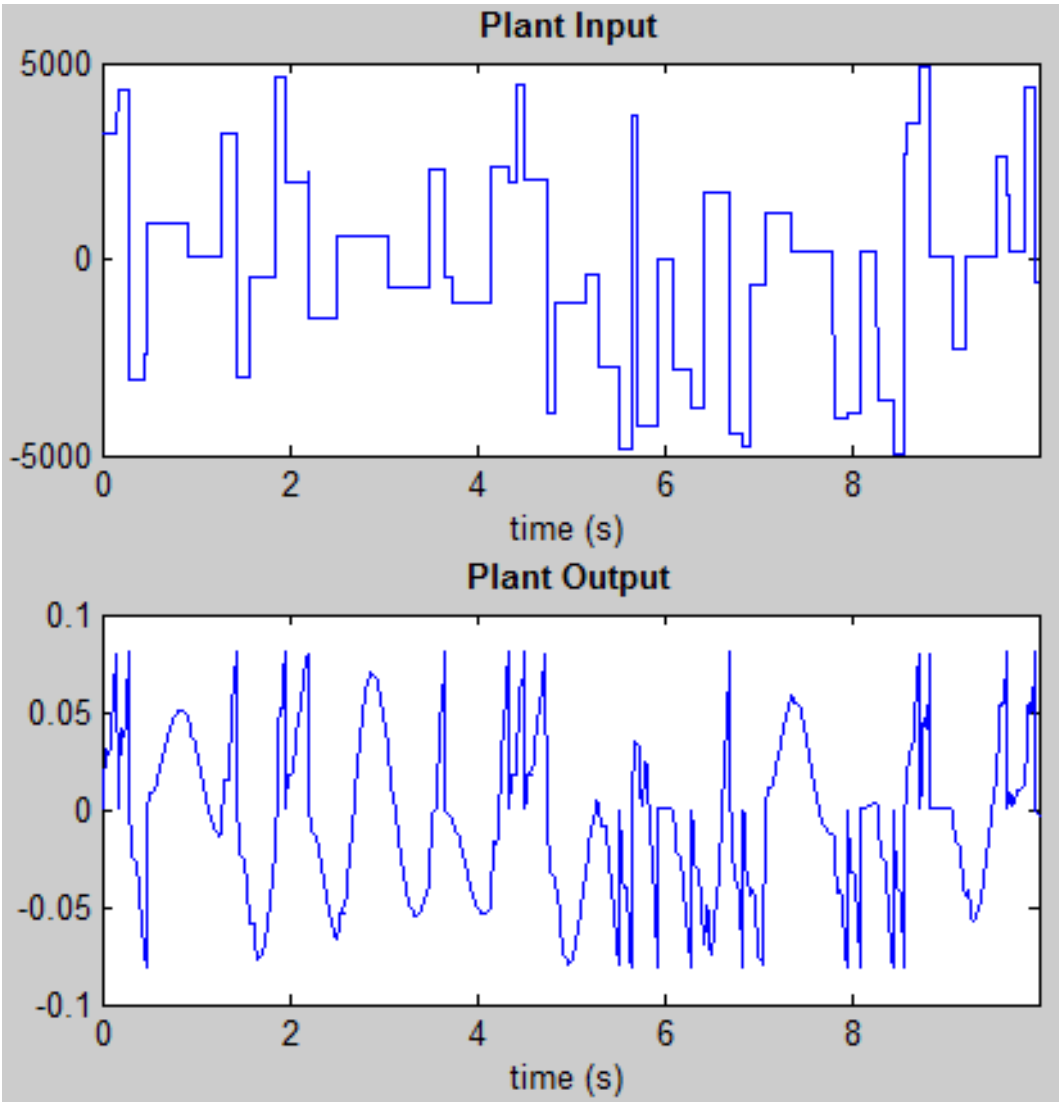

Figure 7.4: Front suspension I/O data for Neural Network system identification for NNFBL control.

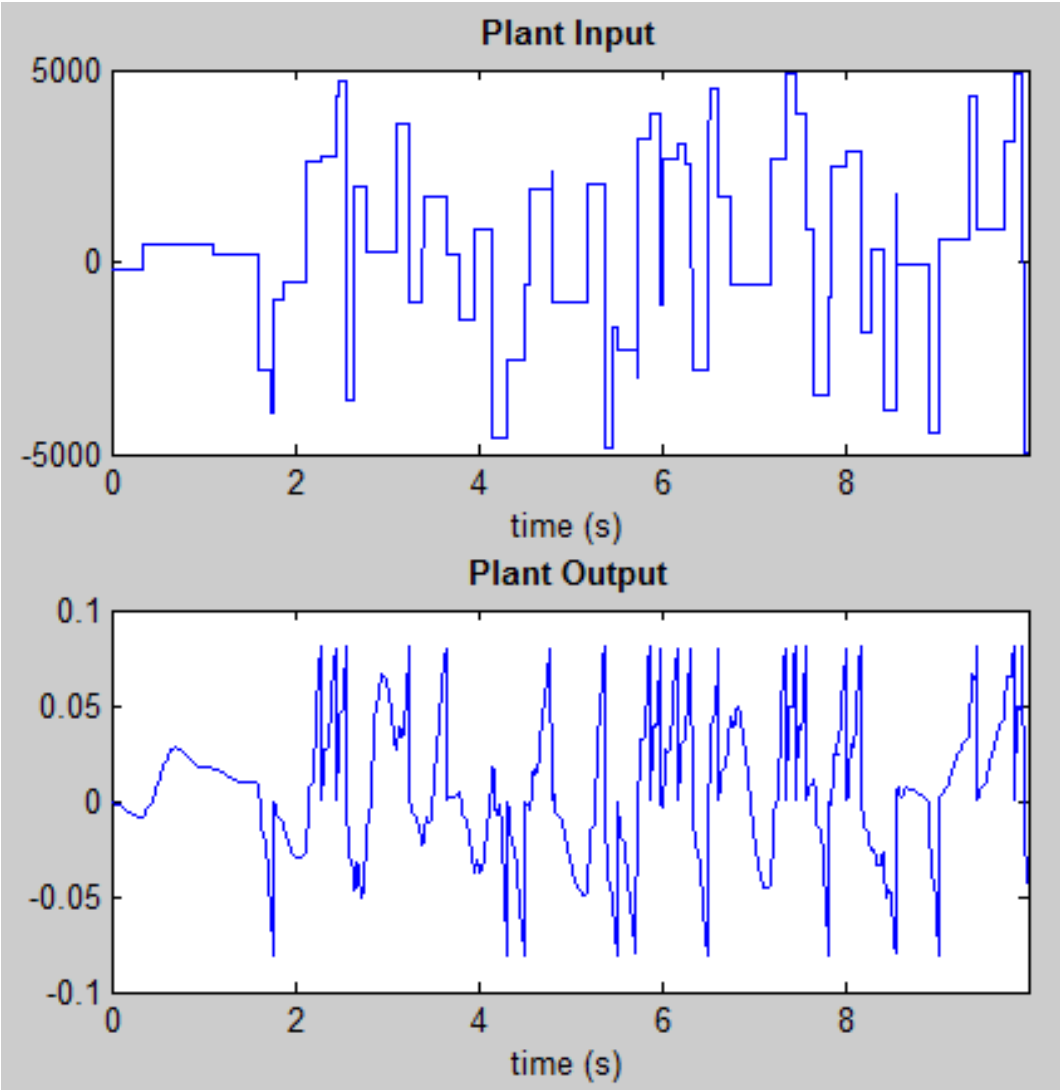

Figure 7.5: Rear suspension I/O data for Neural Network system identification for NNFBL control.

7.2.2.2 Model Structure Selection

The NARMA models given in Equation 7.4, in which d is the system delay, na is the number of past inputs, nb is the number of past outputs and F is a nonlinear function, were trained to present the half-car AVSS model's forward dynamics. The nonlinear function F is approximated by the NN during identification (Pedro et al., 2009; Beale et al., 2010).

$$\begin{aligned} y_i(k+d) &= F\left[y_i(k), y_i(k-1), \ldots, y_i(k-na+1), u_i(k), u_i(k-1), \right. \\ &\quad \left. \ldots, u_i(k-nb+1)\right] \end{aligned} \tag{7.4}$$

FBL involves cancellation of nonlinear system dynamics into linear. The NARMA-L2 controller achieves this by training two MLP NN to approximate the nonlinear functions $f[\cdot]$ and $g[\cdot]$, as shown in Figure 7.6. The MLP NN models have two layers. The first layer is the hidden layer which contains neurons with tangent-sigmoid (hyperbolic-tangent) activation function:

$$\begin{aligned} tansig(n) &= \frac{2}{1+e^{-2(n)}} - 1 \\ &= \frac{1-e^{-2(n)}}{1+e^{-2(n)}} \end{aligned} \tag{7.5}$$

The second layer is the output layer which contains neurons with linear activation function. Both the hidden and output layers contain a bias. Figure 7.6 shows the input, hidden and output layers of the MLP NN. The companion form (in which the next controller input, $u(k)$, is not contained inside the nonlinearity) is expressed in Equation 7.6. This form enables tracking of reference signal $y_{ri}(k+d)$. However, because $y_i(k)$ is required to calculate $u_i(k)$ and both occur at the same sampling instant, the resulting controller (see Equation 7.7) is not practically feasible (Pedro et al., 2009; Beale et al., 2010).

$$\begin{aligned} \hat{y}_i(k+d) &= f\left[y_i(k), y_i(k-1), \ldots, y_i(k-n+1), u_i(k), u_i(k-1), \right. \\ &\quad \left. \ldots, u_i(k-na+1)\right] + g\left[y_i(k), y_i(k-1), \ldots, y_i(k-n+1), \right. \\ &\quad \left. u_i(k-1), \ldots, u_i(k-nb+1)\right] \cdot u_i(k) \end{aligned} \tag{7.6}$$

$$\begin{aligned} u_i(k) &= \left(y_{ri}(k+d) - f\left[y_i(k), y_i(k-1), \ldots, y_i(k-n+1), u_i(k-1), \ldots, \right.\right. \\ &\quad \left.\left. u_i(k-na+1)\right]\right) \div \left(g[y_i(k), y_i(k-1), \ldots, y_i(k-n+1), u_i(k-1), \right. \\ &\quad \left. \ldots, u_i(k-nb+1)]\right) \end{aligned} \tag{7.7}$$

By setting the plant delay $d \geq 2$ with a model order $n = na = nb = 2$, a NARMA model and therefore a practical NARMA-L2 controller can be developed as given in Equations 7.8 and 7.9 respectively. Figure 7.7 illustrates use of the identified

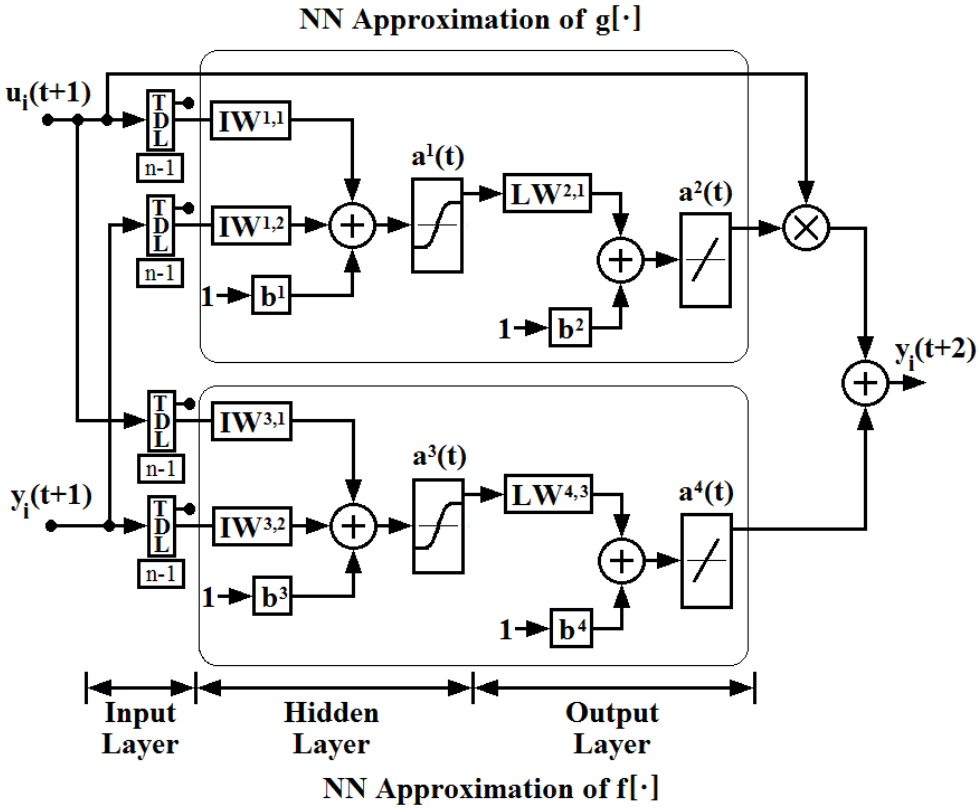

Figure 7.6: NARMA-L2 NN model for approximation of nonlinear functions $f[\cdot]$ and $g[\cdot]$.

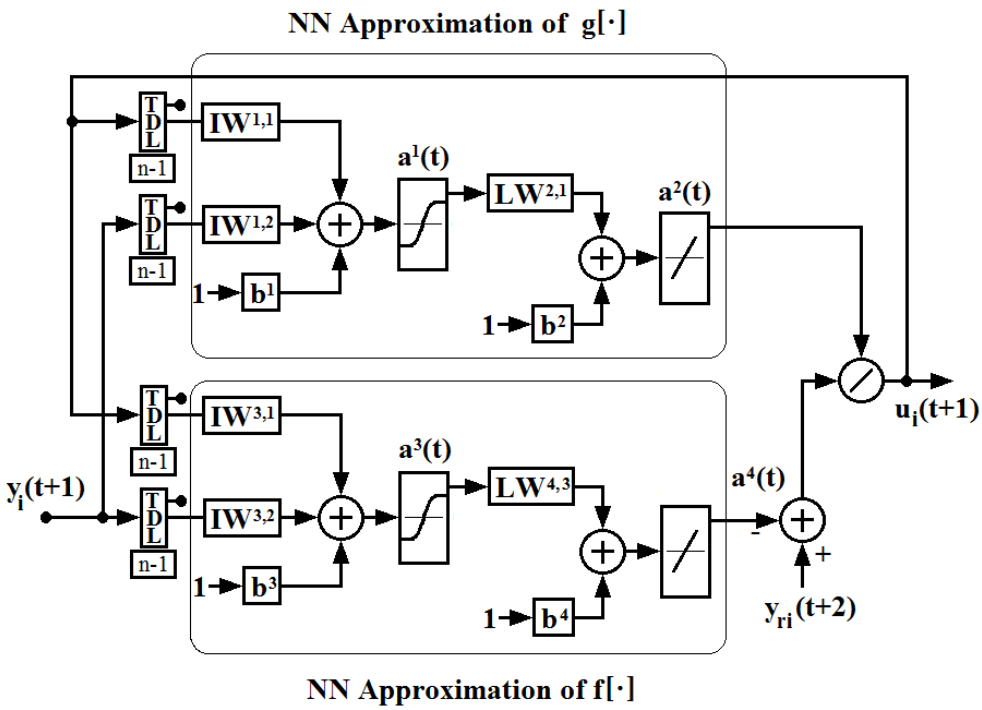

Figure 7.7: Use of the identified NARMA model to obtain NARMA-L2 control input $u_i(t+1)$.

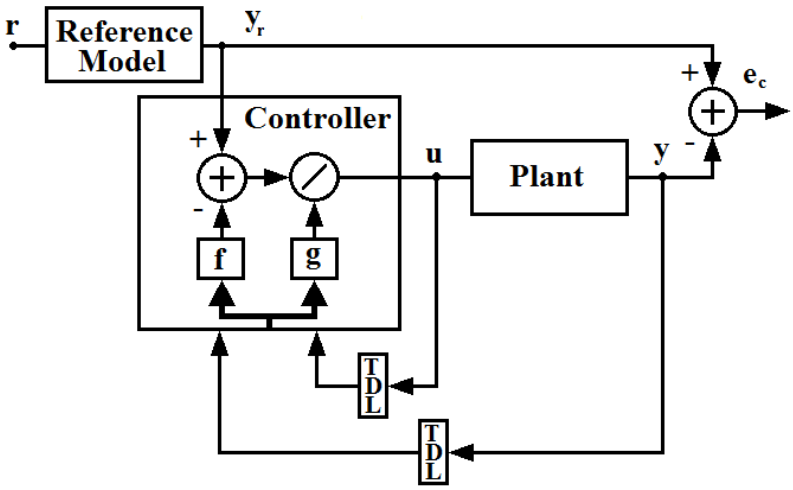

Figure 7.8: NARMA-L2 Controller implementation.

NARMA model to obtain the control signal for the NARMA-L2 controller implementation in Figure 7.8 (Pedro et al., 2009; Beale et al., 2010).

$$\begin{aligned} y_i(k+d) &= f[y_i(k), y_i(k-1), \ldots, y_i(k-n+1), u_i(k), u_i(k-1), \\ &\quad \ldots, u_i(k-n+1)] + g[y_i(k), y_i(k-1), \ldots, y_i(k-n+1), \\ &\quad u_i(k-1), \ldots, u_i(k-n+1)] \cdot u_i(k+1) \end{aligned} \tag{7.8}$$

$$u_i(k) = \frac{y_{ri}(k+d) - f[y_i(k), \ldots, y_i(k-n+1), u_i(k), \ldots, u_i(k-n+1)]}{g[y_i(k), \ldots, y_i(k-n+1), u_i(k), \ldots, u_i(k-n+1)]} \tag{7.9}$$

7.2.2.3 Model Estimation

Model estimation is the process of training the NN to approximate the desired function using the I/O data collected. The NNs were trained using the backpropagation method. In this method, NN weights are updated backwards through the NN by calculating the Jacobian and gradient of the weights. There are several backpropagation algorithms, for training NN. Thus, selection of the NN training algorithm was based on reduction of the Mean Square Error (MSE), for a given maximum allowable number of epochs to reach convergence (Beale et al., 2010; Dahunsi and Pedro, 2010).

MSE is an indication of the accuracy of the identified NN model of the AVSS plant. A smaller MSE means that the NN model of the AVSS plant is more accurate. For AVSS plant outputs $y_f = z_{tf} - zc + l_f \sin\theta$ and $y_r = z_{tr} - zc - l_r \sin\theta$ and NN model

outputs y_{mf} and y_{mr}, the NN model MSE is calculated as follows:

$$\begin{aligned} MSE &= \frac{1}{n}\sum_{i=1}^{n}(e_i)^2 \\ &= \frac{1}{n}\sum_{i=1}^{n}(y_i - y_{mi})^2 \end{aligned} \tag{7.10}$$

where e_i is the error between the AVSS plant output and the neural network model output and n is the number of training samples.

The NNFBL parameters for both the Front and Rear Suspension are listed in Table 7.2. Results from the NN training of the front and rear suspension system controllers NN models are listed in Table 7.3. The results indicate that the LM algorithm was the best training algorithm, producing MSEs of 1.6736×10^{-7} after 13 training epochs and 3.8147×10^{-7} after 28 training epochs for the front and rear suspension NNs, respectively.

Table 7.2: NNFBL parameters for front and rear suspension

Parameters	Value
Number of layers	2
Number of hidden layer neurons	5
Number of delayed plant inputs	2
Number of delayed plant outputs	2
Sampling interval T_s	$0.001\,s$
Normalize training data	No
Number of training samples	10000
Maximum plant input	$5000\,N$
Minimum plant input	$-5000\,N$
Maximum plant output	$0.08\,m$
Minimum plant output	$-0.08\,m$
Maximum interval value	$0.5\,s$
Minimum interval value	$0.1\,s$
Maximum Number of training epochs	1000
Total sampling time	$10\,s$

7.2.2.4 Model Validation

50% of the I/O data is used for NN training, 25% for validation and the remaining 25% for testing of the NN models. Figures 7.9 to 7.14 show that the NN model

Table 7.3: Performance of NNFBL training algorithms for front and rear suspension

Training Algorithm	Full Name of Algorithm	Front Suspension		Rear Suspension	
		Number of Epochs	MSE	Number of Epochs	MSE
trainbfg	Broyden-Fletcher -Goldfarb-Shanno (BFGS)quasi-Newton backpropagation	27	9.9943×10^{-4}	24	5.0564×10^{-3}
trainbr	Bayesian Regulation	12	2.6265	32	1.1742×10^{-3}
traincgb	Powell-Beale conjugate gradient backpropagation	13	1.177×10^{-3}	9	7.5448×10^{-4}
traincgf	Fletcher-Powell conjugate gradient backpropagation	8	0.080791	10	0.25491
traincgp	Polak-Ribiere conjugate gradient backpropagation	8	0.046266	4	0.054292
traingd	Gradient descent backpropagation	1000	7.38587×10^{-3}	1000	7.24×10^{-3}
traingdm	Gradient descent with momentum backpropagation	6	15.5732	6	2.16
traingda	Gradient descent with adaptive learning backpropagation	31	24.3319	33	3.3688
traingdx	Gradient with momentum and adaptive learning backpropagation	55	4.0851	48	0.24551
trainlm	Levenberg-Marquardt backpropagation	13	1.6736×10^{-7}	28	3.8147×10^{-7}
trainoss	One step secant backpropagation	8	1.1389×10^{-3}	27	9.6757×10^{-4}
trainrp	Resilient backpropagation	27	1.089×10^{-3}	39	8.6774×10^{-4}
trainscg	Scaled conjugate gradient backpropagation	28	0.039994	29	0.039014

output closely matched the plant model output for the front and rear suspension training, validation and testing data, with errors in the order 10^{-3}. The front and rear suspension regression plots in Figures 7.15 and 7.16, respectively, show good NN fitting of the I/O data, without any outliers. The MSE plots obtained with the LM training algorithm for both the front and rear suspensions are shown in Figures 7.17 and 7.18. The training state plots in Figures 7.19 and 7.20 show the variation of the NN gradient, Mu and the number of completed validation checks at convergence respectively.

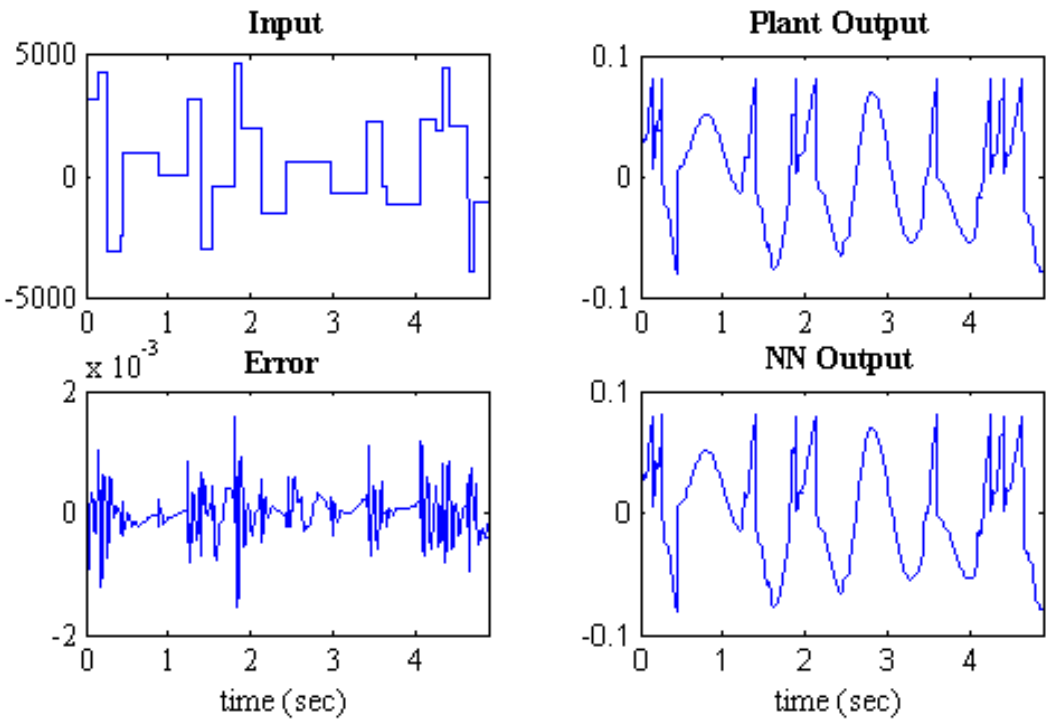

Figure 7.9: Front suspension NN training data for NNFBL control.

7.3 Simulation Results and Discussion

The half-car AVSS model was built in the MATLAB/Simulink® environment. The MATLAB Ordinary Differential Equation (ODE)-3 (Bogacki-Shampine) fixed-step solver, with sampling time set to $T_s = 0.0001s$, was selected for use in the simulations. Fixed-step solvers allow users to set a fixed-sampling time for the duration of the simulation. The magnitude of the smallest step size is lower than the fastest half-car AVSS model dynamics, enabling observation of all model dynamics (Dahunsi and Pedro, 2010). The tasking mode for periodic sampling times was set to "Single Tasking", since the model does not have multiple sampling times.

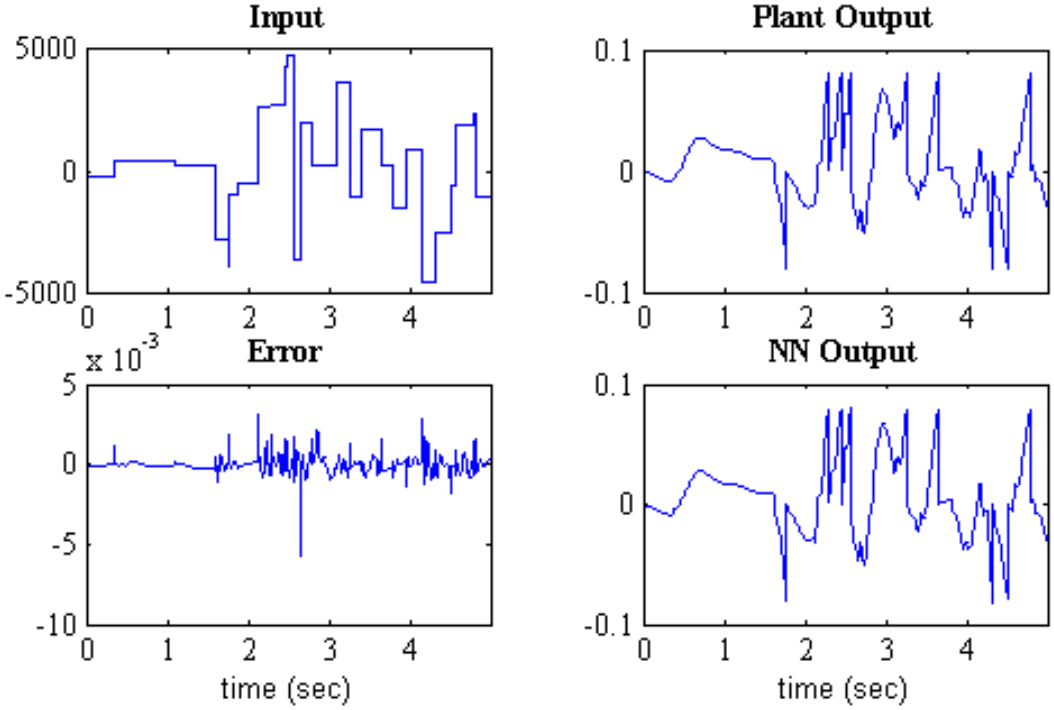

Figure 7.10: Rear suspension NN training data for NNFBL control.

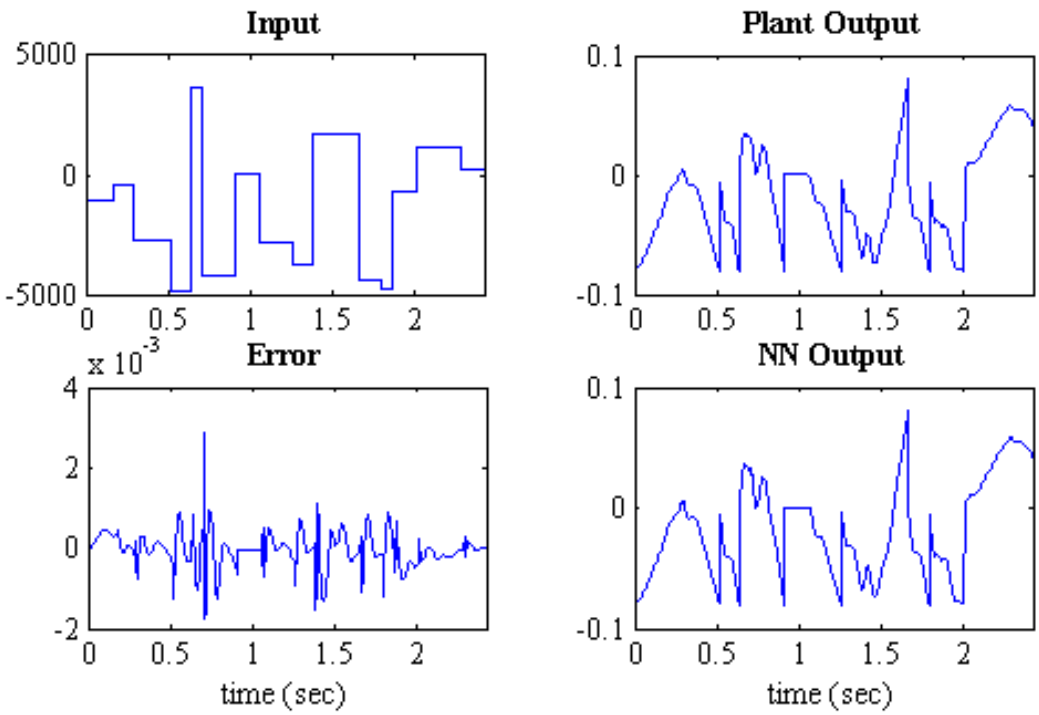

Figure 7.11: Front suspension NN validation data for NNFBL control.

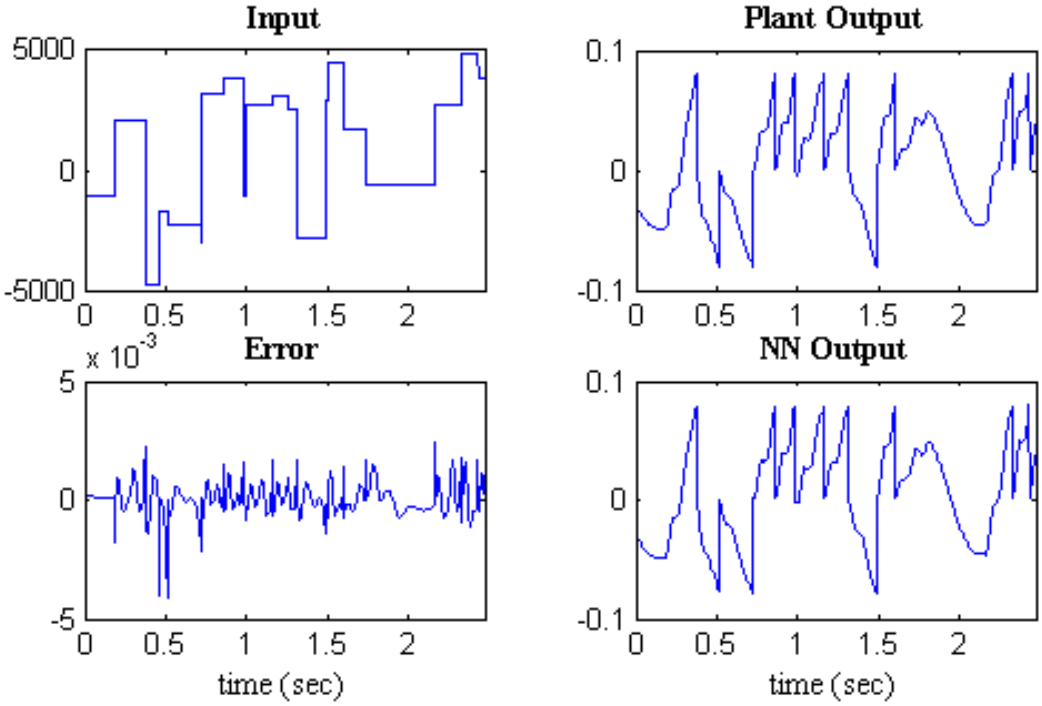

Figure 7.12: Rear suspension NN validation data for NNFBL control.

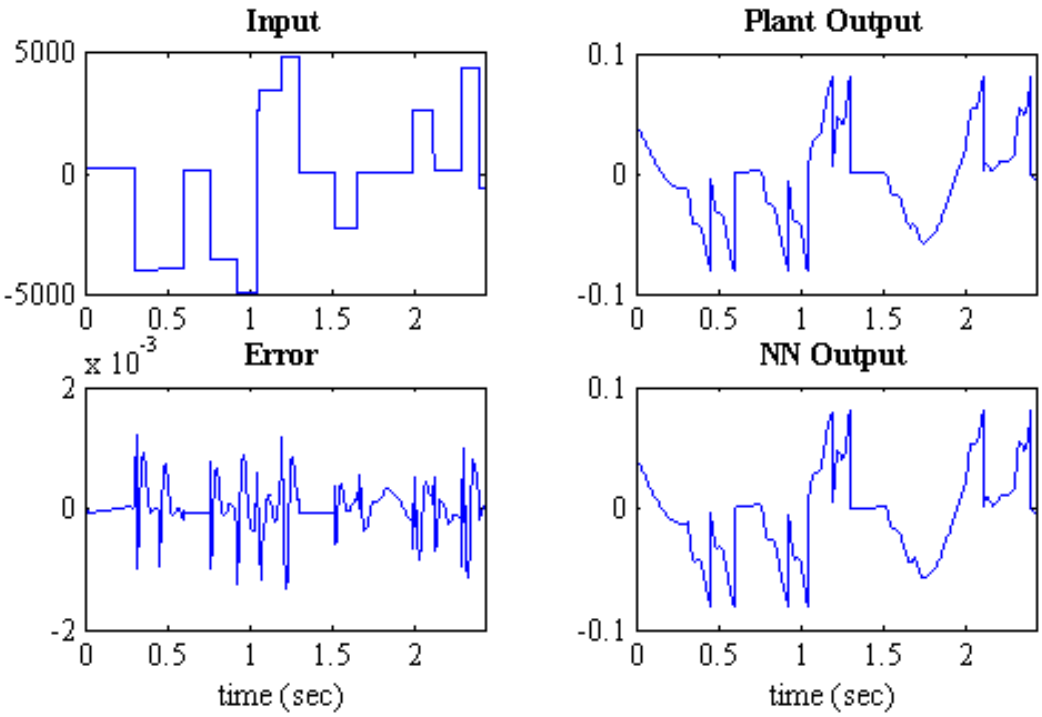

Figure 7.13: Front suspension NN testing data for NNFBL control.

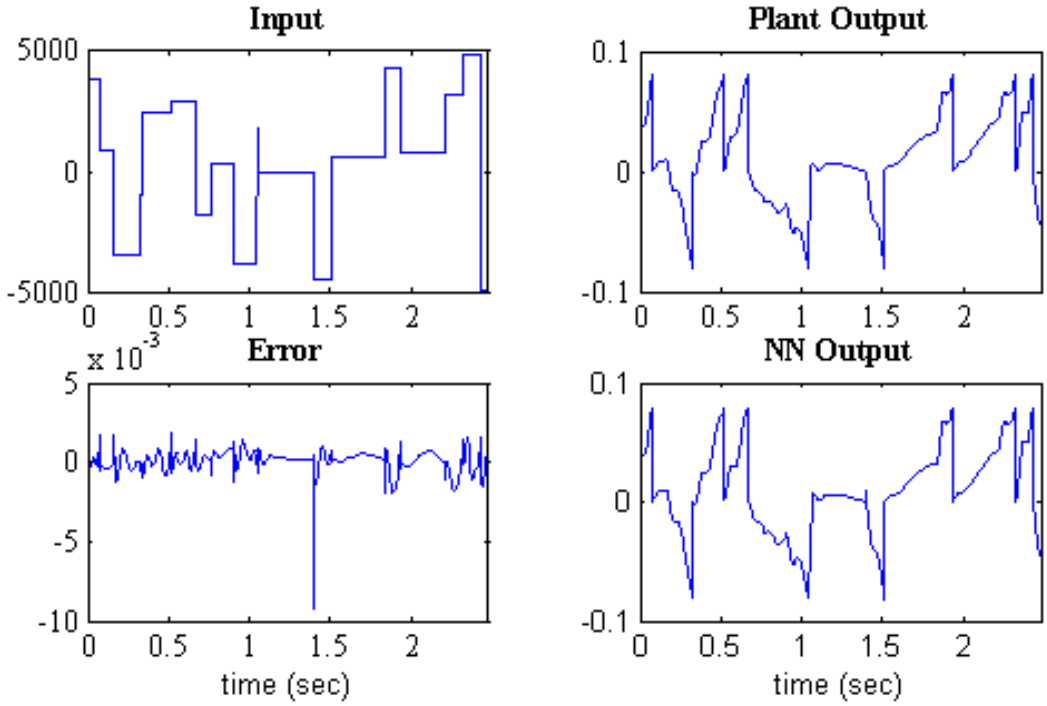

Figure 7.14: Rear suspension NN testing data for NNFBL control.

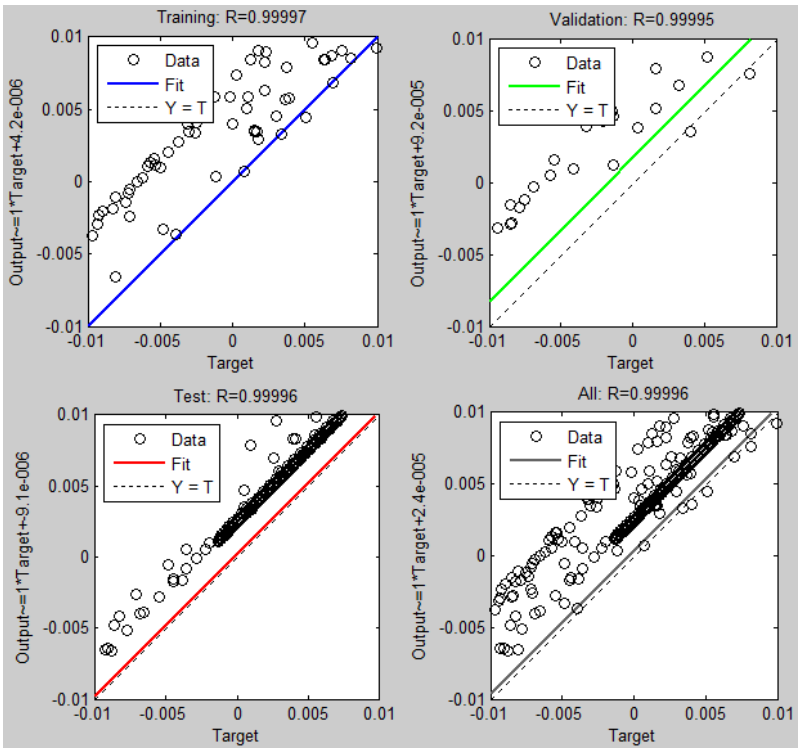

Figure 7.15: Front suspension data regression plot for NNFBL Input-Output (I/O) data.

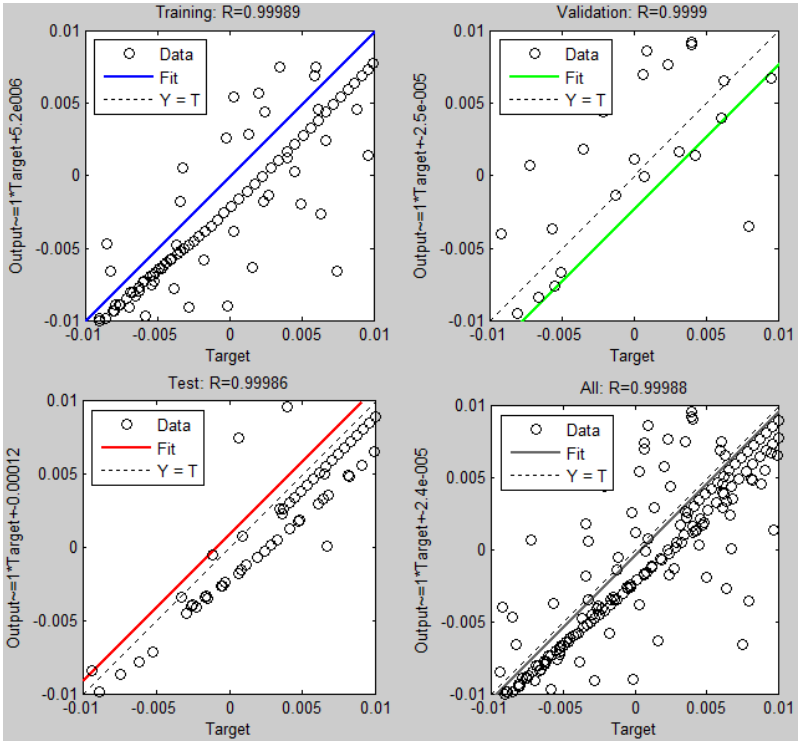

Figure 7.16: Rear suspension data regression plot for NNFBL Input-Output (I/O) data.

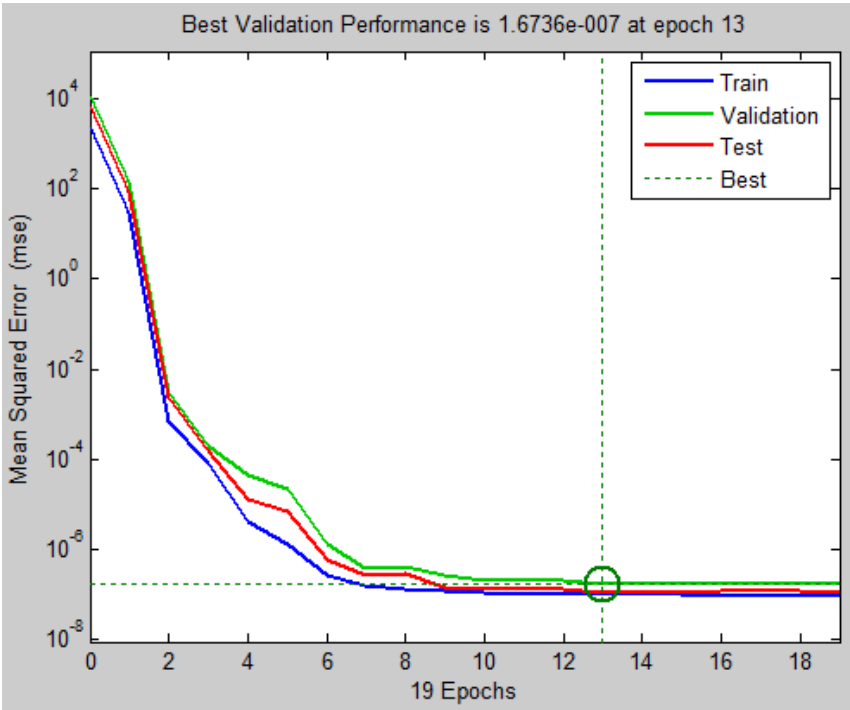

Figure 7.17: Front suspension data MSE plot for NNFBL Input-Output (I/O) data.

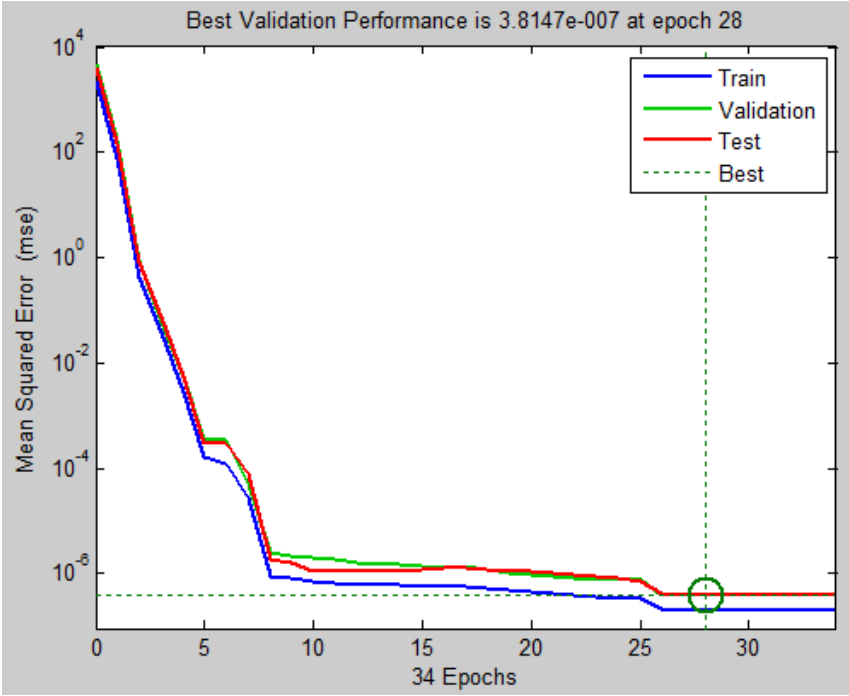

Figure 7.18: Rear suspension data MSE plot for NNFBL Input-Output (I/O) data.

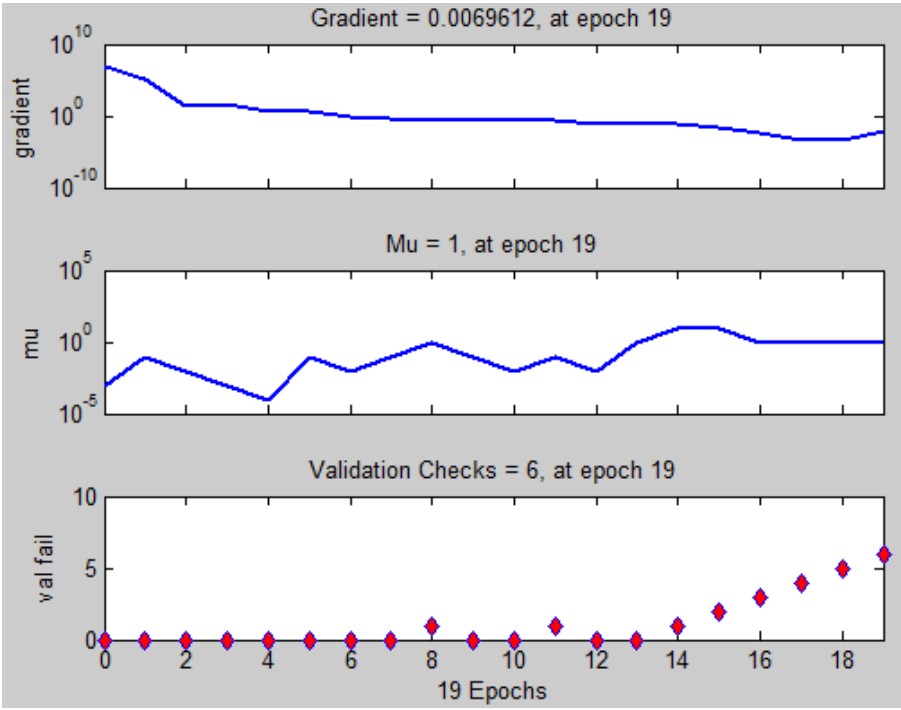

Figure 7.19: Front suspension data training state plot for NNFBL Input-Output (I/O) data.

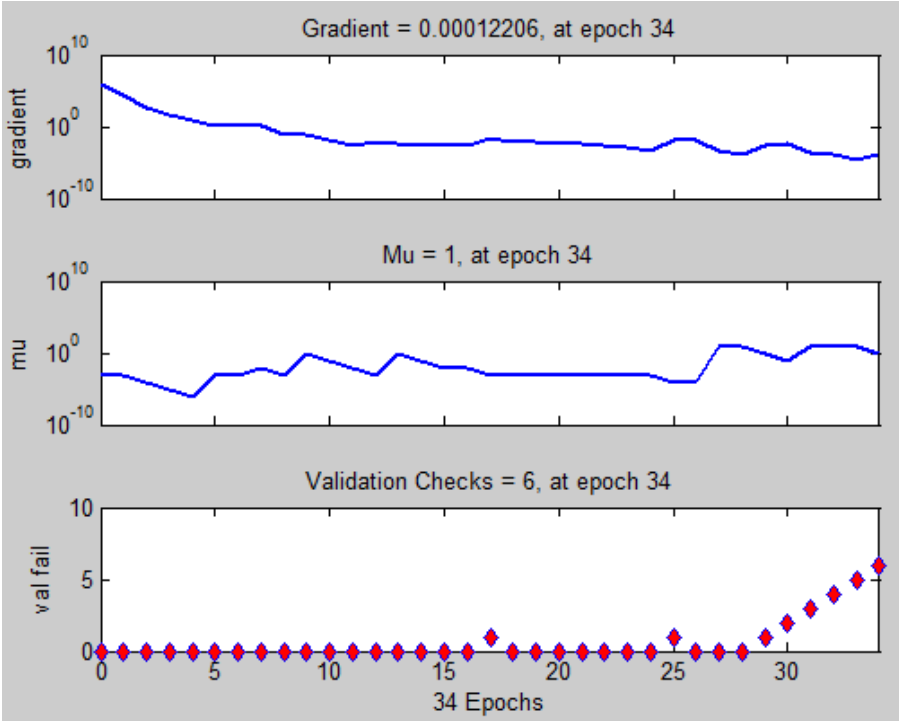

Figure 7.20: Rear suspension data training state plot for NNFBL Input-Output (I/O) data.

The Half-Car Suspension system was set to pass over two different Road Input disturbances for suspension travel regulation ($R_i(t) = 0$). The two input disturbances are listed below:

1. A $0.075m$ amplitude sinusoidal bump on a smooth road (Weber and Braaksma, 2000).
2. A random Class E (Poor) road profile disturbance of road roughness $\mathrm{G}(n_0) = 256 \times 10^{-6}\, m^2/(cycle/m)$ as given in Table 3.2.

To test the controller's robustness to parameter variation, two tests were conducted as the vehicle traversed the road input disturbances:

1. Variation of vehicle forward velocity, V:
   The vehicle forward velocity remains constant through the duration of the simulation, however, different forward velocities are used:
   (a) $V = 45\, km/h$.
   (b) $V = 60\, km/h$.
   (c) $V = 75\, km/h$.

2. Variation of vehicle sprung mass payload, Ms:
   The sprung mass payload Ms was varied $\pm 20\%$ of its nominal value, $Ms = 580\,kg$. Therefore, three values for sprung mass were tested (Du et al., 2008):

   (a) $80\% Ms = 464\,kg$

   (b) $100\% Ms = 580\,kg$

   (c) $120\% Ms = 696\,kg$

   Since the pitch moment of inertia I_θ is related to the vehicle body mass, it is assumed that the pitch moment of inertia also varies by the same amount about its nominal value (Chen et al., 2005)

The likelihood of parameter variation at different speeds motivated observation of the controller performance with sprung mass payload variation at each speed. The simulation results are therefore presented and discussed in that format.

7.3.1 Sinusoidal Bump Input Disturbance

7.3.1.1 System Response at $V = 45\,km/h$

The RMS values obtained as the PVSS and AVSS traversed a sinusoidal bump input disturbance at $V = 45\,km/h$ are given in Table 7.4. Although the AVSS performance is significantly better than that of the PVSS, RMS results for both the front and rear suspension (see Table 7.4), indicate that increase in vehicle sprung mass causes a reduction in AVSS suspension travel performance at $V = 45\,km/h$. The minimum and maximum peak front and rear suspension travel values obtained by the AVSS are also lower that those of the PVSS. Increase in vehicle mass causes the suspension travel workspace to reduce. Figures 7.21 and 7.22 suggest that the AVSS is less likely to hit the suspension travel limits ($\pm 0.08\,m$) than the PVSS as the mass of the vehicle increases.

The front and rear dynamic tyre force is shown in Figures 7.23 and 7.24. The RMS front dynamic tyre force for the AVSS improved with each increase in the sprung mass loading compared with the PVSS, while the rear dynamic tyre force remained roughly 2% worse than the PVSS as shown in Table 7.4. Both the AVSS and PVSS peak values obtained for the front and rear dynamic tyre forces were well below the specified limits (see Chapter 4, Table 4.1).

The AVSS and PVSS sprung mass acceleration are shown in Figure 7.25. Table 7.5

Table 7.4: RMS values for discrete input disturbance with ±20% variation in sprung mass loading about the nominal value, $Ms = 580\,kg$, at $V = 45\,km/h$

Parameters	$80\%Ms = 464\,kg$			$100\%Ms = 580\,kg$			$120\%Ms = 696\,kg$		
	PVSS	AVSS	% Reduction by AVSS	PVSS	AVSS	% Reduction by AVSS	PVSS	AVSS	% Reduction by AVSS
Front Suspension Travel $[m]$	0.0154	0.0092	40.26	0.0186	0.0114	38.71	0.0212	0.0131	38.21
Rear Suspension Travel $[m]$	0.0069	0.0047	31.88	0.0085	0.0059	30.59	0.0099	0.0069	30.30
Front Dynamic Tyre Force $[N]$	481.8700	403.2163	16.32	588.8717	477.3755	18.93	675.2629	531.9246	21.23
Rear Dynamic Tyre Force $[N]$	222.0276	228.1489	-2.76	262.2865	268.3490	-2.31	302.0889	305.2787	-1.06
Sprung Mass Acceleration $[m/s^2]$	1.0753	0.8285	23.20	1.1293	0.8658	23.33	1.1395	0.8673	23.89
Pitch Angular Acceleration $[rad/s^2]$	0.6453	0.6166	4.45	0.5849	0.5559	4.96	0.5231	0.4944	5.49
Front Actuator Control Voltage $[V]$	–	0.2703	–	–	0.3078	–	–	0.3305	–
Rear Actuator Control Voltage $[V]$	–	0.1585	–	–	0.1845	–	–	0.2073	–
Front Spool-Valve Displacement $[m]$	–	2.5352×10^{-4}	–	–	2.9075×10^{-4}	–	–	3.1383×10^{-4}	–
Rear Spool-Valve Displacement $[m]$	–	1.3761×10^{-4}	–	–	1.6414×10^{-4}	–	–	1.8729×10^{-4}	–
Front Actuator Force $[N]$	–	147.6000	–	–	181.9876	–	–	208.3218	–
Rear Actuator Force $[N]$	–	77.9343	–	–	95.7125	–	–	112.3025	–

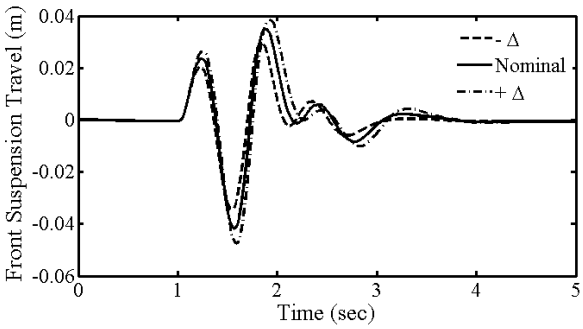

(a) AVSS

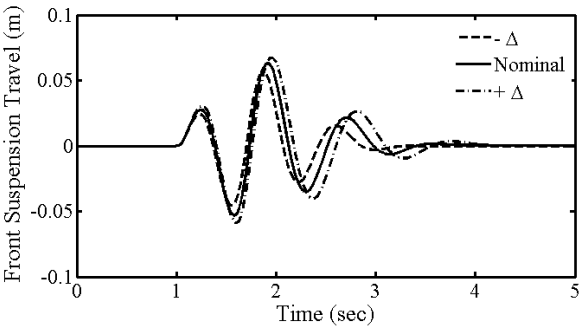

(b) PVSS

Figure 7.21: Front suspension travel for 80%, 100% and 120% Ms at $V = 45\,km/h$.

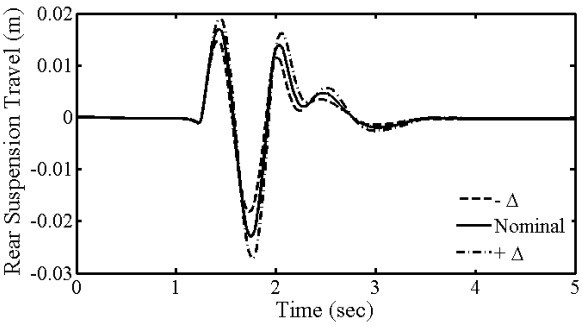

(a) AVSS

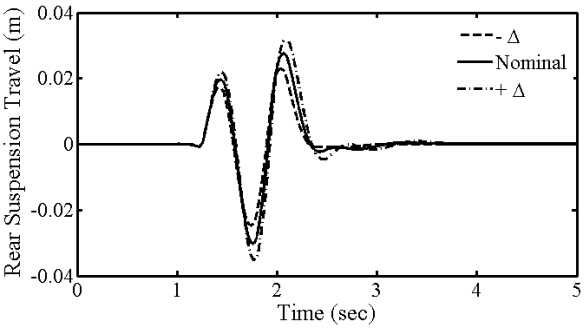

(b) PVSS

Figure 7.22: Rear suspension travel for 80%, 100% and 120% Ms at $V = 45\,km/h$.

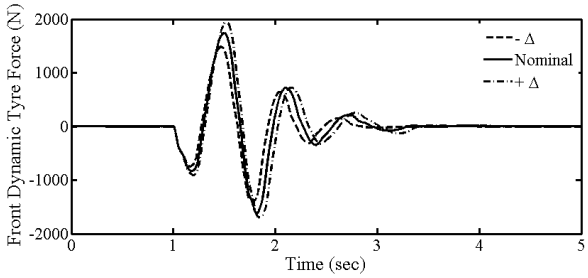

(a) AVSS

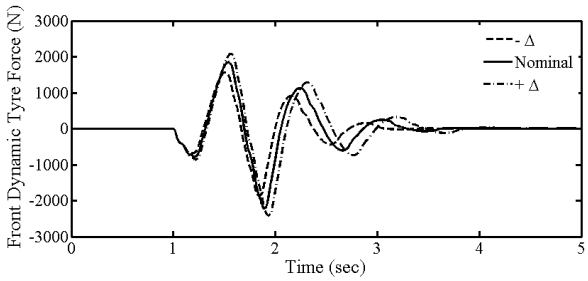

(b) PVSS

Figure 7.23: Front dynamic tyre force for 80%, 100% and 120% Ms at $V = 45\,km/h$.

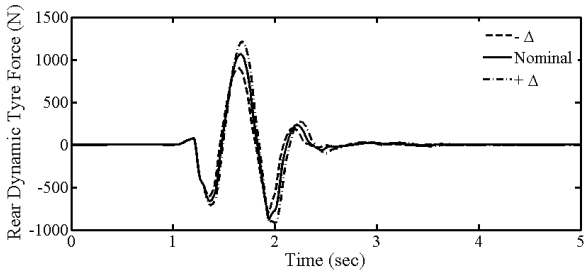

(a) AVSS

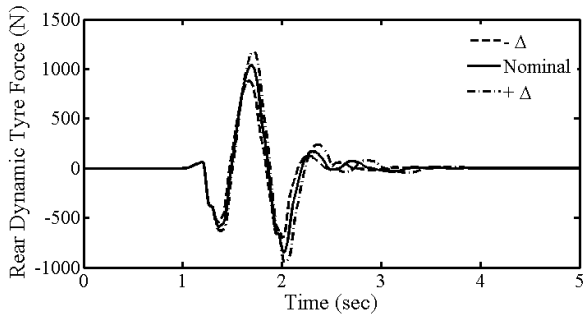

(b) PVSS

Figure 7.24: Rear dynamic tyre force for 80%, 100% and 120% Ms at $V = 45\,km/h$.

shows that although both the AVSS and PVSS maintained a "Not Uncomfortable" level of discomfort throughout, the AVSS performance was $21.45 - 23.18\%$ better than that of the PVSS in terms of ISO 2631-1 weighted RMS acceleration, for all values of Ms tested.

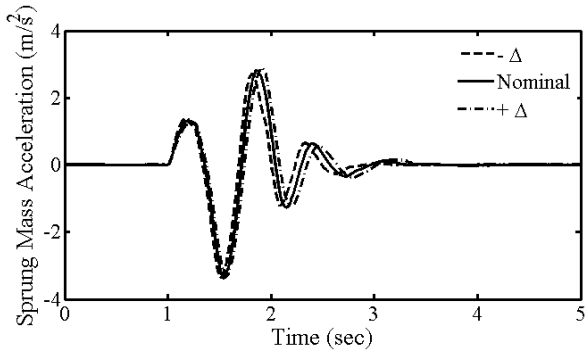

(a) AVSS

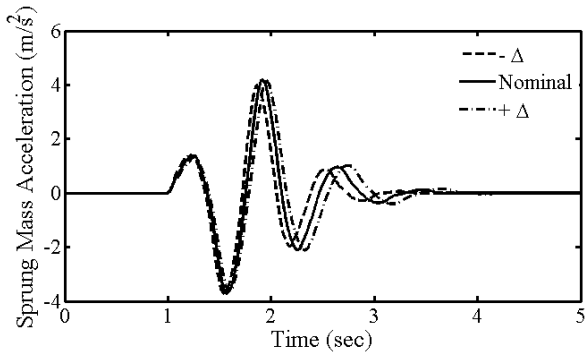

(b) PVSS

Figure 7.25: Sprung mass acceleration for 80%, 100% and 120% Ms at $V = 45\,km/h$.

With regards to pitch angular acceleration, RMS values in Table 7.4 indicate that AVSS performance deteriorated with increase in vehicle mass. The AVSS peak pitch angular acceleration values in Figure 7.26 tend to be higher when compared with the corresponding PVSS values. However, close examination of Figure 7.26 shows that although the AVSS values are higher, the control action of the AVSS dampens the oscillation approximately $0.5\,s$ faster than the PVSS.

Figures 7.27 , 7.28 and 7.29 depict the front and rear actuator control voltage, spool-valve displacement and force for $\pm 20\%$ sprung mass variation at $V = 45\,km/h$. The actuator force increased as the vehicle mass increased from $464\,kg$ to $696\,kg$. This is atributed to the fact that more actuator force is required to overcome the additional sprung mass weight. Thus the required control input voltage and spool-valve displacement increase with vehicle sprung mass. The peak actuator force values, $[-582.4N, 425.0N]$ for the front and $[-330.1N, 218.3N]$ for the rear at $80\% Ms$,

Table 7.5: Weighted RMS acceleration and discomfort levels as PVSS and AVSS traverse a sinusoidal bump input disturbance at $V = 45\,km/h$

	PVSS		AVSS		%
	Weighted RMS Acceleration a_{wi}^{RMS}	ISO 2631-1 Level of Discomfort	Weighted RMS Acceleration a_{wi}^{RMS}	ISO 2631-1 Level of Discomfort	Reduction of a_{wi}^{RMS} by AVSS
80% Ms	0.2117	Not Uncomfortable	0.1663	Not Uncomfortable	21.4454
100% Ms	0.2205	Not Uncomfortable	0.1714	Not Uncomfortable	22.2676
120% Ms	0.2217	Not Uncomfortable	0.1703	Not Uncomfortable	23.1845

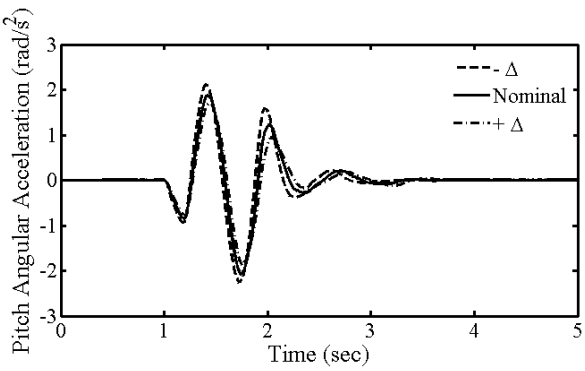

(a) AVSS

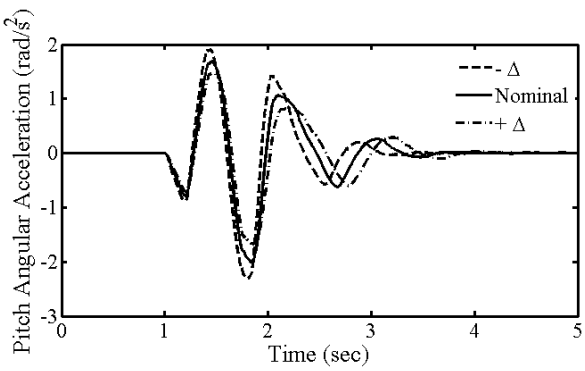

(b) PVSS

Figure 7.26: Pitch angular acceleration for 80%, 100% and 120% Ms at $V = 45\,km/h$.

$[-682.1N, 592.9N]$ for the front and $[-401.2N, 262.3N]$ for the rear at $100\% Ms$ and $[-738.4N, 600.8N]$ for the front and $[-461.6N, 299.6N]$ for the rear at $120\% Ms$, are considerably lower than the specified limits in Chapter 4. The front actuator control voltage remained below the maximum allowable control voltage, ($|u_i| \leq u_{max}$), throught out the simulation. However, the rear actuator voltage spiked to $+10V$ during the first $0.05\,s$ of the simulation. This can be ignored because it did not have any visible effects on both the actuator force and the spool-valve displacement during the same period.

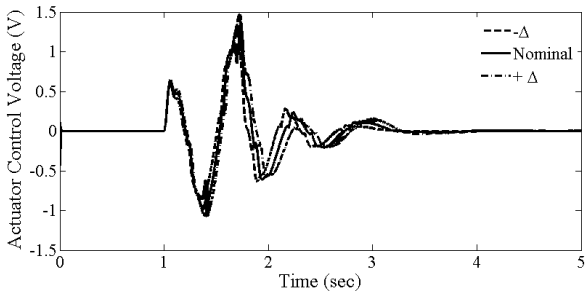

(a) Front suspension

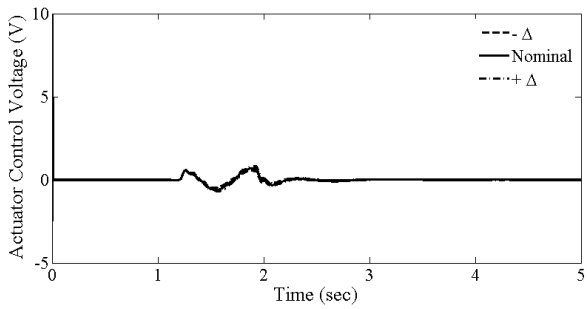

(b) Rear suspension

Figure 7.27: Front and rear actuator control voltage for 80%, 100% and 120% Ms at $V = 45\,km/h$.

7.3.1.2 System Response at $V = 60\,km/h$

The RMS values obtained as the PVSS and AVSS traversed a sinusoidal bump input disturbance at $V = 60\,km/h$ are listed in Table 7.6.

Comparing the front and rear RMS suspension travel values listed in Tables 7.4 and 7.6, there is approximately an 8% reduction in the overall performance of the AVSS front suspension travel and 3% reduction for the rear suspension travel, compared with the corresponding PVSS values. This deterioration of performance is due to increase in vehicle forward velocity, V, from $45\,km/h$ to $60\,km/h$. The peak suspension travel values at $60\,km/h$, show that although both the AVSS and PVSS peaks

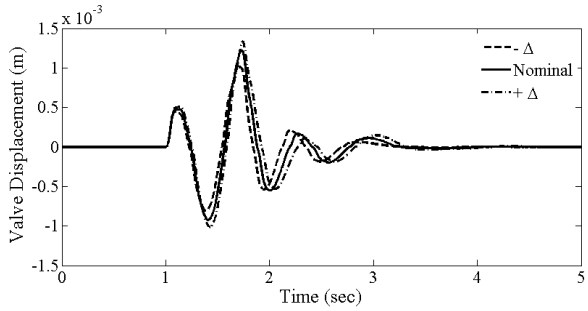

(a) Front suspension

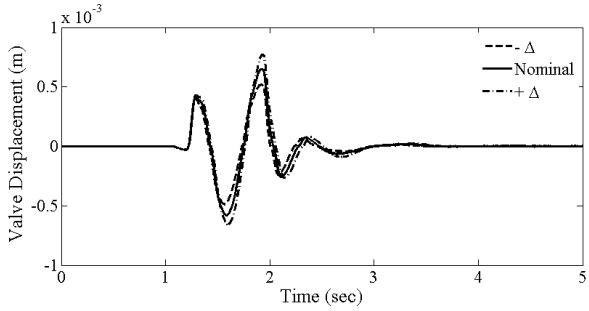

(b) Rear suspension

Figure 7.28: Front and rear actuator spool-valve displacement for 80%, 100% and 120% Ms at $V = 45\,km/h$.

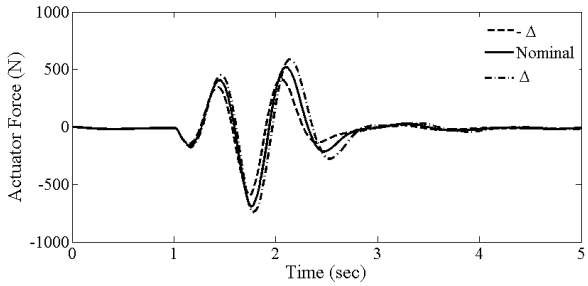

(a) Front suspension

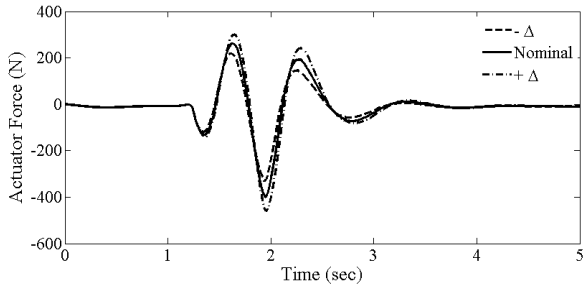

(b) Rear suspension

Figure 7.29: Front and rear actuator force for 80%, 100% and 120% Ms at $V = 45\,km/h$.

Table 7.6: RMS values for discrete input disturbance with ±20% variation in sprung mass loading about the nominal value, $Ms = 580\,kg$, at $V = 60\,km/h$

Parameters	$80\%Ms = 464\,kg$			$100\%Ms = 580\,kg$			$120\%Ms = 696\,kg$		
	PVSS	AVSS	% Reduction by AVSS	PVSS	AVSS	% Reduction by AVSS	PVSS	AVSS	% Reduction by AVSS
Front Suspension Travel $[m]$	0.0177	0.0121	31.64	0.0196	0.0134	31.63	0.0210	0.0144	31.43
Rear Suspension Travel $[m]$	0.0090	0.0065	27.78	0.0107	0.0077	28.04	0.0122	0.0088	27.87
Front Dynamic Tyre Force $[N]$	579.4022	551.2944	4.85	640.9934	601.3988	6.18	678.6571	628.4856	7.39
Rear Dynamic Tyre Force $[N]$	297.4318	321.3982	-8.06	344.9889	369.0825	-6.98	388.1406	409.6739	-5.55
Sprung Mass Acceleration $[m/s^2]$	1.5390	1.3839	10.08	1.4553	1.3134	9.75	1.3521	1.2165	10.03
Pitch Angular Acceleration $[rad/s^2]$	0.6472	0.7181	-10.95	0.5333	0.5984	-12.21	0.4468	0.5087	-13.85
Front Actuator Control Voltage $[V]$	–	0.4238	–	–	0.4342	–	–	0.4335	–
Rear Actuator Control Voltage $[V]$	–	0.2712	–	–	0.3035	–	–	0.3258	–
Front Spool-Valve Displacement $[m]$	–	3.8879×10^{-4}	–	–	4.0177×10^{-4}	–	–	4.0300×10^{-4}	–
Rear Spool-Valve Displacement $[m]$	–	2.3704×10^{-4}	–	–	2.6943×10^{-4}	–	–	2.9218×10^{-4}	–
Front Actuator Force $[N]$	–	183.1388	–	–	209.0919	–	–	226.5828	–
Rear Actuator Force $[N]$	–	98.0662	–	–	118.0903	–	–	136.0921	–

were below the specified limit, the AVSS produced smaller deflections. Figures 7.30 and 7.31 show that increase in vehicle sprung mass had less effect on the control performance of the AVSS than on the PVSS.

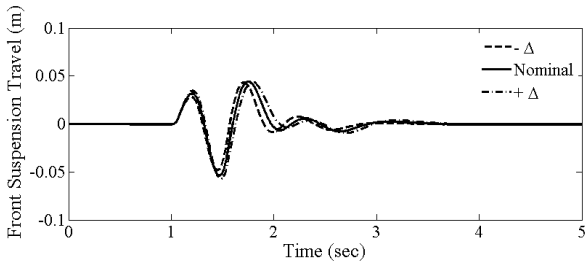

(a) AVSS

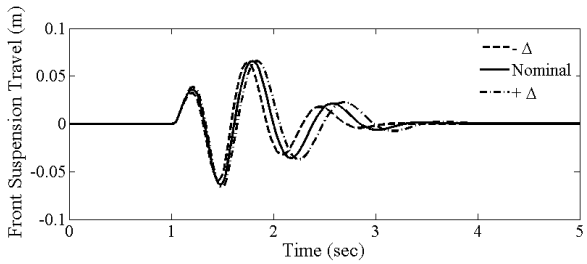

(b) PVSS

Figure 7.30: Front suspension travel for 80%, 100% and 120% Ms at $V = 60\,km/h$.

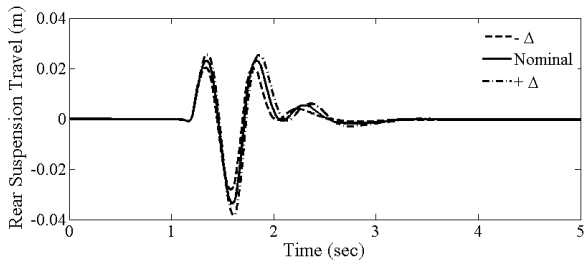

(a) AVSS

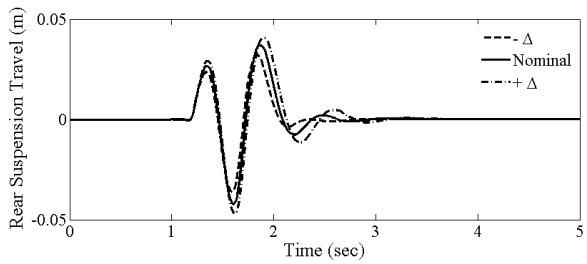

(b) PVSS

Figure 7.31: Rear suspension travel for 80%, 100% and 120% Ms at $V = 60\,km/h$.

The AVSS and PVSS front and rear dynamic tyre force plots as Ms varied by ±20% at $60\,km/h$ are illustrated in Figures 7.23 and 7.24. The figures show that the front

AVSS suspension minimized the dynamic tyre force approximately $0.25\,s$ faster than the PVSS. However, the AVSS front suspension peak dynamic tyre force exceeded the limit for $80\%Ms$ given in Table 4.1 (Chapter 4). Comparing the RMS values obtained at $V = 45\,km/h$ to those obtained at $V = 60\,km/h$, there was a noticeable reduction in overall performance of the AVSS over the PVSS (compare Table 7.4 to 7.6) in terms of dynamic tyre load. In spite of this, the AVSS front suspension dynamic tyre load improved with increase in vehicle mass, from 1.37% to 3.25% to 5.08%, while the rear suspension dynamic load remained relatively steady at approximately -6% worse than the PVSS. The deterioration in performance is linked to the increase in tyre dynamic load due to higher vehicle forward velocity. This increases the likelihood of exceeding the specified limits, which are not dependent on vehicle speed (refer to Equation 4.6).

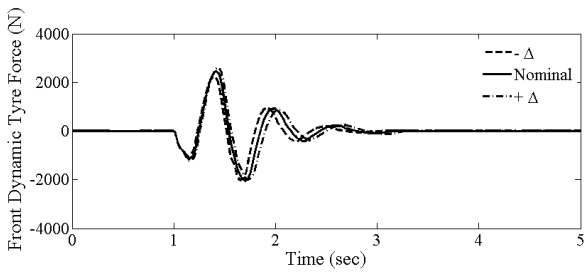

(a) AVSS

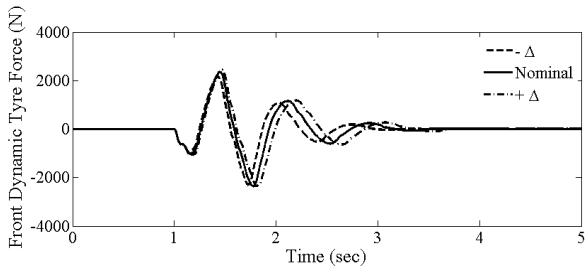

(b) PVSS

Figure 7.32: Front dynamic tyre force for 80%, 100% and 120% Ms at $V = 60\,km/h$.

Figure 7.34 shows the sprung mass acceleration, with accompanying ISO 2631-1 weighted RMS acceleration is given in Table 7.7. The AVSS performance in terms of acceleration reduction was $6.46-7.34\%$ better than that of the PVSS for all values of Ms. Comparing Table 7.5 with 7.7, the AVSS the overall percentage reduction in weighted RMS acceleration reduced by about $14-15\%$ with the increase in velocity from $45\,km/h$ to $60\,km/h$ (compare Table 7.5 with 7.7).

The peak pitch angular accelerations experienced by the AVSS were higher than the PVSS as shown in Figure 7.35. The overall percentage reduction in RMS pitch

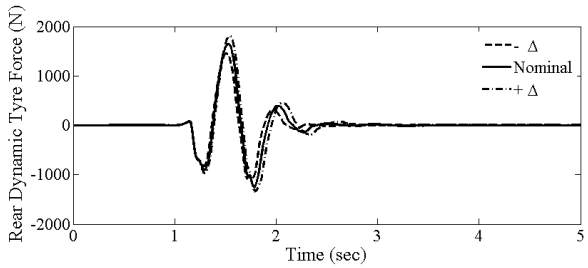

(a) AVSS

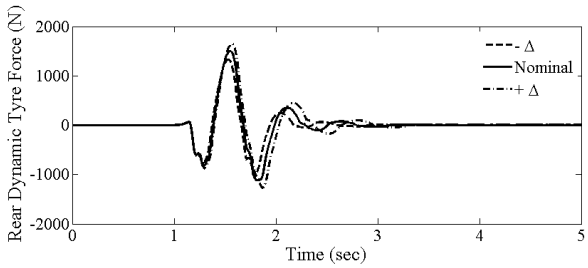

(b) PVSS

Figure 7.33: Rear dynamic tyre force for 80%, 100% and 120% Ms at $V = 60\,km/h$.

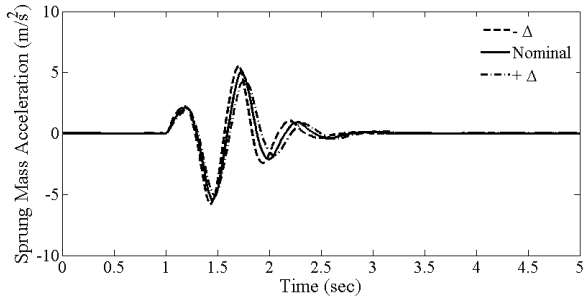

(a) AVSS

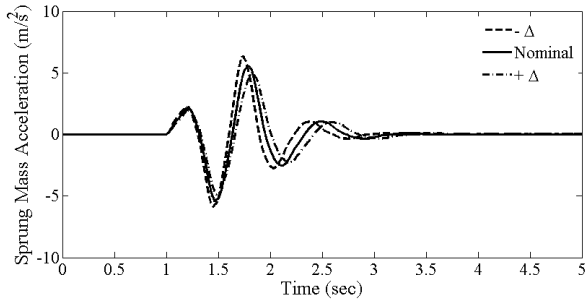

(b) PVSS

Figure 7.34: Sprung mass acceleration for 80%, 100% and 120% Ms at $V = 60\,km/h$.

Table 7.7: Weighted RMS acceleration and discomfort levels as PVSS and AVSS traverse a sinusoidal bump input disturbance at $V = 60\,km/h$

	PVSS		AVSS		%
	Weighted RMS Acceleration a_{wi}^{RMS}	ISO 2631-1 Level of Discomfort	Weighted RMS Acceleration a_{wi}^{RMS}	ISO 2631-1 Level of Discomfort	Reduction of a_{wi}^{RMS} by AVSS
80% Ms	0.3160	A Little Uncomfortable	0.2956	Not Uncomfortable	6.4557
100% Ms	0.2916	Not Uncomfortable	0.2727	Not Uncomfortable	6.4815
120% Ms	0.2671	Not Uncomfortable	0.2475	Not Uncomfortable	7.3381

angular acceleration by the AVSS deteriorated with the increase in velocity from $V = 45\,km/h$ to $V = 60\,km/h$ (compare Table 7.4 to 7.6). In spite of this, the AVSS attenuated the pitch angular acceleration faster than the PVSS.

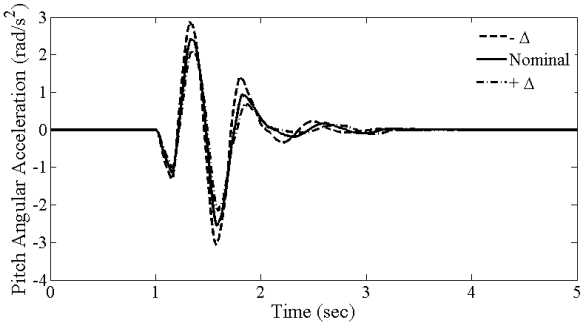

(a) AVSS

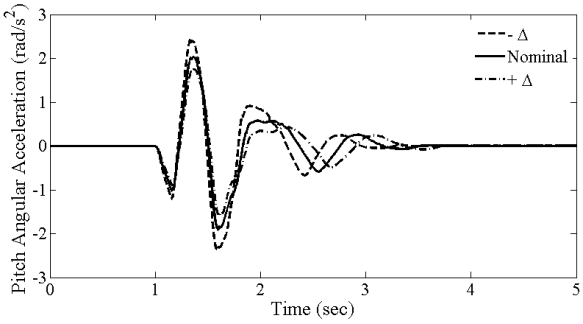

(b) PVSS

Figure 7.35: Pitch angular acceleration for 80%, 100% and 120% Ms at $V = 60\,km/h$.

The front and rear actuator voltages and spool-valve displacements are shown in Figures 7.36 and 7.37, respectively. The front and rear actuator voltages remained lower than the $\pm 10\,V$ limit for all values of Ms.

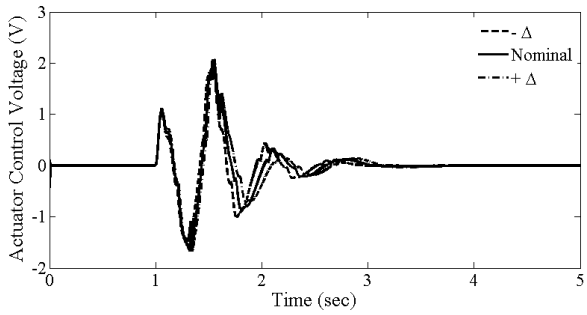

(a) Front suspension

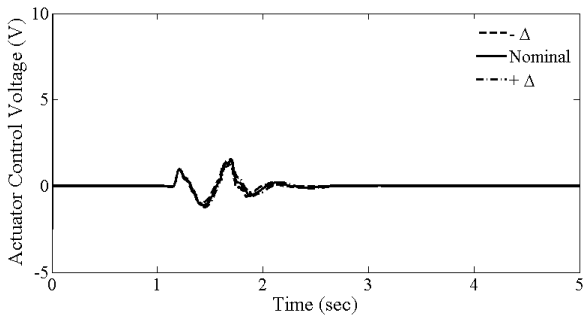

(b) Rear suspension

Figure 7.36: Front and rear actuator control voltage for 80%, 100% and 120% Ms at $V = 60\,km/h$.

The overall actuator force at $V = 60\,km/h$ increased when compared to the force required at $V = 45\,km/h$. This is evident when comparing the RMS and peak forces experienced at $45\,km/h$ (see Figure 7.29) to those experienced at $60\,km/h$ (see Figure 7.38). An increase in force is required to overcome the greater dynamic forces exerted by the road disturbance and vehicle at higher speed. The actuator forces shown in Figure 7.38 remained within the specified limits.

7.3.1.3 System Response at $V = 75\,km/h$

The RMS values obtained as the PVSS and AVSS traversed a sinusoidal bump input disturbance at $V = 75\,km/h$ are listed in Table 7.8. The AVSS front suspension travel RMS remained relatively constant at 23% better than the PVSS, while the AVSS rear suspension travel percentage improvement over the PVSS reduced from

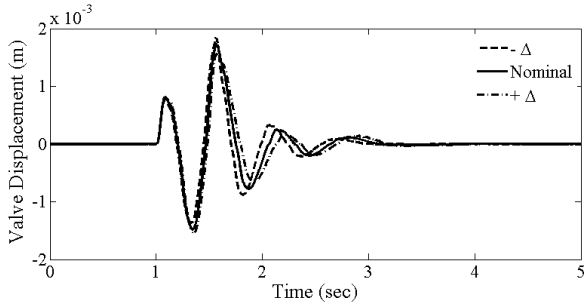

(a) Front suspension

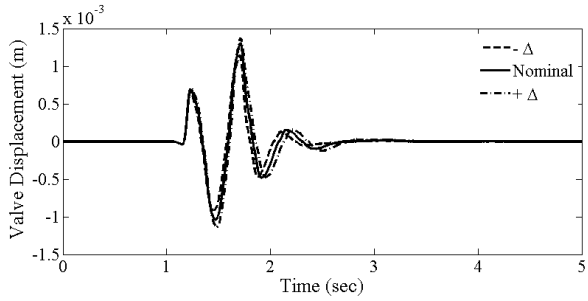

(b) Rear suspension

Figure 7.37: Front and rear actuator spool-valve displacement for 80%, 100% and 120% Ms at $V = 60\,km/h$.

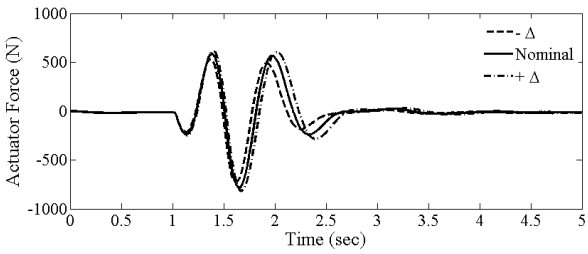

(a) Front suspension

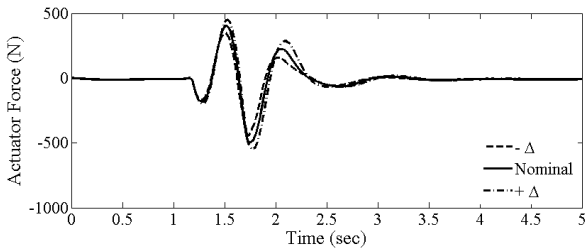

(b) Rear suspension

Figure 7.38: Front and rear actuator force for 80%, 100% and 120% Ms ator $V = 60\,km/h$.

Table 7.8: RMS values for discrete input disturbance with ±20% variation in sprung mass loading about the nominal value, $Ms = 580\,kg$, at $V = 75\,km/h$

Parameters	$80\%Ms = 464\,kg$			$100\%Ms = 580\,kg$			$120\%Ms = 696\,kg$		
	PVSS	AVSS	% Reduction by AVSS	PVSS	AVSS	% Reduction by AVSS	PVSS	AVSS	% Reduction by AVSS
Front Suspension Travel $[m]$	0.0173	0.0130	24.86	0.0183	0.0137	25.14	0.0188	0.0141	25
Rear Suspension Travel $[m]$	0.0104	0.0079	24.04	0.0119	0.0091	23.53	0.0132	0.0100	24.24
Front Dynamic Tyre Force $[N]$	573.9147	605.0656	-5.43	593.7066	624.8438	-5.24	598.9838	628.3077	-4.90
Rear Dynamic Tyre Force $[N]$	355.9515	396.1078	-11.28	396.8327	439.8761	-10.85	428.4287	472.4706	-10.28
Sprung Mass Acceleration $[m/s^2]$	1.7252	1.7303	-0.30	1.5206	1.5356	-0.99	1.3408	1.3565	-1.17
Pitch Angular Acceleration $[rad/s^2]$	0.5890	0.7156	-21.49	0.4736	0.5828	-23.06	0.3969	0.4917	-23.89
Front Actuator Control Voltage $[V]$	–	0.5168	–	–	0.5053	–	–	0.4890	–
Rear Actuator Control Voltage V	–	0.3849	–	–	0.4101	–	–	0.4224	–
Front Spool-Valve Displacement $[m]$	–	4.6235×10^{-4}	–	–	4.5468×10^{-4}	–	–	4.4190×10^{-4}	–
Rear Spool-Valve Displacement $[m]$	–	3.3039×10^{-4}	–	–	3.5622×10^{-4}	–	–	3.6975×10^{-4}	–
Front Actuator Force $[N]$	–	189.9674	–	–	206.6806	–	–	216.7412	–
Rear Actuator Force $[N]$		112.6723	–	–	131.7128	–	–	147.5424	–

23.14% to 21.85% at $V = 75\,km/h$. The AVSS and PVSS suspension travel peak values were lower than the limits. The AVSS minimized suspension deflection faster than the PVSS as visible in Figures 7.39 and 7.40. Comparing the AVSS performance improvement over the PVSS in Tables 7.4, 7.6 and 7.8, show that increase in vehicle speed caused a slight drop in overall RMS suspension travel.

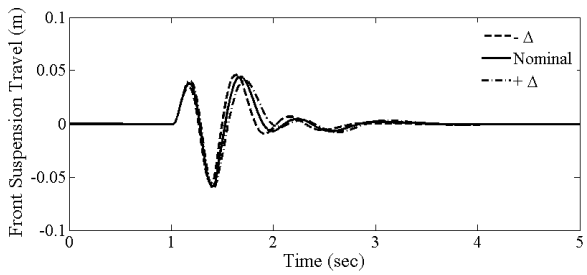

(a) AVSS

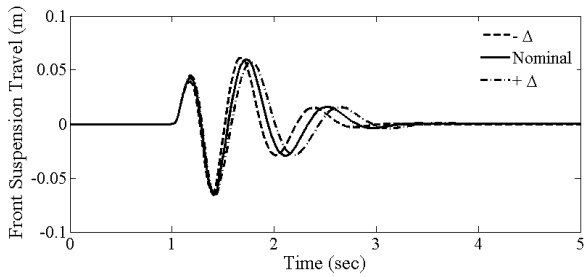

(b) PVSS

Figure 7.39: Front suspension travel for 80%, 100% and 120% Ms at $V = 75\,km/h$.

Both AVSS and PVSS exceeded the maximum allowable front wheel dynamic tyre force for 80%Ms (refer to Figure 7.41). The AVSS exceeded the maximum allowable front wheel dynamic tyre force at 100%Ms (refer to Figure 7.41). The rear AVSS and PVSS dynamic tyre force remained below the specified limits for all values of Ms. Figures 7.41 and 7.42 show that although the peak AVSS dynamic tyre loads are greater than those of the PVSS, the AVSS dampens the forces faster than the PVSS (approximately $0.5\,s$ faster in the front wheel and $0.25\,s$ faster in the rear wheel). Analysis of the RMS performance of the AVSS at $V = 45\,km/h$, $60\,km/h$ and $75\,km/h$ indicates that the AVSS dynamic road holding performance deteriorated with increase in vehicle speed. Increase in sprung mass caused some improvements in the front tyre road holding performance.

The AVSS and PVSS sprung mass acceleration and ISO 2631-1 weighted RMS acceleration are given in Figure 7.43 and Table 7.9, respectively. Table 7.9 shows that the PVSS performance was between 5.74 and 6.41% better than that of the AVSS. The table also shows that both the AVSS and PVSS weighted RMS acceleration reduced

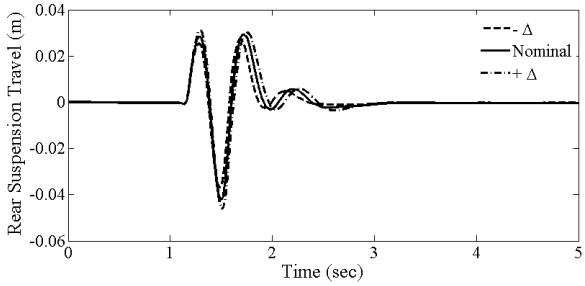

(a) AVSS

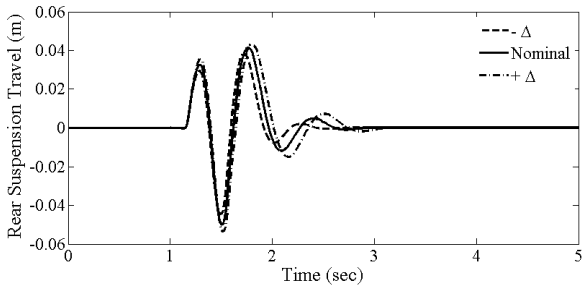

(b) PVSS

Figure 7.40: Rear suspension travel for 80%, 100% and 120% Ms at $V = 75\,km/h$.

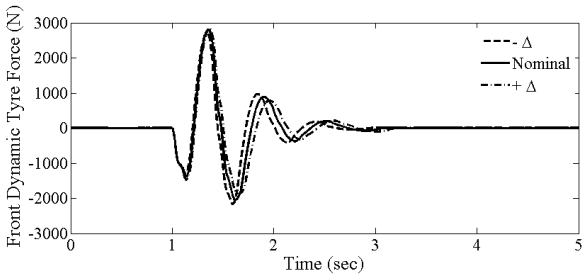

(a) AVSS

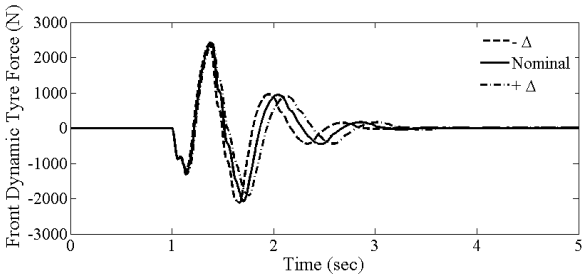

(b) PVSS

Figure 7.41: Front dynamic tyre force for 80%, 100% and 120% Ms at $V = 75\,km/h$.

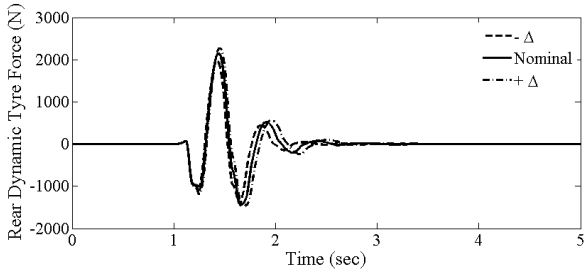

(a) AVSS

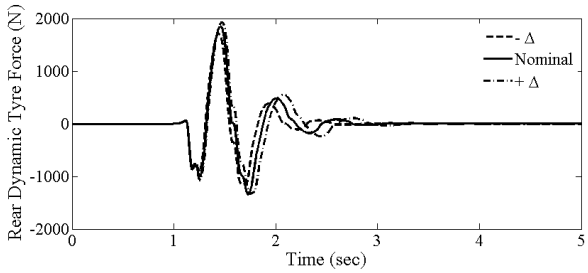

(b) PVSS

Figure 7.42: Rear dynamic tyre force for 80%, 100% and 120% Ms at $V = 75\,km/h$.

with increase in sprung mass loading; beginning at "A Little Uncomfortable" ISO discomfort level at 80%Ms then dropping to "Not Uncomfortable" ISO discomfort level. The overall performance by the AVSS in terms of reducing sprung mass acceleration deteriorated with increase in vehicle speed from $45\,km/h$ to $60\,km/h$ to $75\,km/h$ (see Tables 7.5, 7.7 and 7.9).

Table 7.9: Weighted RMS acceleration and discomfort levels as PVSS and AVSS traverse a sinusoidal bump input disturbance at $V = 75\,km/h$

	PVSS		AVSS		%
	Weighted RMS Acceleration a_{wi}^{RMS}	ISO 2631-1 Level of Discomfort	Weighted RMS Acceleration a_{wi}^{RMS}	ISO 2631-1 Level of Discomfort	Reduction of a_{wi}^{RMS} by AVSS
80% Ms	0.3682	A Little Uncomfortable	0.3918	A Little Uncomfortable	-6.4096
100% Ms	0.3140	Not Uncomfortable	0.3341	A Little Uncomfortable	-6.4013
120% Ms	0.2719	Not Uncomfortable	0.2875	Not Uncomfortable	-5.7374

At $75\,km/h$, the AVSS produces larger peak pitch angular acceleration values when

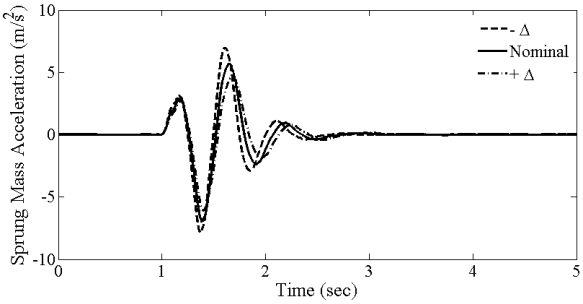

(a) AVSS

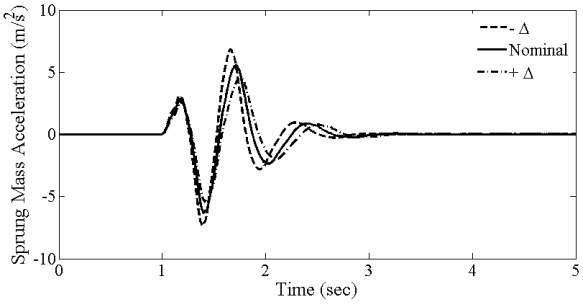

(b) PVSS

Figure 7.43: Sprung mass acceleration for 80%, 100% and 120% Ms at $V = 75\,km/h$.

compared with the PVSS (refer to Figure 7.44). Further examination of Figure 7.44 shows that the AVSS reduced the pitch angular acceleration faster than the PVSS, for all the values of Ms tested. In terms of RMS performance improvement against the PVSS, the AVSS pitch angular acceleration performance dropped from 23% to 25%, against the PVSS. The overall AVSS RMS pitch angular acceleration performances deteriorated with increase in vehicle forward velocity.

Figure 7.45 shows the variation of AVSS front and rear actuator voltage at $V = 75\,km/h$. The minimum and maximum voltages for the front and rear actuators at $75\,km/h$ remained below the $\pm 10\,V$ limit. Voltage required increased with the velocity (from $45\,km/h$ to $75\,km/h$) as well as increasing with vehicle mass ($\pm 20\% Ms$). The spool-valve displacement obtained at $V = 75\,km/h$ is displayed in Figure 7.46. spool-valve displacement also increased with vehicle mass as well as velocity. The AVSS required the greater force at $V = 75\,km/h$ compared with $V = 45\,km/h$ and $V = 60\,km/h$. The peak front and rear actuator forces were lower than the specified limits. The front and rear AVSS forces are shown in Figure 7.47.

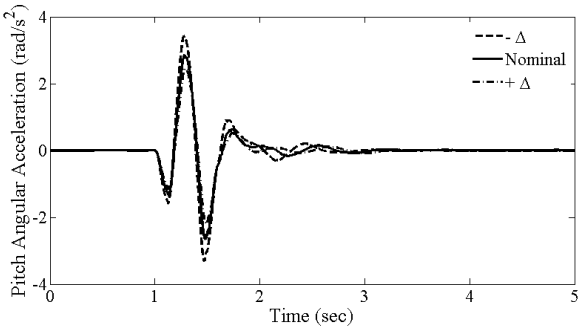

(a) AVSS

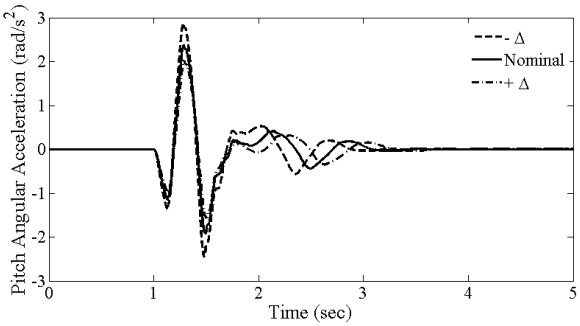

(b) PVSS

Figure 7.44: Pitch angular acceleration for 80%, 100% and 120% Ms at $V = 75\,km/h$.

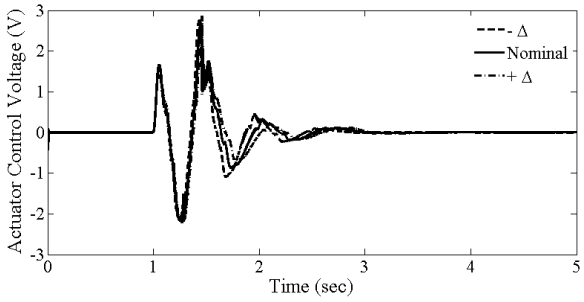

(a) Front suspension

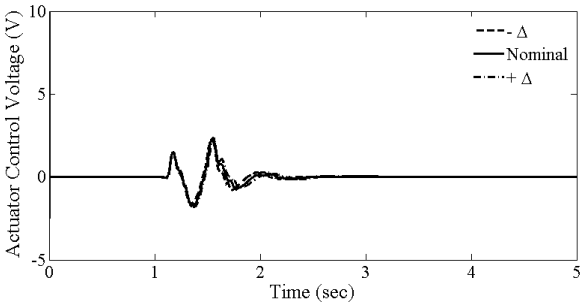

(b) Rear suspension

Figure 7.45: Front and rear actuator control voltage for 80%, 100% and 120% Ms at $V = 75\,km/h$.

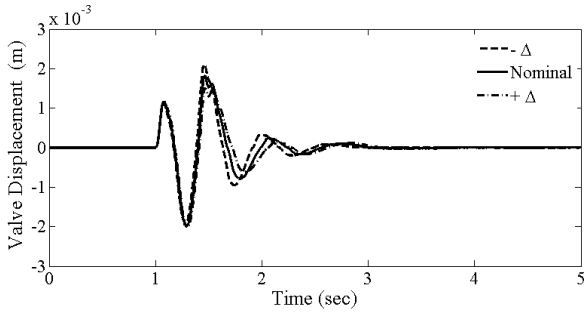

(a) Front suspension

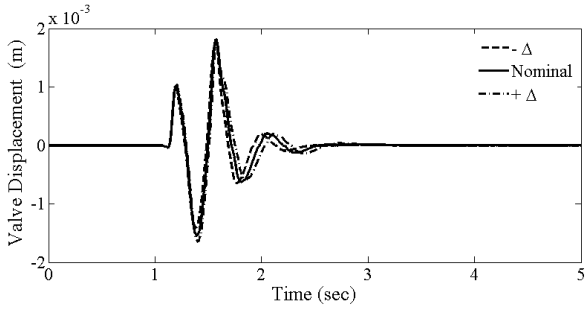

(b) Rear suspension

Figure 7.46: Front and rear actuator spool-valve displacement for 80%, 100% and 120% Ms at $V = 75\,km/h$.

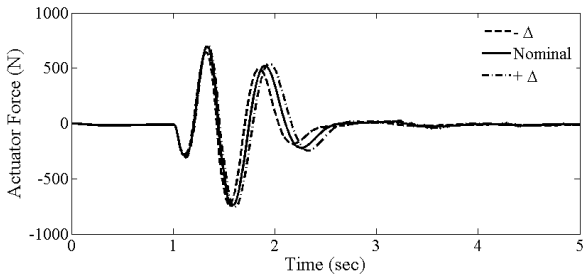

(a) Front suspension

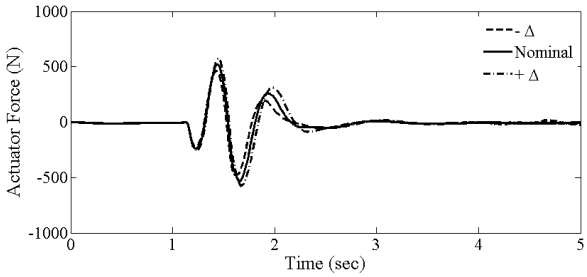

(b) Rear suspension

Figure 7.47: Front and rear actuator force for 80%, 100% and 120% Ms at $V = 75\,km/h$.

7.3.2 Random Input Disturbance

7.3.2.1 System Response at $V = 45\,km/h$

The RMS values obtained as the PVSS and AVSS traversed a random road input disturbance at $V = 45\,km/h$ are given in Table 7.10. RMS front suspension travel given in Table 7.10, indicate that the percentage reduction in front suspension travel by the AVSS improved as the sprung mass increased from $464\,kg$ to $696\,kg$, compared with the PVSS. The AVSS rear suspension travel improvement over the PVSS fluctuated between 15.38% at 80%Ms and 14.29% at 120%Ms. The front and rear suspension travel are shown in Figures 7.48 and 7.49, respectively. Both the AVSS and PVSS suspension travel remained below the specified limits at the peaks.

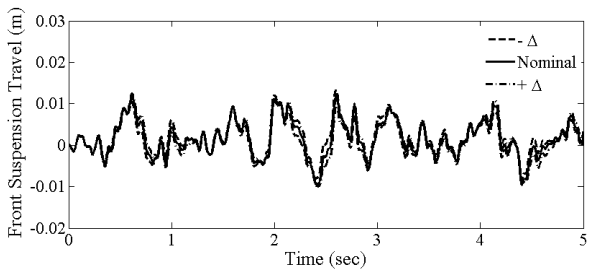

(a) AVSS

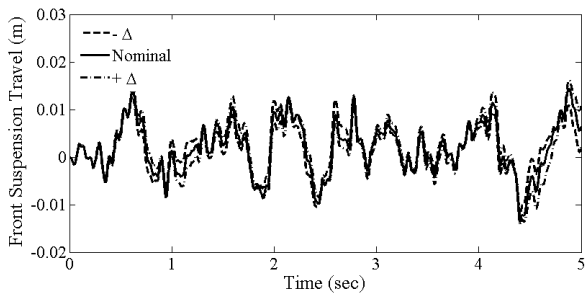

(b) PVSS

Figure 7.48: Front suspension travel for 80%, 100% and 120% Ms at $V = 45\,km/h$.

The dynamic tyre forces for the front and rear suspension are shown in Figures 7.50 and 7.51. The peak dynamic tyre forces for both the AVSS and PVSS remained below the specified limits in Chapter 4. The front AVSS dynamic tyre force percentage reduction improved with increase in sprung mass, from 0.98% at 80%Ms to 3.37% at 120%Ms, whereas the rear AVSS dynamic tyre force percentage reduction improved but remained just under 1%.

Figure 7.52 and Table 7.11 give the sprung mass acceleration and ISO 2631-1

Table 7.10: RMS values for random input disturbance with ±20% variation in sprung mass loading about the nominal value, $Ms = 580\,kg$, at $V = 45\,km/h$

Parameters	$80\%Ms = 464\,kg$			$100\%Ms = 580\,kg$			$120\%Ms = 696\,kg$		
	PVSS	AVSS	% Reduction by AVSS	PVSS	AVSS	% Reduction by AVSS	PVSS	AVSS	% Reduction by AVSS
Front Suspension Travel $[m]$	0.0053	0.0044	16.98	0.0058	0.0046	20.69	0.0062	0.0047	24.19
Rear Suspension Travel $[m]$	0.0039	0.0033	15.38	0.0041	0.0035	14.63	0.0042	0.0036	14.29
Front Dynamic Tyre Force $[N]$	371.2132	368.1687	0.82	373.9010	365.9484	2.13	377.7547	364.5020	3.51
Rear Dynamic Tyre Force $[N]$	355.5504	353.8113	0.49	352.3982	350.2616	0.61	350.7665	348.0230	0.78
Sprung Mass Acceleration $[m/s^2]$	0.6619	0.7333	-10.79	0.5466	0.5959	-9.02	0.4732	0.5029	-6.28
Pitch Angular Acceleration $[rad/s^2]$	0.4625	0.5410	-16.97	0.3714	0.4349	-17.10	0.3088	0.3628	-17.49
Front Actuator Control Voltage $[V]$	–	0.7714	–	–	0.7699	–	–	0.7782	–
Rear Actuator Control Voltage $[V]$	–	0.7319	–	–	0.7304	–	–	0.7292	–
Front Spool-Valve Displacement $[m]$	–	3.1602×10^{-4}	–	–	3.1357×10^{-4}	–	–	3.1131×10^{-4}	–
Rear Spool-Valve Displacement $[m]$	–	2.9693×10^{-4}	–	–	2.9593×10^{-4}	–	–	2.9485×10^{-4}	–
Front Actuator Force $[N]$	–	66.6235	–	–	69.8425	–	–	72.5576	–
Rear Actuator Force $[N]$	–	53.0996	–	–	55.8901	–	–	57.9989	–

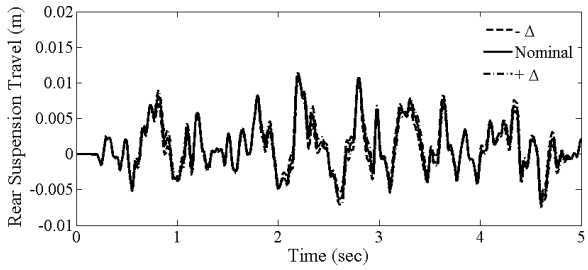

(a) AVSS

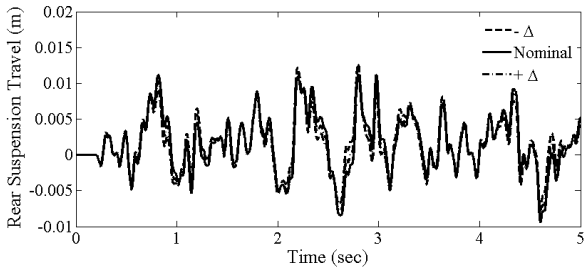

(b) PVSS

Figure 7.49: Rear suspension travel for 80%, 100% and 120% Ms at $V = 45\,km/h$.

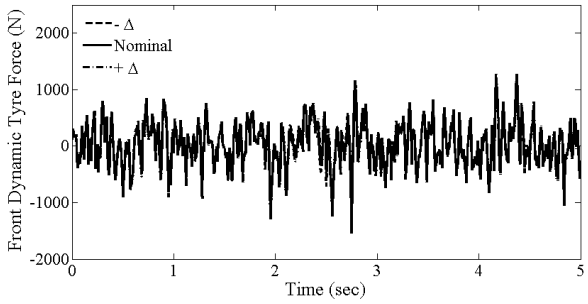

(a) AVSS

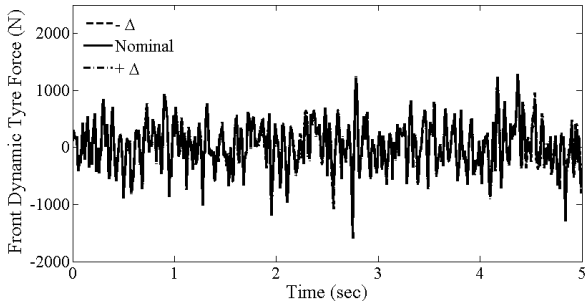

(b) PVSS

Figure 7.50: Front dynamic tyre force for 80%, 100% and 120% Ms at $V = 45\,km/h$.

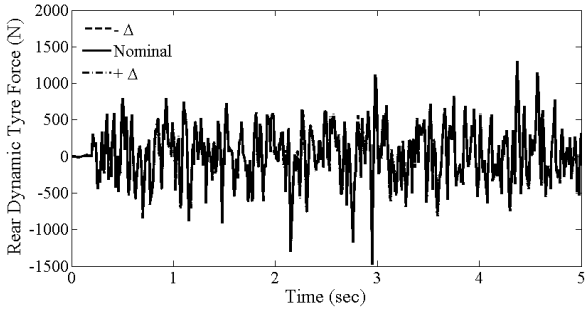

(a) AVSS

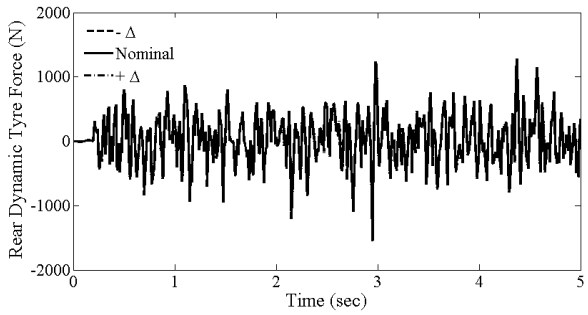

(b) PVSS

Figure 7.51: Rear dynamic tyre force for 80%, 100% and 120% Ms at $V = 45\,km/h$.

weighted RMS acceleration obtained at at $V = 45\,km/h$, respectively. The AVSS weighted RMS was between 10.66 and 12.54% higher than that of the PVSS. Both the AVSS and PVSS weighted RMS acceleration remained at a "Not Uncomfortable" level of discomfort as the sprung mass loading was increased.

Table 7.11: Weighted RMS acceleration and discomfort levels as PVSS and AVSS traversed a random road input disturbance at $V = 45\,km/h$

	PVSS		AVSS		%
	Weighted RMS Acceleration a_{wi}^{RMS}	ISO 2631-1 Level of Discomfort	Weighted RMS Acceleration a_{wi}^{RMS}	ISO 2631-1 Level of Discomfort	Reduction of a_{wi}^{RMS} by AVSS
80% Ms	0.2296	Not Uncomfortable	0.2585	Not Uncomfortable	-12.5871
100% Ms	0.1834	Not Uncomfortable	0.2053	Not Uncomfortable	-11.9411
120% Ms	0.1538	Not Uncomfortable	0.1702	Not Uncomfortable	-10.6632

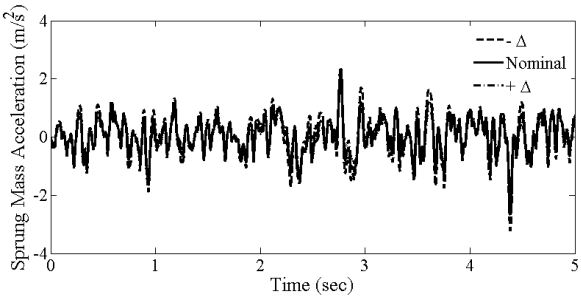

(a) AVSS

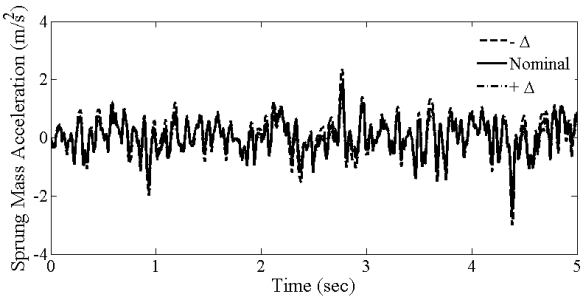

(b) PVSS

Figure 7.52: Sprung mass acceleration for 80%, 100% and 120% Ms at $V = 45\,km/h$.

The pitch angular acceleration is shown in Figure 7.53. The AVSS RMS pitch angular acceleration was worse than the PVSS RMS pitch angular acceleration by 16.76% at the minimum sprung mass load and 17.31% at the maximum sprung mass load. The peak pitch angular acceleration values for the AVSS were also higher than those of the PVSS.

Figures 7.54 and 7.55 show the front and rear actuator voltages and spool-valve displacement respectively. The front and rear actuator control voltages were lower than the specified limit.

The front and rear actuator forces are shown in Figure 7.56. The front and rear actuator forces increased to compensate for the increase in sprung mass. This is shown by the increase in RMS front and rear actuator forces in Table 7.10. The peak actuator forces were well within the limits specified in Chapter 4. Examining the magnitudes of the RMS actuator forces experienced for the sinusoidal bump and random input disturbances shows that the required actuator force reduces with input disturbance amplitude.

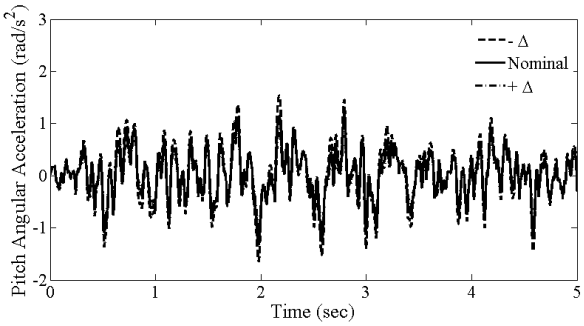

(a) AVSS

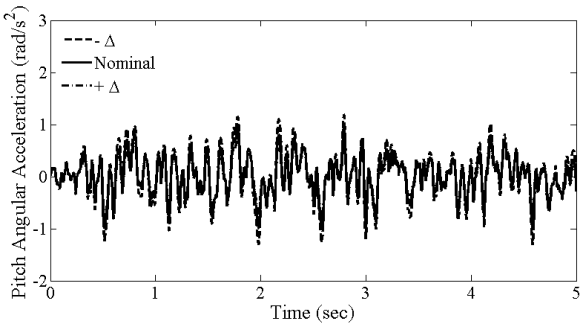

(b) PVSS

Figure 7.53: Pitch angular acceleration for 80%, 100% and 120% Ms at $V = 45\,km/h$.

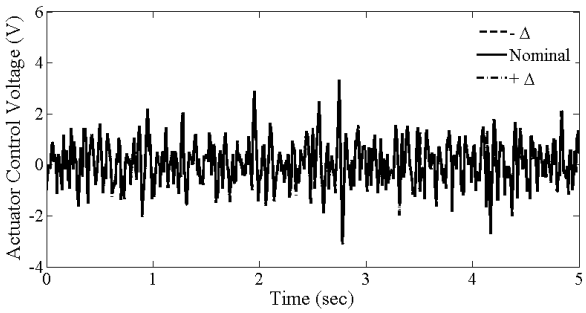

(a) Front suspension

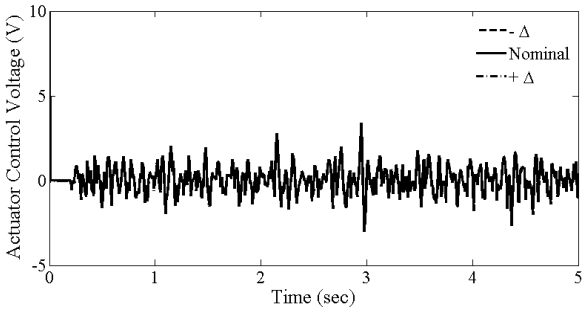

(b) Rear suspension

Figure 7.54: Front and rear actuator control voltage for 80%, 100% and 120% Ms at $V = 45\,km/h$.

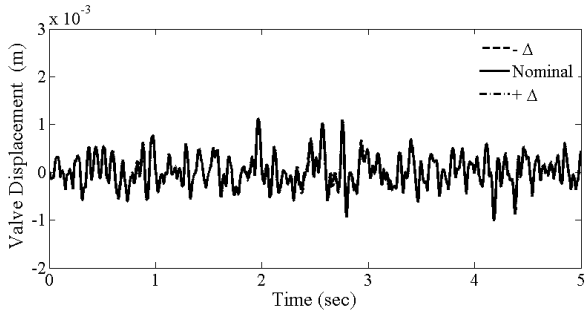

(a) Front suspension

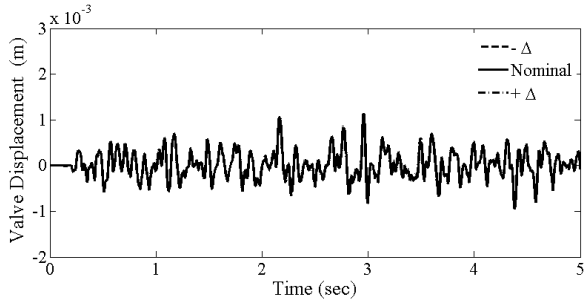

(b) Rear suspension

Figure 7.55: Front and rear actuator spool-valve displacement for 80%, 100% and 120% Ms at $V = 45\,km/h$.

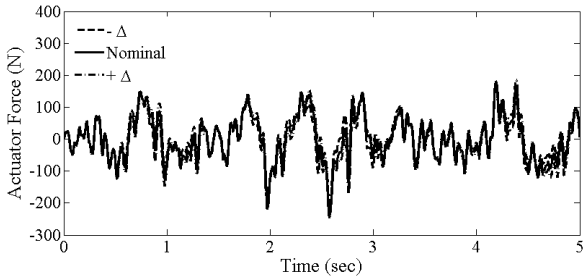

(a) Front suspension

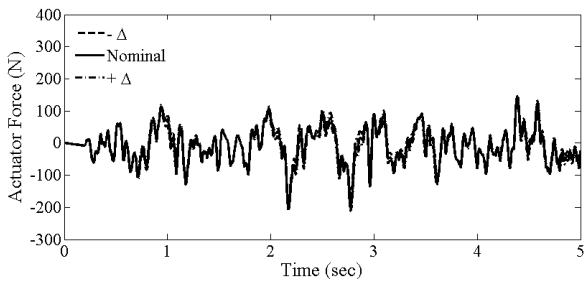

(b) Rear suspension

Figure 7.56: Front and rear actuator force for 80%, 100% and 120% Ms at $V = 45\,km/h$.

7.3.2.2 System Response at $V = 60\,km/h$

The RMS values obtained as the PVSS and AVSS traversed a random road input disturbance at $V = 60\,km/h$ are given in Table 7.12. The front and rear suspension travel are shown in Figures 7.57 and 7.58. The minimum and maximum suspension travel obtained for the AVSS and PVSS were below the specified $\pm 0.08\,m$ limit. Compared to the response to the random road disturbance at $V = 45\,km/h$, the percentage reduction in RMS front suspension travel by the AVSS at $60\,km/h$ dropped; ranging between 17.31% and 24.19% at $45\,km/h$ compared with 16.36% and 20.97% at $60\,km/h$. The percentage reduction in RMS by the AVSS at the rear suspension improved with increase in vehicle speed; from ranging between 15.38% and 14.29% at $45\,km/h$ compared with 16.67% and 17.39% at $60\,km/h$ (compare Table 7.10 to Table 7.12).

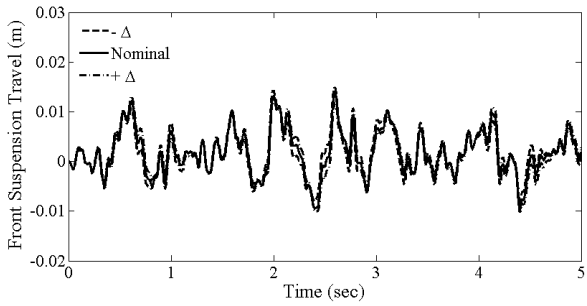

(a) AVSS

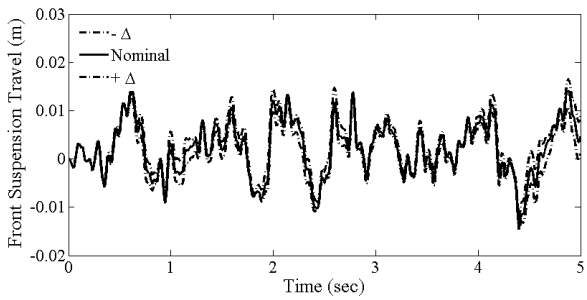

(b) PVSS

Figure 7.57: Front suspension travel for 80%, 100% and 120% Ms at $V = 60\,km/h$.

The overall dynamic tyre forces increased with vehicle speed, this is noticeable when comparing the minimum and maximum peak values obtained at $45\,km/h$ to those at $60\,km/h$ (compare the RMS dynamic tyre forces in Table 7.10 with the RMS dynamic tyre forces Table 7.12). This is due to higher dynamic forces exerted by the road and the vehicle at higher speed. The front and rear dynamic tyre forces are shown in Figures 7.59 and 7.60, respectively. The peak dynamic tyre forces for both the AVSS and PVSS were lower than the limits specified in Table 4.1, Chapter

Table 7.12: RMS values for random input disturbance with ±20% variation in sprung mass loading about the nominal value, $Ms = 580\,kg$, at $V = 60\,km/h$

Parameters	$80\%Ms = 464\,kg$			$100\%Ms = 580\,kg$			$120\%Ms = 696\,kg$		
	PVSS	AVSS	% Reduction by AVSS	PVSS	AVSS	% Reduction by AVSS	PVSS	AVSS	% Reduction by AVSS
Front Suspension Travel $[m]$	0.0056	0.0047	16.07	0.0059	0.0048	18.64	0.0063	0.0049	22.22
Rear Suspension Travel $[m]$	0.0042	0.0035	16.67	0.0044	0.0037	15.91	0.0046	0.0039	15.23
Front Dynamic Tyre Force $[N]$	422.4601	415.1180	1.74	423.2846	411.9475	2.68	425.4429	409.4946	3.75
Rear Dynamic Tyre Force $[N]$	408.6404	401.6217	1.72	405.6346	398.1854	1.84	404.5175	395.8939	2.13
Sprung Mass Acceleration $[m/s^2]$	0.7692	0.8693	-13.01	0.6311	0.7082	-12.22	0.5410	0.5958	-10.13
Pitch Angular Acceleration $[rad/s^2]$	0.4807	0.5517	-14.7	0.3837	0.4404	-14.78	0.3184	0.3668	-15.20
Front Actuator Control Voltage $[V]$	–	0.8978	–	–	0.8968	–	–	0.8952	–
Rear Actuator Control Voltage $[V]$	–	0.8581	–	–	0.8571	–	–	0.8559	–
Front Spool-Valve Displacement $[m]$	–	3.6153×10^{-4}	–	–	3.5894×10^{-4}	–	–	3.5626×10^{-4}	–
Rear Spool-Valve Displacement $[m]$	–	3.4067×10^{-4}	–	–	3.3983×10^{-4}	–	–	3.3890×10^{-4}	–
Front Actuator Force $[N]$	–	71.5819	–	–	74.2045	–	–	76.2000	–
Rear Actuator Force $[N]$	–	56.6766	–	–	59.7867	–	–	62.1547	–

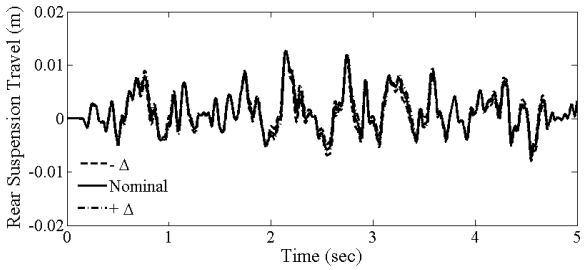

(a) AVSS

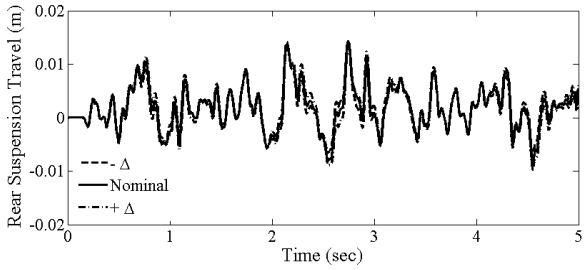

(b) PVSS

Figure 7.58: Rear suspension travel for 80%, 100% and 120% Ms at $V = 60\,km/h$.

4. Further examination of Figures 7.59 and 7.60 show that the peak dynamic tyre forces for the AVSS tend to be lower than those of the PVSS.

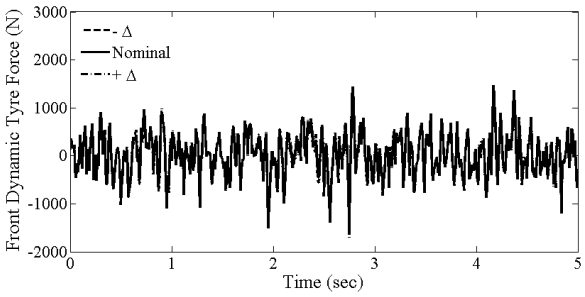

(a) AVSS

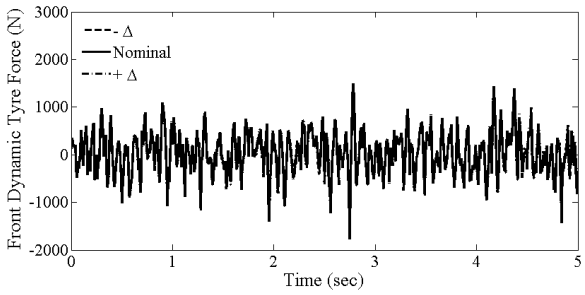

(b) PVSS

Figure 7.59: Front dynamic tyre force for 80%, 100% and 120% Ms at $V = 60\,km/h$.

Figure 7.61 shows the vehicle sprung mass acceleration, while Table 7.7 gives the

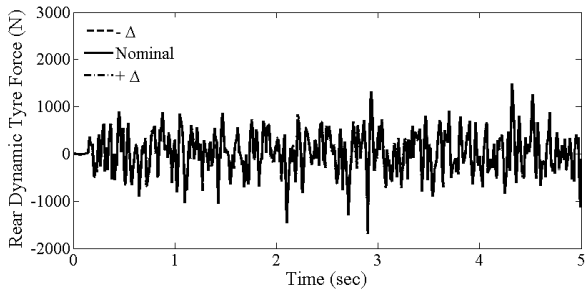

(a) AVSS

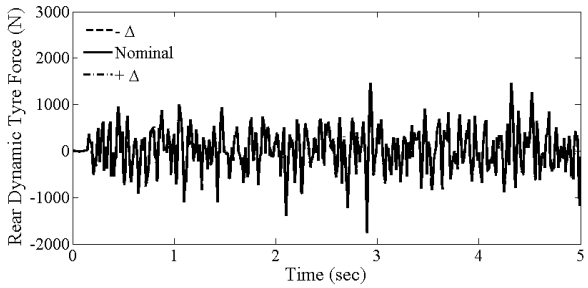

(b) PVSS

Figure 7.60: Rear dynamic tyre force for 80%, 100% and 120% Ms at $V = 60\,km/h$.

ISO 2631-1 weighted RMS acceleration. Both the AVSS and PVSS weighted RMS values fell within range of the "Not Uncomfortable" discomfort level, however, the AVSS values were between 12.80 and 14.25% higher than those of the PVSS for all values of Ms) tested (see Table 7.7). Compared with the performance at $45\,km/h$, there was an approximate 2% drop in the overall AVSS performance at $60\,km/h$ (compare Table 7.11 with 7.13).

Table 7.13: Weighted RMS acceleration and discomfort levels as PVSS and AVSS traversed a random road input disturbance at $V = 60\,km/h$

	PVSS		AVSS		%
	Weighted RMS Acceleration a_{wi}^{RMS}	ISO 2631-1 Level of Discomfort	Weighted RMS Acceleration a_{wi}^{RMS}	ISO 2631-1 Level of Discomfort	Reduction of a_{wi}^{RMS} by AVSS
80% Ms	0.2667	Not Uncomfortable	0.3047	Not Uncomfortable	-14.2482
100% Ms	0.2131	Not Uncomfortable	0.2424	Not Uncomfortable	-13.7494
120% Ms	0.1781	Not Uncomfortable	0.2009	Not Uncomfortable	-12.8018

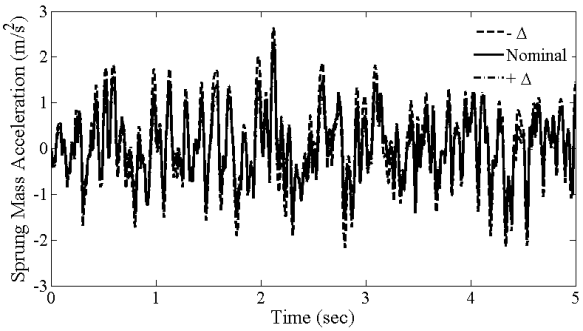

(a) AVSS

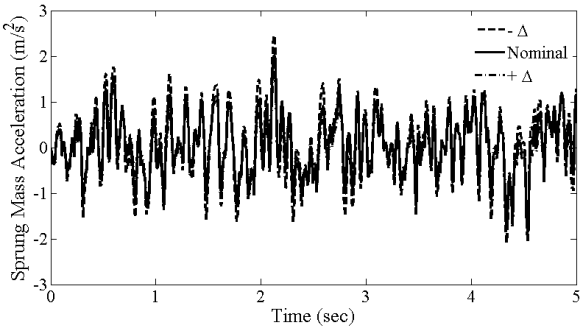

(b) PVSS

Figure 7.61: Sprung mass acceleration for 80%, 100% and 120% Ms at $V = 60\,km/h$.

Figure 7.62 shows the AVSS and PVSS pitch angular acceleration. Though poorer than the PVSS, the overall percentage reduction in RMS pitch angular acceleration by the AVSS improved from between -16.76% and -17.31% at $V = 45\,km/h$ to -14.65% and -15.07% at $V = 60\,km/h$. The peak AVSS pitch angular acceleration values tend to be higher than PVSS.

The actuator voltages and spool-valve displacements are shown in Figures 7.63 and 7.64, respectively. The front and rear actuator voltages remained within the specified limits, for all values of Ms tested. The overall actuator voltages and spool-valve displacements increased with increase in vehicle velocity.

The front and rear actuator forces are shown in Figure 7.65. The peak forces obtained remained within the specified limits for all values of Ms. The RMS actuator forces increased with increase in sprung mass loading (see Table 7.12). Comparing the RMS actuator forces required at $45\,km/h$ to those at $60\,km/h$, there was an overall increase in force required at the higher speed.

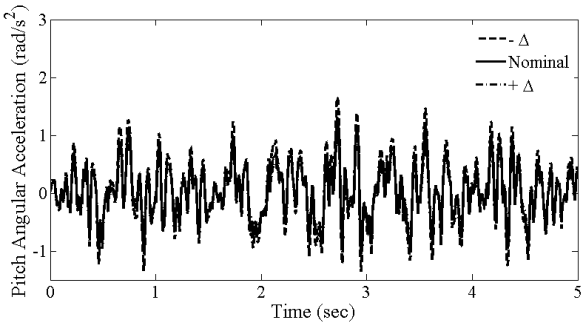

(a) AVSS

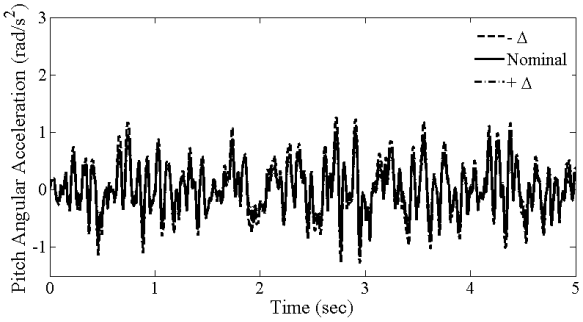

(b) PVSS

Figure 7.62: Pitch angular acceleration for 80%, 100% and 120% Ms at $V = 60\,km/h$.

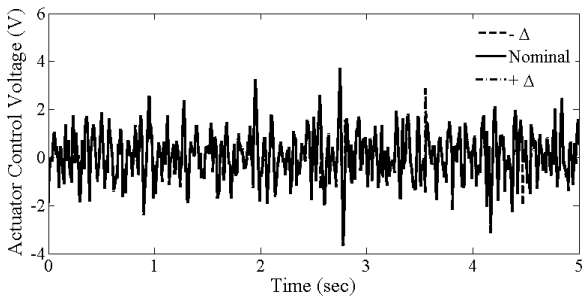

(a) Front suspension

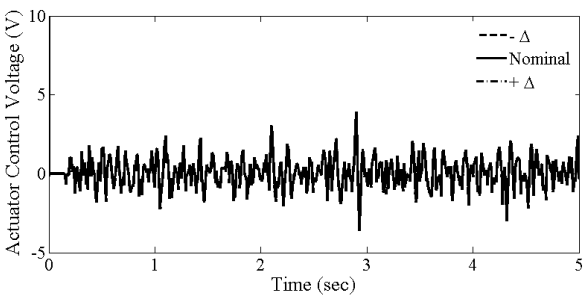

(b) Rear suspension

Figure 7.63: Front and rear actuator control voltage for 80%, 100% and 120% Ms at $V = 60\,km/h$.

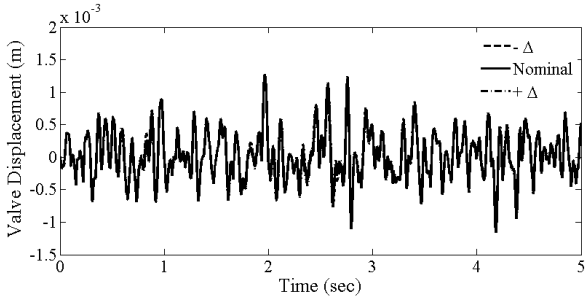

(a) Front suspension

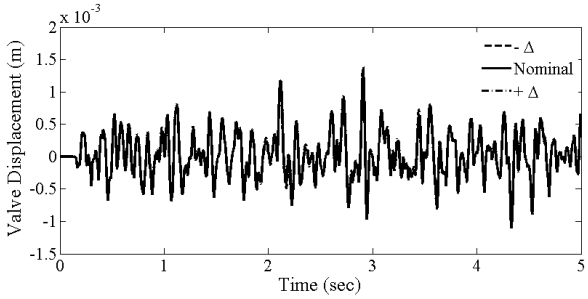

(b) Rear suspension

Figure 7.64: Front and rear actuator spool-valve displacement for 80%, 100% and 120% Ms at $V = 60\,km/h$.

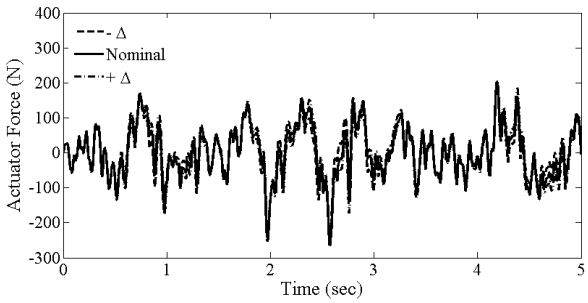

(a) Front suspension

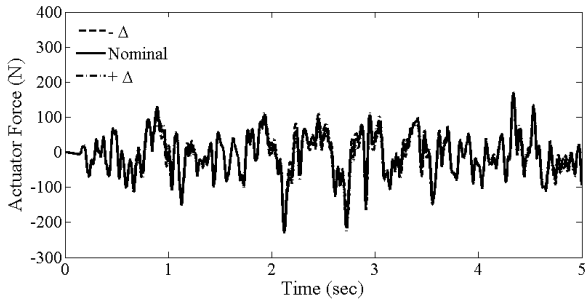

(b) Rear suspension

Figure 7.65: Front and rear actuator force for 80%, 100% and 120% Ms at $V = 60\,km/h$.

7.3.2.3 System Response at $V = 75\,km/h$

The RMS values obtained as the PVSS and AVSS traversed a random road input disturbance at $V = 75\,km/h$ are given in Table 7.14. Figure 7.66 and 7.67 show the front and rear suspension travel. The percentage reduction in RMS suspension travel by the AVSS over the PVSS improved with sprung mass load increase for the front suspension, while it deteriorated by roughly 1% comparing the performance at the minimum with that at the maximum sprung mass loading (Table 7.14. The peak suspension travel values for both the AVSS and PVSS were lower than the specified $\pm 0.08\,m$ limit, although the PVSS values were higher than those of the AVSS. Relating to response to speed variation, the RMS front suspension travel percentage reduction appeared to deteriorate slightly as speed increased, while the RMS rear suspension travel improved slightly with increase in vehicle velocity (see Tables 7.10, 7.12 and 7.14).

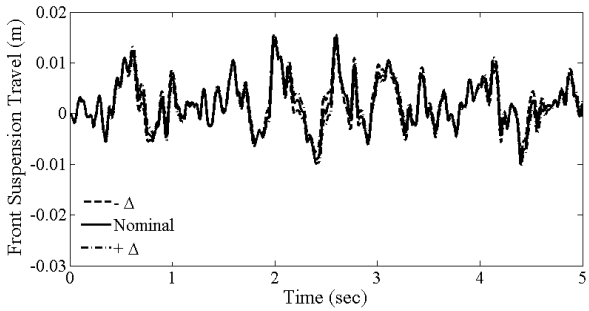

(a) AVSS

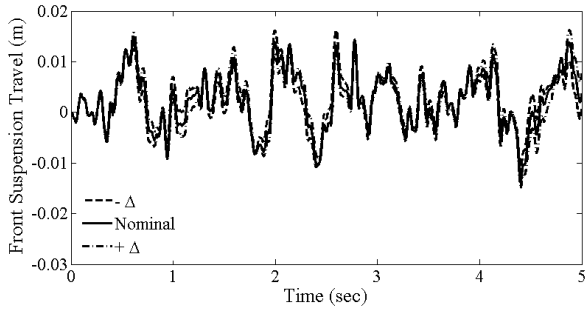

(b) PVSS

Figure 7.66: Front suspension travel for 80%, 100% and 120% Ms at $V = 75\,km/h$.

The front and rear dynamic tyre forces are shown in Figure 7.68 and 7.69 respectively. The peak front and rear dynamic tyre forces were below the limits specified in Table 4.1, Chapter 4. Table 7.14 shows that both the percentage reduction in RMS front and rear dynamic tyre forces improved slightly as the sprung mass loading increased. The overall percentage reduction in RMS dynamic tyre force by the

Table 7.14: RMS values for random input disturbance with ±20% variation in sprung mass loading about the nominal value, $Ms = 580\,kg$, at $V = 75\,km/h$

Parameters	$80\%Ms = 464\,kg$			$100\%Ms = 580\,kg$			$120\%Ms = 696\,kg$		
	PVSS	AVSS	% Reduction by AVSS	PVSS	AVSS	% Reduction by AVSS	PVSS	AVSS	% Reduction by AVSS
Front Suspension Travel $[m]$	0.0057	0.0048	15.79	0.0060	0.0050	16.67	0.0063	0.0050	20.63
Rear Suspension Travel $[m]$	0.0045	0.0037	17.78	0.0047	0.0039	17.02	0.0049	0.0041	16.33
Front Dynamic Tyre Force $[N]$	465.1005	452.6613	2.67	465.1192	448.9020	3.49	466.1840	446.1227	4.30
Rear Dynamic Tyre Force $[N]$	453.4244	441.7745	2.57	449.8584	438.1334	2.61	448.5289	435.3388	2.94
Sprung Mass Acceleration $[m/s^2]$	0.8096	0.9179	-13.38	0.6619	0.7487	-13.11	0.5649	0.6287	-11.29
Pitch Angular Acceleration $[rad/s^2]$	0.5282	0.6003	-13.65	0.4208	0.4779	-13.57	0.3489	0.3977	-13.99
Front Actuator Control Voltage $[V]$	–	1.0049	–	–	1.0038	–	–	1.0031	–
Rear Actuator Control Voltage $[V]$	–	0.9640	–	–	0.9631	–	–	0.9616	–
Front Spool-Valve Displacement $[m]$	–	3.9760×10^{-4}	–	–	3.9494×10^{-4}	–	–	3.9243×10^{-4}	–
Rear Spool-Valve Displacement $[m]$	–	3.7790×10^{-4}	–	–	3.7713×10^{-4}	–	–	3.7605×10^{-4}	–
Front Actuator Force $[N]$	–	74.2285	–	–	76.4600	–	–	78.0123	–
Rear Actuator Force $[N]$	–	60.5332	–	–	63.7255	–	–	66.0108	–

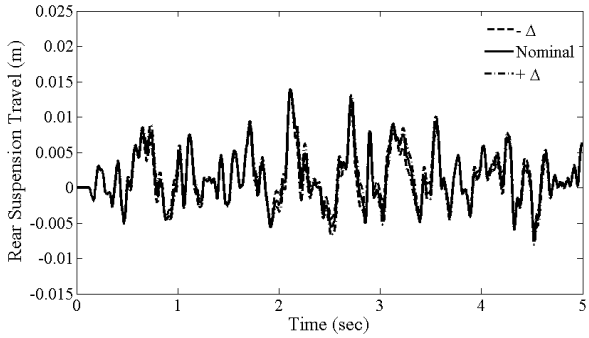

(a) AVSS

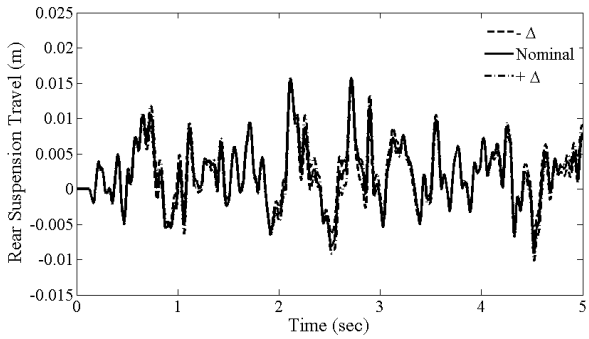

(b) PVSS

Figure 7.67: Rear suspension travel for 80%, 100% and 120% Ms at $V = 75\,km/h$.

AVSS by the PVSS improved slightly as the vehicle speed increased from $45km$ to $60\,km/h$ and finally $75\,km/h$, this can be seen by comparing the values in Table 7.10, 7.12 and 7.14.

The sprung mass acceleration and ISO 2631-1 weighted RMS acceleration are given in Figure 7.70 and Table 7.15 respectively. At $75\,km/h$, the AVSS ISO 2631-1 weighted RMS acceleration was between 11.87 and 12.96% higher than that of the PVSS (see Table 7.15). Although the PVSS comfort level remained at "Not Uncomfortable" throughout, the AVSS comfort level varied between "Not Uncomfortable" and "A Little Uncomfortable" due to the change in sprung mass loading. The overall AVSS performance deteriorated as the vehicle velocity increased from $45\,km/h$ to $60\,km/h$ then improved slightly when the vehicle velocity increased further to $75\,km/h$ (see Tables 5.3, 5.5 and 5.7).

The AVSS and PVSS pitch angular acceleration for 80%, 100% and 120% Ms at $V = 75\,km/h$ are given in Figures 7.71(a) and 7.71(b) respectively. The RMS pitch angular acceleration of the AVSS was higher than the PVSS as shown in Table 7.14. The percentage reduction in RMS pitch angular acceleration by the AVSS when compared with the PVSS showed a trend of improving with vehicle velocity.

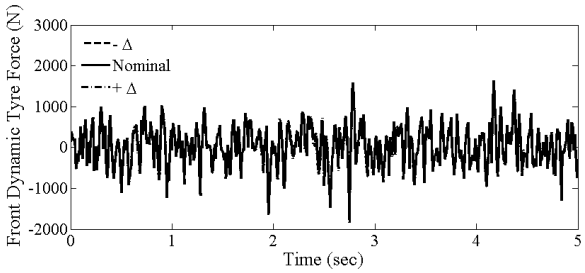

(a) AVSS

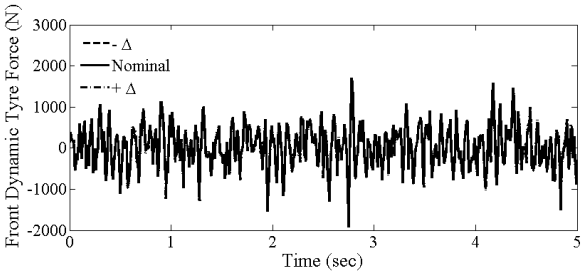

(b) PVSS

Figure 7.68: Front dynamic tyre force for 80%, 100% and 120% Ms at $V = 75\,km/h$.

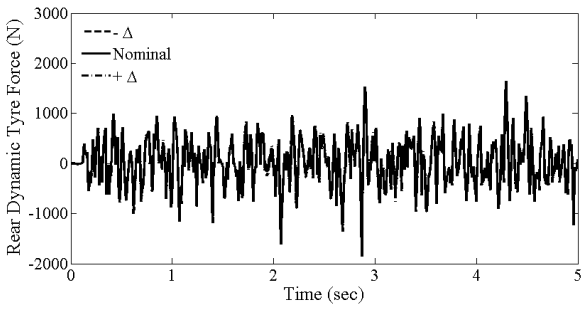

(a) AVSS

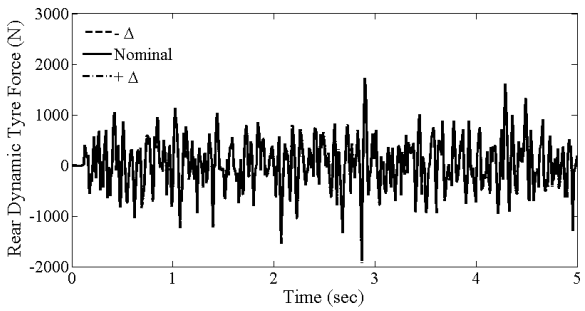

(b) PVSS

Figure 7.69: Rear dynamic tyre force for 80%, 100% and 120% Ms at $V = 75\,km/h$.

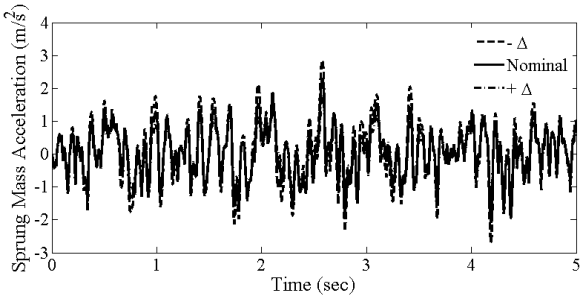

(a) AVSS

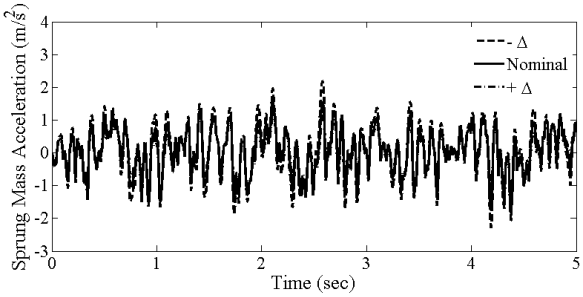

(b) PVSS

Figure 7.70: Sprung mass acceleration for 80%, 100% and 120% Ms at $V = 75\,km/h$.

Table 7.15: Weighted RMS acceleration and discomfort levels as PVSS and AVSS traversed a random road input disturbance at $V = 75\,km/h$

	PVSS		AVSS		%
	Weighted RMS Acceleration a_{wi}^{RMS}	ISO 2631-1 Level of Discomfort	Weighted RMS Acceleration a_{wi}^{RMS}	ISO 2631-1 Level of Discomfort	Reduction of a_{wi}^{RMS} by AVSS
80% Ms	0.2800	Not Uncomfortable	0.3163	Not to A Little Uncomfortable	-12.9643
100% Ms	0.2238	Not Uncomfortable	0.2523	Not Uncomfortable	-12.7346
120% Ms	0.1870	Not Uncomfortable	0.2092	Not Uncomfortable	-11.8717

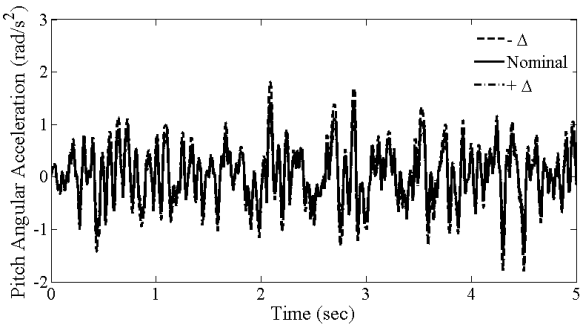

(a) AVSS

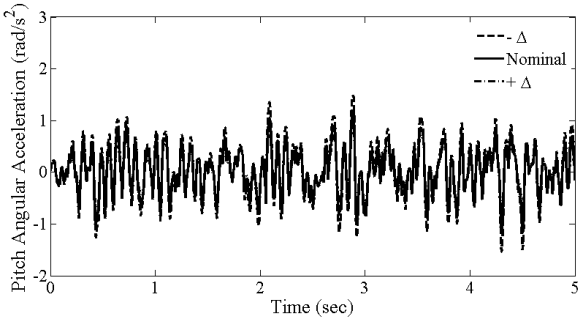

(b) PVSS

Figure 7.71: Pitch angular acceleration for 80%, 100% and 120% Ms at $V = 75\,km/h$.

The actuator voltage and spool-valve displacement at $V = 75\,km/h$ are shown in Figures 7.73 and 7.74, respectively. The peak values of the front and rear actuator voltages at $V = 75\,km/h$ remained below the specified limit. Comparing the RMS voltage at $V = 45\,km/h$, $V = 60\,km/h$ and $V = 75\,km/h$ shows that the required actuator voltage increases with velocity as well as sprung mass loading, see Tables 7.10, 7.12 and 7.14. The actuator spool-valve displacement RMS values are given in Table 7.14.

Figure 7.74 shows the front and rear actuator force. The actuator force at $V = 75\,km/h$ increased with increase in sprung mass loading (see Table 7.14). The peak actuator forces were lower than the limit specified in Chapter 4. The overall RMS actuator force increased with vehicle velocity, compare Tables 7.10, 7.12 and 7.14.

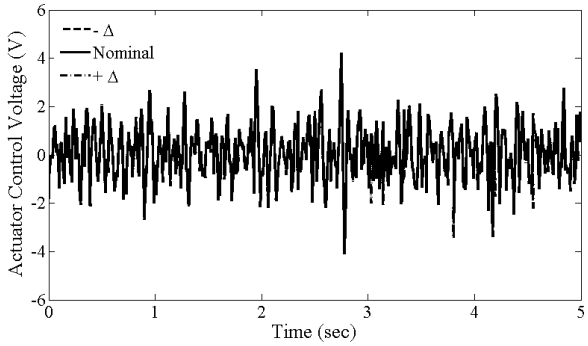

(a) Front suspension

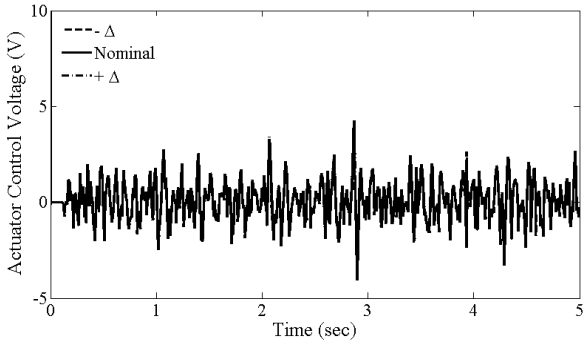

(b) Rear suspension

Figure 7.72: Front and rear actuator control voltage for 80%, 100% and 120% Ms at $V = 75\,km/h$.

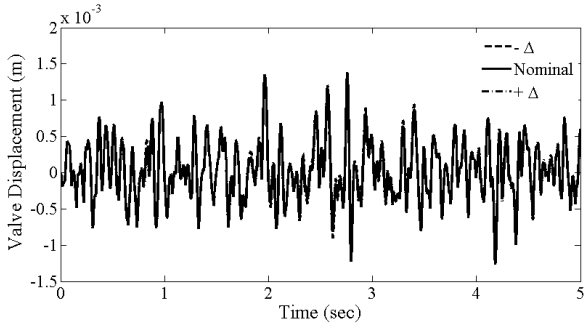

(a) Front suspension

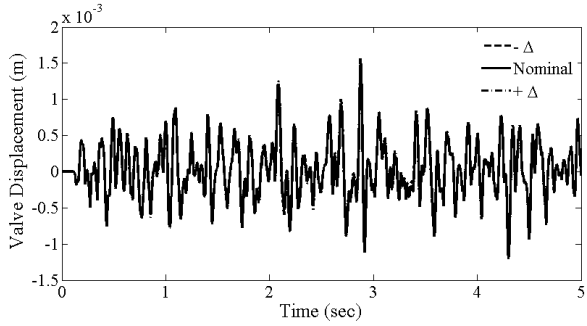

(b) Rear suspension

Figure 7.73: Front and rear actuator spool-valve displacement for 80%, 100% and 120% Ms at $V = 75\,km/h$.

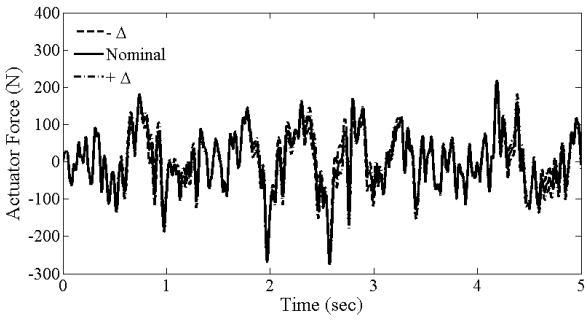

(a) Front suspension

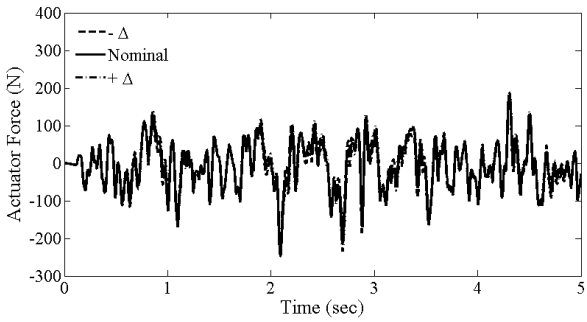

(b) Rear suspension

Figure 7.74: Front and rear actuator force for 80%, 100% and 120% Ms at $V = 75\,km/h$.

7.3.3 Uncertainty Analysis

Uncertainty analysis was performed by taking the frequency responses of both the AVSS and PVSS. The models were built in the MATLAB/Simulink® environment. The MATLAB fixed-step solver, ODE-3, was selected with sampling time set to $T_s = 0.0001s$ and the tasking mode was set to "Single Tasking". The frequency sweep method similar to that used by Savaresi et al. (2010) was applied here, by use of a chirp road input disturbance signal of amplitude $\pm 15\,mm$ (Sammier et al., 2003) with frequency varying between $0 - 100\,Hz$, over a simulation period of $100\,s$. The frequency was set to vary between $0 - 100\,Hz$ in order to expose the vehicle to a wide range of input disturbance frequencies.

The MATLAB Welch algorithm/spectral estimator was utilized to perform a spectral analysis of the AVSS and PVSS model outputs. The "Hamming" window setting with segment length of $N/100$ (where N is the total number of samples) and a percentage overlap of 2^{14} was found to produce clear frequency response plots (The MathWorks Inc., 2001).

The following vehicle parameters were varied and the corresponding frequency responses plotted:

1. Sprung mass loading Ms:
   The sprung mass loading Ms, was varied by $\Delta = \pm 20\%$ (Du and Zhang, 2009). Since the pitch moment of inertia I_θ is related to the vehicle body mass, it is assumed that the pitch moment of inertia also varies by the same amount about its nominal value (Chen et al., 2005).

2. Suspension Spring Coefficients:
   Both the linear and nonlinear spring coefficients ks_i^l and ks_i^{nl} respectively, were varied by $\Delta = \pm 30\%$ about their nominal values (Chen et al., 2005).

3. Suspension Damping Coefficients:
   The linear, nonlinear and symmetric damping coefficients bs_i^l, bs_i^{nl} and bs_i^{sym} respectively, were varied by $\Delta = \pm 30\%$ about their nominal values.

7.3.3.1 Variation of Sprung Mass Loading

Figures 7.75(a) and 7.75(b) show the AVSS and PVSS front suspension travel PSD responses for $\Delta = \pm 20\%$ variation in sprung mass loading Ms and pitch moment of inertia I_θ. The magnitude of the AVSS response at the "knee" between $1\,Hz$ and

the body-hop frequency ($\approx 2\,Hz$) is smaller than that of the PVSS. In the frequency range below $4\,Hz$ and between $4-8\,Hz$, both the AVSS and PVSS perform similarly. At the wheel-hop frequency ($\approx 12\,Hz$), the magnitude of the AVSS response is smaller than that of the PVSS. At high frequencies ($> 20\,Hz$), the AVSS and PVSS behave similarly.

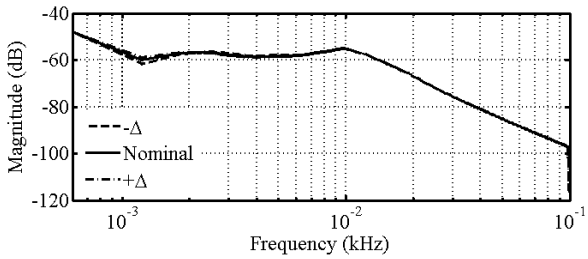

(a) AVSS

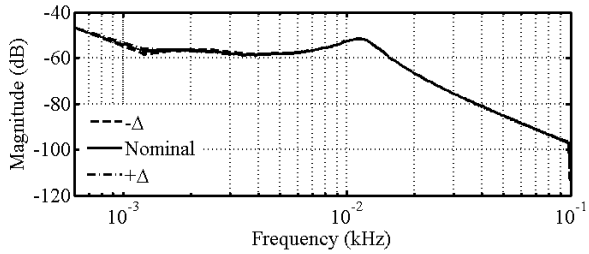

(b) PVSS

Figure 7.75: Front suspension travel PSD for $\Delta = \pm 20\%$ variation in Ms and I_θ about their nominal values.

The AVSS and PVSS rear suspension travel PSD responses for $\Delta = \pm 20\%$ variation in Ms and I_θ are given in Figures 7.75(a) and 7.75(b) respectively. Between $1-2\,Hz$, the magnitude of the "knee" of the AVSS is smaller than that of the PVSS. Both the AVSS and PVSS perform similarly between $4-8\,Hz$ and above $20\,Hz$. The magnitude of the AVSS response is smaller than that of PVSS at the wheel-hop frequency ($\approx 12\,Hz$).

Figures 7.77(a) and 7.77(b) show the AVSS and PVSS front dynamic tyre force PSD for $\Delta = \pm 20\%$ variation in Ms and I_θ, respectively. At the body-hop frequency ($\approx 2\,Hz$), the response of the AVSS is greater in magnitude compared with that of the PVSS. The AVSS is less sensitive to variations in Ms and I_θ than the PVSS, at frequencies below $4\,Hz$. At the wheel-hop frequency ($\approx 12\,Hz$), the PVSS response is greater in magnitude than that of the AVSS. Above $20\,Hz$, both the PVSS and AVSS perform similarly.

Figures 7.78(a) and 7.78(b) show the rear dynamic tyre force PSD for $\Delta = \pm 20\%$

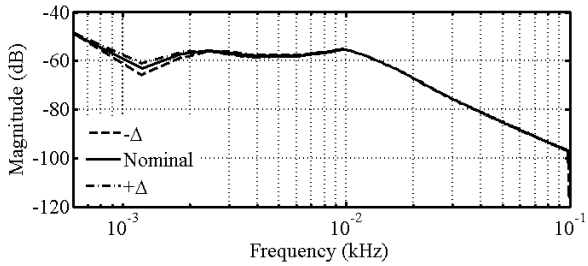

(a) AVSS

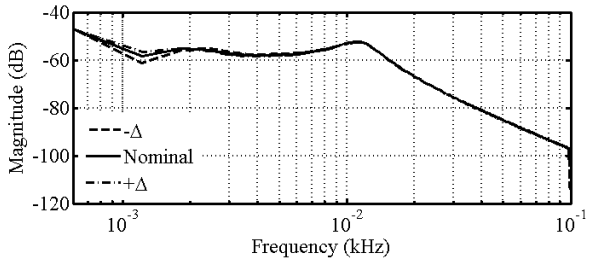

(b) PVSS

Figure 7.76: Rear suspension travel PSD for $\Delta = \pm 20\%$ variation in Ms and I_θ about their nominal values.

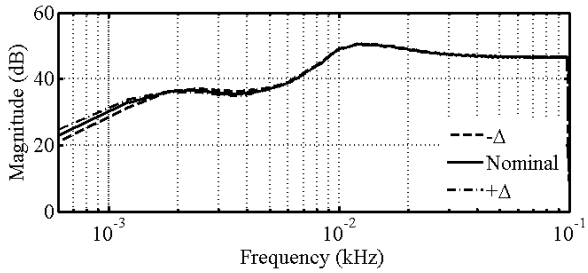

(a) AVSS

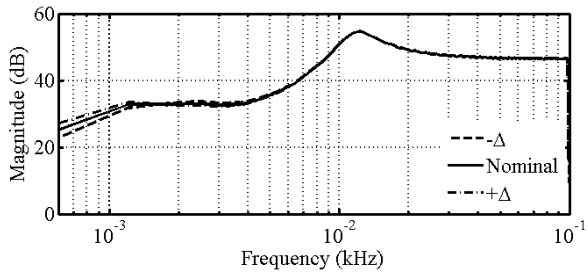

(b) PVSS

Figure 7.77: Front dynamic tyre force PSD for $\Delta = \pm 20\%$ variation in Ms and I_θ about their nominal values.

variation in Ms and I_θ, for the AVSS and PVSS respectively. Below $4\,Hz$, the AVSS is less sensitive to variations in Ms and I_θ than the PVSS. The response of the AVSS at the body-hop frequency ($\approx 2\,Hz$) is greater in magnitude than that of the PVSS. The magnitude of the AVSS response at the wheel-hop frequency ($\approx 12\,Hz$) is smaller than that of the PVSS. Above $20\,Hz$, the performance of the AVSS and PVSS is similar.

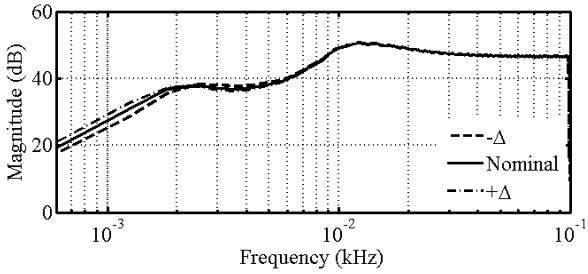

(a) AVSS

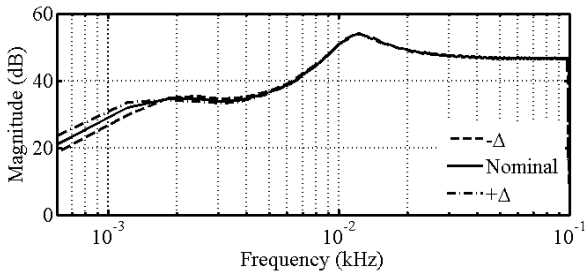

(b) PVSS

Figure 7.78: Rear dynamic tyre force PSD for $\Delta = \pm 20\%$ variation in Ms and I_θ about their nominal values.

Figures 7.79(a) and 7.79(b) show the sprung mass acceleration PSD responses for $\Delta = \pm 20\%$ variation in Ms and I_θ about their nominal values for the AVSS and PVSS respectively. At low frequencies (below $4\,Hz$), the AVSS is less sensitive to variation in Ms and I_θ than the PVSS. The response of the AVSS about wheel-hop frequency ($\approx 12\,Hz$) appears more rounded than that of the PVSS. Above $20\,Hz$ both the AVSS and PVSS behave similarly.

The pitch angular acceleration PSD responses for $\Delta = \pm 20\%$ variation in Ms and I_θ about their nominal values, are given in Figure 7.80(a) for the AVSS and Figure 7.80(b) for the PVSS. At frequencies less than $4\,Hz$, the AVSS is less sensitive than the PVSS to variations in Ms and I_θ, although the magnitude of the AVSS response is greater than that of the PVSS within this frequency range. In the $4 - 8\,Hz$ frequency range, around the wheel-hop frequency and above $20\,Hz$, the AVSS and PVSS behave similarly.

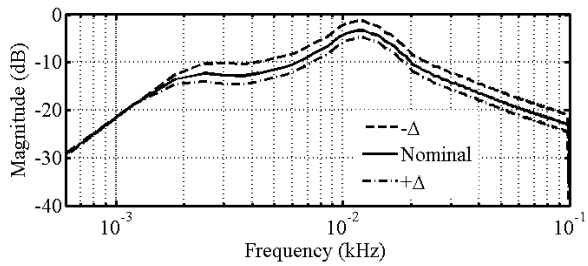

(a) AVSS

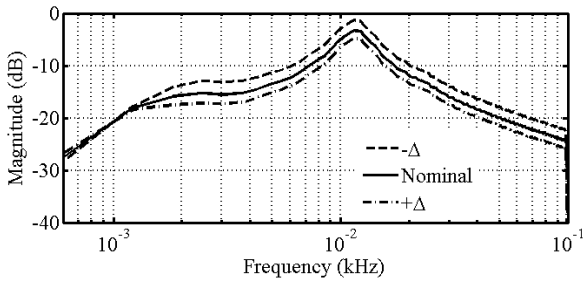

(b) PVSS

Figure 7.79: Sprung mass acceleration PSD for $\Delta = \pm 20\%$ variation in Ms and I_θ about their nominal values.

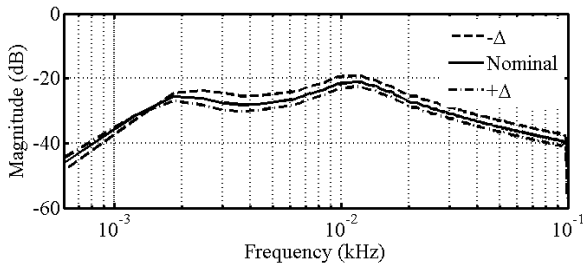

(a) AVSS

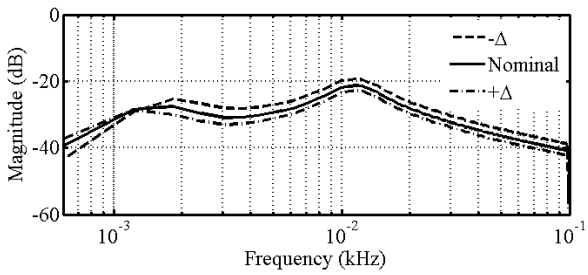

(b) PVSS

Figure 7.80: Pitch angular acceleration PSD for $\Delta = \pm 20\%$ variation in Ms and I_θ about their nominal values.

7.3.3.2 Variation of Suspension Spring Coefficient

Figures 7.81(a) and 7.81(b) show the AVSS and PVSS front suspension travel PSD responses respectively, for $\Delta = \pm 30\%$ variation in ks_i^l and ks_i^{nl} about their nominal values. Below $4\,Hz$, the AVSS front suspension travel performance is less sensitive to variations in the spring coefficients than that of the PVSS. The AVSS and PVSS perform similarly between $4 - 8\,Hz$ as well as above $20\,Hz$. At the wheel-hop frequency ($\approx 12\,Hz$), the magnitude of the peak obtained for the AVSS is lower than that of the PVSS.

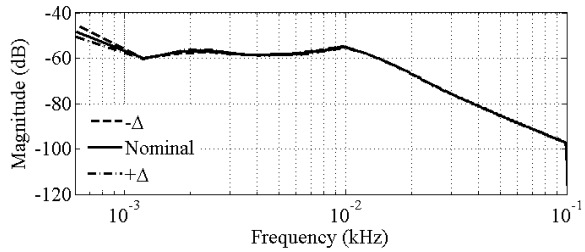

(a) AVSS

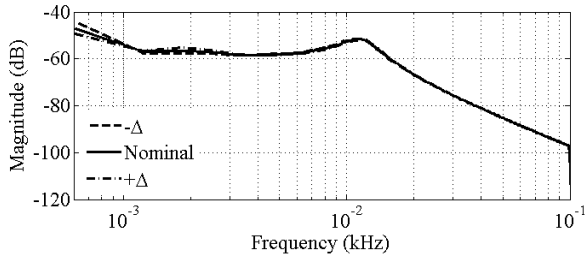

(b) PVSS

Figure 7.81: Front suspension travel PSD for $\Delta = \pm 30\%$ variation in ks_i^l and ks_i^{nl} about their nominal values.

Figures 7.82(a) and 7.82(b) show the AVSS and PVSS rear suspension travel PSD responses respectively, for $\Delta = \pm 30\%$ variation in ks_i^l and ks_i^{nl} about their nominal values. For frequencies less than $4\,Hz$, the AVSS rear suspension travel is less sensitive to variation of the spring coefficients than the PVSS. In the region between $4 - 8\,Hz$, both the AVSS and PVSS perform similarly. The magnitude of the peak at the wheel-hop frequency, ($\approx 12\,Hz$), is lower for the AVSS than for the PVSS. Above $20\,Hz$, the AVSS and PVSS both perform similarly.

The front dynamic tyre force PSD for $\Delta = \pm 30\%$ variation in ks_i^l and ks_i^{nl} about their nominal values for the AVSS in Figure 7.83(a) and for the PVSS in Figure 7.83(b). For frequencies below $4\,Hz$ and between $4 - 8\,Hz$ the AVSS front dynamic tyre force is less sensitive to variation of the spring coefficients than that of the

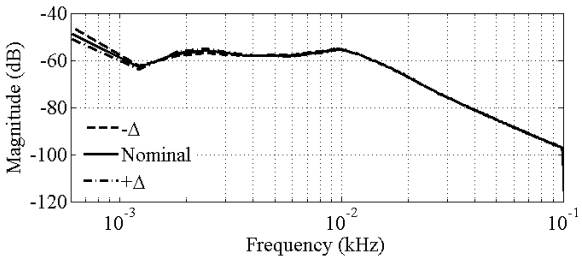

(a) AVSS

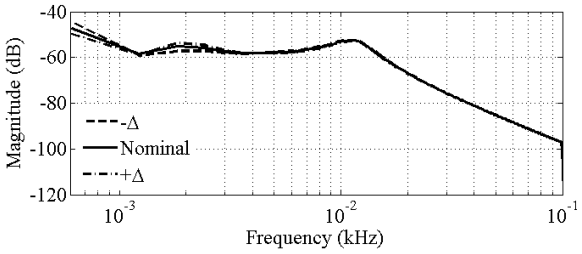

(b) PVSS

Figure 7.82: Rear suspension travel PSD for $\Delta = \pm 30\%$ variation in ks_i^l and ks_i^{nl} about their nominal values.

PVSS. At the wheel-hop frequency ($\approx 12\,Hz$), the magnitude of the AVSS is lower than that of the PVSS. For frequencies above $20\,Hz$, the performance of both the AVSS and PVSS is similar.

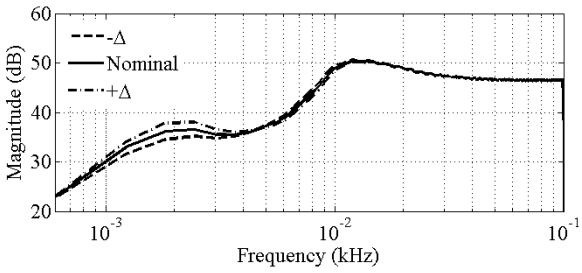

(a) AVSS

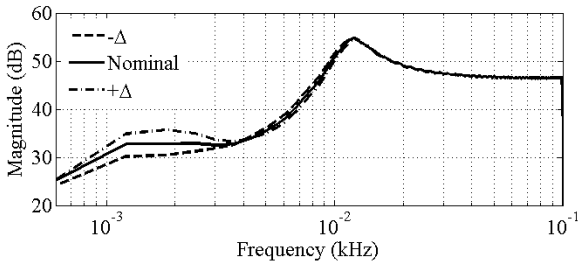

(b) PVSS

Figure 7.83: Front dynamic tyre force PSD for $\Delta = \pm 30\%$ variation in ks_i^l and ks_i^{nl} about their nominal values.

Figures 7.84(a) and 7.84(b) show the AVSS and PVSS rear dynamic tyre force PSDs, respectively. Below $4\,Hz$ as well as between $4-8\,Hz$, the AVSS is less sensitive than the PVSS to variation of the spring coefficients. At the wheel-hop frequency ($\approx 12\,Hz$), the magnitude of the AVSS response is lower than that of the PVSS. Above $20\,Hz$, both the AVSS and PVSS perform similarly.

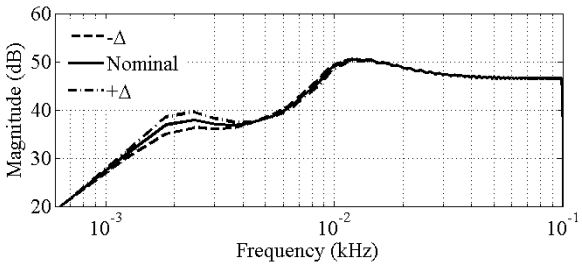

(a) AVSS

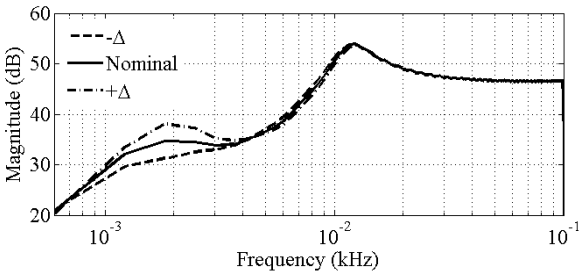

(b) PVSS

Figure 7.84: Rear dynamic tyre force PSD for $\Delta = \pm 30\%$ variation in ks_{si}^{l} and ks_{i}^{nl} about their nominal values.

Figures 7.85(a) and 7.85(a) give the AVSS and PVSS sprung mass acceleration PSD responses respectively, for $\Delta = \pm 30\%$ variation in ks_{i}^{l} and ks_{i}^{nl} about their nominal values. At frequencies below $4\,Hz$ the AVSS is less sensitive to variations in the spring coefficients than the PVSS. Both the AVSS and PVSS perform similarly at frequencies between $4-8\,Hz$ as well as frequencies above $20\,Hz$. The AVSS produces a less harsh response than that of the PVSS around wheel-hop frequency.

The pitch angular acceleration PSD responses for $\Delta = \pm 30\%$ variation in ks_{i}^{l} and ks_{i}^{nl} about their nominal values for the AVSS in Figure 7.86(a) and for the PVSS in Figure 7.86(b). At frequencies below $4\,Hz$ the AVSS is less sensitive than the PVSS to variation of the spring coefficients. Between $4-8\,Hz$, at the wheel-hop frequency and above $20\,Hz$ both the AVSS and PVSS perform similarly.

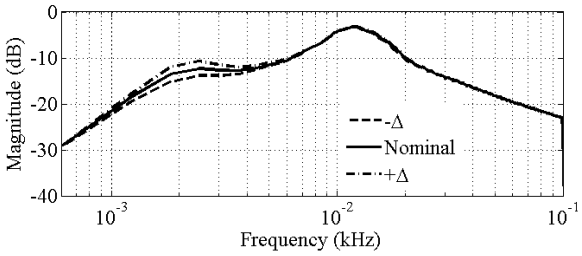

(a) AVSS

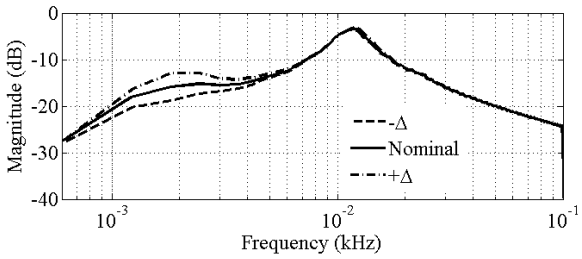

(b) PVSS

Figure 7.85: Sprung mass acceleration PSD for $\Delta = \pm 30\%$ variation in ks_i^l and ks_i^{nl} about their nominal values.

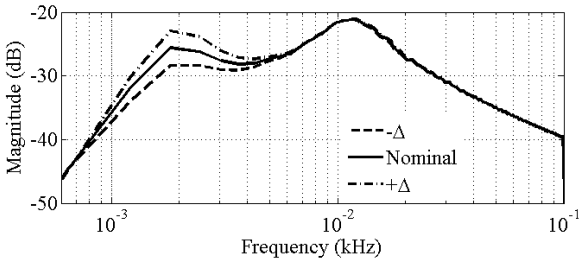

(a) AVSS

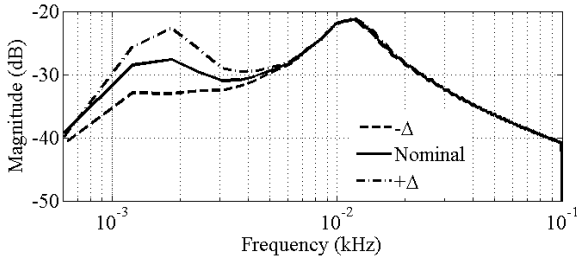

(b) PVSS

Figure 7.86: Pitch angular acceleration PSD for $\Delta = \pm 30\%$ variation in ks_i^l and ks_i^{nl} about their nominal values.

7.3.3.3 Variation of Suspension Damping Coefficient

The AVSS and PVSS front suspension travel PSD responses are given in Figures 7.87(a) and 7.87(b) respectively. The AVSS response is more robust to variation in suspension damping coefficients than that of the PVSS for frequencies below $4\,Hz$ and the region around the wheel-hop frequency ($\approx 12\,Hz$). The magnitude of the response at the peak is higher for the PVSS than for the AVSS at the wheel-hop frequency. The AVSS and PVSS perform similarly at frequencies between $4-8\,Hz$ as well as above $20\,Hz$.

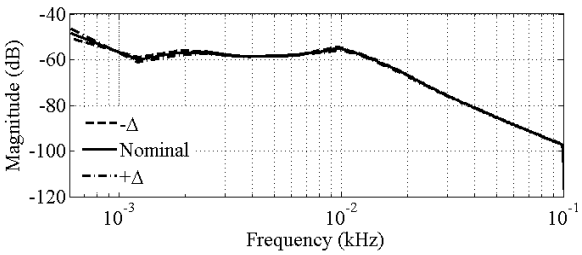

(a) AVSS

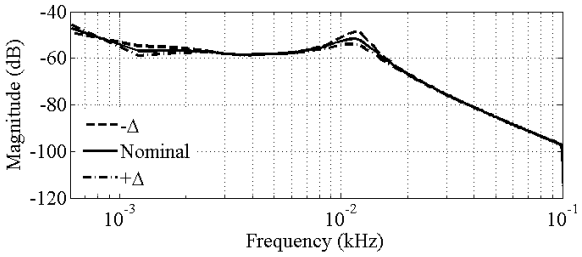

(b) PVSS

Figure 7.87: Front suspension travel PSD for $\Delta = \pm 30\%$ variation in bs_i^l, bs_i^{nl} and bs_i^{sym} about their nominal values.

Figures 7.88(a) and 7.88(b) show the rear suspension travel PSD responses for $\Delta = \pm 30\%$ variation in suspension damping coefficients for the AVSS and PVSS, respectively. Comparing the AVSS response with that of the PVSS, the Figures indicate the AVSS is more robust to variation in suspension damping coefficients for frequencies lower than $4\,Hz$ and around the wheel-hop frequency ($\approx 12\,Hz$). The magnitude of the AVSS response at the wheel-hop frequency is lower compared with that of the PVSS. The figures also show that the AVSS and PVSS responses at frequencies between $4-8\,Hz$ and above $20\,Hz$ are similar.

Figures 7.89(a) and 7.89(b) show the front dynamic tyre force PSD responses for $\Delta = \pm 30\%$ variation in suspension damping coefficients for the AVSS and PVSS,

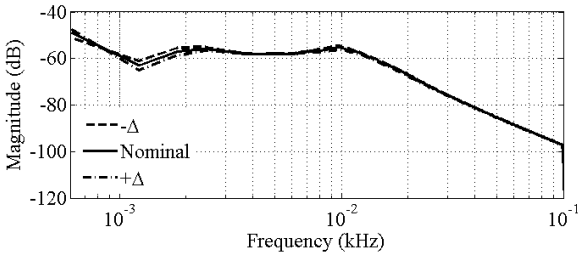

(a) AVSS

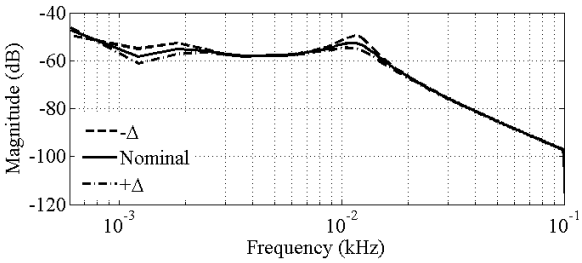

(b) PVSS

Figure 7.88: Rear suspension travel PSD for $\Delta = \pm 30\%$ variation in bs_i^l, bs_i^{nl} and bs_i^{sym} about their nominal values.

respectively. At frequencies less than $4\,Hz$ and at the wheel-hop frequency the AVSS is more robust to variation in suspension damping coefficients than the PVSS. Compared with the PVSS, the AVSS response between $4 - 8\,Hz$ is improves, though by a small amount. Above $20\,Hz$ both the AVSS and PVSS perform similarly.

The rear dynamic tyre force PSD for $\Delta = \pm 30\%$ variation in bs_i^l, bs_i^{nl} and bs_i^{sym} about their nominal values for the AVSS and PVSS are shown in Figures 7.90(a) and Figure 7.90(b) respectively. At frequencies less than $4\,Hz$ and at the wheel-hop frequency, the AVSS is less sensitive than the PVSS to variations in suspension damping. There is an improvement in performance by the AVSS over the PVSS in the region between $4 - 8\,Hz$. Both the AVSS and PVSS perform similarly at frequencies greater than $20\,Hz$.

The sprung mass acceleration PSD for $\Delta = \pm 30\%$ variation in suspension damping for the AVSS and PVSS are given in Figures 7.91(a) and 7.91(b) respectively. Comparing the performance of the AVSS with that of the PVSS, the AVSS is more robust to to variations in suspension damping coefficients in the regions below $4\,Hz$, between $4 - 8\,Hz$, around the wheel-hop frequency and at frequencies greater than $20\,Hz$.

Figures 7.92(a) and 7.92(b) show the pitch angular acceleration PSD for $\Delta = \pm 30\%$

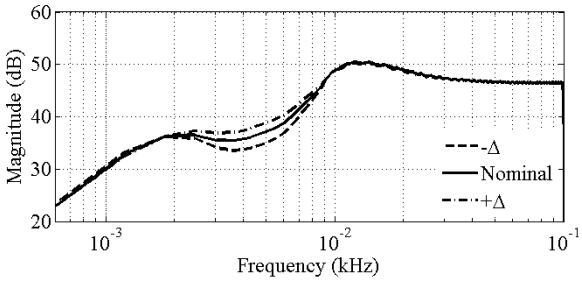

(a) AVSS

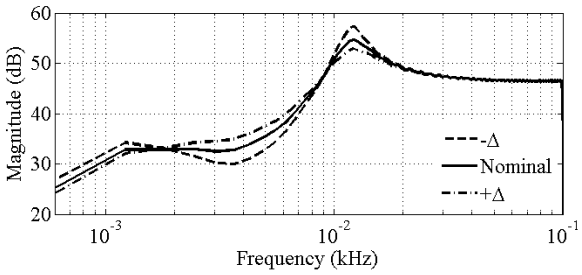

(b) PVSS

Figure 7.89: Front dynamic tyre force PSD for $\Delta = \pm 30\%$ variation in bs_i^l, bs_i^{nl} and bs_i^{sym} about their nominal values.

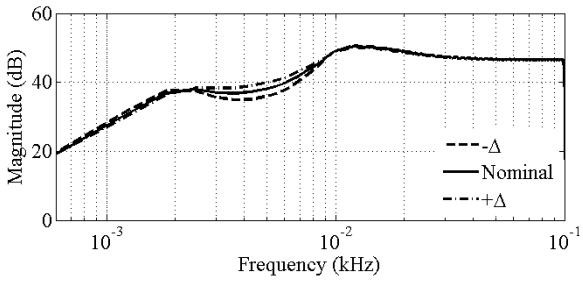

(a) AVSS

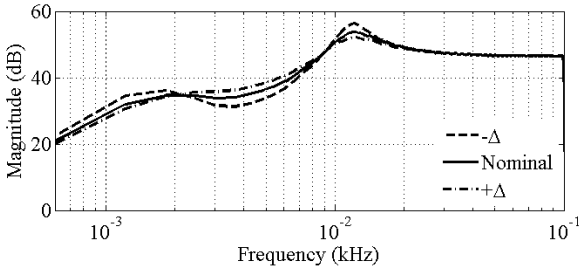

(b) PVSS

Figure 7.90: Rear dynamic tyre force PSD for $\Delta = \pm 30\%$ variation in bs_i^l, bs_i^{nl} and bs_i^{sym} about their nominal values.

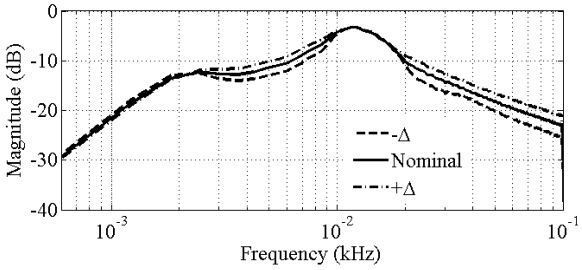

(a) AVSS

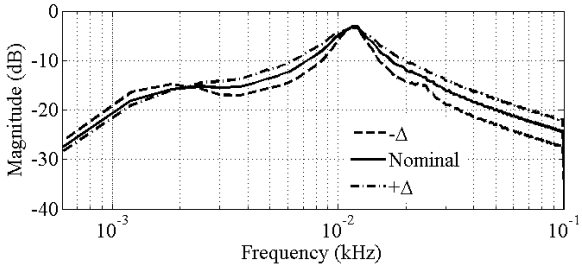

(b) PVSS

Figure 7.91: Sprung mass acceleration PSD for $\Delta = \pm 30\%$ variation in bs_i^l, bs_i^{nl} and bs_i^{sym} about their nominal values.

variation in suspension damping coefficients for the AVSS and PVSS respectively. The figures show that the AVSS is more robust to variations in suspension damping compared with the PVSS or the entire range of frequencies plotted.

7.4 Conclusion

The design of a NNFBL controller for a nonlinear AVSS by application of PID force feedback has been completed, with NNFBL NN identification and PID controller design. The NNFBL controller was able to address the conflict between vehicle ride comfort and road holding by converting the nonlinear suspension model into a linear model by FBL, thereafter applying NNFBL suspension travel control. The NN approximation of the AVSS was performed using two-layer MLP NNs with tansig activation function.

To test controller robustness to parameter variation, the vehicle sprung mass loading was varied by $\pm 20\%$, at the same time, the vehicle velocity was increased from $45\,km/h$ to $60\,km/h$ and finally $75\,km/h$. This was done as the vehicle travelled over two different road input disturbances. In most instances, the AVSS performance in terms of reducing RMS parameters was better than that of the PVSS. Though

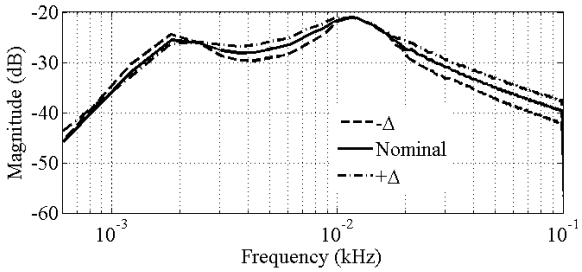

(a) AVSS

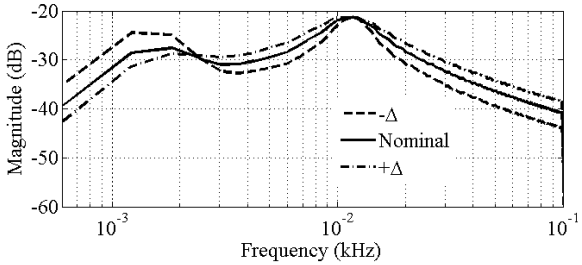

(b) PVSS

Figure 7.92: Pitch angular acceleration PSD for $\Delta = \pm 30\%$ variation in bs_i^l, bs_i^{nl} and bs_i^{sym} about the nominal values.

the front actuator voltage remained within the specified limits throughout, the rear actuator of the AVSS repeatedly peaked at $+10V$ during the first few seconds of the simulations, however, examination of the related plots showed no noticeable effect. The AVSS suspension travel was significantly lower than the PVSS suspension travel, both remaining within the specified limits throughout. The AVSS exceeded the front dynamic tyre force limits on a few instances for the sinusoidal input disturbance, however, it attenuated the forces faster than the PVSS. The AVSS rear dynamic tyre force tended to be higher than that of the PVSS for the sinusoidal input disturbance. The AVSS maintained the actuator force well below the specified limits. The AVSS RMS pitch angular acceleration was higher than that of the PVSS.

Uncertainty analysis was performed on the AVSS and PVSS for variations in sprung mass loading and pitch moment of inertia, suspension spring coefficients and suspension damping coefficients. The results showed that the AVSS possesses greater robustness uncertainties than the PVSS, particularly at frequencies below $4\,Hz$ and around the wheel-hop frequency. The AVSS performance was occasionally better than that of the PVSS for frequencies between $4-8\,Hz$, however, their performances tended to be similar. Above $20\,Hz$ the AVSS and PVSS performed similarly.

8 CONCLUSIONS AND FUTURE RECOMMENDATIONS

8.1 Conclusions

In this work, design and implementation of PID, MPC and NNFBL suspension travel controllers for AVSS via a two-loop control configuration has been presented. Control of these AVSSs is achieved by application of PID control based hydraulic actuator force feedback by simulation studies in the MATLAB/Simulink® simulation environment. The work was presented in the context of the current literature on AVSS control.

The AVSS model is a nonlinear, 4-DOF half-car with hydraulic actuator dynamics. The PVSS model is also a nonlinear, 4-DOF half-car with model parameters similar to those of the AVSS. Hydraulic actuators are the most widely used of all actuators in AVSS, their selection for use in this work is brought forward in the light of their benefits and drawbacks. The motivation for including nonlinearity in the VSS models is to obtain realistic results, whereas the half-car model was chosen for its lower computational complexity compared with the full-car model and the additional observable VSS output states, compared with the quarter-car model.

The results were presented in the frequency domain; by spectral analysis of VSS output states obtained by employing a frequency sweeping road input disturbance. Time domain results were acquired by use of two of the most frequently encountered road input disturbances: a road bump and random road surface roughness. AVSS and PVSS performances were compared in the presence of parametric uncertainty in the form of variations in vehicle forward velocity, sprung mass loading, suspension spring stiffness coefficients and suspension damper coefficients.

Suspension travel was selected as the controlled variable in the outer control loop due to ease of measurement by displacement transducers and the added benefit

of preventing vehicular damage caused by banging of suspension components onto suspension workspace limits (suspension travel "topping" or "bottoming").

The need for control of force generating actuators in AVSS by application of actuator force feedback control has been presented and addressed. Actuator force feedback stabilizes the actuator enabling force tracking and therefore, improved control of the AVSS.

Specifications for controller performance, vehicle input and output constraints and performance measures such as the ISO 2631-1 weighted RMS acceleration for ride comfort analysis, were outlined.

The motivation for application of the various control techniques presented in this thesis have been given. These include the simplicity and ease of tuning of PID control, linearization of nonlinear dynamic models by Feedback Linearization (FBL), constraint handling capability of MPC and the learning and generalizing ability of NNs as an advantage in the presence of model uncertainties. Furthermore, application of NNFBL and MPC has mostly been focused on quarter-car AVSS models, thus, their application to half-car AVSS is an important contribution.

The overall performance of the various AVSSs in reducing RMS parameters in the presence of uncertainty in model parameters was better than that of the PVSS, providing better ride comfort and road holding with minimum suspension travel in most cases. The AVSSs tended to perform best over the sinusoidal bump road input disturbance followed by the random road input disturbance. This confirmed the frequency domain results which indicated that the AVSSs were more robust to uncertainty in the low frequency region (below $4\,Hz$) and performed similarly to the PVSS in the high frequency region (above $20\,Hz$), since the bump is of low frequency while the random road is of high frequency. This is visible on examination of the AVSS and PVSS time histories. In the region between $4-8\,Hz$, the AVSS and PVSS performances were not too different, however, when differences occurred, the AVSS performance was better than that of the PVSS. The AVSS responses were lower in magnitude compared with those for the PVSS around the wheel-hop frequency ($\approx 12\,Hz$), for the various controllers.

8.2 Future Recommendations

The following is a list of areas for future research:

- Combine the constraint handling ability of MPC with the linearization capabilities of FBL to create a hybrid Model Predictive/Feedback Linearization Control (MP/FBLC) suspension travel feedback controller for the outer control loop and further augment it with NNs to form Neural Network-based Model Predictive/Feedback Linearization Control (NNMP/FBLC).

- Incorporate NN-based control into the inner hydraulic actuator force feedback loop to improve performance.

- Investigate the effects of uncertainty of additional model parameters not included in this work, such as: variation in unsprung mass loading, tyre stiffness, tyre damping and hydraulic supply pressure on performance of VSS, comparing an AVSS with a PVSS.

- Investigate the effects of uncertainty in VSS parameters occurring concurrently, as opposed to individually. This would shed light on interaction of these parameters and their combined effect on performance.

- Extend the AVSS and PVSS mathematical models to include vehicle seats for further ride comfort analysis.

- Include aerodynamic effects as an additional input disturbance in the AVSS and PVSS mathematical models.

REFERENCES

Akcay, H. and Turkay, S. (2008). RMS performance limitations and constraints for quarter-car active suspensions, *Proceedings of the Mediterranean Conference on Control and Automation, MED'08*, Ajaccio, France, pp. 425 – 430.

Akcay, H. and Turkay, S. (2009). Influence of tire damping on mixed H_2/H_∞ synthesis of half - car active suspensions, *Journal of Sound and Vibration* **322**(1-2): 15–28.

Al-Holou, N., Lahdhiri, T., Joo, D. S., Weaver, J. and Al-Abbas, F. (2002). Sliding model Neural Network inference fuzzy logic control for active suspension system, *IEEE Transactions on Fuzzy System* **10**(2): 234–245.

Anakwa, W. K. N., Thomas, D. R., Jones, S. C., Bush, J., Green, D., Anglin, G. W., Rio, R., Sheng, J., Garrett, S. and Chen, L. (2002). Development and control of a prototype pneumatic active suspension system, *IEEE Transactions on Education* **45**(1): 43 – 49.

Astrom, K. J. and Hagglund, T. (2004). Revisiting the Ziegler-Nichols step response method for PID control, *Journal of Process Control* **14**(6): 635–650.

Ballo, I. (2007). Comparison of the properties of active and semiactive suspension, *Vehicle System Dynamics* **45**(11): 1065 – 1073.

Beale, M. H., Hagan, M. T. and Demuth, H. B. (2010). *Neural Network Toolbox^{TM} 7 User's Guide*, The MathWorks, Inc., Natick, MA.

Bemporad, A., Morari, M. and Ricker, N. L. (2011). *Model Predictive Control Toolbox^{TM} User's Guide*, The MathWorks, Inc., Natick, MA.

Bessa, W. M., Dutra, M. S. and Kreuzer, E. (2010). Sliding mode control with adaptive fuzzy dead-zone compensation of an electro-hydraulic servo-system, *Journal of Intelligent and Robotic Systems: Theory and Applications* **58**(1): 3 – 16.

Bouazara, M., Richard, M. J. and Rakheja, S. (2006). Safety and comfort analysis of a 3-D vehicle model with optimal non-linear active seat suspension, *Journal of Terramechanics* **43**(2): 97–118.

Buckner, G. D., Schuetze, K. T. and Beno, J. H. (2000). Active vehicle suspension control using intelligent feedback linearization, *Proceedings of the American Control Conference*, Vol. 6, Chicago, IL, USA, pp. 4014 – 4018.

Burns, R. S. (2001). *Advanced control engineering*, Butterworth-Heinemann, Oxford, Boston.

Canale, M., Milanese, M. and Novara, C. (2006). Semi-active suspension control using fast model-predictive techniques, *IEEE Transactions on Control Systems Technology* **14**(6): 1034–1046.

Cao, J., Liu, H., Li, P. and Brown, D. (2008). State of the art in vehicle active suspension adaptive control systems based on intelligent methodologies, *IEEE Transactions of Intelligent Transportation Systems* **9**(3): 392–405.

Chantranuwathana, S. and Peng, H. (2004). Adaptive robust force control for vehicle active suspension, *International Journal of Adaptive Control and Signal Processing* **18**(2): 83–102.

Chen, H., Liu, Z. Y. and Sun, P. Y. (2005). Application of constrained H_∞ control to active suspension systems on half-car models, *Journal of Dynamic Systems, Measurement and Control, Transactions of the ASME* **127**(3): 345 – 354.

Chen, H. and Scherer, C. W. (2004). An LMI based model predictive control scheme with guaranteed H_∞: Performance and Its Application to Active Suspension, *Proceedings of the American Control Conference*, Vol. 2, Boston, MA, United states, pp. 1487 – 1492.

Chen, P. C. and Huang, A. C. (2005a). Adaptive multiple-surface sliding control of hydraulic active suspension systems based on the function approximation technique, *Journal of Vibration and Control* **11**(5): 685–706.

Chen, P. C. and Huang, A. C. (2005b). Adaptive sliding control of non-autonomous active suspension systems with time-varying loadings, *Journal of Sound and Vibration* **282**(3-5): 1119–1135.

Chien, T. L., Chen, C. C., Chiu, H. C., Cheng, H. W. and Chen, Y.-C. (2008). Almost disturbance decoupling control of nonlinear MIMO uncertain system and application to half-car active suspension system, *International Journal of Vehicle Design* **46**(4): 367 – 392.

Dahunsi, O. A. and Pedro, J. O. (2010). Neural Network-based identification and approximate predictive control of a servo-hydraulic vehicle suspension system, *Engineering Letters* **18**(4): 357–368.

Dahunsi, O. A., Pedro, J. O. and Nyandoro, O. T. (2009). Neural Network-based model predictive control of a servo-hydraulic vehicle suspension system, *Proceedings of the International IEEE Africon 2009*, Nairobi, Kenya, pp. 1–6.

Dahunsi, O. A., Pedro, J. O. and Nyandoro, O. T. (2010). System identification and Neural Network based PID control of servo-hydraulic vehicle suspension system, *SAIEE Africa Research Journal, Research Journal of the South African Institute of Electrical Engineers* **101**(3): 93–105.

Deng, J., Becerra, V. and Stobart, R. (2009). Input constraints handling in an MPC/Feedback Linearization Scheme, *International Journal of Applied Mathematics and Computer Science* **19**(2): 219–232.

Du, H. and Zhang, N. (2007). H_∞ control of active vehicle suspensions with actuator time delay, *Journal of Sound and Vibration* **301**(1-2): 236–252.

Du, H. and Zhang, N. (2008). Designing H_∞/GH_2 static - output feedback controller for vehicle suspensions using linear matrix inequalities and genetic algorithms, *Vehicle Systems Dynamics* **46**(5): 385–412.

Du, H. and Zhang, N. (2009). Fuzzy control for nonlinear uncertain electrohydraulic active suspensions with input constraint, *IEEE Transactions on Fuzzy Systems* **17**(2): 343–356.

Du, H., Zhang, N. and Lam, J. (2008). Parameter-dependent input-delayed control of uncertain vehicle suspensions, *Journal of Sound and Vibration* **317**(3-5): 537 – 556.

Elizer Jr., R. M. (1993). Guidelines for the design and application of speed humps, *ITE Journal (Institute of Transportation Engineers)* **63**(5): 11 – 15.

Farong, K. and Zongde, F. (2007). An experimental investigation into the design of vehicle fuzzy active suspension, *Proceedings of the IEEE International Conference on Automation and Logistics, ICAL 2007*, Jinan, China, pp. 959 – 963.

Fateh, M. M. (2010). Robust impedance control of a hydraulic suspension system, *International Journal of Robust and Nonlinear Control* **20**(8): 858–872.

Fateh, M. M. and Alavi, S. S. (2009). Impedance control of an active suspension system, *Mechatronics* **19**(1): 134–140.

Fiahlo, I. and Balas, G. J. (2002). Road adaptive active suspension using linear parameter-varying gain-scheduling, *IEEE Transactions on Control Systems Technology* **10**(1): 43–54.

Fischer, D. and Isermann, R. (2004). Mechatronic semi-active and active vehicle suspensions, *Control Engineering Practice* **12**(11): 1353–1367.

Foale, T. (2006). *Motorcycle handling and chassis design: the art and science, 2nd edn.*, Tony Foale, Benidoleig, Spain.

Gao, H., Lam, J. and Wang, C. (2006). Multi-objective control of vehicle active suspension systems via load-dependent controllers, *Journal of Sound and Vibration* **290**(3-5): 654–675.

Gao, Z. (2002). From linear to nonlinear control means: A practical progression, *ISA Transactions* **41**(2): 177–189.

Gaspar, P. and Kuti, I. (2005). Robust control design based on high-complexity models, *Periodica Polytechnica Transportation Engineering* **33**(1-2): 149 – 156.

Gaspar, P. and Szederkenyi, G. (2007). Combined LPV and nonlinear control of an active suspension system, *IEEE International Symposium on Industrial Electronics*, Vigo, Spain, pp. 215 – 220.

Giorgetti, N., Bemporad, A., Tseng, H. E. and Hrovat, D. (2006). Hybrid model predictive control application towards optimal semi-active suspension, *International Journal of Control* **79**(5): 521 – 533.

Griffin, M. (2007). Discomfort from feeling vehicle vibration, *Vehicle System Dynamics* **45**(7-8): 679–698.

Guclu, R. (2003). Active control of seat vibrations of a vehicle model using various suspension alternatives, *Turkish Journal of Engineering and Environmental Sciences* **27**(6): 361–373.

Guclu, R. and Gulez, K. (2008). Neural Network control of seat vibrations of a nonlinear full vehicle model using PMSM, *Mathematical and Computer Modelling* **47**(11-12): 1356 – 1371.

Guglielmino, E. and Edge, K. A. (2004). A controlled friction damper for vehicle applications, *Control Engineering Practice* **12**(4): 431–443.

Guglielmino, E., Sireteanu, T., Stammers, C. W., Ghita, G. and Giuclea, M. (2008). *Semi-active Suspension Control: Improved Vehicle Ride and Road Friendliness*, Springer–Verlag, London.

Gysen, B. L. J., Janssen, J. L. G., Paulides, J. J. H. and Lomonova, E. A. (2009). Design aspects of an active electromagnetic suspension system for automotive applications, *IEEE Transactions on Industrial Applications* **45**(5): 1589 – 1597.

Gysen, B. L. J., Paulides, J. J. H., Janssen, J. L. G. and Lomonova, E. A. (2010). Active electromagnetic suspension system for improved vehicle dynamics, *IEEE Transactions on Vehicular Technology* **59**(3): 1156 – 1163.

Hagan, M. T., Demuth, H. B. and De Jesus, O. (2002). An introduction to the use of Neural Networks in control systems, *International Journal of Robust and Nonlinear Control* **12**(11): 959 – 985.

Hanafi, D. (2010). PID controller design for semi-active car suspension based on model from intelligent system identification, *Proceedings of the Second International Conference on Computer Engineering and Applications*, Bali Island, Indonesia, pp. 60–63.

Hassanzadeh, I., Alizadeh, G., Shirjoposht, N. P. and Hashemzadeh, F. (2010). A new optimal nonlinear approach to half car active suspension, *IACSIT International Journal of Engineering and Technology* **2**(1): 78–84.

Hrovat, D. (1997). Survey of advanced suspension developments and related optimal control applications, *Automatica* **33**(10): 1781 – 1817.

Huang, C.-J., Li, T.-H. S. and Chen, C.-C. (2009). Fuzzy feedback linearization control for MIMO nonlinear system and its application to full-vehicle suspension system, *Circuits, Systems, and Signal Processing* **28**(6): 959 – 991.

Huang, C., Lin, J. and Chen, C. (2010). Road adaptive algorithm design of half-car active suspension system, *Expert Systems with Applications* **37**(6): 4392–4402.

Huang, S. J. and Lin, W. C. (2007). A Neural Network based sliding mode controller for active vehicle suspension, *Proceedings of the Institution of Mechanical Engineers, Part D: Journal of Automobile Engineering* **221**(11): 1381 – 1397.

Hunt, K. J., Sbarbaro, D., Zbikowski, R. and Gawthrop, P. J. (1992). Neural Networks for control systems :- A Survey, *Automatica* **28**(6): 1083 – 1112.

International Organization for Standardization (1997). *Mechanical Vibration and Shock - Evaluation of Human Exposure to Whole Body Vibration (Part 1: General Requirements),(ISO 2631-1:1997) second edition*, International Standards, Geneva, Switzerland.

Ji, X. D., Wan, K. J., Hai, N. Y. and Bae, K. Y. (2007). Time delay force control for vehicle active suspension system, *Proceedings of the 26th Chinese Controls Conference,(CCC 2007)*, Zhangjiajie, Hunan, China, pp. 640–645.

Jones, W. D. (2005). Easy ride: Bose Corp. uses speaker technology to give cars adaptive suspension, *Spectrum, IEEE* **42**(5): 12 – 14.

Kashtiban, A. M., Pourqorban, N., Alizadeh, G. and Hasanzadeh, I. (2009). Nonlinear optimal control of a half car active suspension, *Proceedings of the 2nd International Conference on Computer and Electrical Engineering, (ICCEE '09)*, Vol. 2, Dubai, United Arab Emirates, pp. 460 – 464.

Koch, G., Fritsch, O. and Lohmann, B. (2010). Potential of low bandwidth active suspension control with continuously variable damper, *Control Engineering Practice* **18**(11): 1251 – 1262.

Kumar, M. S. (2008). Development of an active suspension system for automobiles using PID controller, *Proceedings of the World Congress on Engineering (WCE 2008)*, London, UK.

Lauwerys, C., Swevers, J. and Sas, P. (2005). Robust linear control of an active suspension on a quarter-car test-rig, *Control Engineering Practice* **13**(5): 577 – 586.

Lee, S. and Kim, W.-J. (2010). Active suspension control with direct-drive tubular linear brushless permanent-magnet motor, *IEEE Transactions on Control Systems Technology* **18**(4): 859 – 870.

Lei, J. and Tang, G.-Y. (2008). Optimal vibration control for active suspension sampled-data systems with actuator and sensor delays, *Proceedings of the IEEE 10th International Conference on Control, Automation, Robotics and Vision, ICARCV 2008*, Hanoi, Vietnam, pp. 2828–2833.

Li, G., Stoten, D. P. and Tu, J. Y. (2010). Model predictive control of dynamically substructured systems with application to a servohydraulically actuated mechanical plant, *IET Control Theory and Applications* **4**(2): 253 – 264.

Li, J. Y., Chuan, Y. T. and Li, H. (2008). Research on vehicle suspension systems based on fuzzy logic control, *Proceedings of the IEEE International Conference on Automation and Logistics, ICAL 2008*, Vol. 5, Qingdao, China, pp. 1817 – 1821.

Liberzon, A., Rubinstein, D. and Gutman, P. O. (2001). Active suspension for single wheel station of off-road track vehicle, *International Journal of Robust and Nonlinear Control* **11**(10): 977 – 999.

Liu, Z. and Luo, C. (2006). Road adaptive active suspension control design, *IMACS Multiconference on "Computational Engineering in Systems Applications", CESA*, Beijing, China, pp. 1347 – 1350.

Lu, Y., Yang, S. and Li, S. (2010). Heavy vehicle dynamics with balanced suspension based on enveloping tire model, *Frontiers of Mechanical Engineering in China* **5**(4): 476–482.

Mantaras, D. A. and Luque, P. (2006). Ride comfort performance of different active suspension systems, *International Journal of Vehicle Design* **40**(1-3): 106 – 125.

Martins, I., Esteves, J., Marques, G. D. and da Silva, F. P. (2006). Permanent-magnets linear actuators applicability in automobile active suspensions, *IEEE Transactions on Vehicular Technology* **55**(1): 86 – 94.

Marusak, P. M. and Kuntanapreeda, S. (2011). Constrained model predictive force control of an electrohydraulic actuator, *Control Engineering Practice* **19**(1): 62–73.

Marzbanrad, J., Ahmadi, G., Hojjat, Y. and Zohoor, H. (2002). Optimal active control of vehicle suspension system including time delay and preview for rough roads, *Journal of Vibration and Control* **8**(7): 967 – 991.

Mehra, R. K., Amin, J. N., Hedrick, K. J., Osorio, C. and Gopalasamy, S. (1997). Active suspension using preview information and model predictive control, *Proceedings of IEEE Conference on Control Applications*, Hartford, CT, USA, pp. 860 – 865.

Pedro, J. and Dahunsi, O. (2011). Neural Network based feedback linearization control of a servo-hydraulic vehicle suspension system, *International Journal of Applied Mathematics and Computer Science* **21**(1): 137 – 147.

Pedro, J. O. (2003). Design and performance of an active vehicle suspension system, *Proceedings of the 2nd International Conference on Applied Mechanics and Materials, ICAMM 2003*, Durban, South Africa, pp. 203–209.

Pedro, J. O. (2006). Modelling and H_∞ multivariable control of an active suspension system, *Presented at the 5th South African Conference on Applied Mechanics, SACAM' 06*, Cape Town, South Africa.

Pedro, J. O. (2007). H_2 - LQG/LTR controller design for active suspension systems, *R and D Journal of the South African Institution of Mechanical Engineering* **23**(2): 32–41.

Pedro, J. O. and Mgwenya, T. R. (2004). LQR control of a full - car active suspension with actuator dynamics, *Proceedings of the 4th South African Conference on Applied Mechanics, SACAM '04*, Johannesburg, South Africa.

Pedro, J. O., Nyandoro, O. T. C. and John, S. (2009). Neural Network based feedback linearisation slip control of an anti-lock braking system, *Proceedings of the 7th Asian Control Conference*, Hong Kong, China.

Priyandoko, G., Mailah, M. and Jamaluddin, H. (2009). Vehicle suspension system using skyhook adaptive neuro active force control, *Mechanical Systems and Signal Processing* **23**(3): 855–868.

Qin, S. J. and Badgwell, T. A. (2003). A survey of industrial model predictive control technology, *Control Engineering Practice* **11**(7): 733 – 764.

Renn, J. and Wu, T. (2007). Modelling and control of a new $\frac{1}{4}t$ servo-hydraulic vehicle active suspension system, *Journal of Marine Science and Technology* **15**(3): 265–272.

Ryu, S., Kim, Y. and Park, Y. (2008). Robust H_∞ preview control of an active suspension system with norm-bounded uncertainties, *International Journal of Automotive Technology* **9**: 585–592.

Sahin, H., Fukushima, N., Mochizuki, T. and Hagiwara, I. (2010). HIL simulation evaluation of a novel hybrid-type self-powered active suspension system, *Proceedings of the IEEE International Conference on Industrial Technology*, Vina del Mar, Chile, pp. 1123 – 1130.

Sam, Y. M. and Hudha, K. (2006). Modelling and force tracking of hydraulic actuator for an active suspension system, *Proceedings of the IEEE Conference on Industrial Electronics and Applications, (ICIEA 2006)*, Singapore, Singapore, pp. 1–6.

Sammier, D., Sename, O. and Dugard, L. (2003). Skyhook and H_∞ control of semi-active suspensions: Some practical aspects, *Vehicle System Dynamics* **39**(4): 279 – 308.

Savaresi, S. M., Poussot-Vassal, C., Spelta, C., Sename, O. and Dugard, L. (2010). *Semi-Active Suspension Control Design for Vehicles*, Butterworth-Heinemann, Boston, pp. 177 – 192.

Shi, J. W., Li, X. W. and Zhang, J. W. (2010). Feedback linearization and sliding mode control for active hydropneumatic suspension of a special-purpose vehicle, *Proceedings of the Institution of Mechanical Engineers, Part D: Journal of Automobile Engineering* **224**(1): 41 – 53.

Shoukry, Y., El-Kharashi, M. W. and Hammad, S. (2010). MPC-on-chip: An embedded GPC coprocessor for automotive active suspension systems, *IEEE Embedded Systems Letters* **2**(2): 31–34.

Spentzas, K. N. and Kanarachos, S. A. (2002). A Neural Network approach to the design of a vehicle's non-linear hybrid suspension system, *Proceedings of the Institution of Mechanical Engineers, Part B: Journal of Engineering Manufacture* **216**(5): 833 – 838.

Sun, P.-Y. and Chen, H. (2003). Multiobjective output-feedback suspension control on a half-car model, *Proceedings of the IEEE Conference on Control Applications CCA 2003*, Vol. 1, Istanbul, Turkey, pp. 290 – 295.

Szaszi, I., Gaspar, P. and Bokor, J. (2002). Nonlinear active suspension modelling using linear parameter varying approach, *Proceedings of the 10th Mediterranean Conference on Control and Automation (MED2002)*, Lisbon, Portugal, pp. 1–10.

The MathWorks Inc. (2001). Signal Processing Toolbox for use with Matlab® User's Guide version 5.1, Natick, MA.

Turkay, S. and Akcay, H. (2007). Effect of tire damping on the ride performance potential of active suspension systems, *Proceedings of the SICE Annual Conference*, Takamatsu, Japan, pp. 1209 – 1216.

Van Zeebroeck, M., Lombaert, G., Dintwa, E., Ramon, H., Degrande, G. and Tijskens, E. (2008). The simulation of the impact damage to fruit during the passage of a truck over a speed bump by means of the discrete element method, *Biosystems Engineering* **101**(1): 58 – 68.

Vatankhah, R., Rahaeifard, M. and Alasty, A. (2009). Vibration control of vehicle suspension system using adaptive critic-based neurofuzzy controller, *Proceedings of the 6th International Symposium on Mechatronics and its Applications,(ISMA 2009)*, Sharjah, UAE,.

Weber, P. A. and Braaksma, J. P. (2000). Towards a North American geometric design standard for speed humps, *ITE Journal (Institute of Transportation Engineers)* **70**(1): 30–34.

Williams, R. A. (1997a). Automotive active suspensions part 1: basic principles, *Proceedings of the Institution of Mechanical Engineers, Part D: Journal of Automobile Engineering* **211**(6): 415 – 426.

Williams, R. A. (1997b). Automotive active suspensions part 2: practical considerations, *Proceedings of the Institution of Mechanical Engineers, Part D: Journal of Automobile Engineering* **211**(6): 427 – 444.

Xiao, J. and Kulakowski, B. T. (2003). Sliding mode control of active suspension for transit buses based on a novel air-spring model, *Proceedings of the American Control Conference*, Vol. 5, Denver, CO, United States, pp. 3768 – 3773.

Yagiz, N. and Hacioglu, Y. (2008). Backstepping control of a vehicle with active suspensions, *Control Engineering Practice* **16**(12): 1457 – 1467.

Yoshimura, T., Kume, A., Kurimoto, M. and Hino, J. (2001). Construction of an active suspension system of a quarter-car model using the concept of sliding mode control, *Journal of Sound and Vibration* **239**(2): 187 – 199.

Yoshimura, T. and Teramura, I. (2005). Active suspension control of a one-wheel car model using single input rule modules fuzzy reasoning and a disturbance observer, *Journal of Zhejiang University Science* **6A**(4): 251–256.

Youn, I., Im, J. and Tomizuka, M. (2006). Level and attitude control of the active suspension system with integral and derivative action, *Vehicle System Dynamics* **44**(9): 659 – 674.

Yousefi, A., Akbari, A. and Lohmann, B. (2007). Low order robust controllers for active vehicle suspensions, *Proceedings of the IEEE International Conference on Control Applications*, Munich, Germany, pp. 693 – 698.

Zuo, L. and Nayfeh, S. A. (2003). Low order continuous-time filters for approximation of the ISO 2631-1 human vibration sensitivity weightings, *Journal of Sound and Vibration* **265**(2): 459 – 465.

APPENDIX A Mathematical Model Implementation in Matlab/Simulink®

The following section contains figures of Matlab/Simulink® implementation of the mathematical model presented in Chapter 3.

A.1 Nonlinear Suspension Implementation

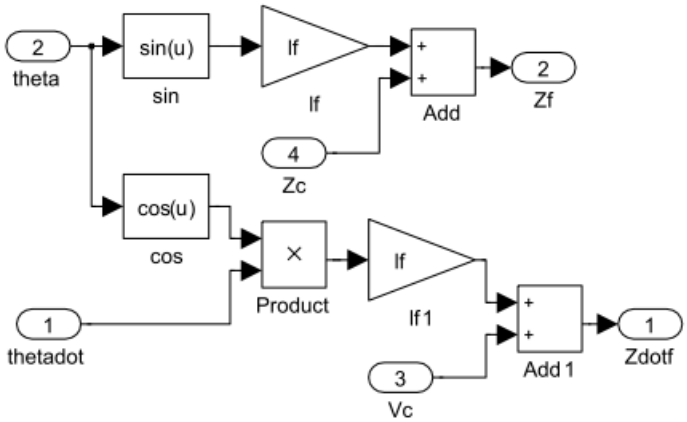

Figure A.1: Matlab/Simulink® implementation of front displacement z_f and front velocity $\dot{z}_f$ of the vehicle body (sprung mass) for large angular displacements about the vehicle center of gravity from Equations 3.1 and 3.2, in Section 3.3.

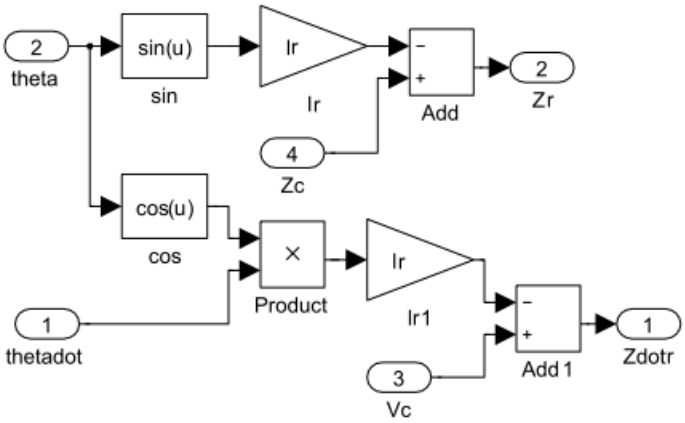

Figure A.2: Matlab/Simulink® implementation of rear displacement z_r and rear velocity $\dot{z}_r$ of the vehicle body (sprung mass) for large angular displacements about the vehicle center of gravity from Equations 3.3 and 3.4, in Section 3.3.

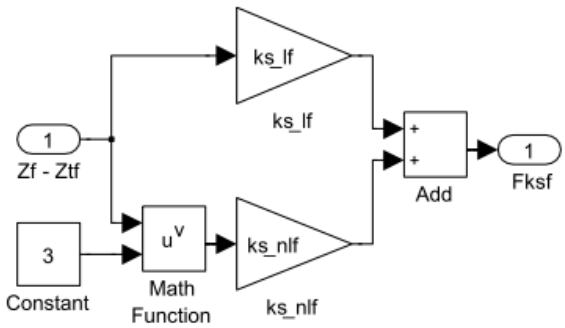

Figure A.3: Matlab/Simulink® implementation of the nonlinear front suspension spring force F_{ksf} of Equation 3.5, Section 3.3.

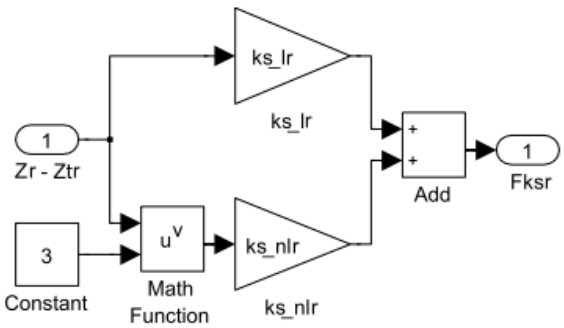

Figure A.4: Matlab/Simulink® implementation of the nonlinear rear suspension spring force F_{ksr} of Equation 3.6, Section 3.3.

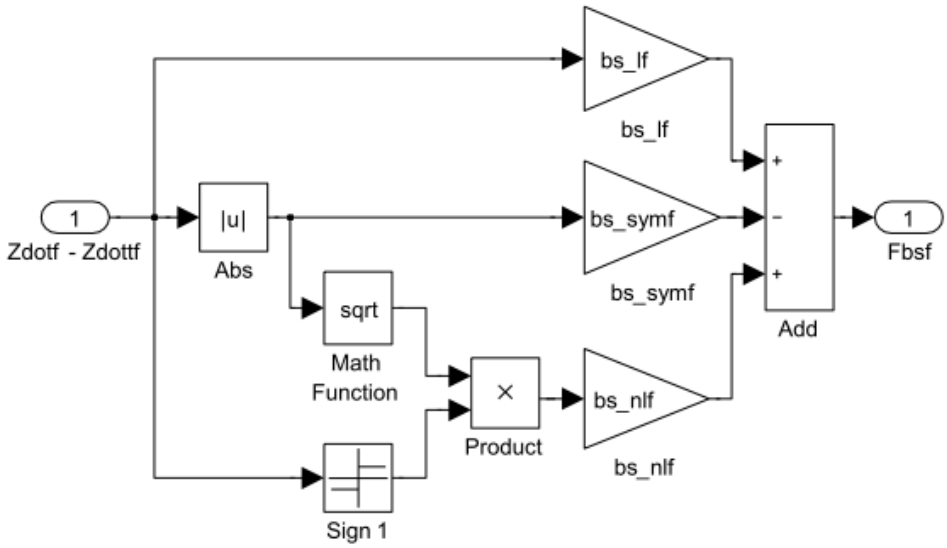

Figure A.5: Matlab/Simulink® implementation of nonlinear front suspension damper force F_{bsf} of Equation 3.7, Section 3.3.

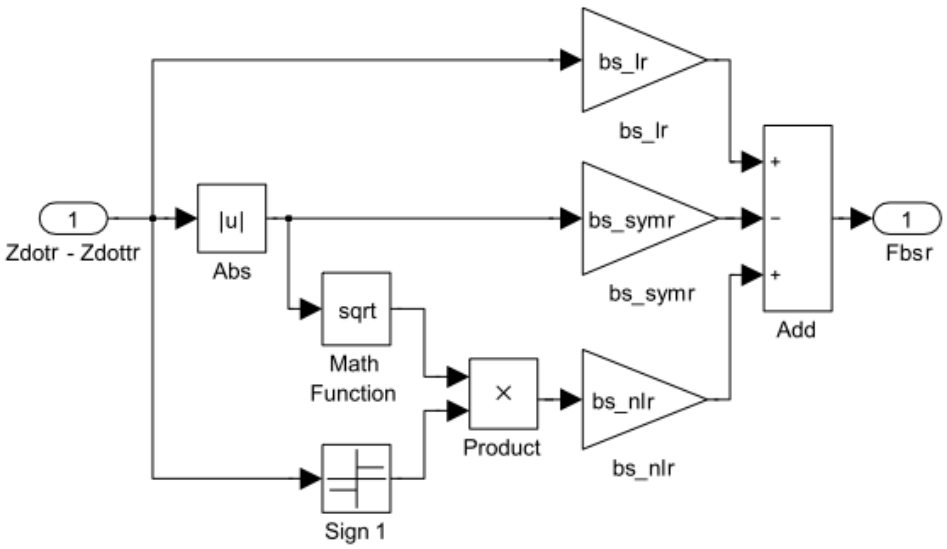

Figure A.6: Matlab/Simulink® implementation of nonlinear rear suspension damper force F_{bsr} of Equation 3.8, Section 3.3.

A.2 Tyre Model Implementation

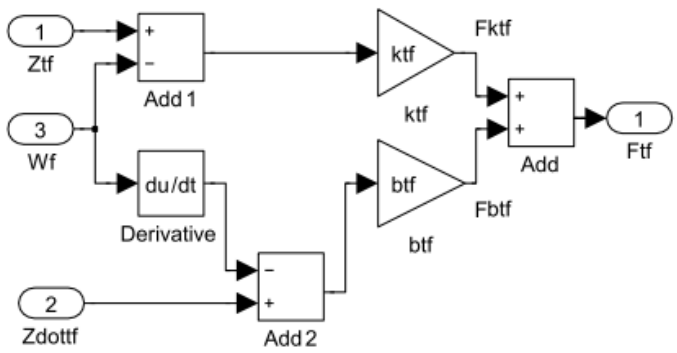

Figure A.7: Matlab/Simulink® implementation of front tyre force F_{tf}, the sum of F_{ktf} (front tyre spring force) given in Equation 3.11 and F_{btf} (front tyre damping force) of Equation 3.12, Section 3.4.

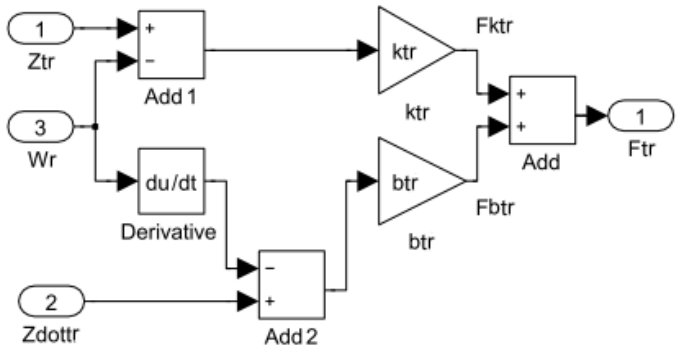

Figure A.8: Matlab/Simulink® implementation of rear tyre force F_{tr}, the sum of F_{ktr} and F_{btr}, rear tyre spring force and rear tyre damping force given in Equations 3.14 and 3.15 respectively, Section 3.4.

A.3 Input Disturbance Implementation

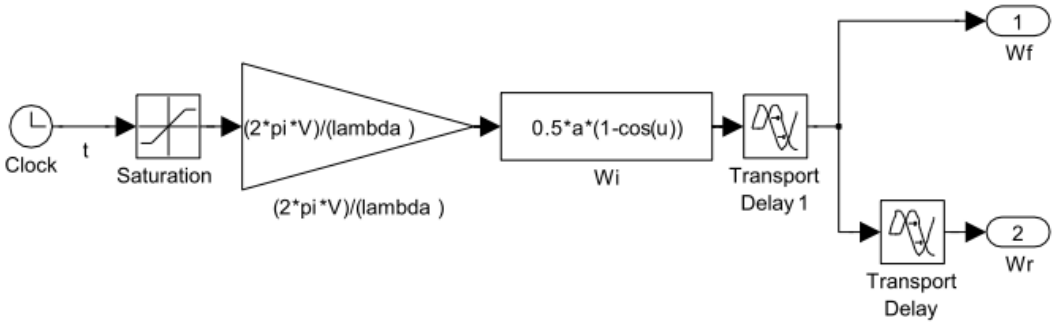

Figure A.9: Matlab/Simulink® implementation of the Discrete Input Disturbance at the front wheel, w_f, (see Equation 3.17, Section 3.5.1).

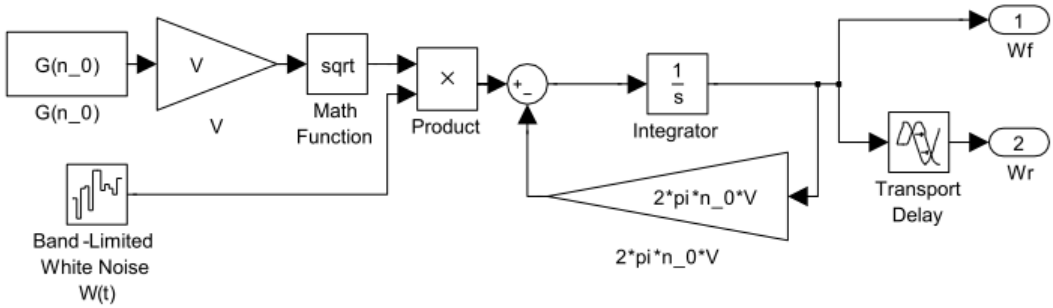

Figure A.10: Matlab/Simulink® implementation of the Random Input Disturbance at the front wheel, w_f, (see Equation 3.21, Section 3.5.2).

A.4 Hydraulic Actuator Implementation

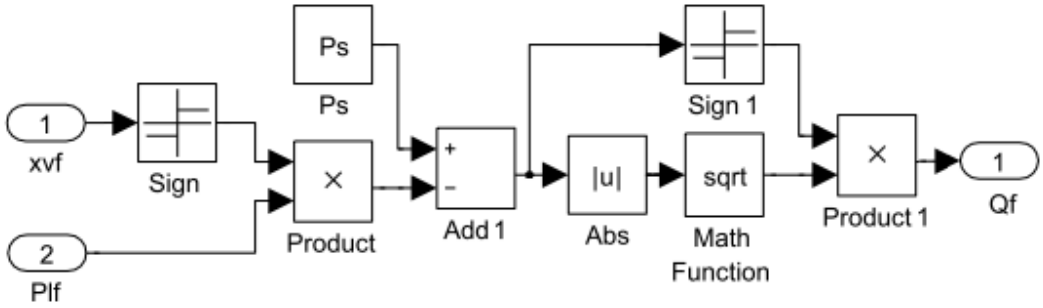

Figure A.11: Matlab/Simulink® implementation of front actuator hydraulic load flow, Q_f, (see Equation 3.29 from Section 3.6).

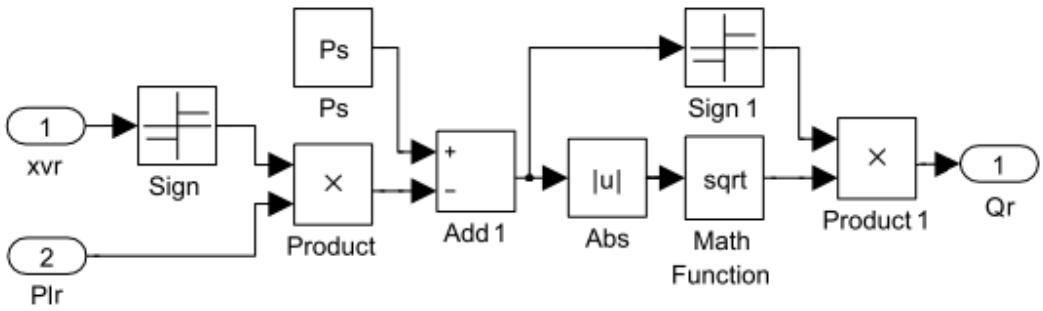

Figure A.12: Matlab/Simulink® implementation of rear actuator hydraulic load flow, Q_r, (see Equation 3.29 from Section 3.6).

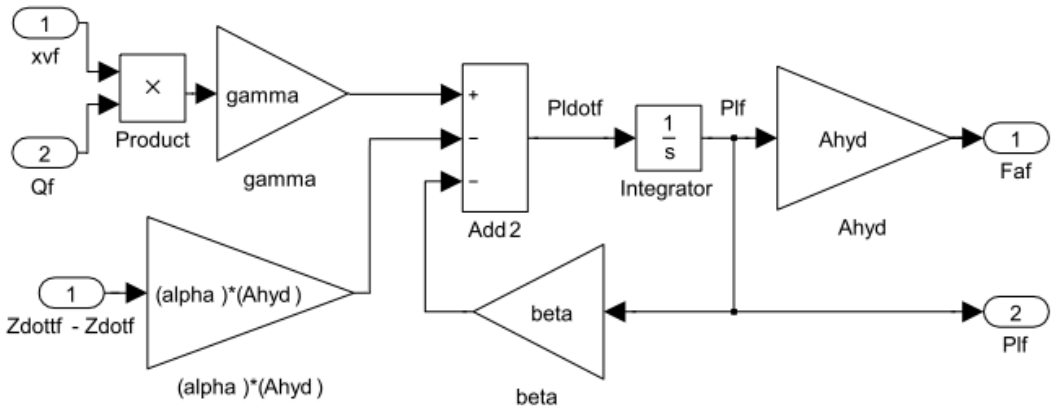

Figure A.13: Matlab/Simulink® implementation of front actuator pressure drop across the hydraulic piston, Pl_f, (see Equation 3.30 from Section 3.6).

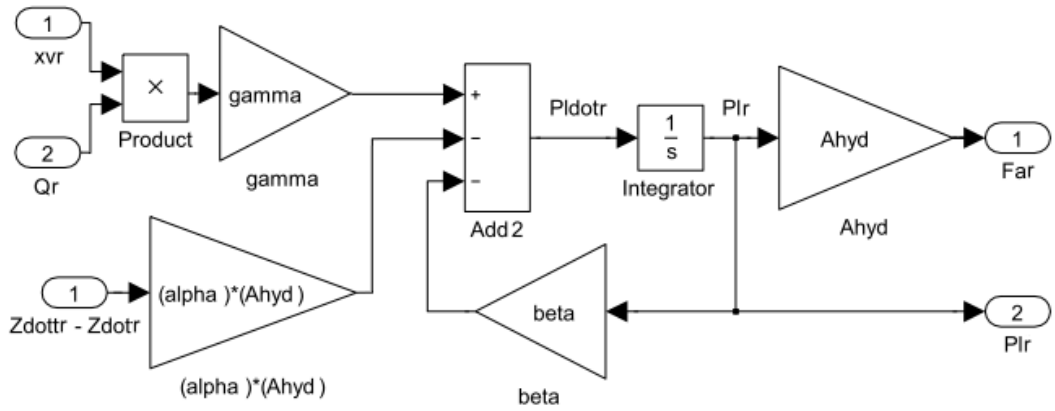

Figure A.14: Matlab/Simulink® implementation of rear actuator pressure drop across the hydraulic piston, Pl_r, (see Equation 3.30 from Section 3.6).

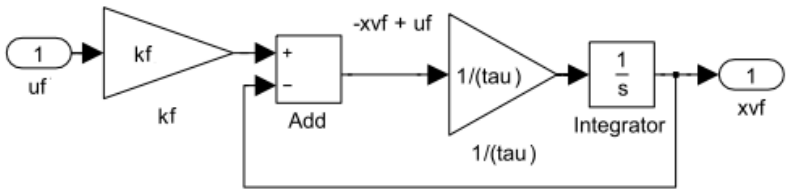

Figure A.15: Matlab/Simulink® implementation of front hydraulic actuator Servo-Valve displacement, x_{vf}, from Equation 3.23, in Section 3.6.

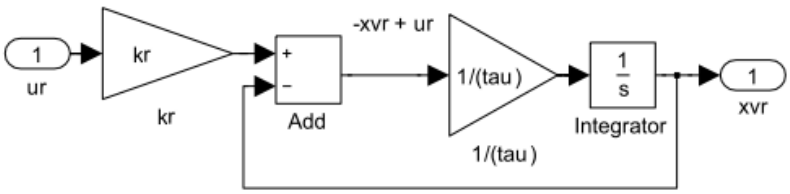

Figure A.16: Matlab/Simulink® implementation of rear hydraulic actuator Servo-Valve displacement, x_{vr}, from Equation 3.23, in Section 3.6.

A.5 Nonlinear Suspension with Hydraulic Actuator Dynamics

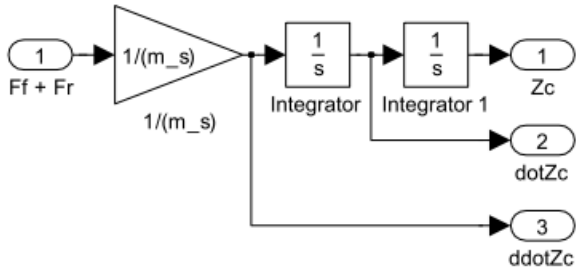

Figure A.17: Matlab/Simulink® implementation of $\ddot{z}_c$, acceleration of the sprung mass center of gravity given in Equation 3.34, in Section 3.7.

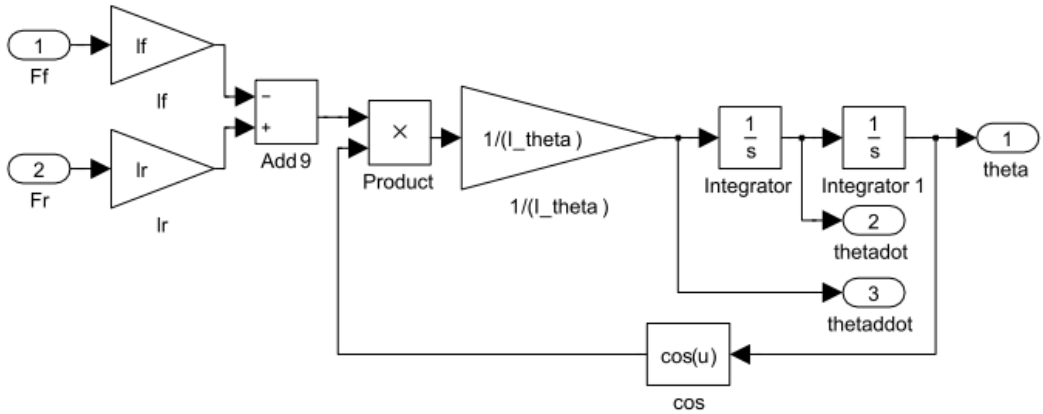

Figure A.18: Matlab/Simulink® implementation of sprung mass inertia, I_θ, see Equation 3.35, in Section 3.7.

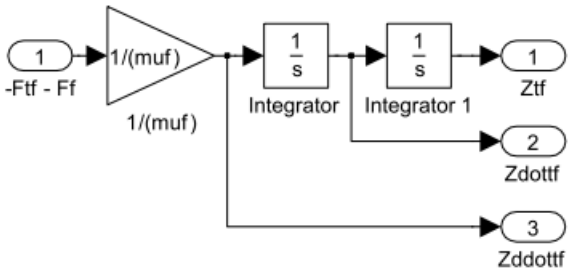

Figure A.19: Matlab/Simulink® implementation of $\ddot{z}_{tf}$, front unsprung mass acceleration, in Equation 3.36, Section 3.7.

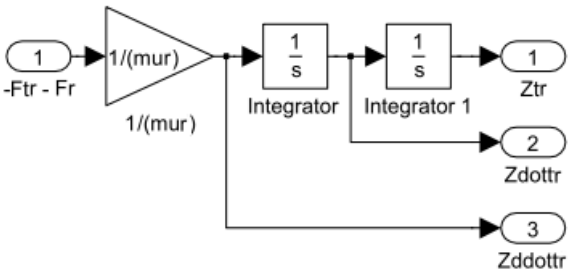

Figure A.20: Matlab/Simulink® implementation of $\ddot{z}_{tr}$, rear unsprung mass acceleration, in Equation 3.37, Section 3.7.